3-14-2014

# Wigner Distribution Functions as a Tool for Studying Gas Phase Alkali Metal Plus Noble Gas Collisions

Keith A. Wyman


# WIGNER DISTRIBUTION FUNCTIONS AS A TOOL FOR STUDYING GAS PHASE ALKALI METAL PLUS NOBLE GAS COLLISIONS

THESIS

Keith A. Wyman, Second Lieutenant, USAF

AFIT-ENP-14-M-39

**DEPARTMENT OF THE AIR FORCE**
**AIR UNIVERSITY**

***AIR FORCE INSTITUTE OF TECHNOLOGY***

**Wright-Patterson Air Force Base, Ohio**

The views expressed in this thesis are those of the author and do not reflect the official policy or position of the United States Air Force, the Department of Defense, or the United States Government.

AFIT-ENP-14-M-39

# WIGNER DISTRIBUTION FUNCTIONS AS A TOOL FOR STUDYING GAS PHASE ALKALI METAL PLUS NOBLE GAS COLLISIONS

THESIS

Presented to the Faculty

Department of Electrical and Computer Engineering

Graduate School of Engineering and Management

Air Force Institute of Technology

Air University

Air Education and Training Command

in Partial Fulfillment of the Requirements for the

Degree of Master of Science in Applied Physics

Keith A. Wyman, B.S.P.

Second Lieutenant, USAF

March 2014

AFIT-ENP-14-M-39

# WIGNER DISTRIBUTION FUNCTIONS AS A TOOL FOR STUDYING GAS PHASE ALKALI METAL PLUS NOBLE GAS COLLISIONS

Keith A. Wyman, B.S.P.
Second Lieutenant, USAF

Approved:

| | |
|---|---|
| //signed// | 17 Mar 1014 |
| David E. Weeks, PhD (Chairman) | Date |
| //signed// | 17 Mar 2014 |
| William F. Bailey, PhD (Member) | Date |
| //signed// | 17 Mar 2014 |
| Glen P. Perram, PhD (Member) | Date |

AFIT-ENP-14-M-39


## Abstract

Wave packet propagation methods are used to compute scattering Wigner Distribution Functions for the square well potential, square barrier potential, the $H + H_2$ and $OH + CO$ molecular collisions, and several $M + Ng$ atomic collisions. The scattering Wigner Distribution Functions are used to interpret how probabilities flow among various potential energy surfaces as a function of time during a collision. Positive values of the scattering Wigner Distribution Function correspond to the addition of probability to scatter into the state that corresponds to the asymptotic limit of the potential energy surface of interest. Negative values correspond to the loss of probability to scatter into the state that corresponds to the asymptotic limit of the surface of interest, and zero values correspond to probability associated with the wave packet that is still in the interaction region. The loss of probability on one surface corresponds to the addition of probability on another surface at different times. Bands of oscillating peaks and valleys that form in the structure of the Wigner Distribution Function correspond to presence of secondary transmission or reflection with significant probability. The square well frequencies at which probability arrive in a scattering channel corresponds to the depth and width of the well. Scattering Wigner Distribution Functions were computed for the following combinations: $K + He$, $K + Ne$, $K + Ar$, $Rb + He$, $Rb + Ne$, $Rb + Ar$, $Cs + Ne$, and $Cs + Ar$. The scattering Wigner Distribution Function revealed that as the mass of the noble gas increased, a significant proportion of probability was transferred from the ${}^2P_{\frac{3}{2}}$ pump state to the ${}^2P_{\frac{1}{2}}$ lasing state for a larger number of total angular momentum values. Similarily, as the mass of the alkali metal decreased, there was a reduced transfer of probability to make a transition from the ${}^2P_{\frac{3}{2}}$ state to the ${}^2P_{\frac{1}{2}}$ state. The reduced probability to make a transition from the ${}^2P_{\frac{3}{2}}$ to the ${}^2P_{\frac{1}{2}}$ manifolds for the $M + He$ collisions is compensated by the large average velocity of

$He$. As a result, the $K + He$ system exhibits a large collisional transition rate despite the kinetic bottleneck caused by the light mass of $He$.

*I dedicate this to my family and friends, who always believed in me.*

**Acknowledgments**

Thank you Dr. Weeks for all the lessons, joys, and disappointments that we faced while working on this project. I'd also like to thank Dr. Bailey and Dr. Perram for putting up with me and providing helpful advice.

Keith A. Wyman

## Table of Contents

Page

## List of Figures

Figure Page

Figure Page

Figure Page

Figure Page

## List of Tables

## List of Other Symbols

| Symbol | Definition |
|---|---|
| $J$ | Total Angular Momentum |
| $E$ | Energy |
| $\omega$ | Frequency |
| $t$ | Time |
| $\tau$ | Time Delay |
| $x$ | Coordinate |
| $k$ | Momentum |
| $\mu$ | Reduced Mass |
| $R$ | Internuclear Separation Distance |
| $\eta$ | Expansion Coefficient |
| $\psi$ | Wavefunction |
| $c(t)$ | Correlation Function |
| $c(\omega)$ | Fourier Transform of Correlation Function |
| $s(E)$ | S-Matrix Element |
| $T(E)$ | Transmission Coefficient |
| $W(t,E)$ | Wigner Distribution Function |

## List of Acronyms

| Acronym | Definition |
|---|---|
| WDF | Wigner Distribution Function |
| PES | Potential Energy Surface |
| DPAL | Diode Pumped Alkali Laser |
| CPM | Channel Packet Method |

WIGNER DISTRIBUTION FUNCTIONS AS A TOOL FOR STUDYING GAS PHASE ALKALI METAL PLUS NOBLE GAS COLLISIONS

# I. Introduction

A laser has three properties. The first property is that there must be an active medium that interacts with photons. Second, a population inversion of the active medium must be achieved in order to achieve gain. The population inversion occurs when more constituents of the active medium are at a higher energy level relative to a lower energy level. Because a population inversion doesn't occur naturally for long durations of time, energy must be provided to the laser system from an external source. The process of exciting constituents of the active medium into a higher energy level is known as pumping. When a constituent is excited to a higher energy level, the constituent will spontaneously emit a photon and de-excite to a lower energy level. This spontaneously emitted photon will travel through the active medium and interact with the other constituents. If there is another constituent at the same energy level as the previous constituent that spontaneously emitted the photon, then the photon can stimulate the new constituent to emit a photon. This stimulated emitted photon will travel in the same direction with the same phase as the spontaneously emitted photon. This process is repeated as long as the photons aren't lost to the laser system. This implies that the third property that a laser must have is an optical feedback system in order to maintain the stimulated emission process. Diode Pumped Alkali Lasers Diode Pumped Alkali Laser (DPAL) has an active medium that consists of an alkali metal generally in the gas phase. As shown in Fig. 1.1, the alkali atoms are in their ground state, the $^2S_{\frac{1}{2}}$ energy level. The ground state alkali atoms are excited by laser light emitted from diode lasers

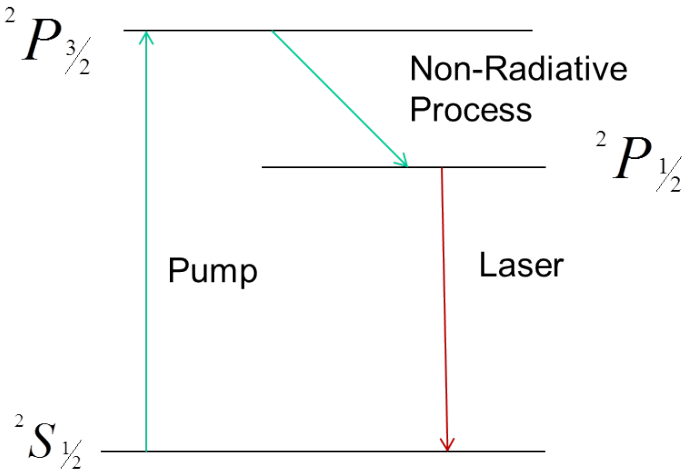


Figure 1.1: Energy Level Diagram for an arbitrary DPAL .

(hence the name DPAL) into the $^2P_{\frac{3}{2}}$ manifold. Through non-radiative processes such as collisions, the alkali atoms are quickly de-excited to the $^2P_{\frac{1}{2}}$ energy level. Because the $^2P_{\frac{1}{2}}$ energy level is a meta-stable state for the alkali atoms, a build-up of alkali atoms can occur on the $^2P_{\frac{1}{2}}$ from the $^2P_{\frac{3}{2}}$ manifold. If the atoms are pumped fast enough to the $^2P_{\frac{3}{2}}$ manifold and are quickly de-excited to the $^2P_{\frac{1}{2}}$ state, then a population inversion between the $^2P_{\frac{1}{2}}$ and $^2S_{\frac{1}{2}}$ energy levels can exist. If this population inversion exists, then lasing can be achieved between the $^2P_{\frac{1}{2}}$ and $^2S_{\frac{1}{2}}$ energy levels at a frequency determined by the difference in energy of these two states.

One potential problem can occur when the non-radiative processes isn't quick enough to produce a build-up of atoms on the $^2P_{\frac{1}{2}}$ energy level before the atoms on the $^2P_{\frac{1}{2}}$ spontaneously decay to the $^2S_{\frac{1}{2}}$ energy level. In order to maximize the output power of a laser, we need to maximize the number of photons that underwent stimulated emission. This implies that we want to maximize the number of atoms in the $^2P_{\frac{1}{2}}$ level relative to the $^2S_{\frac{1}{2}}$ level. Therefore, we want to minimize the amount of time that it takes for an atom in the $^2P_{\frac{3}{2}}$ energy level to decay to $^2P_{\frac{1}{2}}$ energy level.

The primary non-radiative process that de-excites an alkali atom from the $^2P_{\frac{3}{2}}$ energy level to the $^2P_{\frac{1}{2}}$ energy level is a collision with a buffer gas. Various buffer gasses have been experimentally examined as potential collision partners; however, using a noble gas atom as a buffer gas is of interest to us because the noble gas does not undergo a chemical reaction with the alkali atoms which depletes the number of atoms available as an active medium. We are interested in the rate at which alkali atoms in the $^2P_{\frac{3}{2}}$ level are de-excited to the $^2P_{\frac{1}{2}}$ energy level. This rate is related to the probability that an alkali atom on the degenerate $^2P_{\frac{3}{2}}$ energy level before the collision will end up on the $^2P_{\frac{1}{2}}$ energy level after the collision. For this reason we will look at the scattering of an alkali metal ($M$) with a noble gas ($Ng$) at the quantum level in order to determine which noble gas maximizes the probability transfer to the $^2P_{\frac{1}{2}}$ energy level.

Previous studies of a collision involved the use of the correlation function to produce s-matrix elements via the Channel Packet Method (CPM) [8, 9, 11, 16, 17]. The correlation function is a time signal that is produced when the wavefunction of an evolving reactant (initial constituents to a collision) is compared with the wavefunction of a stationary product (final constituents of a collision). The s-matrix elements, which contain all of the information of a scattering event, can be related to the probability that a reactant with a given energy ended up as the product. The problem with this is that we do not know how the probability was transferred between the various possible states that a reactant could end up in during the collision. The tool that we will use to accomplish this task involves the scattering Wigner Distribution Function (WDF). The scattering WDF is the Fourier transform of the autocorrelation of the correlation function with respect to a time delay. The result of this Fourier transform is a quasi-probability distribution as a function of time and energy.

Although the Wigner Distribution Function has been well studied in the past [2, 7, 14, 15, 21], the application of the WDF as a tool in analyzing a collision is new. Previous work

involving the use of the WDF as a tool to analyzing a collision examined the scattering of a reactant in a finite square well potential [7]. The results from this work can be used to compare the accuracy of any code that generates a scattering WDF for a square well potential. For this reason, scattering WDFs were produced for the square well problem. Another reason for producing scattering WDFs for the square well problem is to gain further insight into the meaning of the scattering WDF. Lacy was interested in comparing the scattering WDF with other signal processing techniques such as a spectrogram and determining what features of the WDF can be related back to the parameters of the square well potential or the transmission coefficient [7]. Because our work focused on the transfer of probability among the various states in an alkali metal plus noble gas ($M+Ng$) collision, we will use the simple case of the square well potential to interpret the meaning behind the values that the scattering WDF and how the structure of the scattering WDF can be used to determine where or how probability was transferred during the collision.

Once the scattering WDF for the square well are produced and analyzed, scattering WDF are computed for the finite square barrier potential which has never been done before. The reason for this is that the potential involved in the $M + Ng$ collision contains features that can be roughly estimated by a square barrier. scattering WDFs are also produced for the $H + H_2$ and $OH + CO$ collisions. The correlation functions used to produce the scattering WDFa for the square well were generated by code that I developed; however, the correlation functions for the $M + Ng$ system of interest were developed by Loper [9]. The $H + H_2$ and $OH + CO$ correlation functions were also computed by Weeks [11], and the accuracy of the code in producing scattering WDFs from correlation functions collected by other sources can be compared with the previously produced scattering WDFs for the one case of $H + H_2$. In addition, these collisions also allow us to confirm our understanding of the scattering WDF developed from the square well potential.

Finally, scattering WDFs are computed for 8 different combinations of alkali metal plus noble gas collisions. From these scattering WDFs we hope to find the combination of $M$ and $Ng$ such that the transfer of alkali atoms from the $^2P_{\frac{3}{2}}$ energy level to the $^2P_{\frac{1}{2}}$ level is optimized. Because the $^2P_{\frac{3}{2}}$ energy level is degenerate when there are no other collisional partners present, there will be several states that the probability can flow to other than the states associated with the $^2P_{\frac{1}{2}}$ energy level. Some of these states do not allow for a transfer of probability directly to the states associated with the $^2P_{\frac{1}{2}}$ energy level, and we are interested to know if the probability that ends up on these states in the $^2P_{\frac{3}{2}}$ manifold can quickly find its way to the states associated with the $^2P_{\frac{1}{2}}$ energy level or if there is only a one time transfer of probability among the various states. Because the strength of the forces that allow probability to transfer among these states changes as a function of total angular momentum, we will produce scattering WDFs at various total angular momentum values. From our analysis of these scattering WDFs, we hope to provide conclusions as to which combination of alkali metal and noble gas can optimize the lazing performance of the DPAL system that other sources of scattering information such as the evolving wavefunction, correlation functions, or the s-matrix elements can not easily provide.

# II. Scattering Theory

## 2.1 Scattering Operator

A collision consists of reactants that approach each other and interact in some way. When the reactants are infinitely far apart from each other (the asymptotic region), the individual reactants do not exert a force on each other. Instead the only forces present at the location of a reactant are the forces that make up the reactant. These forces can be described by a Hamiltonian, and the sum of the Hamiltonians for each reactant in this regime make up a Hamiltonian designated as the asymptotic Hamiltonian, $\hat{H}^0$. As the reactants approach each other, the reactants exert a force on each other. This force has an associated potential that is called the interaction potential. The region where the interaction potential is non-zero is called in the interaction region. When the interaction potential is summed with asymptotic Hamiltonian, a new Hamiltonian, $\hat{H}$ is created, and this new Hamiltonian is called the full Hamiltonian since it includes all forces involved in a collision. After the reactants interact with each other, the states that result from the collision are called product states [4]. If $|\psi_{reactant}>$ and $|\psi_{product}>$ are the initial quantum states of the reactants and products respectively, then the time evolution of these quantum states in the asymptotic regions is: $\hat{U}^0|\psi_{reactant}>$ and $\hat{U}^0|\psi_{product}>$ where the time evolution operator in the asymptotic region, $\hat{U}^0$, is

$$\hat{U}^0 = e^{\frac{-i\hat{H}^0 t}{\hbar}}. \tag{2.1}$$

Now let $|\psi(t=0)>$ be an initial quantum state subjugated to the full Hamiltonian of the scattering event. The vector, $|\psi(t=0)>$, is called the Møller state. The time evolution of the Møller state is $\hat{U}|\psi(t=0)>$ where $\hat{U}$ is the time evolution operator of the full Hamiltonian which includes the interaction potential. The Møller state is of interest for the scattering problem because the Møller state results from an intermediate quantum state that started in the asymptotic region and propagated to time $t=0$ under the full Hamiltonian.

The reactant state is also created from this intermediate state located in the asymptotic region except the intermediate state was propagated under the asymptotic Hamiltonian. In the infinite past, the quantum states $|\psi(t = 0) >$ and $|\psi_{reactant} >$ must be indistinguishable (came from the same intermediate state), and similarly, in the infinite future, $|\psi(t = 0) >$ and $|\psi_{product} >$ must be the same. The mathematical statement that is equivalent to this concept is

$$\lim_{t\to-\infty} ||\hat{U}|\psi(t = 0) > -\hat{U}^0|\psi_{reactant} > || = 0 \tag{2.2}$$

$$\lim_{t\to\infty} ||\hat{U}|\psi(t = 0) > -\hat{U}^0|\psi_{product} > || = 0. \tag{2.3}$$

This condition imposes a restriction that the interaction potential tends to zero faster than $\frac{1}{r}$. All interaction potentials used in this study meet this requirement. The Møller state, $|\psi(t = 0) >$, can be solved for in Eq. 2.2:

$$|\psi(t = 0) >= \lim_{t\to-\infty} \hat{U}^\dagger \hat{U}^0|\psi_{reactant} >= \hat{\Omega}_+|\psi_{reactant} > \tag{2.4}$$

$$|\psi(t = 0) >= \lim_{t\to\infty} \hat{U}^\dagger \hat{U}^0|\psi_{product} >= \hat{\Omega}_-|\psi_{product} > . \tag{2.5}$$

where $\hat{\Omega}_+$ and $\hat{\Omega}_-$ are the Møller In and Møller Out operators respectively as defined by Eq. 2.4. The Møller operators produce a Møller state from an initial state. As seen by Eq. 2.4, the initial reactant (product) is propagated backward (foward) into the infinite past (future) under the asymptotic Hamiltonian creating an intermediate state. This intermediate state is then propagated forward (backward) in time under the full Hamiltonian until $t = 0$ The intermediate state created by the Møller In operator is $|\psi_+(t) >$, and the intermediate state produced by the Møller Out operator is $|\psi_-(t) >$. Because the Hilbert Space can be divided into two orthogonal spaces: the bounded and unbounded spaces, every state vector $|\psi(t) >$ that belongs to the unbounded (scattered) space can be produced from either $|\psi_{reactant} >$ or $|\psi_{product} >$ using the Møller In and Møller out operators respectively. Setting the two equations grouped in Eq. 2.4 equal to each other and using the property that Møller operators are isometric, the product state vector can be solved in terms of the reactant state

vector as shown below:

$$|\psi_{product}>=\hat{\Omega}_{-}^{\dagger}\hat{\Omega}_{+}|\psi_{reactant}>=\hat{S}|\psi_{reactant}> \tag{2.6}$$

where $\hat{S}$ is the $\hat{S}$ operator [6, 8, 9, 16]. The $\hat{S}$ operator, which is a unitary operator, contains all of the information regarding the scattering event. Thus the probability that a reactant makes a transition to a product is given by $\mathcal{P}_{i\to f} = |<\psi_{product}|\hat{S}|\psi_{reactant}>|^2$. In order to determine the matrix elements of the $\hat{S}$ operator, the channel packet method is used.

## 2.2 Channel Packet Method

In order to determine the matrix elements of the $\hat{S}$ operator, a basis must be chosen in order to represent the operator. The asymptotic Hamiltonian can be separated into a Hamiltonian that describes the internal motion of the reactant or product and into a Hamiltonian that describes the relative momentum of the reactants or products with the internal states. If $\gamma$ is a quantum number that describes all the internal quantum states of the asymptotic Hamiltonian and $|k_\gamma>$ specifies the relative momentum, then the vector $|k_\gamma,\gamma>$ spans the vector which is known as the $\gamma$ arrangement channel, and this vector is an eigenvector of the asymptotic Hamiltonian. When the Møller operators act on this basis, the $|k_\gamma,\gamma>$ is transformed into a vector labelled $|k_\gamma,\gamma_\pm>$. Because of the intertwining relation of the Møller Operators ($\hat{\Omega}_{\pm}^{\gamma}\hat{H}_{\gamma}^{0} = \hat{H}\hat{\Omega}_{\pm}^{\gamma}$), it can be shown that the transformed basis, $|k_\gamma,\gamma_\pm>$, is an eigenvector of the full Hamiltonian. The reactant or product state expanded as a linear combination of the $|k_\gamma,\gamma>$ basis is

$$|\psi_{in}^{\gamma}>=\int_{-\infty}^{\infty}\eta_{\pm}(k_\gamma)|k_\gamma,\gamma> \tag{2.7}$$

where $\eta_{\pm}(k_\gamma)$ are the expansion coefficients. When the reactant or product state is transformed into the Møller state via the Møller operators, the expansion coefficients of the Møller state with respect to the $|k_\gamma,\gamma_\pm>$ are the same as the expansion coefficients for the reactant or product state in Eq. 2.7.

In order to find the s-matrix elements [8, 9, 11, 16, 17], the Fourier transform of the time evolution of the reactant Møller state, labelled $|A_+^\gamma(E)>$, is taken:

$$|A_+^\gamma(E)>=\int_{-\infty}^{\infty} e^{\frac{-i\hat{H}t}{\hbar}}|\psi_+^\gamma> e^{iEt}dt. \tag{2.8}$$

Substituting the expansion coefficients into Eq. 2.8, using the fact that $|k_\gamma, \gamma_\pm>$ is an eigenvector of the full Hamiltonian, taking the projection of Eq. 2.8 onto the product Møller state, and using the orthogonality relations of $|k_\gamma, \gamma_\pm>$, Eq. 2.8 reduces to

$$<\psi_-^{\gamma'}|A_+^\gamma(E)>=\frac{2\pi\mu}{(|k_{\gamma'}||k_\gamma|)^{\frac{1}{2}}} \tag{2.9}$$

$$\begin{aligned}
&[\eta_-^*(+k'_{\gamma'})\eta_+(+k_\gamma)\mathbf{S}^{\gamma'\gamma}_{+k'_{\gamma'},+k_\gamma}\\
&+\eta_-^*(+k'_{\gamma'})\eta_+(-k_\gamma)\mathbf{S}^{\gamma'\gamma}_{+k'_{\gamma'},-k_\gamma}\\
&+\eta_-^*(-k'_{\gamma'})\eta_+(+k_\gamma)\mathbf{S}^{\gamma'\gamma}_{-k'_{\gamma'},+k_\gamma}\\
&+\eta_-^*(-k'_{\gamma'})\eta_+(-k_\gamma)\mathbf{S}^{\gamma'\gamma}_{-k'_{\gamma'},-k_\gamma}]
\end{aligned}$$

where the + and − sign represent asymptotic states with positive or negative momentum. From Eq. 2.9, we see that careful consideration of the expansion coefficients allows one to isolate a particular s-matrix element. For example, if the reactants were to only have momentum in the direction of the interaction potential and if the products were to only have momentum away from the interaction potential, then only the $\mathbf{S}^{\gamma'\gamma}_{-k'_{\gamma'},+k_\gamma}$ would survive because $\eta_+(-k_\gamma) = \eta_-^*(+k'_{\gamma'}) = 0$. If the expansion coefficients were chosen with care, the s-matrix elements are

$$\mathbf{S}^{\gamma'\gamma}_{\pm k'_{\gamma'},\pm k_\gamma} = \frac{\hbar^2(|k_{\gamma'}||k_\gamma|)^{\frac{1}{2}}}{2\pi\mu\eta_-^*(\pm k'_{\gamma'})\eta_+(\pm k_\gamma)} <\psi_-^{\gamma'}|A_+^\gamma(E)> \tag{2.10}$$

where $<\psi_-^{\gamma'}|A_+^\gamma(E)>$ is the Fourier transform of $<\psi_-^{\gamma'}|e^{\frac{-i\hat{H}t}{\hbar}}|\psi_+^\gamma>$, and $<\psi_-^{\gamma'}|e^{\frac{-i\hat{H}t}{\hbar}}|\psi_+^\gamma>$ is the correlation function, $c_{\gamma'\gamma}(t)$. The correlation function is the overlap between evolving reactant Møller state at each point in time with a product state that is stationary in time for a particular arrangement channel. The correlation function is a time signal that depends upon

the accuracy of the propagation scheme of the reactant Møller state [8, 9, 11, 16, 17]. In Eq. 2.10, the correlation function is used as a tool to calculate s-matrix elements; however, because the correlation function is akin to a signal in time that contains information about the scattering event, other time signal-processing tools can be performed on the correlation function to hopefully determine information about the scattering event. One such signal-processing technique involves the Wigner Distribution Function [21].

# III. Wave Packet Propagation

In order to produce correlation functions that can be used to generate Wigner Distribution Functions, the propagation of the reactant Møller state must be accurate. The Split Operator Equation will be used to propagate the reactant Møller state, and the accuracy of the Split Operator Method will be verified with the propagation of a wave packet in free space and a coherent state in a quantum harmonic oscillator.

## 3.1 Split Operator Theory

The time evolution of a quantum system is governed by Schrdinger's Equation:

$$|\psi(t)>= e^{\frac{i\hat{H}t}{\hbar}}|\psi(t=0)> . \tag{3.1}$$

One method to finding an analytical solution to $|\psi(t)>$ consists of constructing the Hamiltonian and then constructing the appropriate transformation matrix that diagonalizes the Hamiltonian. The transformation operator is applied to Eq. 3.1, and $|\psi(t)>$ is transformed to the eigenvector basis of the Hamiltonian. For the scattering problem, we wish to instead express the Hamiltonian in terms of the kinetic and potential operators,

$$|\psi(t)>= e^{\frac{I(\hat{T}+\hat{V})t}{\hbar}}|\psi(t=0)> \tag{3.2}$$

where $\hat{T}$ is the kinetic energy operator and $\hat{V}$ is the potential operator. The Taylor Series expansion of Eq. 3.2 is given by:

$$|\psi(\Delta t)>= [\hat{1} - \frac{i\Delta t}{\hbar}(\hat{T}+\hat{V}) - \frac{\Delta t^2}{2\hbar^2}(\hat{T}^2 + \hat{T}\hat{V} + \hat{V}\hat{T} + \hat{V}) + ...]|\psi(t=0)> . \tag{3.3}$$

To third order, this equation is equivalent to the Taylor Series expansion of

$$|\psi(\Delta t)>= e^{\frac{-i\hat{V}\Delta t}{2\hbar}} e^{\frac{-i\hat{T}\Delta t}{\hbar}} e^{\frac{-i\hat{V}\Delta t}{2\hbar}}|\psi(t=0)> . \tag{3.4}$$

Eq. 3.4 is called the Split Operator Equation [7–9, 11, 17]. The potential operator is diagonalized in the position basis, and the kinetic operator is diagonalized in the momentum

basis. In order to study the time evolution of a wave packet, we need to apply a transformation to the momentum basis and back to the position basis. The transformation between position and momentum basis is the inverse Fourier transform.

### *3.1.1 Fourier Transform and Discrete Fourier Transform.*

The Fourier transform belongs to a class of transformations that transforms a vector in one basis to a vector in another basis. For example, the inverse Fourier transform transforms the function $\psi(x) =< x|\psi >$ from the coordinate representation of the vector $|\psi >$ into the momentum representation of $|\psi >$ which is $\psi(k) =< k|\psi >$. In order to accomplish a transformation between one representation of a vector into another representation, the projection of the one basis onto the other basis must be known. For example, to obtain $\psi(k)$, we use completeness of the coordinate vector to show that $< k|\psi >=< k| \int |x >< x|dx|\psi >= \int < k|x >< x|\psi > dx$. The projection of the coordinate vector onto the momentum vector, $< k|x >$, is $e^{-ikx}$, and from properties of linear algebra $< x|k >=< k|x >^* = e^{ikx}$. The Fourier transform, $\mathcal{F}$, is defined to be a transformation from one basis to another such that the projection of the continuous basis onto the other continuous basis is $e^{ikx}$, and the inverse Fourier transform,$\mathcal{F}^{-1}$ will have the projection equal to $e^{-ikx}$. In terms of functions, the Fourier transform looks like

$$\psi(k) = \int_{-\infty}^{\infty} \psi(x) e^{-ikx} dx \tag{3.5}$$

$$\psi(x) = \frac{1}{2\pi} \int_{-\infty}^{\infty} \psi(k) e^{ikx} dk. \tag{3.6}$$

The factor $\frac{1}{2\pi}$ arises from the fact that the Fourier transform and the inverse Fourier transform are not symmetric. Without the two pi factor, $\mathcal{F}\mathcal{F}^{-1}[\psi(x)] \neq \psi(x)$, and the result would be off by a constant factor [3].

The Fourier transform assumes that the basis vectors are continuous; however, due to the limits of a computer, a discrete set of points, $N$, are sampled. As a result, the integral

must be approximated by a discrete sum, and the Fourier transform and its inverse are now:

$$\psi(k) = \Delta x \sum_{j=0}^{N-1} \psi(x_j) e^{ik_j x_j} \tag{3.7}$$

$$\psi(x) = \frac{1}{N} \sum_{j=0}^{N-1} \psi(k_j) e^{ik_j x_j}. \tag{3.8}$$

The discrete Fourier transform requires on the order of $N^2$ calculations. For large arrays with lengths such as $10^6$, this can take up to two weeks of CPU time. In order to create a more efficient algorithm to calculate the discrete Fourier transform, the Fast Fourier Transform was developed (FFT). The idea behind the FFT is that a discrete Fourier transform of length N can be rewritten as the sum of two discrete Fourier transforms, each of length $\frac{N}{2}$. This process can be done recursively such that each component is further divided into two discrete Fourier transforms each with half the length. If the original number of sampled points, $N$, is an integer power of two, then the discrete Fourier transform can be reduced to a series of transforms of length one. Using bit reversal and combining pairs, the discrete Fourier transform can be calculated on the order of $Nlog_2N$ calculations which reduces the CPU time to 30 seconds for an array of length $10^6$. If the number of sampled points is not an integer power of two, then Press [3] recommends that data set is at a minimum padded with zeros until the length of the data set is a power of two.

### *3.1.2 Fast Fourier Transform.*

Due to the sampling theorem [3], the grid sizes of conjugate variables are linked in an FFT. The coordinate grid will consist of $n$ evenly spaced points ranging from a minimum value, $x_{min}$, to a maximum value $x_{max}$. The spacing of the coordinate grid, $\Delta x$ is simply,

$$\Delta x = \frac{x_{max} - x_{min}}{n - 1}. \tag{3.9}$$

The maximum and minimum values of $k$ which depend upon the sampling interval, $\Delta x$, are given by the Nyquist critical momentum, and the evenly spaced interval of the momentum grid also depends upon the resolution of the coordinate grid and the number of sampled

points. The momentum grid is defined as:

$$k_{max/min} = \pm\frac{2\pi}{2\Delta x} \tag{3.10}$$

$$\Delta k = \frac{2\pi}{n\Delta x}. \tag{3.11}$$

As shown in Eq. 3.10, increasing the resolution in the coordinate system (decreasing $\Delta x$) decreases the resolution of the momentum grid and the bandwidth of momentum that can be sampled. The increments between data points in each grid system must be capable of resolving the features of the wavefunction in the basis defined by the grid. Similarly, the range of momentum for a particular wavefunction must be within the bounds established by the Nyquist critical momentum. Otherwise, distortions will appear in the FFT because the momentum that fall outside the range in Eq. 3.10 will be falsely translated into the domain. This phenomenon is called aliasing [3, 7]. To avoid aliasing, the initial conditions of the wavefunction must have momentum that falls to zero within machine error near the maximum and minimum values of momentum, or the wavefunction must contain at least two points per cycle of the highest momentum value present. Although the Fourier transform between the momentum and coordinate representations of a function were focused on, the Fourier transform can also transform a time signal into a frequency spectrum, and the same considerations applies. The FFT used in this project was FFTPack5 which is a Fortran subroutine library writen by Paul Swarztrauber and Richard Valent. The FFT package is independent of the grid that the Fourier transform is taking place on, so it is up to the user to properly analyze the resulting grid.

### 3.2 Free Particle Propagation

A particle in free space experiences no potential by definition [4]. As a result, there are no boundary conditions to restrict the energy eigenvalues of the Hamiltonian, and the particle is expected to have a continuous range of energy values. Although the plane wave is a solution to Schrdinger's equation to a particle in free space, the plane wave does not

belong to the Hilbert space because the plane wave is not a square integrable function. This means that the plane wave is not a physically realizable quantum state. Instead the superposition of plane waves which is square integrable is used as a solution to Schrdinger's Equation [19]. Mathematically, a this superposition of plane waves which is called a wave packet has the following general form:

$$< x|\psi(t) >= N \int_{-\infty}^{\infty} c(k) e^{ikx} dk \tag{3.12}$$

where $N$ is the normalization factor for the wave packet, $c(k) =< k|\psi(t = 0) >$ are the expansion coefficients, and $e^{ikx}$ is the plane wave. One set of expansion coefficients, $c(k) = (\frac{2\delta^2}{\pi})^{\frac{1}{4}} Exp[-\delta^2(k - k_o)^2 - ik_o x_o]$ where $\delta$ is the spread of Gaussian wave packet projected onto the coordinate representation (the uncertainty in x or the width of the Gaussian), $x_0$ is the initial displacement of the Gaussian, and $k_0$ is the initial displacement of the Gaussian wave packet, creates a special type of wave packet called the Gaussian wave packet. The evolution of a free particle that was initially in a Gaussian state will have the following analytical solution:

$$\psi(x,t) = (2\pi\delta^2)^{-\frac{1}{4}}(1 + \frac{i\hbar t}{2\mu\delta})^{-\frac{1}{2}} Exp[\frac{-\frac{(x-x_o)^2}{4\delta^2} + ik_o(x - x_o) - \frac{ik_o^2 t\hbar}{2\mu}}{1 + \frac{i\hbar t}{2\mu\delta^2}}]. \tag{3.13}$$

The Gaussian wave packet projected onto the momentum representation which is the inverse Fourier transform of Eq. 3.13 is

$$\psi(k,t) = (\frac{2\delta^2}{\pi})^{\frac{1}{4}} Exp[-\delta^2(k - k_o)^2 - ik_o x_o - \frac{ik^2\hbar t}{2\mu}] \tag{3.14}$$

The propagation of a Gaussian wave packet is known analytically as described by Eq. 3.13. Because the particle is in free space, the potential is assumed to be zero for all values of position, and the potential operator reduces to the zero operator. As a result, the kinetic operator now commutes with the potential operator, and the wavefunction determined by the split operator method, Eq. 3.4, reduces to

$$|\psi(\delta t) >= e^{\frac{i\hat{T}\delta t}{\hbar}} |\psi(t = 0) > . \tag{3.15}$$

which is exact. Eq. 3.13 and Eq. 3.15 will produce the same result regardless of the step size in time. The kinetic operator is diagonalized in the momentum representation. The values in a diagonalized matrix are the eigenvalues of the associated operator that the matrix represents. Because $|\psi(t = 0) >$ is initially projected onto the coordinate representation, an FFT from the coordinate representation of the initial wavefunction to the momentum representation is required. Because

$$F(\hat{A})|\phi >= F(a)|\phi > \tag{3.16}$$

where $F$ is a function of the operator $\hat{A}$, $a$ is the eigenvalue of the operator, and $|\phi >$ is the eigenvector of the operator, $|\psi(\delta t) >$ is a diagonalized matrix. In order to find the wavefunction at a particular time $|\psi(t) >$, the process is iterated with $|\psi(n\delta t) >$ becoming the initial condition for $|\psi((n + 1)\delta t) >$ where $n$ is an integer. Generally, the coordinate representation is preferred, so another Fourier transform is required to transform $|\psi(t) >$ into the coordinate representation.

The parameters of the initial Gaussian wave that was propagated along with the propagation parameters and grid sizes are in Table 3.1. The purpose of the free particle propagation was to test the propagation and FFT codes for a simple case, so the parameters were chosen for simplicity and have no resemblance to any physical phenomenon. The wave packet was propagated for 2 atomic units and compared to the analytical results. Fig. 3.1(a) shows the initial wave packet and Fig. 3.1(b) shows the analytical and computation results. As evident in Fig. 3.1(b) , the analytical and computation results overlap. Fig. 3.2 shows the relative error between the propagated wavepacket and the analytical wavepacket.

Table 3.1: Gaussian Wave Packet Parameters

| variable | value | meaning |
|---|---|---|
| $n_{time}$ | 2048 | number of time grid points |
| $x_0$ | 0 | initial reactant coordinate displacement |
| $k_0$ | 0 | initial reactant momentum displacement |
| $\delta$ | 1 | initial spread of reactant in x |
| $t_{min}$ | 0 | minimum time |
| $t_{max}$ | 2 | maximum time |

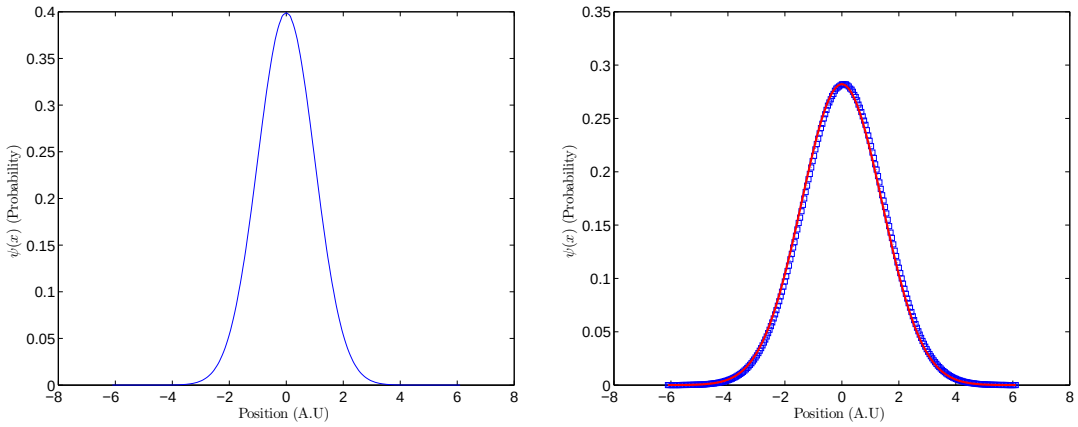


(a) The initial Gaussian wavepacket

(b) The propagated wavepacket

Figure 3.1: The norm of the initial Gaussian wavepacket, with parameters described in table 3.1, propagated for a time of 2 atomic units in coordinate space. The norm of the evolved Gaussian wavepacket, blue squares, is plotted on the same figure as the norm of the analytical solution, red.

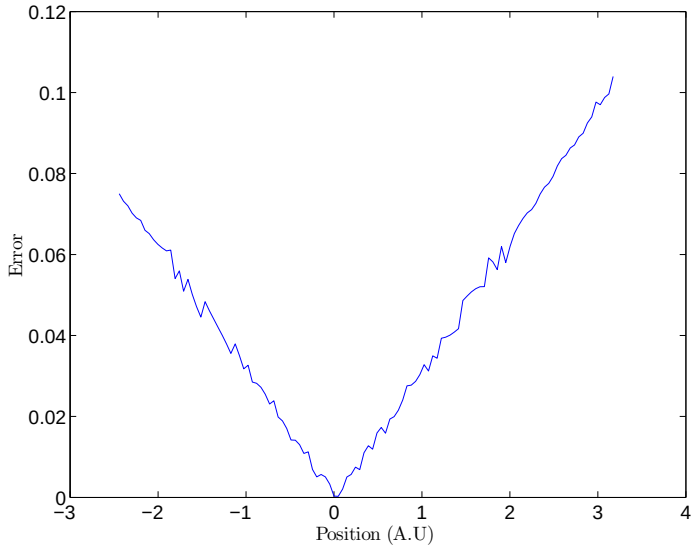


Figure 3.2: The relative error between the propagated wavepacket and the analytical wavepacket.

### 3.3 Propagation of a Coherent State of a Quantum Harmonic Oscillator

A coherent state of the harmonic oscillator is defined as the quantum state where the expectation value of observed quantities equals the classical value of the same observable for all time in the limit of large quantum numbers [4]. For example, the momentum and position of a classical particle in a harmonic potential oscillate between a minimum and maximum value. The expectation values of the momentum and position operators of a coherent state will match these values for all time. Using the displacement, raising, and lowering operators, it can be shown that the displacement operator acting on the ground state of the quantum harmonic oscillator is a coherent state. The displacement operator simply boosts and translates the ground state, which is a Gaussian with parameters that depend upon the harmonic potential. If $< x >$ is the expectation value of the coordinate $x$, $< P >$ is the expectation value of momentum $P$, $\omega$ is the frequency of the oscillator, $m$ is the mass of the particle, $\alpha$ is a complex number, and $\theta$ is a phase factor, then the coherent state for the harmonic oscillator is defined as

$$\psi_\alpha(x) = e^{i\theta_\alpha}\left(\frac{m\omega}{\pi\hbar}\right)^{\frac{1}{4}} e^{-\left[\frac{x-<x>_\alpha}{2\Delta x_\alpha}\right]^2 + i<P>_\alpha \frac{x}{\hbar}} \tag{3.17}$$

Because the ground state of the harmonic oscillator is stationary state, the time evolution of the coherent state is straightforward:

$$\begin{aligned}
\psi(x,t) &= e^{i\theta_\alpha(t)}\left(\frac{m\omega}{\pi\hbar}\right)^{\frac{1}{4}} e^{-\left[\frac{x-<x>_\alpha(t)}{2\Delta x_\alpha}\right]^2 + i\left[<P>_\alpha(t)\frac{x}{\hbar} - \frac{\omega t}{2}\right]} \\
< x > (t) &= \sqrt{\frac{2\hbar}{m\omega}} Re[\alpha(t)] \\
< p > (t) &= \sqrt{2m\hbar\omega}\, Im[\alpha(t)] \\
\Delta x &= \sqrt{\frac{\hbar}{2m\omega}} \\
\Delta P &= \sqrt{\frac{m\hbar\omega}{2}} \\
\theta_\alpha(t) &= \frac{\alpha^*(t)^2 - \alpha(t)^2}{4}
\end{aligned} \tag{3.18}$$

We see that when $|\alpha| >> 1$, the expectation values of the position and momentum operators equal the classical trajectories. A particle in a classical harmonic trajectory will oscillate between a maximum position and a minimum position where momentum is zero at these positions. The center of the oscillation will have the largest momentum. From Eq. 3.18, the width and amplitude of the wave packet does not vary with time. Physically, this is due to the fact that spreading of the Gaussian wave packet is overcome by the squeezing of the harmonic potential. This squeezing of the wave packet from the harmonic potential results from the tendency to move away from the edges of the potential where the potential is large [4]. This feature of the coherent state is very valuable because the Gaussian wave packet can remain localized to the harmonic oscillator throughout the entire oscillation and because the norm of the Gaussian wave packet ($\psi * \psi$) translates back and forth without changing shape.

Because the propagation of a coherent state of a quantum harmonic oscillator is known analytically for all time, the solution arrived at using the split operator method can be compared with analytical results, Eq. 3.18. A coherent state solution is a displaced ground state as discussed previously, and the displaced ground state, which is a Gaussian wave packet, will oscillate with expectation values matching classical trajectories. For our code,

a Gaussian wave packet was placed at the amplitude of oscillation, and the resulting wave packet was recorded at various times.

Because the potential operator and the kinetic operator do not commute, a set of basis vectors cannot simultaneously diagonalize both the kinetic and potential operators. The basis for which the potential operator is diagonal is the coordinate basis. Because the initial condition is given in the coordinate representation, we can apply Eq. 3.16 directly to the initial condition. Because the kinetic operator is diagonalized in the momentum representation, an FFT is used to transform $e^{\frac{i\hat{V}\delta t}{\hbar}}|\psi(t=0)>$ into the momentum representation. After applying Eq. 3.16, another FFT is used to transform the result back into the coordinate representation since the potential operator is diagonalized in the coordinate representation. The evolution of the initial wavefunction at a small time step later, $|\psi(\Delta t)>$, is known after applying Eq. 3.16 one last time. The code to propagate the initial wave packet now looks like

$$\psi(x,\Delta t) = e^{\frac{-i\hat{V}\Delta t}{2}}\mathcal{F}[e^{\frac{i\hat{T}\Delta t}{\hbar}}\mathcal{F}^{-1}[e^{\frac{-i\hat{V}\Delta t}{2}}\psi(x,0)]] \tag{3.19}$$

In order to determine the wavefunction at a particular time $t$, Eq. 3.19 is calculated iteratively [7–9]. Because the amplitude and width of the coherent state remains constant and because the coherent state can oscillate on a grid that fits within the computational window, the evolution of the coherent state can be observed for large times. Small errors that occur in a single iteration of the split operator method will grow and after many iterations can become large. We can use this concept to determine the if the size of the time step used in the split operator was sufficient for the split operator to approximate. It was shown by Lacy [7] and verified here that a time step of approximately $\Delta t = 0.01$ atomic units is sufficient for the split operator approximation.

The parameters of the initial coherent state, the propagation parameters, the grid sizes, and the potential parameters are shown in Table 3.2. The purpose of the coherent state propagation was to test the propagation code, so the parameters were again chosen for

simplicity and have no resemblance to any physical system. Because the coherent state follows the classical trajectory of a particle in the same potential, the initial coherent state was set up at the maximum amplitude of oscillation. The coherent state was propagated for $t = 50.25\pi$ atomic units and compared to the analytical results for the corresponding times. The frequency of the oscillator is 1 atomic unit. Fig. 3.3(a) shows the initial coherent state and Fig. 3.3(b) shows the analytical and computation results. As evident in Fig. 3.3(b) , the analytical and computation results overlap.

Table 3.2: Coherent State Parameters

| variable | value | meaning |
|---|---|---|
| $n_{time}$ | 4096 | number of time grid points |
| $t_{min}$ | 0 | minimum time |
| $t_{max}$ | $50.25\pi$ | maximum time |
| $< x_0 >$ | 5 | initial coordinate displacement |
| $< k_0 >$ | 0 | initial momentum displacement |
| $\delta$ | 0.707 | initial spread of reactant in x |
| $\omega$ | 1 | frequency of oscillator |
| $\mu$ | 1 | mass of particle |

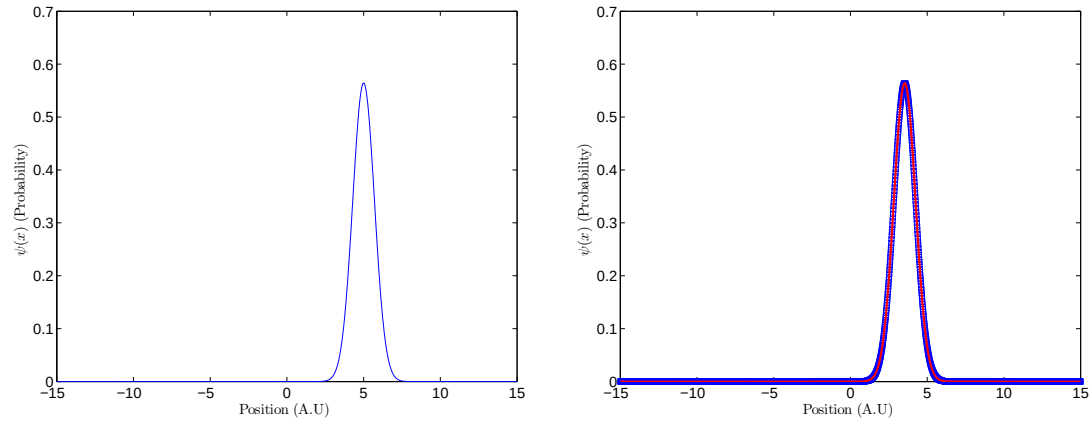


Figure 3.3: The Coherent State of quantum harmonic oscillator. The potential parameters and the initial condition of the coherent state are found in table 3.2. The initial coherent state which is a displaced Gaussian wavepacket is shown in the figure on the left. The coherent state is propagated to a time of $50.25\pi\omega$ atomic units in coordinate space in the figure on the right. The numerically computed coherent state, blue squares, is plotted in the same figure on the right as the analytical solution, red. Both figures overlap.

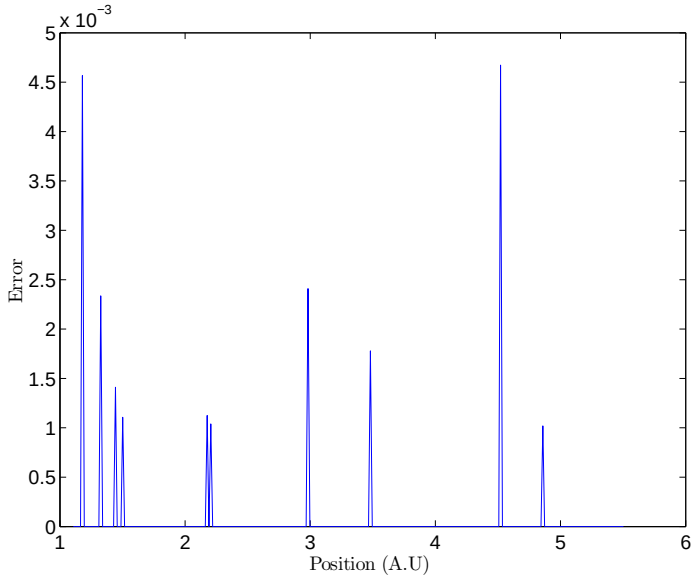


Figure 3.4: The relative error between the propagated coherent state at time $t = 50.25\pi\omega$ atomic units and the analytical coherent state.

# IV. Square Well

## 4.1 Square Well

The square well potential allows for both bounded states ($E < 0$) and scattering states ($E > 0$) [4, 5]; however, we will only consider scattering states. The square well potential has three regions on the position grid. In the first and third regions, the potential is assumed to be zero; however, in the second region, the potential is a constant value, $V$, over a length of $L$. Each of these regions assumes a solution to the wavefunction in the form of

$$\psi(x) = A_i e^{ik_i x} + B_i e^{-ik_i x} \tag{4.1}$$

where $i$ labels the region and $A$ and $B$ are constants in the $i^{th}$ region. Eq 4.1 is the superposition of an incoming plane wave with an outgoing plane wave for each value of momentum. An incoming wave is defined as a plane wave heading towards the square well and the outgoing wave is defined as a plane heading away from the square potential.

At the boundaries of the square well, the potential jumps from the constant potential to the zero potential; however, the wavefunction must be continuous and the first derivative of the wavefunction must also be continuous. Applying the continuity conditions at both boundaries of the well boundaries, we have a system of four equations with six unknowns. Solving the coefficients of the first region in terms of the coefficients in the second region, and solving the second region's coefficients in terms of the third regions coefficients, the first region can be solved in terms of the third region for a given energy. The connection between the first and third region can be accomplished with a $2 \times 2$ transformation matrix for each value of momentum, $k$. The first and third regions are akin to the asymptotic regions described in the scattering theory section, and the second region is equivalent to the interaction region. Instead of a matrix that transforms the third region into the first region, we seek a matrix, the s-matrix, that connects the incoming waves to the outgoing waves. The outgoing waves of the first and third region can be solved using algebra in

terms of the outgoing waves of the first and third region for a given energy. If we assume that there are no incoming waves in the third region, then the outgoing waves, $B_1$ and $A_3$ , can be expressed in terms the incoming wave, $A_1$ using only two s-matrix elements. The s-matrix element, $s_{k_1,k_3}$, that relates $A_3$ with $A_1$ is related to the transmittance of $A_1$ through the square well while the s-matrix element, $s_{k_1,k_1}$, that relates $B_1$ with $A_1$ is related to the reflectance of $A_1$ through the square well. The transmission coefficient is

$$T(E) = |S_{k_1,k_3}|^2 = \frac{1}{1 + \frac{V^2}{4E(E+V)} sin^2(\frac{2L}{\hbar}\sqrt{2m(E+V)})}. \tag{4.2}$$

where $L$ is the length of the well, $m$ is the mass of the particle, $E$ is energy, and $V$ is the magnitude of the well depth. Eq. 4.2 provides an analytical solution to compare the computationally produced transmission coefficient. Because the computationally produced transmission coefficient involved the channel packet method, Eq. 4.2 was used to verify the accuracy of the correlation function produced.

The sinusoidal term in Eq. 4.2 creates a series of oscillating peaks and valleys between the values of one and zero. The location of the peaks in the transmission coefficient align with the eigenvalues of the infinite square well potential. The eigenvalues of the infinite square well potential are $E_n = \frac{\hbar^2\pi^2n^2}{2mL^2}$ where $n$ is the $n^{th}$ eigenvalue, so the location of the peaks is given by $E = E_n - V$. The location of the valleys of the transmission coefficient can be approximated as the average between two consecutive peaks. The difference between the peak and valley describes the resonance of the square well. The larger the difference between the peak and valley, the greater the resonance. The degree of resonance in the peaks of the transmission coefficient is quantized by a parameter value, $\beta$ which depends upon the characteristics of the square well as shown below [24]:

$$\beta = \frac{L\sqrt{2mV}}{\hbar}. \tag{4.3}$$

Re-expressing Eq. 4.2 in terms of $\beta$ and the eigenvalues of the infinite square well, we have

$$T(E) = |S_{k_1,k_3}|^2 = \frac{1}{1 + \frac{V\beta^2}{4\pi n^2(E_n - V)} sin^2(\frac{2L}{\hbar}\sqrt{2m(E+V)})}. \tag{4.4}$$

We see that $\beta$ influences the amplitude of the sinusoidal term. When the argument of the sine function in Eq. 4.4 is zero, the transmission coefficient is a maximum, but when the argument of the sine function is $\frac{\pi}{2}$ radians, the transmission coefficient is a minimum. The amplitude of this minimum is determined by the amplitude of the sine function which is $\frac{V\beta^2}{4\pi n^2(E_n-V)}$. As $\beta$ increases, the difference between the maximum and minimum values increases. From Eq. 4.3, we see that increasing the depth of the well increases the $\beta$ parameter or resonance of the transmission coefficient which was produced from the correlation function.

In order to calculate the correlation function, a wave packet was propagated through a one-dimensional finite square well potential in order to calculate s-matrix elements which determine the transmission coefficient. To summarize the propagation scheme:

1. Set up the initial wavefunction, $|\psi(0)>$, in coordinate space: $< x|\psi(0) >$
2. Operate on the wavefunction with $e^{\frac{-i\hat{V}\Delta t}{2}}$
3. Transform the resulting wavefunction to momentum space via an inverse FFT
4. Operate on the wavefunction with $e^{\frac{i\hat{T}\Delta t}{\hbar}}$
5. Transform the resulting wavefunction to coordinate space via a FFT
6. Operate on the resulting wavefunction with $e^{\frac{-i\hat{V}\Delta t}{2}}$
7. Repeat items 2-6 for each $\Delta t$ step until $< x|\psi(t) >$ is obtained

The resolution of the time grid must be taken into consideration in order for the above propagation scheme to work. The split-operator theory is only accurate with the Taylor Series expansion of Schrdinger's equation up to third order assuming that $\Delta t$ is small. As shown with the harmonic oscillator, a time step of $\Delta t \approx 0.01$ is sufficient for propagation. Similarly, the resolution of the x grid is important not only because of Eq. 3.10 but because

of the boundary of the square potential. For a square potential, the potential function can be thought of as a step function at the edges of the potential. If $\Delta x$ was too large, then the distance between two points on the x grid would be large, and the potential would no longer drop off like a step function. Instead, the square well or square barrier would become a trapezoidal potential which has different properties than the square potential, and the code would not match the analytical results.

### 4.2 Absorbing Boundary Conditions

Another consideration that needs to be taken into account are the boundaries of the computational window [7, 11]. In Fortran, if a function extends passed the window, it loops back to the other side. Consequently, a propagating wavefunction with positive momentum that reaches the maximum x grid coordinate will loop back to the minimum x grid coordinate and add to the component of the wavefunction that was present at $x_{min}$. This issue has not been a problem with previous potentials because we were not concerned with either propagating the wavefunction for long periods or the wavefunction was trapped oscillating within the window for infinity; however, because calculating s-matrix elements and Wigner Distribution Functions requires the correlation function to die off, the wave packet must be propagated for long periods of time. One fix to the issue would be to extend the grid to larger values of x. Unfortunately, this solution comes with the trade-off in computation time. In order to be able to keep the resolution of the wavefunction, the number of sampled points must increase as the size of the grid increases.

An alternative solution would be to impose absorbing boundary conditions. Absorbing boundary conditions force the wavefunction at the boundaries to decay to zero in order to minimize artificial contributions to the correlation function when the wavefunction loops to the other side [7, 11]. To accomplish this, an imaginary potential term localized at the edges of the computation window will be added to the interaction potential such that $\hat{V} = \hat{V}_{int} + i\hat{V}_{abc}$ where $\hat{V}_{abc}$ is the absorbing boundary potential and $\hat{V}$ is the interaction

potential. When the potential operator is exponentiated in Eq. 3.4 the imaginary component becomes real, and if the potential has eigenvalues that are negative when x is positive or positive when x is negative, the wavefunction will be dampened. Although many potentials are available as candidates, we do not want to drastically dampen the wavefunction on one extreme or slowly dampen the wavefunction on the other extreme such that the correlation function is altered. As a result, we choose the following form

$$V_{abc}(x) = V_{abs}e^{-(\frac{x-x_{min}}{V_d})^2} + V_{abs}e^{-(\frac{x-x_{max}}{V_d})^2} \tag{4.5}$$

where $V_{abs}$ is the strength of the absorbing boundary potential and $V_d$ is the spread of the absorbing boundary condition. Eq. 4.5 is the sum of two Gaussian functions centered at the edges of computational grid.

### 4.3 Reactant and Product States

The transmission coefficient for a finite square has analytical solution according Eq. 4.2 which was compared to numerical results. In order to determine the transmission coefficient, the correlation function between a reactant Møller state and a product Møller state for the finite square well must be calculated. The reactant state was a Gaussian wave packet with positive momentum placed to the left of the square well. The product state was a Gaussian wave packet with positive momentum placed to the right of the square well. As mentioned previously, the channel packet method relies on intelligently choosing the expansion coefficients of the momentum representation of the reactant and product states in order to isolate and solve for a particular s-matrix element. Because we are interested in the transmission coefficient, we are interested in the wavefunction that propagated through the square potential. For a reactant state placed to the left of the well and a product state placed to the right of the well, both states must have non-zero expansion coefficients for only positive values of momentum. Because the reactant and product states are Gaussian wave packets, the expansion coefficients, which is a Gaussian wave packet in the momentum

representation, are known analytically from Eq. 3.14. Because the reactant and product states were placed outside the well where the potential is zero, the reactant Møller and product Møller states are the same as the initial reactant and product state respectively. A Gaussian wave packet propagated to infinity under zero potential and then back to its initial location under zero potential will be the same as the initial Gaussian as verified by Eq. 3.13. Consequently, $|\psi_{reactant/product}>=|\psi_{\pm}>$, and no numerical computations had to be made to produce the Møller states.

The parameters of the reactant state and product states, the propagation parameters, and grid sizes are in Table 4.1. The parameters of the reactant and product states were intended to match the parameters of the $H_2$ molecule; however, the propagation times necessary to produce a correlation function that captured the full scattering event required millions of data points. Because the purpose of the square well was to provide confidence in the accuracy of the WDFs and to gain insight into the affect of potential depths (or heights) on the features of the WDF, some of the $H_2$ parameters were reduced in order to reduce the number of time data points to a manageable number to save on computation time. A lighter particle with large energies takes less time to travel a given distance than a heavier particle with lower energies. If the resolution of the time grid has to remain fixed at approximately $\Delta t = 0.01$, then a shorter range in time required less grid points to maintain the resolution. As a result, a fourth of the reduced mass of $H_2$ was used instead of 918.076 atomic mass units, and the average energy of the molecule was 3.486 Hartree energy which corresponds to 94.844 eV. The well depths of the square well were based upon the well depth of the ground state of $H_2$ which is 0.166 Hartree. The potential was then varied to determine the impact of large resonant structures in the transmission coefficient on the WDF. The minimum well depth was 0.166 Hartree while the maximum well depth was 16.611 Hartree (100 times larger than the minimum well depth). Fig. 4.1 shows the initial set up for the reactant and product states with a well depth of 11.628 Hartree. Fig. 4.3(a)

shows the momentum representation of the reactant state which is the same as the product state. As shown in Fig. 4.3(b) , $\psi(k)$ is very small at $k \leq$ which is necessary in order to solve for $\mathbf{S}^{\gamma'\gamma}_{+k'_{\gamma'},+k_\gamma}$ in Eq. 2.9.

Table 4.1: Square Well and Square Barrier Parameters

| variable | square well value | square barrier value | meaning |
|---|---|---|---|
| $x_{max}$ | 95 | 450 | maximum coordinate |
| $x_{min}$ | -95 | -450 | minimum coordinate |
| $t_{max}$ | 180 | 1250 | maximum time |
| $t_{min}$ | 0 | 0 | minimum time |
| $x_0$ | -2.8 | -2.8 | initial reactant coordinate displacement |
| $k_0$ | 40 | 40 | initial reactant momentum displacement |
| $\delta$ | 0.075 | 0.075 | initial spread of reactant in x |
| $xp_0$ | 2.8 | 2.8 | product state coordinate displacement |
| $kp_0$ | 40 | 40 | product state momentum displacement |
| $\delta p$ | 0.075 | 0.075 | initial spread of product state in x |
| $\mu$ | 229.519 | 229.519 | reduced mass |
| $a$ | 4 | 4 | well length |
| $v_{abs}$ | 1 | 1 | strength of absorbing boundary |
| $v_d$ | 2 | 2 | spread of absorbing boundary |
| $n$ | 8192 | 32768 | number of spatial grid points |
| $n_{time}$ | 8192 | 131072 | number of time grid points |
| $n_\tau$ | 8192 | 32768 | number of tau grid points |
| $ds$ | 1 | 4 | number of points down sampled |

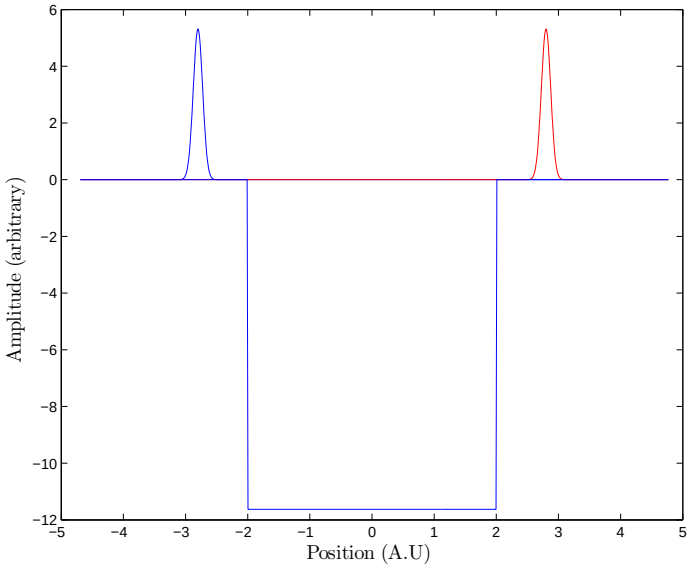


Figure 4.1: The initial setup to the square well problem. The square well of width 4 A.U. is centered about $x = 0$. For this example, the depth of the square well is 11.628 Hartree. The reactant state is the blue Gaussian wavepacket to the left of the square well and the product state is the red Gaussian wavepacket to the right at the square well. The parameters of the reactant and product states are found in table 4.2

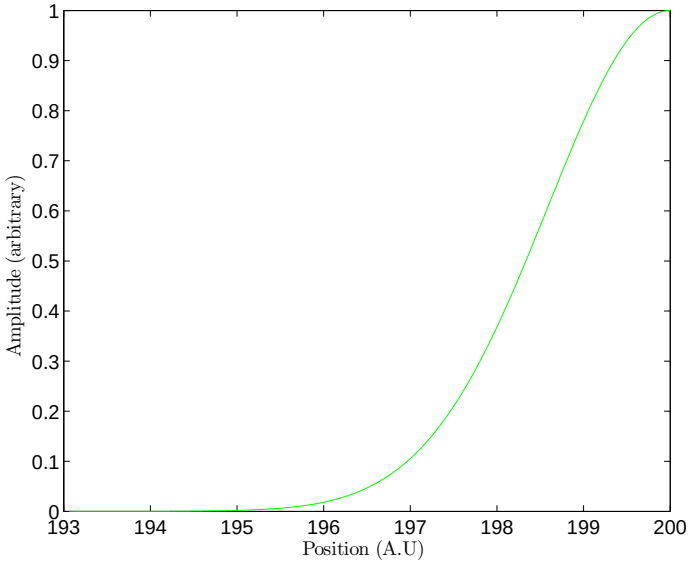


Figure 4.2: The absorbing boundary conditions are shown as the green Gaussians at the edge of the coordinate grid for the same well shown in Fig. 4.1. The parameters of the reactant and product states are found in table 4.2. The absorbing boundary condition is shown for the positive coordinate values; however, there is a symmetric Gaussian at the edge of the grid for the negative coordinate values.

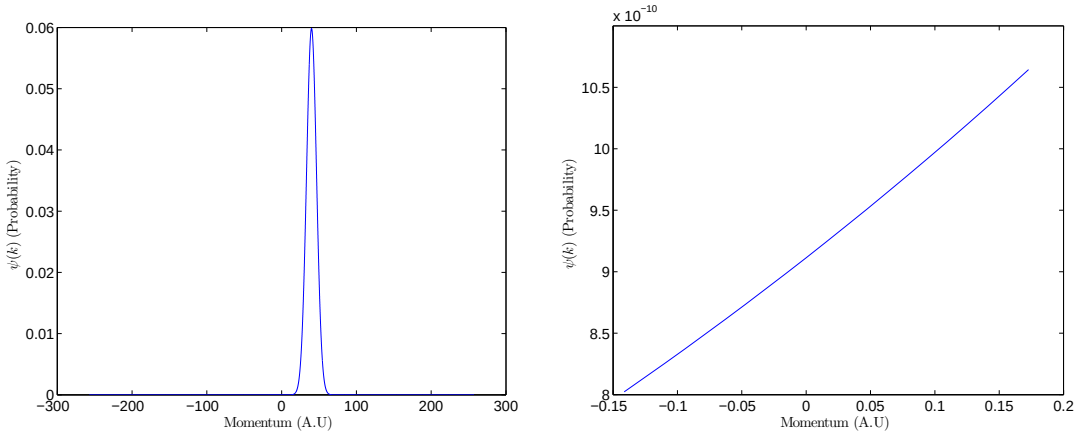


(a) The momentum representation of the reactant state

(b) A zoomed in graphic of the momentum representation of the reactant state

Figure 4.3: The momentum representation of the reactant state associated with the parameters found in Table 4.2. The expansion coefficients are all positive valued and at $k = 0$, the expansion coefficients are computationally equivalent to zero

As shown in Table 4.1, the propagation times for the square well problem was different than the propagation times for the square barrier. The reason for this is that a particle in the square well gains kinetic energy while the particle in square barrier looses kinetic energy. As a result, the particle takes a longer time to propagate through the potential of a square barrier than a square well. If the resolution of the time grid has to remain fixed at approximately $\Delta t = 0.01$, more grid points are needed to specify the time grid for the square barrier compared to the square well potential. Similarly, the range of the coordinate grid increased for the square barrier potential as compared to the square well potential since a wave packet with a longer propagation time travels more distance, so the number of grid points for the coordinate grid also increased. An example of the particle propagated for 180 atomic units through a square well is shown in Fig. 4.4. We can see in Fig. 4.4 that part of the original wave packet was reflected, part of the wave packet was transmitted through, and although very small compared to the rest of the wavefunction, part of the wavefunction exists in the well region.

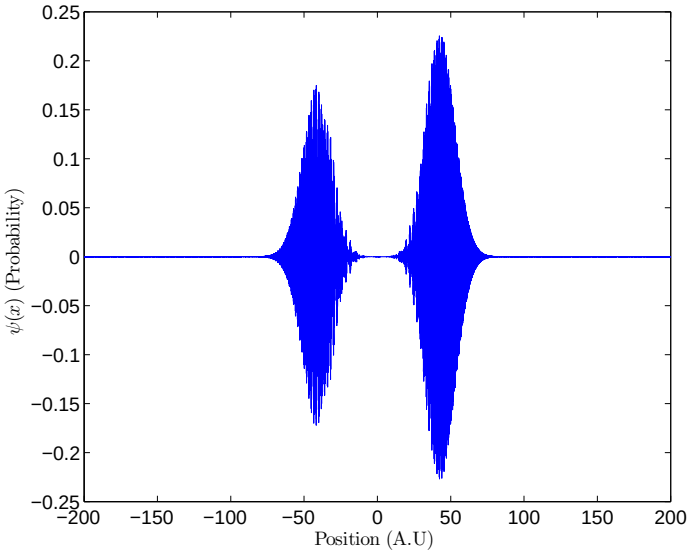


Figure 4.4: The propagated reactant state shown in Fig. 4.1 with a square well depth of $8.305E_H$. Part of the wavefunction transmitted through the well, part of the wavefunction reflected away from the product state, and part of the wavefunction still oscillates inside the well.

## 4.4 Correlation Function

The correlation function, $c_{\gamma'\gamma}(t) =< \psi_-^{\gamma'}|e^{\frac{-i\hat{H}t}{\hbar}}|\psi_+^{\gamma} >$, is the projection of the evolving reactant Møller state onto the product Møller state. Because the Møller states are the same as the initial states, the correlation function for the square potential is

$$c(t) = \int_{-\infty}^{\infty} \psi^*_{product}(x, t_0)\psi_{reactant}(x, t) \tag{4.6}$$

where $\psi_{product}(x, t_0)$ is the product Møller state in the coordinate representation at a particular time $t_0$ and $\psi_{reactant}(x, t)$ is the reactant Møller state in the coordinate representation as a function of time. Eq. 4.6 shows the computational approach to calculating correlation functions for the square potential. The product Møller state remained fixed as the reactant Møller state was then propagated through the square well. The correlation function or overlap between the propagating reactant Møller state with the fixed product Møller state was computed for each time step iteration of the split operator

method. At each time step, the product of the reactant Møller state with the conjugate of the product Møller state was taken at each point on the coordinate grid. The products were summed over the coordinate grid in order to determine a scalar value at that particulate time. These scalar values produce a signal known as the correlation function.

Because the signal depends upon the overlap between the product and reactant Møller states, the signal is expected to be very close to zero as the initial states are localized on either side of the square potential (the initial wavefunctions die off to the same order of magnitude as machine error at the edges of the potential). As the reactant state is propagated through the square well or barrier, the signal increases and peaks as the wavefunction passes through the product state. Due to reflections at the boundaries of the square potential, some of the amplitude of the wave packet will oscillate in the region of the potential before being transmitted through or reflected backwards out of the potential. Consequently, there is asymmetry in the correlation function as components of the reactant Møller state overlap with the product Møller state at later times. The wavefunction must be propagated for a long time in order to ensure that oscillating components of the wavefunction inside the potential are captured and the full scattering event is collected in the signal.

As the reactant state was propagated through the potential, the correlation function was calculate at each position. Fig. 4.5(a) and Fig. 4.5(b) shows an example of the real and imaginary parts of a correlation function for a potential well depth of 11.628 Hartree. In Fig. 4.5, the correlation function is zero for approximately the first 20 atomic units in time. This makes sense since the reactant and product Møller states do not overlap each other. At approximately 20 atomic units in time, the higher energy plane waves that made up the Gaussian wave packet travelled through the square well potential and entered the region where the product Møller state was placed. As time increases, a greater number of plane waves with a larger spread in energy enter the region where the product Møller state is localized increasing the amplitude of overlap. As the transmitted wave packet continues

to propagate, the higher energy plane wave components leave region where the product Møller state is placed, and the norm of the correlation function decreases. At approximately 30 atomic units of time, the correlation function is approximately zero, as most of the transmitted wave packet passed through the localized region of the product Møller state. However, during this time, a percentage of the amplitude of the wave packet was reflected at the boundary of the square well. This reflected wave packet travels the square well and either reflects or transmits each time the wave packet reaches the boundary of the square well. After the smaller in amplitude wave packet traversed the length of the square well three times (is at the positive value boundary a second time), a percentage of the wave packet amplitude transmits through the square well and into the product Møller state region for a second time. This occurs at approximately 40 atomic units. Because a percentage of the wave packet either transmits or reflects at each boundary, the amplitude of the wave packet that overlaps with the product Møller state for a second time is significantly smaller compared to the initial fraction of the wave packet amplitude that transmitted through the well. However, the higher energy plane wave components that make up the wave packet will reach the product Møller state before the lower energy plane wave components do, and the correlation function will have another peak. This process continues to repeat, and in Fig. 4.5 a third peak is still noticeable before the amplitude of wave packet is too small compared to the scale of the initial transmitted wave packet. The correlation function is approximately zero for times greater than 80 atomic units.

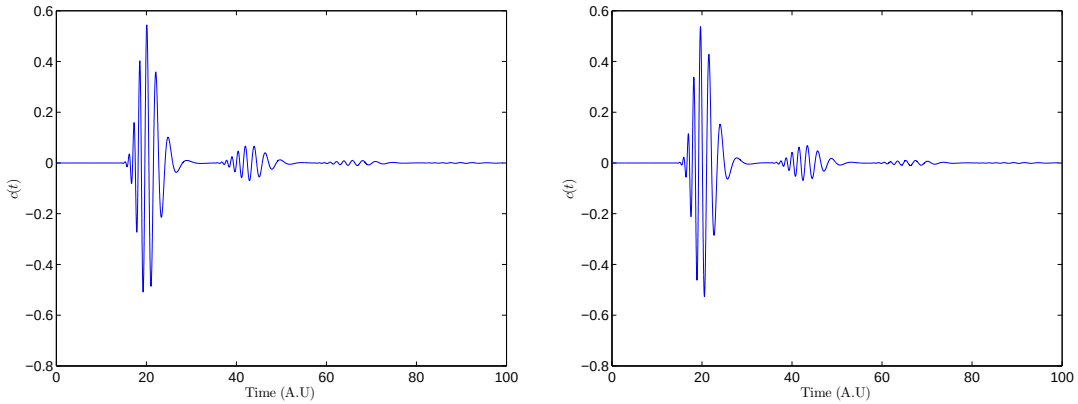


(a) The Real Part of $c(t)$ (b) The Imaginary Part of $c(t)$

Figure 4.5: Correlation Function Plots from the overlap between the reactant state and product state with parameters given in Table 4.2 and a potential of 11.628 Hartree

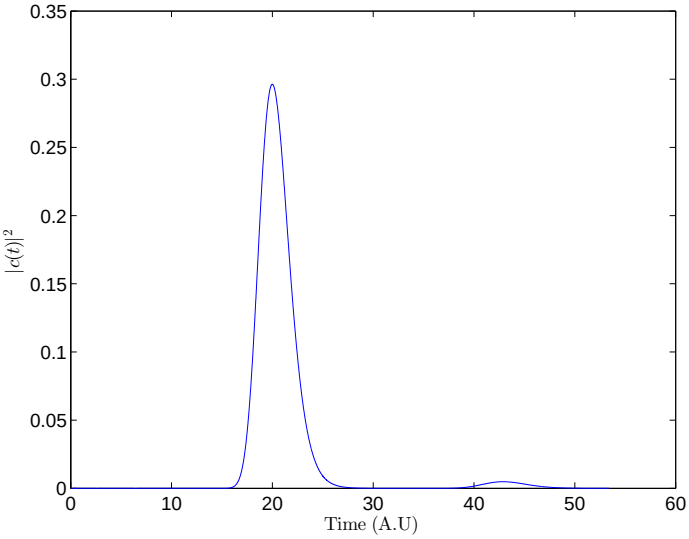


Figure 4.6: The norm of the correlation function shown in Fig. 4.5.

## 4.5 Down Sampling

According to the sampling theorem, at least three points are needed to be sampled for each peak or valley in order to capture a particular feature of a continuous function [3]. Because the split operator method requires the time grid to be sampled with a very

small interval between each point, $\Delta t$, the correlation function may contain a very large number of points. Although a greater number of sampled points more accurately reflects the continuous function, there is a trade off with computational time. In some cases where a large number of points described each feature of the correlation function, it may be necessary to down sample the correlation function in order to significantly reduce the computational time of the correlation function. Down sampling is the elimination of evenly spaced data points from the total set of data points. In this paper, a down sample of one means that every point was used while a down sample of two signifies that every other point was used.

### 4.6 Transmission Coefficient

As discussed previously, the correlation function can be used to determine the s-matrix elements. In order to calculate s-matrix elements, the FFT of the correlation function was taken with respect to the time variable and normalized by the expansion coefficients and momentum as given in Eq. 2.10. Energy can be related back to the momentum of a free particle in order to arrive at the s-matrix elements as a function of energy rather than momentum. For these calculations, only $|S_{+k+k}|^2$ was calculated. Other s-matrix elements such as $|S_{-k+k}|^2$ can be computed if the initial set-up was different. For example, if the product Møller state was instead located to the left of the square well with negative momentum, $|S_{-k+k}|^2$ can be isolated in Eq. 2.9. Finally, the transmission coefficient,$T(E)$, is $|S_{+k+k}(E)|^2$. Comparing the numerically calculated transmission coefficient with the analytical solution provided confidence that the computed correlation function was correct. It is important to note that when the Fourier transform of the correlation function, $c(\omega)$, was divided by the expansion coefficients in the region where both the expansion coefficients and $c(\omega)$ were smaller than the machine error, the s-matrix elements blew up. As a result, there is a range of energy values that correspond to a realistic transmission coefficient (i.e the range of values for which the $T(E)$ is less than one).

With the correlation functions calculated, the transmission coefficients and scattering WDFs were calculated. The square well did not require any down sampling; however, the square barrier did. According to Table 4.1, every fourth point of the correlation function was used. Fig. 4.6 shows the norm squared of the Fourier transform of the correlation function used in Fig. 4.5 with the expansion coefficients plotted on the same scale, and Fig. 4.6 is an example of the transmission coefficient calculated from the correlation function in Fig. 4.5. As shown in Fig. 4.6, the transmission coefficient is only valid for a range of energy values. Outside the range of values, the transmission coefficient blows up because the values of $c(\omega)$ and of the expansion coefficients are smaller than the error in producing the correlation function. Note that because we are in atomic units, energy and frequency are interchangeable since $E = \hbar\omega$. Also note that the transmission coefficient oscillates between one and a value less than one. When $T(E) = 1$, the well is completely transparent to plane waves of energy, $E$. The $\beta$ parameter describes how resonant each of these peaks are. The greater the $\beta$ parameter, the sharper and more spread out these peaks in the transmission coefficient become.

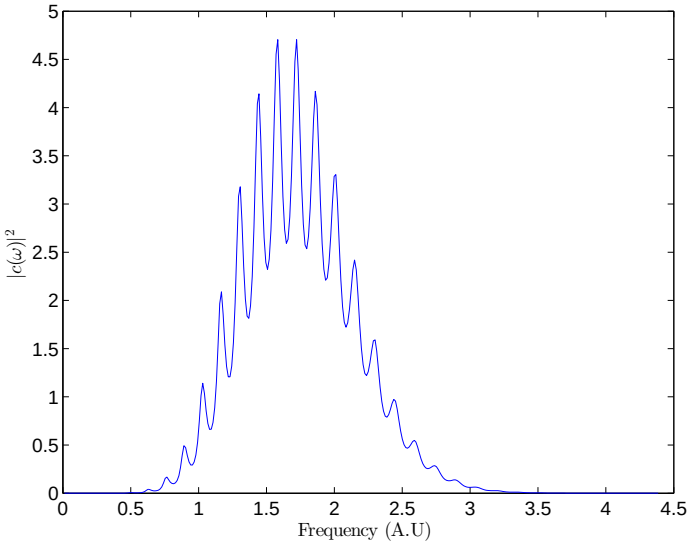


Figure 4.7: [The norm squared of the Fourier transform of the correlation function is plotted as a function of frequency. The correlation function was the overlap between the reactant state and product state with parameters given in Table 4.2 and a potential of 11.628 Hartree.

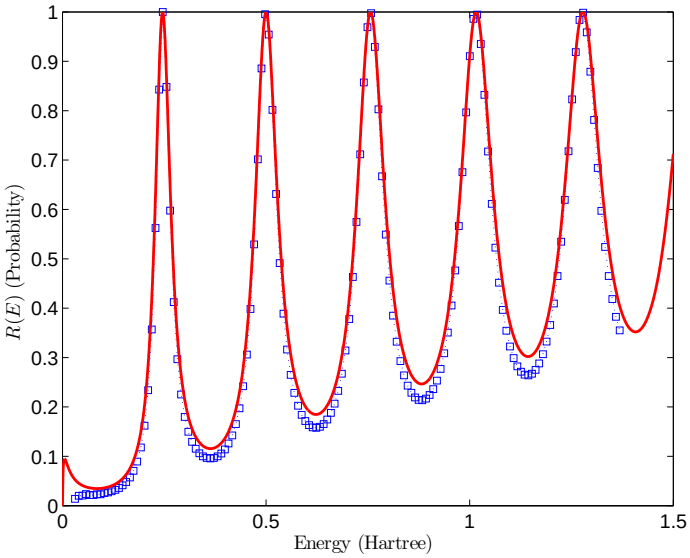


Figure 4.8: The transmission coefficient as a function of energy. The computationally produced transmission coefficient, blue squares, is compared to the analytically determined transmission coefficient, red line. The error is due to the resolution in the coordinate grid. Because the coordinate grid is sampled at discrete points, the finite square well is not perfectly square. There is a slight angle to the edges of the well making it slightly trapezoidal.

## 4.7 Autocorrelation Function

The correlation function was then used to produce the Wigner Distribution Function. The scattering WDF is the Fourier transform of the non-stationary autocorrelation function of the correlation function which is expressed in terms of the time, $t$, and a time lag, $\tau$. As shown in Eq. 4.7, the autocorrelation function is $c^*(t + \frac{\tau}{2})c(t - \frac{\tau}{2})$. The autocorrelation function is the product of the correlation function shifted in the positive time direction with its own complex conjugate shifted by the same amount except in the negative time direction. Theoretically, this product is summed for every shift $\frac{\tau}{2}$ ranging from $-\infty$ to $\infty$; however, computationally this can't be done. Instead, the shifts can only be done in discrete points over a finite range. The range of $\tau$ must be large enough such that the shifted correlation functions have very little overlap at the maximum values of $\tau$. At the maximum or minimum values of $\tau$, the product $c^*(t + \frac{\tau}{2})c(t - \frac{\tau}{2})$ needs to be nearly zero for

all values of $t$. At $\tau = t_{max} - t_{min}$, the distance between $c^*(t + \frac{\tau}{2})$ and $c(t - \frac{\tau}{2})$ is the length of the signal, and the product will be $c^*(t + \frac{\tau}{2})c(t - \frac{\tau}{2})$ for all values of time. This implies that the appropriate range for $\tau$ is $-(t_{max} - t_{min}) + 2\Delta t \leq \tau \leq (t_{max} - t_{min})$.

Another limitation is that the correlation function is an array of length $n_t$, the number of time points. Any shift has to be done such that $c(t_i - \frac{\tau}{2}) = c(t_j)$. In other words, the shifted correlation function needs to still align with the same sampled points on the time grid. This implies that $\Delta\tau = 2(t_{max} - t_{min})$. In addition, the correlation array is of finite length with each element of the array corresponding to a particular point on the time grid. If an indexed value is shifted to a time outside the time grid, then the autocorrelation function is assumed to be zero at that point. In order to determine if the integrand was properly calculated, the autocorrelation function at a time lag of $\tau = 0$ should be equivalent to the magnitude squared of the correlation function, $|c(t)|^2$.

The real and imaginary parts of the autocorrelation function associated with the correlation function in Fig. 4.5 are plotted as contours in Fig. 4.9. The real part can be seen to exhibit an even function centered about $\tau = 0$ atomic units while the imaginary part is an odd function centered about $\tau = 0$. Thus, the scattering WDF must be a real function.

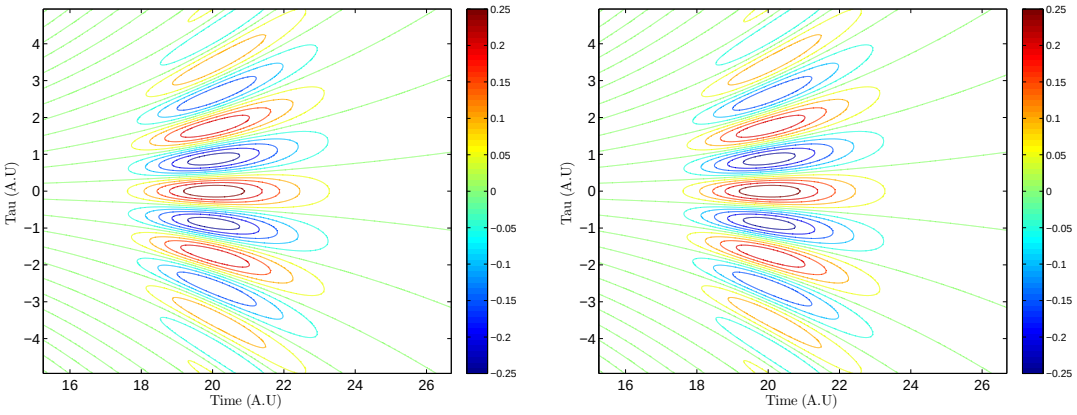


(a) The Real Part of $c^*(t + \frac{\tau}{2})c(t - \frac{\tau}{2})$ (b) The Real Part of $c^*(t + \frac{\tau}{2})c(t - \frac{\tau}{2})$

Figure 4.9: Autocorrelation Function Plot from the overlap between the reactant state and product state with parameters given in Table 4.1 and a potential of 11.628 Hartree. The real part of the autocorrelation function is an even function centered about $\tau = 0$ while the imaginary part of the autocorrelation function is an odd function centered about $\tau = 0$.

## 4.8 Phase Shift

In order to produce the scattering WDF, the FFT of the autocorrelation function was taken with respect to the time delay. Because the autocorrelation function has an even real part and an odd imaginary part, symmetry analysis tells us that the scattering WDF must be a purely real function which is a property that is always true for the scattering WDF. Unfortunately, if FFT of the autocorrelation function was taken without further consideration, the scattering WDF would have an imaginary component. The reason for this is that the FFT package assumes that the minimum value of $\tau$ is zero instead of $\tau_{min} = -(t_{max} - t_{min}) + 2\Delta t$. As a result, the evenness and oddness of a function disappears. In order to properly account for the shift in the time grid, a phase shift must be added to the result of the FFT. The phase shift ,which can be deduced by applying a time shift to the inverse Fourier transform (Eq. 3.5), is $e^{-i\omega\tau_{min}}$, and when the phase shift is taken into account, the imaginary component of the WDF is approximately zero. The phase shift has not been an issue previously because we have been interested in the norm square of any FFT result where the phase information is lost or because the FFT result was transformed back into the original coordinate system using an inverse FFT which undoes the phase shift.

## 4.9 Wigner Distribution Functions

The Wigner Distribution Function is a distribution created by Eugene Wigner in 1932 that attempts to relate quantum mechanics with the classical phase-space picture; however, the Wigner Distribution Function (WDF) can also be found in signal-processing and optics [2, 7, 14, 15, 21]. The Wigner Distribution Function as found in quantum mechanics is the Fourier transform of the density operator with respect to a coordinate variable. The goal of the WDF was to find quantum corrections to classical statistical mechanics and to find a relation between the probability densities in quantum with the trajectories in phase space in classical physics. Due to the uncertainty principle, it is impossible to find a probability distribution in phase space such that the probability distribution is positive

everywhere and that the integral of the product of the probability distribution, $P(x, y)$, and of some observable, $\hat{A}(\hat{x}, \hat{p})$, that is a function of the position and momentum operators produces the expectation value of that operator, $\int\int P(x,p)A(\hat{x},\hat{p})dxdp =< \hat{A} >$. Thus, the Wigner Distribution Function is not a probability distribution function since it can be negative, but the WDF is a quasi-probability distribution function. Although there are other quasi-probability distribution functions that have been proposed, the application of the other quasi-distribution functions has been found to be limited.

The quantum perspective of the scattering Wigner Distribution Function is similar to the time-signal point of view [21]. Instead of density operator, the integrand on the time signal, or in this case the correlation function, is a non-stationary autocorrelation function. The autocorrelation of a signal is the cross-correlation of a signal with itself as a function of time lag. If the signal is only composed of one time series, then the WDF can be simplified to

$$W(t,\omega) = \int_{-\infty}^{\infty} c^*_{\gamma'\gamma}(t + \frac{\tau}{2})c_{\gamma'\gamma}(t - \frac{\tau}{2})e^{-i\omega\tau}d\tau. \tag{4.7}$$

where $\tau$ is a time lag. The scattering WDF in Eq. 4.7 is the Fourier transform of the product of the correlation function shifted by an offset in time with its complex conjugate shifted in the opposite direction in time. Thus, the scattering WDF in Eq. 4.7 is a quasi-spectral distribution function of the correlation function; however, because the correlation function is the overlap between two wavefunctions, the scattering WDF in Eq. 4.7 can be viewed as a quasi distribution of probabilities associated with a particular energy value. In other words, the scattering WDF should describe the flow of energy probabilities of a scattering event as a function of time. As a result, a negative value in the scattering WDF can be interpreted as a decrease in probability.

Some unique properties of the scattering WDF that are of interest for this work are

$$\begin{aligned} \int W(t,\omega)d\omega &= |c_{\gamma'\gamma}(t)|^2 \\ \int W(t,\omega)dt &= |c_{\gamma'\gamma}(\omega)|^2 \end{aligned} \tag{4.8}$$

where $c_{\gamma'\gamma}(\omega)$ is the Fourier transform of the correlation function [2, 14, 15]. Eq. 4.8 states that the projection of the scattering WDF onto the time domain reproduces the norm squared of the correlation function. Similarly, the projection of the scattering WDF onto the frequency domain reproduces the norm squared of the Fourier transform of the correlation function. From the channel packet method, if the Fourier transform of the correlation is divided by the expansion coefficients of the reactant Møller state along with some other prefactors, then the s-matrix elements are obtained as seen by Eq. 2.10. As a result, the scattering WDF contains all of the time and energy information (frequency is related to energy) regarding the scattering event.

### 4.10 WDF for Square Potentials

The scattering WDF is the FFT of the autocorrelation function for every value of time. For a particular value of $t$, the autocorrelation function was determined as a function of $\tau$ which was then sent into the FFT package. The result was multiplied by a phase factor and some constants determined by Eq. 4.7. This process was repeated for each point on the time grid. In order the determine the validity of the scattering WDF, the integrated projections of the scattering WDF onto the time and frequency domains should match the magnitude squared fo the correlation function, $|c(t)|^2$ and the magnitude squared of the Fourier transform of the correlation function, $|c(\omega)|^2$, respectively as shown in Eq. 4.8. The integrals were simply sums multiplied by the respective grid interval. Scattering WDFs were calculated for a particle scattering from 11 different square well potentials. Each square well potential had the same length and the same reactant and product states; however, the depth of the square well varied. The purpose of producing these scattering WDFs for varying well depths was to gain insight into scattering with potentials that had largely resonant peaks in the transmission coefficient such as the HOCO scattering problem. Scattering WDFs were also produced for the finite square barrier with varying barrier heights. The only changes required to the program were the sign on the potential and

the number of time grid points used. The various potential heights and associated $\beta$ values are shown in Table 4.2.

Table 4.2: Square Well and Square Barrier Potentials Tested

| Well Depth | Barrier Height | $\beta$ |
|---|---|---|
| 0.16610929 | 0.16610929 | $\beta_0 = 34.929$ |
| 1.66109294 | 1.66109294 | $\sqrt{10}\beta_0$ |
| 3.32218588 | 3.32218588 | $\sqrt{20}\beta_0$ |
| 4.98327882 | 4.98327882 | $\sqrt{30}\beta_0$ |
| 6.64437176 | 6.64437176 | $\sqrt{40}\beta_0$ |
| 8.30546470 | 8.30546470 | $\sqrt{50}\beta_0$ |
| 9.96655764 | 9.96655764 | $\sqrt{60}\beta_0$ |
| 11.62765058 | 11.62765058 | $\sqrt{70}\beta_0$ |
| 13.28874352 | 13.28874352 | $\sqrt{80}\beta_0$ |
| 14.94983646 | 14.94983646 | $\sqrt{90}\beta_0$ |
| 16.61092940 | 16.61092940 | $10\beta_0$ |

In Fig. 4.10, the scattering WDF is plotted as a function of time and energy. The plot is a color image of the scattering WDF associated with the correlation function in Fig. 4.5. Although the absolute magnitude of the scattering WDF is not easily read from the color image in Fig. 4.10, the location, shape, and relative heights of certain features of the scattering WDF are much easier to see. In Fig. 4.10, we can see a large, negatively chirped peak followed by bands of oscillating peaks and valleys at later times. This chirped peak is positioned such that at high energies and short times, the scattering WDF has non-zero values and at low energies and long times, the scattering WDF also has non-trivial values. This makes sense when one considers the various components of the propagating wave packet. The wave packet, which is a superposition of plane waves, has the high energy

plane waves traveling faster than the low energy plane wave (hence why the wave packet spreads in free space). The plane waves which get a boost from the square well will make it to the location of the stationary product Møller state much sooner than the slower traveling plane waves. As expected, the high energy components of the scattering WDF have peaked values at larger times as compared to the lower energy components of the scattering WDF. In Fig 4.10, one can also observe a secondary band of peaks later in time corresponding to the same energy values as the large chirped peak. This smaller band of non-zero scattering WDF values has a spread that can be described the by same time-energy relation as the large initial chirped peak discussed later.

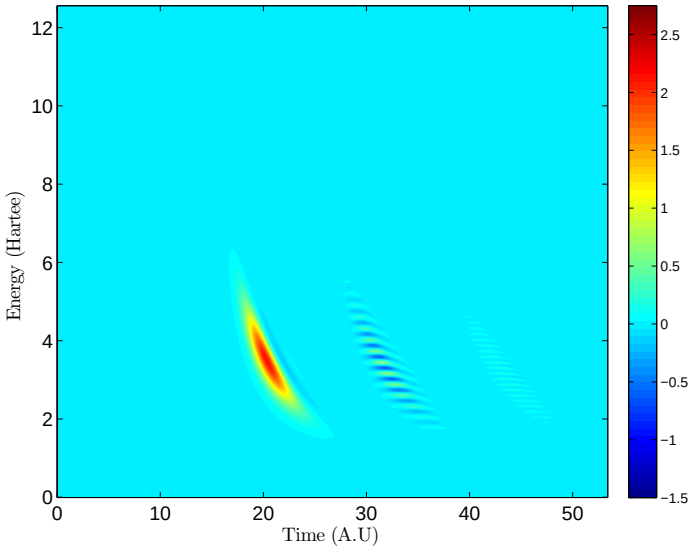


Figure 4.10: A color image of the Wigner Distribution Function for the correlation function calculated with a square well potential of 11.628 Hartree and reactant and product states with parameters specified in Table 4.2.

The projections of the scattering WDF onto the time and frequency domains reproduces the norm squared of the correlation function and the norm squared of the Fourier transform of the correlation function. Fig. 4.11 and Fig. 4.12 shows the overlap between the projections and the associated functions, $|c(t)|^2$ and $|c(\omega)|^2$. In the figure with the projection

of the WDF onto the frequency domain, there is slight disagreement between the projection of the scattering WDF onto the frequency domain and $|c(\omega)^2|$. The scattering WDF is the Fourier transform of the time delay present in the autocorrelation function. The interval between sampled points of the $\tau$ grid is twice the size as the time grid,$\Delta\tau = 2\Delta t$. Because the energy grid is inversely related to the time grid, the spacing between energy points for the projection of the scattering WDF onto the frequency domain (Fourier transform of $\tau$) is half the spacing of $|c(\omega)^2|$ (Fourier transform of $t$). This implies that there is an additional point for the projection of the WDF between two points for $|c(\omega)^2|$. When the same points are compared (i.e. every other point of the projection of the scattering WDF), the projection of the scattering WDF and $|c(\omega)^2|$ are in agreement.

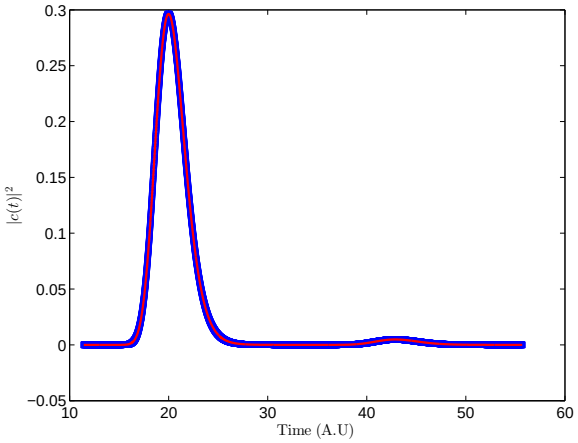


Figure 4.11: The plot of the projection of the scattering WDF (blue) onto the time domain for the square well potential with a depth of 11.628 Hartree is shown. This projection is compared to $|c(t)|^2|$ (red)

With confidence that the WDFs are correct, we began generating scattering WDFs for many square well and square barrier cases. Fig 4.13-Fig 4.20 highlight features of the scattering WDF that change as the magnitude of the square potential increases. We see the same general structure in these figures that we saw in Fig.4.10. Each scattering WDF had a

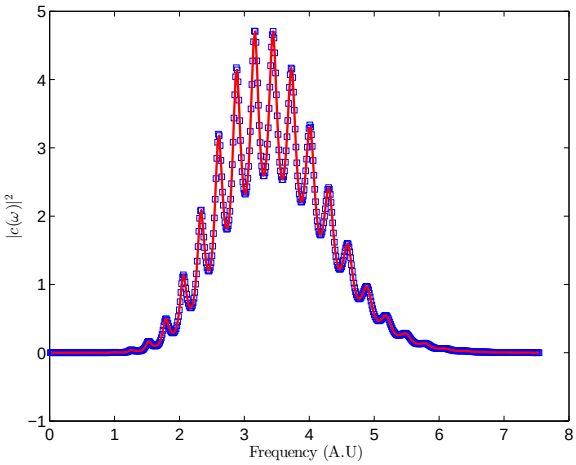


Figure 4.12: The plots of the projection of the WDF (blue) onto the time and frequency domain for the square well depth of 11.628 Hartree are shown. These projections are compared to $|c(t)|^2|$ and $|c(\omega)^2|$ respectively (red). The slight disagreement in amplitude between the projection onto the frequency domain and $|c(\omega)^2|$ results from differences in sampled energy values

.

large chirped peak with the same general shape as Fig. 4.10. The difference between each scattering WDF is that as the depth of the square well increased, the large peak shifted to smaller values of time, and the concavity of its chirp decreased. As the well depth increases, the well adds more kinetic energy and hence more momentum, $k = \frac{\sqrt{2\mu(E-V)}}{\hbar}$, to the evolving reactant Møller state as it propagates in the interaction region. As a result, the wavefunction gets transmitted through the region much faster and the wavefunction that is first transmitted through the well should arrive sooner than for a shallower well. In addition, as the well depth increases, bands with oscillating peaks and valleys appear like in Fig 4.10. The location of these bands correspond to the same moments in time as the peaks in the norm of the correlation function. As the square well depth increased, the number of visible bands grew, the peak amplitude decreased, and the difference between the maximum and minimum values of the scattering WDF decreased.

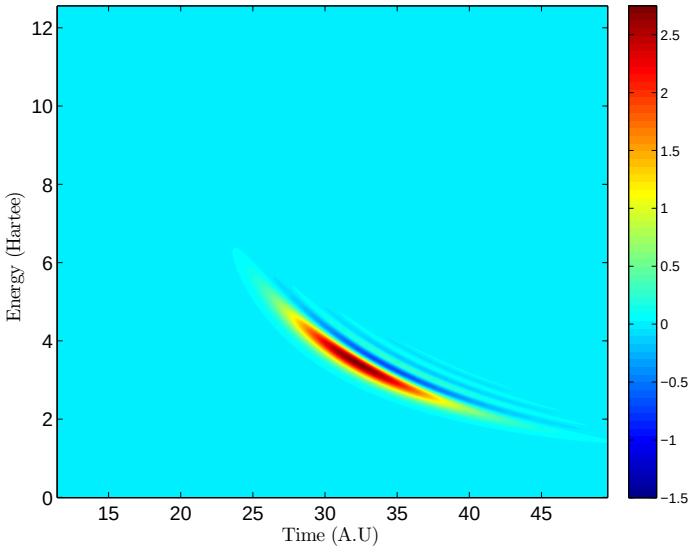


Figure 4.13: Scattering WDF for square well depth of 0.166 Hartree.

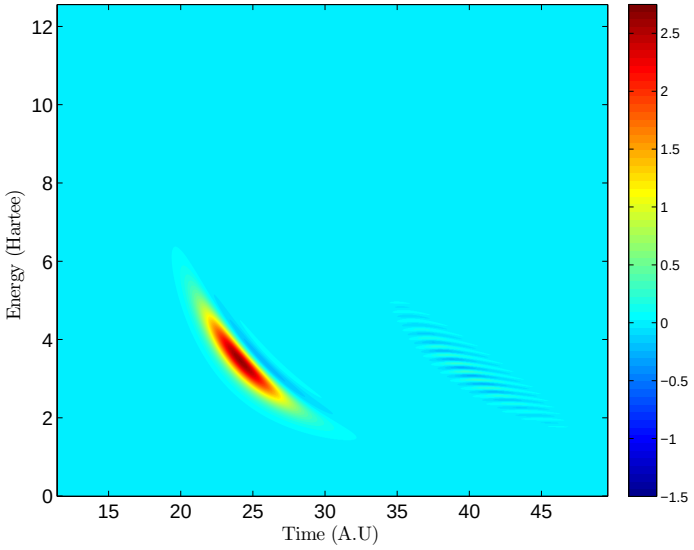


Figure 4.14: Scattering WDF for square well depth of 4.9835 Hartree.

The scattering WDFs for the square barrier potentials have a similar structure as the scattering WDFs for the square well. One of the differences is that as the barrier height increases, the momentum of the plane waves that make up the wave packet decrease. By

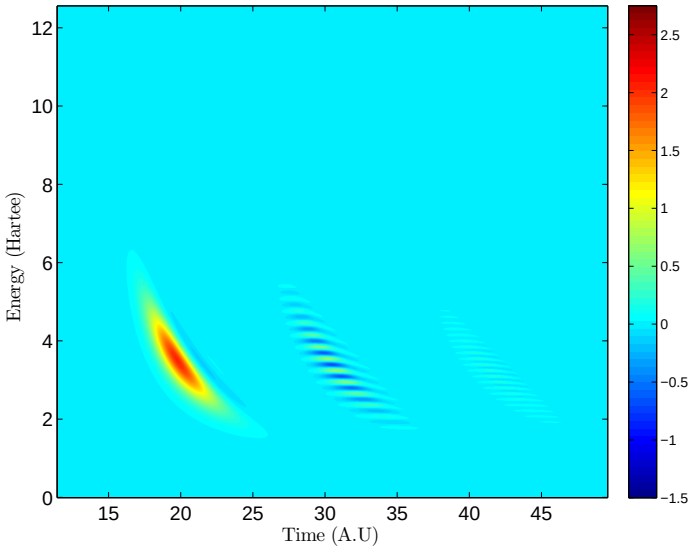


Figure 4.15: Scattering WDF for square well depth of 13.289 Hartree.

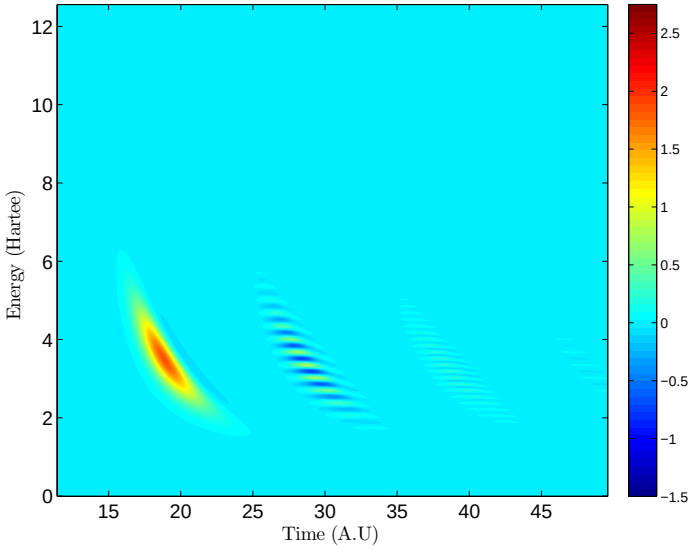


Figure 4.16: Scattering WDF for square well depth of 16.611 Hartree.

the time the barrier height reached 13.289, the transmitted wavefunction was so small that the correlation function was on the same order of magnitude as the error. Thus, scattering WDFs were only calculated up to 11.628 Hartree. One of the major differences is that

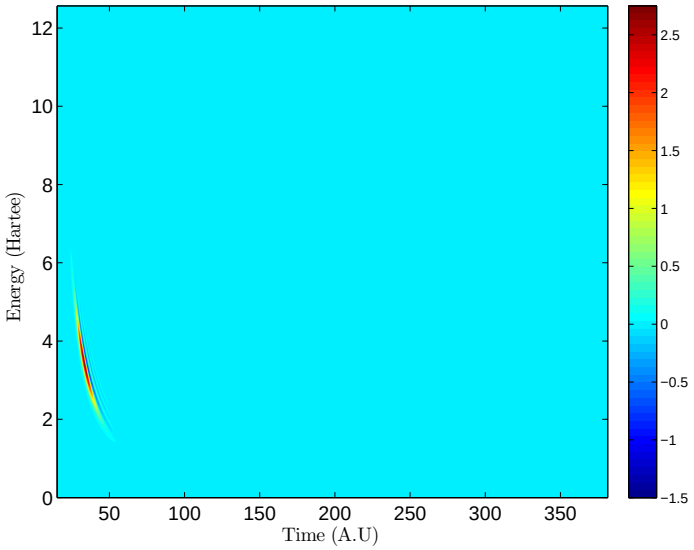


Figure 4.17: Scattering WDF for square barrier height of 0.166 Hartree. The scale is based off of the maximum and minimum values of the scattering WDF.

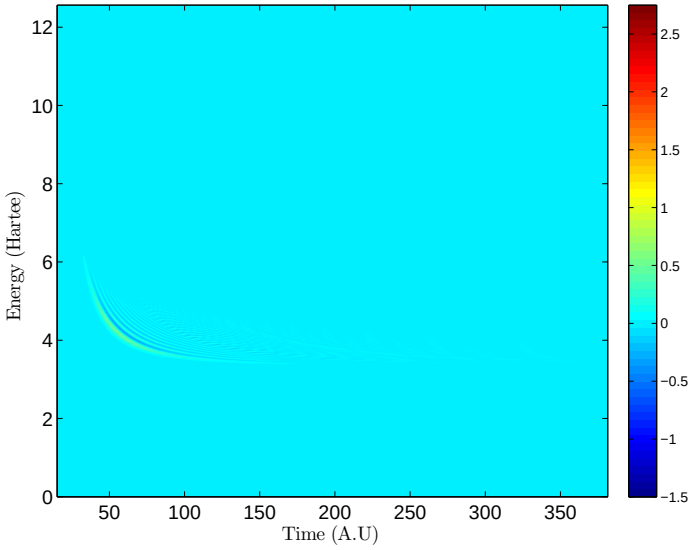


Figure 4.18: Scattering WDF for square barrier height of 3.322 Hartree. Note that the scale is the same as Fig. 4.17. The purpose of this is to observe the diminishing amplitude of the scattering WDF as the barrier height increases.

the bands of oscillating peaks and valleys extend very far out in time as the barrier height increases rather than coalescing together. Another major difference is that as the barrier

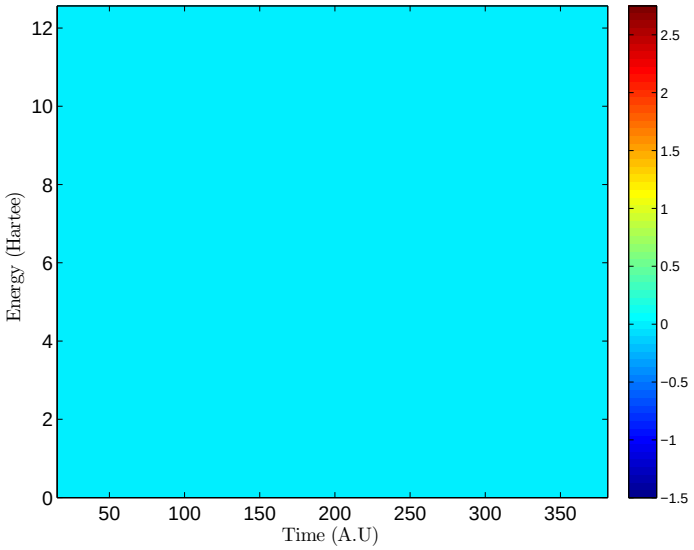


Figure 4.19: Scattering WDF for square barrier height of 4.983 Hartree. Note that the scale is the same as Fig. 4.17. The purpose of this is to observe the diminishing amplitude of the scattering WDF as the barrier height increases. On this scale the scattering WDF is not visible.

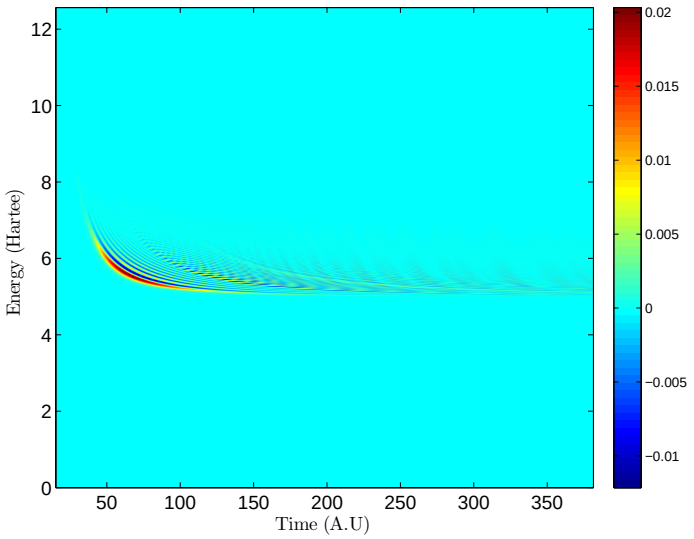


Figure 4.20: Scattering WDF for square barrier height of 4.983 Hartree scaled to the maximum and minimum values of the scattering WDF. Although the amplitude of the scattering WDF if Fig. 4.19 cannot be seen with the scale used in Fig. 4.17, the scattering WDF still exists as shown in this figure .

height increased, the curvature of the bands grew compared to the flattening out of the of the bands in the square well as viewed along the energy axis, so the width of the scattering WDF along the energy axis decreased while also shifting to higher energy levels.

### *4.10.1 Interpretation of Peaks and Valleys.*

Since the Wigner Distribution Function can be negative, there hasn't been a clear interpretation of the WDF in the past. We conjecture that the positive values of the WDF correspond to presence of probability at the location of the product Møller state with a specific energy at a certain time, the negative values correspond to the depletion of probability at the same product Møller state with a specific energy at a certain time, and the zero value corresponds to the presence of probability not at the product Møller state. We arrive at this conjecture from looking at the properties of the WDF defined by Eq. 4.8. The projection of the WDF onto the frequency domain is the norm Fourier transform of the correlation function which is related to the transmission coefficient by a normalization term as shown in Eq. 2.10. According to Eq. 4.8, each point on $|c(\omega)|^2$ is the sum of all values of the WDF at that particular frequency (energy) over all time. Positive values will contribute to the sum at that particular energy while negative values will take away from that sum. If all the valleys in the WDF are on the same order of magnitude as the peaks for a given energy value, then the sum will be close to zero since each valley will approximately cancel with each peak in the sum (the amplitude of the peaks and valleys for each band diminishes over time). This sum will correspond to a near zero value for $|c(\omega)|^2$ and hence a very low transmission coefficient at that associated frequency(energy).

As shown in Fig. 4.21 (a square well with a well depth of 4.984 Hartree), the amplitudes of the valleys are not on the same order of magnitude as the amplitudes of the peaks. For a given energy value, $|c(\omega)|^2$ will be large, and although there are peaks and valleys in the transmission coefficient, the valleys in the transmission coefficient are near one as shown in Fig. 4.23. In contrast as shown in Fig. 4.22 (a square well with a well

depth of 16.611 Hartree), the amplitudes of the valleys are much closer to the amplitudes of the peaks. As such, there are energy values such as 3 Hartree where $T(E = 3)$ is going to be much smaller compared to the same transmission coefficient for a square well depth of 4.984 Hartree. The square well with a well depth of 16.611 Hartree is said to have a much deeper resonance (much larger $\beta$ value) than the square well of depth of 4.984 Hartree. Because the positive values of the WDF contribute to the s-matrix element at a given energy, we say that the positive values of the WDF must correspond to the presence of probability for a given value of energy at a given value of time. On the other hand, the negative values of the WDF must correspond to the loss of probability for a given value of energy at a particular value of time. Because the total probability must be conserved, this depletion of probability must show up elsewhere in the system for a given time, at some other moment in time if the same probability shows up later or earlier in time at the same location (product Møller state), or both. The question of where this probability went will be examined next.

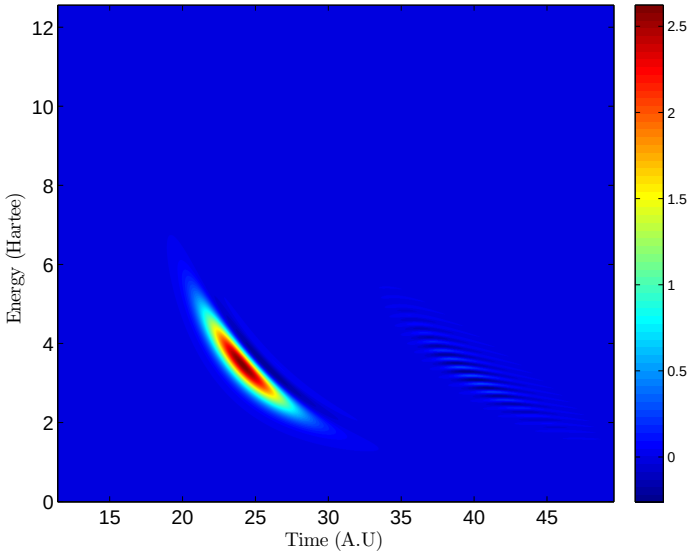


Figure 4.21: WDF for square well depth of 4.984 Hartree. The axis is scaled to the maximum and minimum values of the WDF.

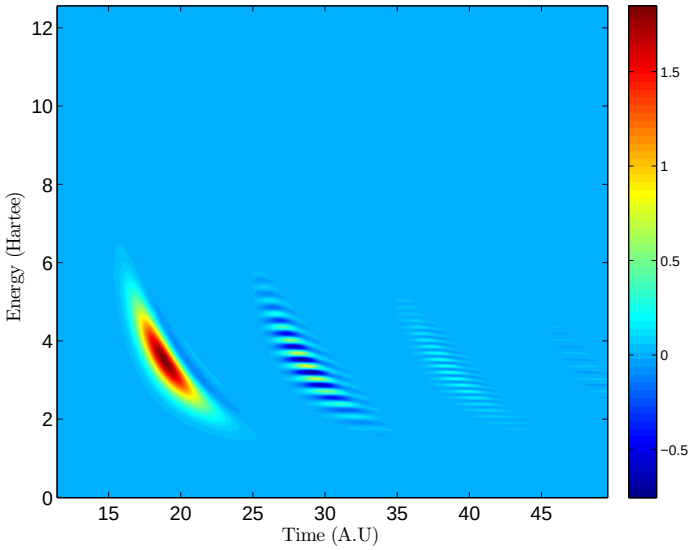


Figure 4.22: WDF for square well depth of 16.611 Hartree. The axis is scaled to the maximum and minimum values of the WDF

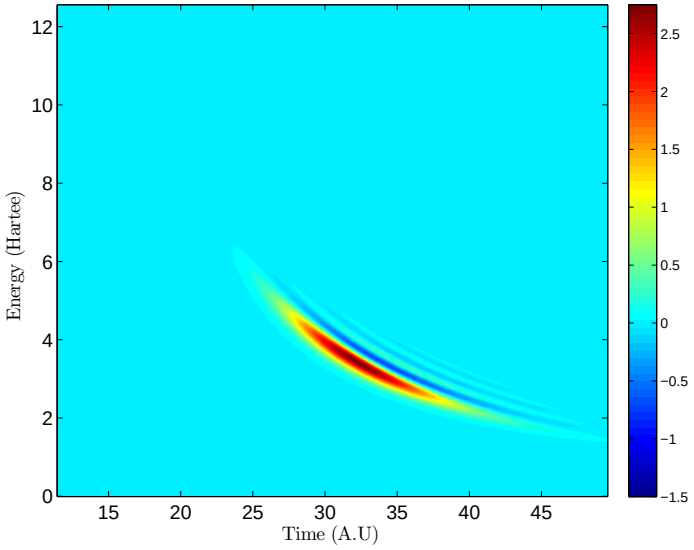


Figure 4.23: WDF for square well depth of 4.984 Hartree.

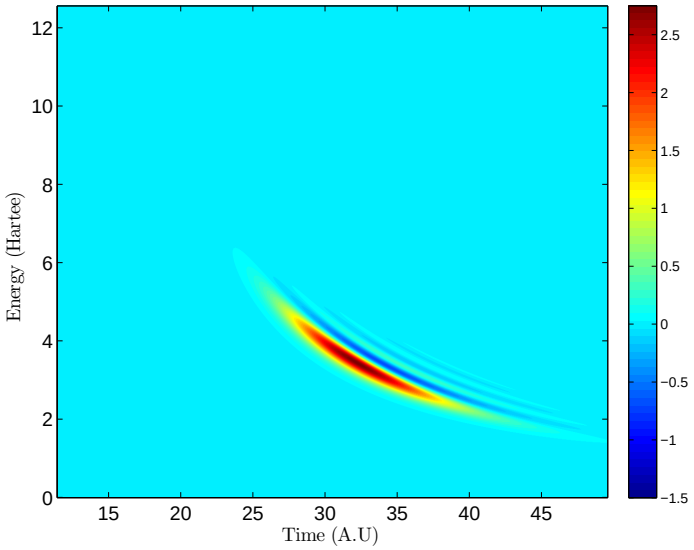


Figure 4.24: WDF for square well depth of 4.984 Hartree.

#### *4.10.1.1 Location of Lost Probability.*

If the probability amplitude for a given energy is not transmitted at a given time, then it must either be transmitted at a later time or appear in the reflection coefficient which is $|S_{-k+k}|^2$. To see if the loss of probability ended up in the reflection coefficient, the Wigner Distribution Function associated with the reflection coefficient had to be produced. This was accomplished by placing the same product Møller state used in the transmission coefficient to the left side of the well with the following changes made to Table 4.1: $xp_0 = -2.8$ and $kp_0 = 40$.

Fig. 4.26 shows the reflection coefficient and Fig. 4.27 shows that the sum of the transmission coefficient and the reflection coefficient is one which gives us confidence that the correlation function for the new set up is correct. The WDF associated with $|S_{-k+k}|^2$ is plotted for a square well with a depth of 11.628 Hartree as shown in Fig. 4.25. This WDF is very similar in structure to the transmission coefficient. There is a large central peak and several bands comprised of oscillating peaks and valleys. The reflection WDF has a large peak before the transmission coefficient since there will be reflection at the left edge of the

square well. The remaining bands in the reflection WDF align in time with the bands in the transmission coefficient. This makes sense for a deep square well because as the time it takes the wave packet to traverse the square well ($t = \frac{L\sqrt{\mu}}{\sqrt{2(E+V)}}$ where $V$ is the magnitude of the well depth and $L$ is the length of the well) is very small compared to the time it takes for the wave packet to traverse the zero potential region ($t = \frac{x_o\sqrt{\mu}}{\sqrt{2E}}$ where $x_o$ is the distance from the well to the center of the peak value of the initial states).

Fig. 4.28 shows the amplitude of the Wigner Distribution Function at a particular energy as a function of time (energy slice) for both the transmission and the reflection WDF. The peak of the transmission coefficient may correspond to a valley in the reflection coefficient; however, this is not true for all peaks and valleys. Fig. 4.29 shows the amplitude of the WDF at a particular moment in time as a function of energy (time slice) for both the transmission and reflection WDF. The peaks and valleys of the WDF do not align. In fact, the frequency of peaks in the reflection WDF is double the frequency of peaks as the transmission coefficient. As shown in Fig. 4.30, when the second transmission band is compared to the second reflection band (instead for example as the first transmission band with the second reflection band in Fig. 4.29), the peaks of the transmission WDF correspond to the valleys of the reflection WDF and vice versa. At high energies, the peaks and valleys no longer match up, but this is due to the chirp. It may be possible that after the initial reflection and transmission, the loss of probability in the $i^{th}$ transmission band may be found in the $i^{th}$ reflection band; however, further study must be done in order to confirm this.

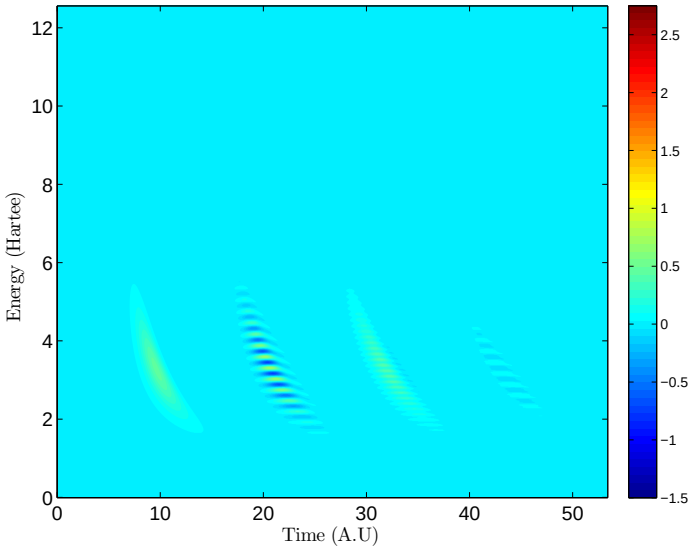


Figure 4.25: WDF for square well depth of 11.628 Hartree and the product state placed to the left of the well. The correlation function and WDF are then related to $|S_{-k+k}|^2$ and the reflection coefficient.

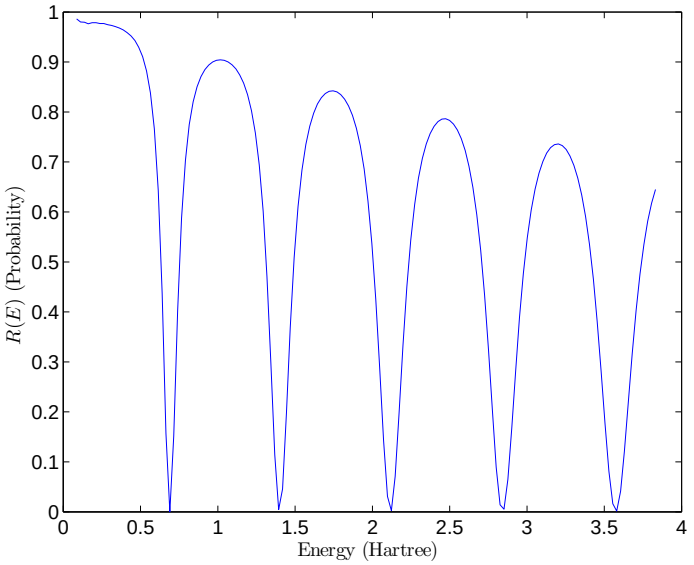


Figure 4.26: Reflection coefficient for square well depth of 11.628 Hartree.

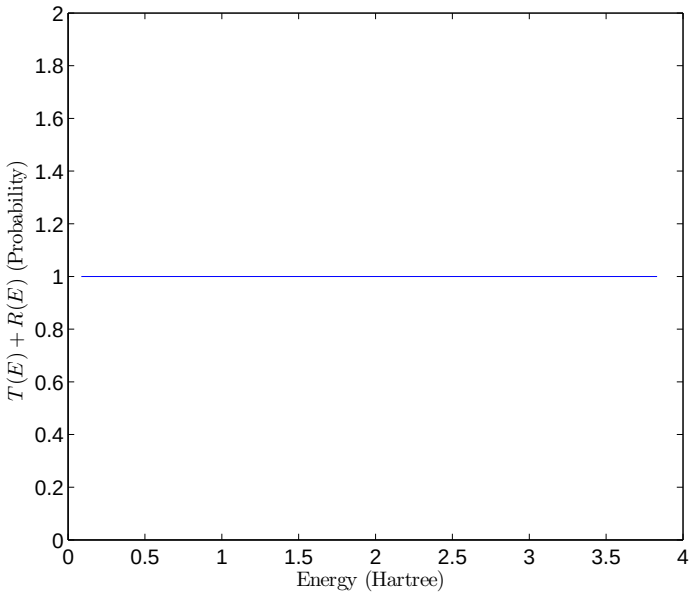


Figure 4.27: The sum of the reflection and transmission coefficient for square well depth of 11.628 Hartree. The sum of the reflection and transmission coefficients is one as expected.

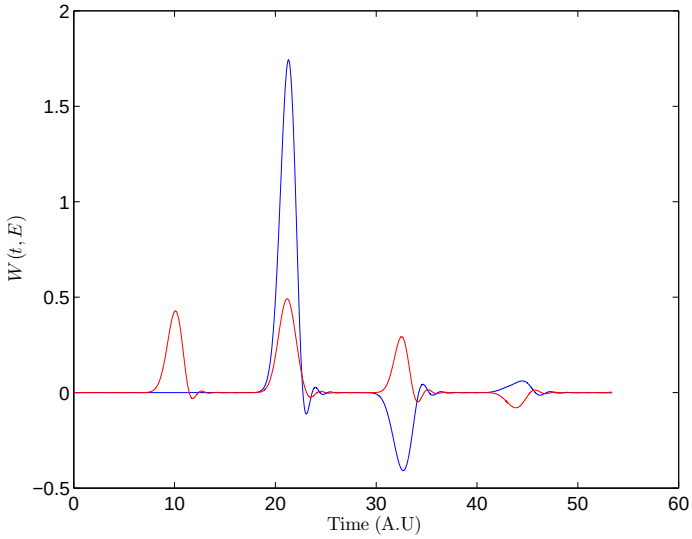


Figure 4.28: The amplitude of the transmission and reflection scattering WDFs at an energy value of 3.033 Hartree as a function of time for the square well potential with a depth of 11.628 Hartree.

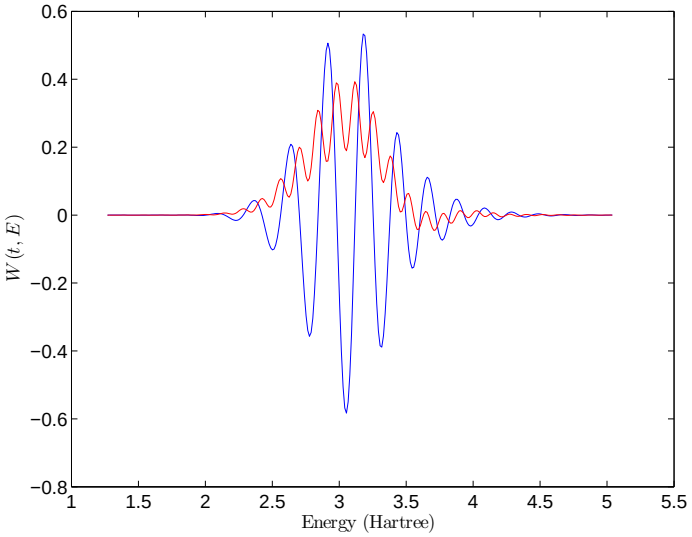


Figure 4.29: The amplitude of the transmission and reflection scattering WDFs at a time of 32 A.U. as a function of energy for the square well potential with a depth of 11.628 Hartree.

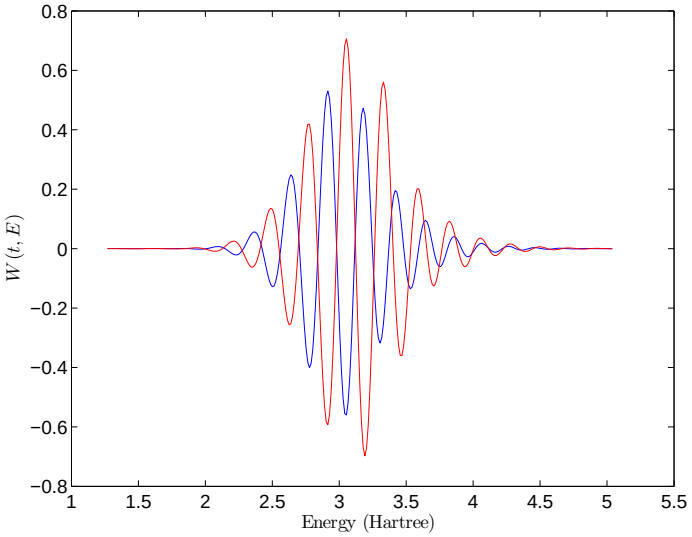


Figure 4.30: The amplitude of the transmission and reflection scattering WDFs at a time of 32 A.U. and 21 A.U. for the square well potential with a depth of 11.628 Hartree. The purpose of this figure is to compare the probability exchange between the second transmission and reflection.

### *4.10.2 Frequency of Arrival.*

Can the Wigner Distribution Function reveal to us more information about the scattering event than the correlation function or the s-matrix elements? In order to answer this question, we examined the Fourier transform of the amplitude of the WDF for a given value of energy over all of time as shown in Fig. 4.31. The slice in energy produces a signal, and as seen in Fig. 4.31, the Fourier transform of these signals shows the spectrum of frequencies present in the signals. For the energy slice, the Fourier transform of this signal will describe the frequency at which probability was transmitted through the square well. Hence, we will refer to the Fourier transform as the frequency of arrival for a given energy value. The peaks present in Fig. 4.31 is the frequency at which a plane wave with a given energy oscillates in the well. This frequency is one over the time it takes for the wave packet to propagate one round trip in the square well. The frequency is given as

$$\omega = \frac{2\pi\sqrt{2(E+V)}}{2L\sqrt{\mu}} \tag{4.9}$$

where $V$ is the magnitude of the depth of the well. The first peak corresponds to the fundamental frequency $\omega = 0.276$ A.U. while other peaks correspond to the odd harmonics of $\omega$. The frequency of arrival is information that is not found in the correlation function of the Fourier transform of the correlation function. As a result, the WDF does provide more information into the scattering event than the correlation function and s-matrix elements.

### *4.10.3 Negative Chirp.*

The shape of the negative chirp of the WDF can be related to the classical motion of a particle. If the distance from the peak of the reactant/product Møller state to the edge of the square well is $x_o$, the length of the square well is $L$, the velocity of the classical particle in the zero potential regions is $v$, and the velocity of the classical particle in the square well

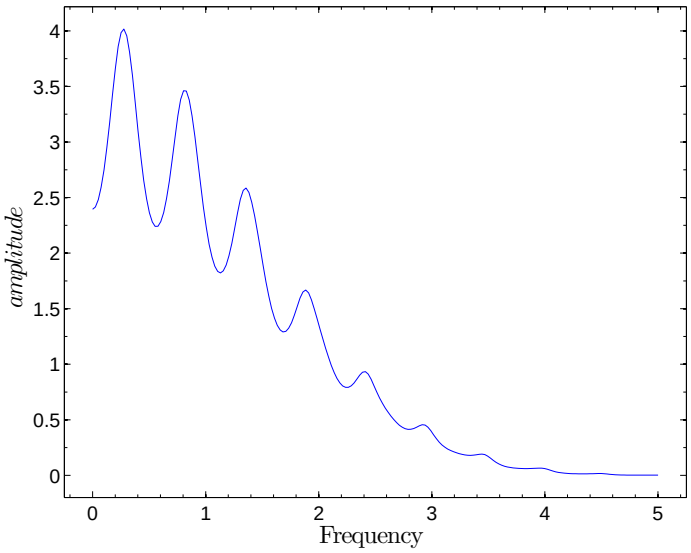


Figure 4.31: The figure is the Fourier transform of the amplitude of the WDF for a square well potential with a depth of 11.628 Hartree. The amplitude of the WDF was taken at 3.033 Hartree over the entire time domain. The first peak corresponds to the frequency at which the wave packet oscillates in the well ($\omega$), the second peak corresponds to ($3\omega$), the third peak corresponds to ($5\omega$) and the trend continues.

is $v'$, then the distances the particle travelled is given by

$$x_o = v\Delta t \tag{4.10}$$

$$L = v'\Delta t' \tag{4.11}$$

With $E = \frac{1}{2}\mu v^2$ and $E + V = \frac{1}{2}\mu v'^2$, the total time, $t$, can be solved for as a function of energy.

$$t = \sqrt{\mu}\left(\frac{2x}{\sqrt{2E}} + \frac{L}{\sqrt{2(E+V)}}\right) \tag{4.12}$$

where V is the magnitude of the depth of the square well.

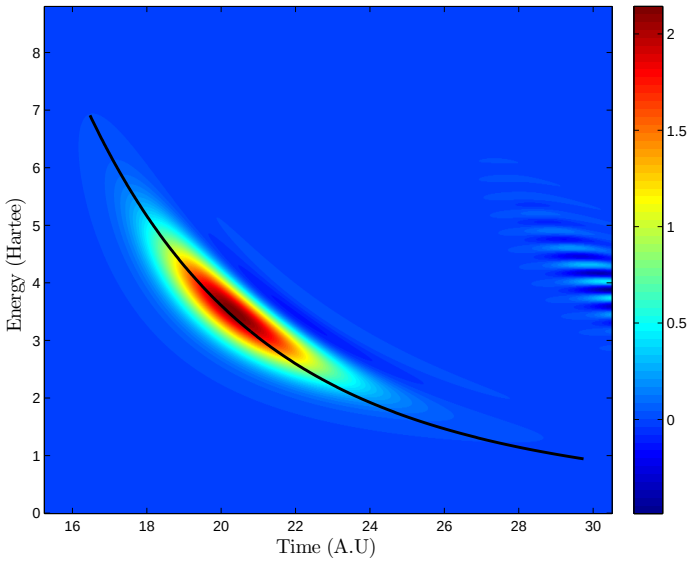


Figure 4.32: The energy-time relation of the WDF for a square well potential with a depth of 11.628 Hartree. Eq. 4.12 is plotted on top of the scattering WDF as the black line.

# V. $H + H_2$ and $OH + CO$ Scattering

After producing scattering WDF for the finite square well and square barrier potentials, scattering WDFs were produced for the $H + H_2$ reaction. Three scattering WDFs were produced for the correlation functions between a reactant Møller state in the ground vibrational state and a product Møller state in each of the first three internal vibrational energy states of $H + H_2$ collision. The correlation function for this scattering reaction was previously calculated by Weeks and Calfas [11], and code was developed to import the correlation functions. In order to calculate the correlation function, Weeks and Calfas [11] used the channel packet method. The reactant state was centered on the Liu-Siegbahn-Truhlar-Horowitz (LSTH) Potential Energy Surface (PES) and coupling was assumed to occur among the first three surfaces [12, 13]. Unlike the square potential, the reactant Møller and product states will not be the same as the initial reactant and product states while on these surfaces. The initial reactant and product states were chosen such that the computed Møller states were localized in the interaction potential. In order to compute the Møller states, the initial reactant and product states were propagated to "infinity" under the asymptotic Hamiltonian and then back to zero under the full Hamiltonian. The correlation function is computed by propagating the reactant Møller state forward in time from $t = 0$ to $t_{max}$ and then backwards in time from $t = 0$ to $t_{min}$ with the aide of absorbing boundary conditions. Because scattering can occur into any of the first three internal vibrational energy states, three product Møller states had to be computed, and the correlation function was computed for each of these product Møller states as the reactant Møller state evolved in time. As a result, three scattering WDFs were computed for each of the correlation functions in the same way that the scattering WDFs were calculated for the square potentials. The purpose of creating scattering WDFs for the $H + H_2$ was to verify the accuracy of the code to import correlation functions and produce scattering

WDFs from these imported functions by comparing the scattering WDF of the ground internal vibrational arrangement channel with the scattering WDF independently calculated for the same arrangement channel. Another purpose was to produce scattering WDFs for the coupling between the ground state with the first two excited internal vibrational states which was never accomplished before. The correlation function for a single arrangement

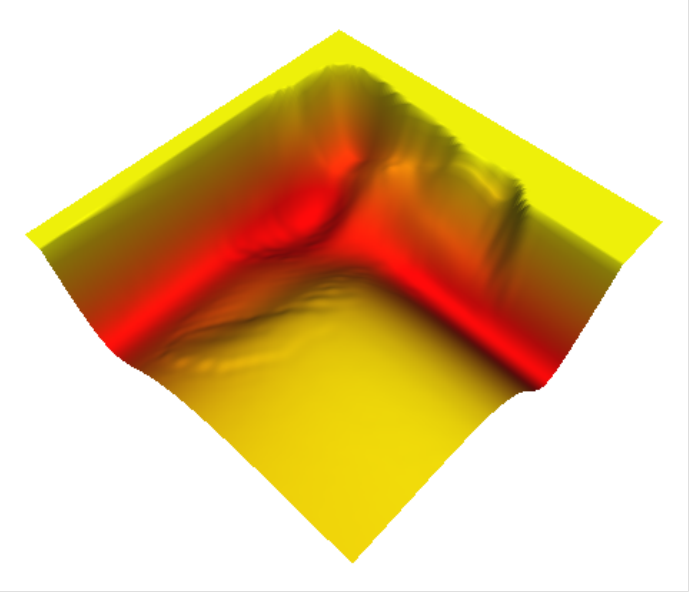

Figure 5.1: The $OH(v = 0) + CO \leftrightarrow OCO(v = 0) + H$ PES.

channel of the $OH(v = 0) + CO \leftrightarrow OCO(v = 0) + H$ channel collision [10] was previously calculated by Weeks using the CPM. The PES used is shown in Fig. 5.1. Like the $H + H_2$ problem, the reactant and product Møller states had to be calculated. The same procedure for calculating the Møller states of the $H + H_2$ collision was used in the Møller states of the $OH + CO$ collision. These Møller states are then used to calculate the correlation function. Again, the correlation function data was imported, and the scattering WDF was calculated exactly in the same manner as the $H + H_2$ problem. The only difference was that the $OH + CO$ correlation function had to be down sampled while the $H + H_2$ did not. Because only one arrangement channel was imported, only one scattering WDF was

calculated. Calculating the scattering WDF for the $OH + CO$ problem has never been computed previously, so the purpose was to produce the $OH + CO$ scattering WDF. Due to the very sharp resonant structures in the transmission coefficient, the $OH + CO$ scattering WDF should consist of unique features. The parameters and grid sizes associated with the correlation functions are shown in Table 5.1.

Table 5.1: $H + H_2$ and $OH + CO$ Parameters

| variable | $H + H_2$ | $OH + CO$ | meaning |
|---|---|---|---|
| $n_{time}$ | 16000 | 1080500 | number of time grid points |
| $n_\tau$ | 8192 | 65536 | number of tau grid points |
| $ds$ | 2 | 20 | number of points down sampled |
| $t_{min}$ | -7999 | -1079999 | minimum time |
| $t_{max}$ | 500 | 8000 | maximum time |

The WDFs for the $H + H_2$ and the $OH + CO$ collisions are different than the square potential problem. In the $H+H_2$ scattering WDFs, a large, positively valued, peak structure still exists; however, this peak structure is more localized than the spread out chirp in the square potentials. A series of bands running nearly parallel to the time axis are also present in the scattering WDFs. The bands seem to diverge from the energy value associated with the large peak and converge towards an asymptotic upper energy limit or an asymptotic lower energy. These asymptotic energies seem to be centered on the width of the large, positive peak. The scattering WDFs for the upper two states have a similar large peak and band structure that appears. The difference between the ground state scattering WDF and the upper two states is that the bands in the upper two states converge asymptotically towards the energy value where the peak value of the scattering WDF lies. Although the ground state scattering WDF is approximately 7.5 times larger than the first vibrational state scattering WDF or approximately 600 times larger than the second vibrational state,

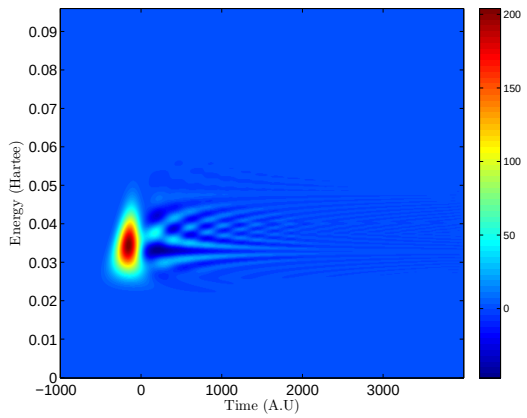


(a) Scattering WDF for for $\nu = 0 \rightarrow \nu' = 0$ internal vibrational state.

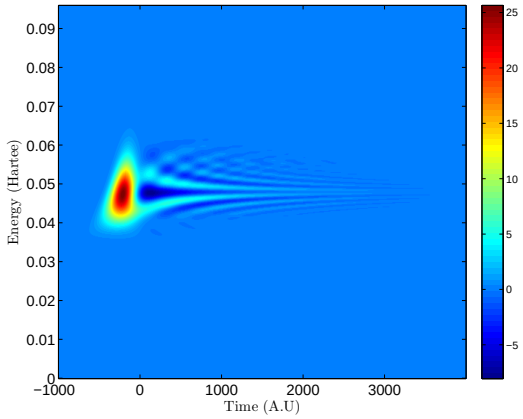


(b) Scattering WDF for for $\nu = 0 \rightarrow \nu' = 1$ internal vibrational state.

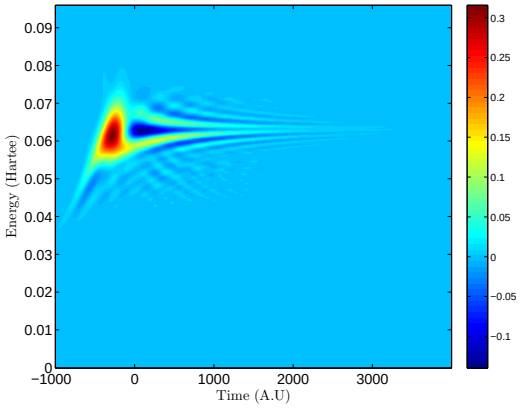


(c) Scattering WDF for for $\nu = 0 \rightarrow \nu' = 2$ internal vibrational state.

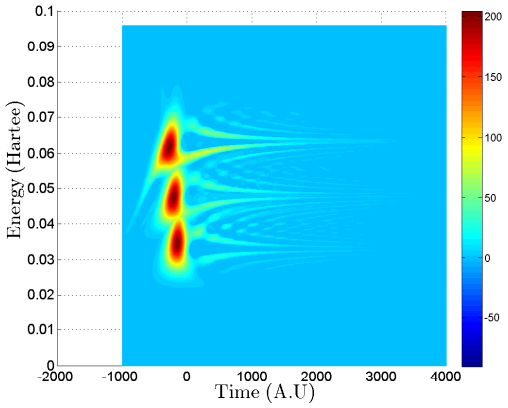


(d) Figure showing all three scaled scattering WDFs for $\nu = 0 \rightarrow \nu' = 0$,$\nu = 0 \rightarrow \nu' = 1$, and $\nu = 0 \rightarrow \nu' = 2$ on the same axis

Figure 5.2: Scattering WDFs for the first three internal vibrational states of the $H + H_2$ collision. The reactant Møller state was placed on the ground vibrational state and correlated with product Møller states on the first three LSTH surfaces labeled by the internal vibrational state, $\nu$. Each scattering WDF contains a large, positive valued single peak and a series of oscillating bands that seem to converge towards certain energy values. A fourth plot contains all three scattering WDFs on the same axis. The $\nu = 0 \rightarrow \nu = 1$ scattering WDF was scaled by a factor of 7.95 and the$\nu = 0 \rightarrow \nu = 2$ scattering WDF was scaled by a factor of 645.92 such that the peaks were equal

an interesting observation occurs when the three scattering WDFs are plotted on the same axis and scaled such that the large central peaks have the same peak value. The three large, single peaks are above each other on the energy scale. The upper bands of the

ground vibrational state seem to converge with the lower bands of the first vibrational state to the center of the first vibrational scattering WDF. Although the upper bands of the first excited vibrational state converged towards the center of the peak of the first excited vibrational state and although the lower bands of the second excited vibrational state converged towards the center of the peak of the second excited vibrational state, together these bands form a region very similar to the region between the ground state and the first vibrational state. Further analysis is required in order to determine what these bands mean.

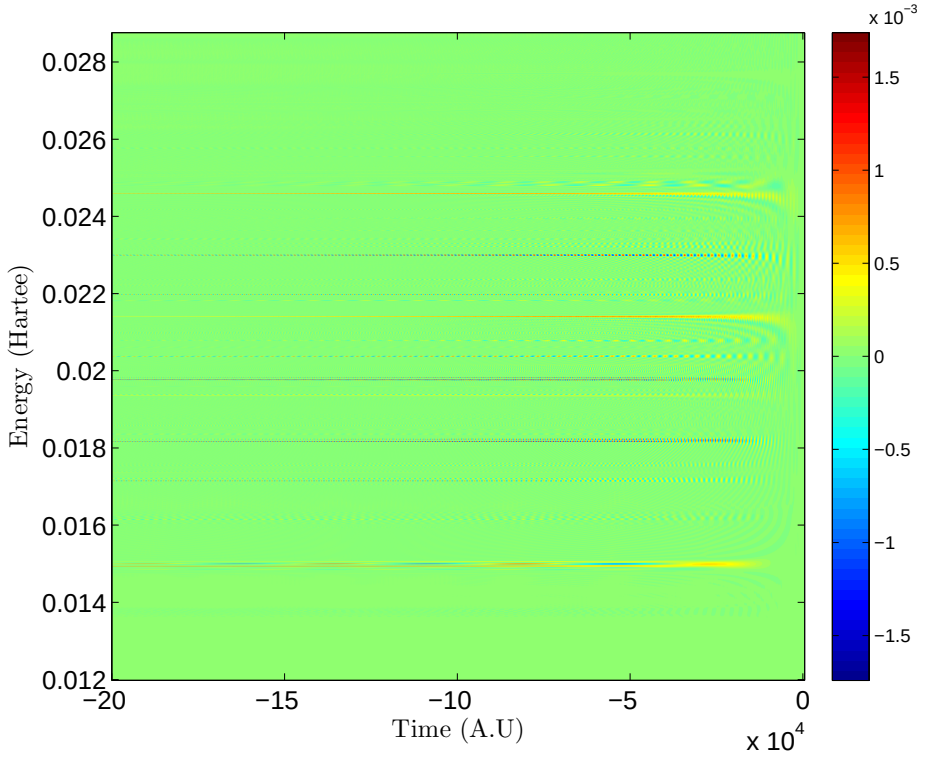


Figure 5.3: Scattering WDF for the $OH(v = 0) + CO \leftrightarrow OCO(v = 0) + H$ collision. The scattering WDF contains very long, narrow bands that contain oscillating peaks and valleys. The frequency of oscillations of peaks vary among the different bands.

The $OH + CO$ scattering WDF has a series of very narrow band structures that run parallel to the time grid for very long periods of time as compared to the $H + H_2$

scattering WDFs. There seems to be a group of bands that are relatively close to each other; however, between each group of bands there is a large region of zero scattering WDF values. For example, there is a group of closely spaced bands at approximately 0.023 Hartree followed by another set of closely spaced bands at approximately 0.0245 Hartree. This is consistent with the transmission coefficient since the transmission coefficient has a group of closely spaced sharp peaks that are spaced relatively far from the next grouping of peaks. Every band in the $OH + CO$ data set contains oscillating positive and negative peaks; however, the width of the peaks or the magnitude of the peaks vary. The very long bands arise from the presence of long lived quasi-bound states trapped by the well of the $OH(v = 0)+CO \leftrightarrow OCO(v = 0)+H$ channel. Further analysis should be done to determine if the frequency of oscillations in the peaks of each band (i.e. the width of each peak) have any relation to the parameters of the well of $OH + CO$ collision. Further analysis should be done to see if the negative values of the scattering WDF correspond to correspond to positive values in the same location for higher vibrational states.

The $H + H_2$ collision is an example where a large single peak is significantly much larger than the smaller oscillating peaks. As a result, when the scattering WDF is projected onto the frequency domain, the large single peak will contribute most to $|c(w)|^2$ as shown below while the oscillating peaks, which will mostly cancel each other out, will have only a small contribution to $|c(w)|^2$. Therefore, the transmission coefficient will resemble Fig. 5.4. On the other extreme, the $HO + CO$ collision does not have a large peak but instead long narrow bands of oscillating peaks that run parallel to the time grid. These bands are the major contributions $|c(w)|^2$. Hence, the transmission coefficient for $OH + CO$ consists of many resonant sharp peaks compared to the $H + H_2$ peaks.

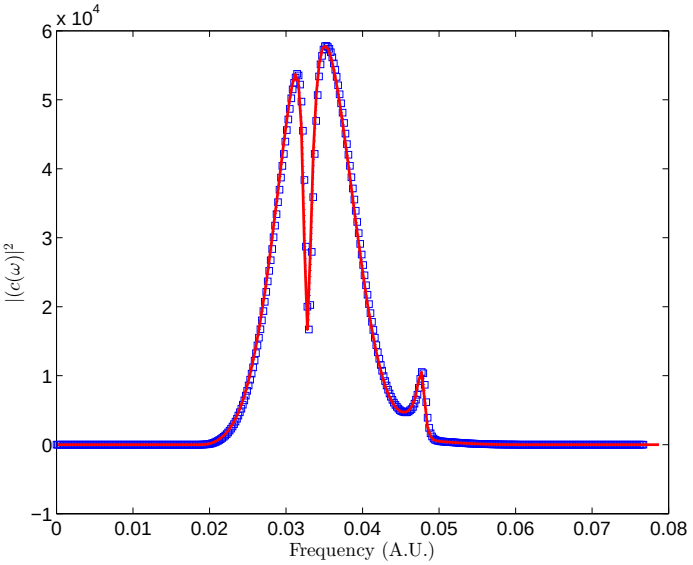


Figure 5.4: The plots of the projection of the scattering WDF (blue) onto frequency domain as compared to $|c(\omega)^2|$ respectively (red) for the $H + H_2(v = 0) \leftrightarrow H + H_2(v = 0)$ collision.

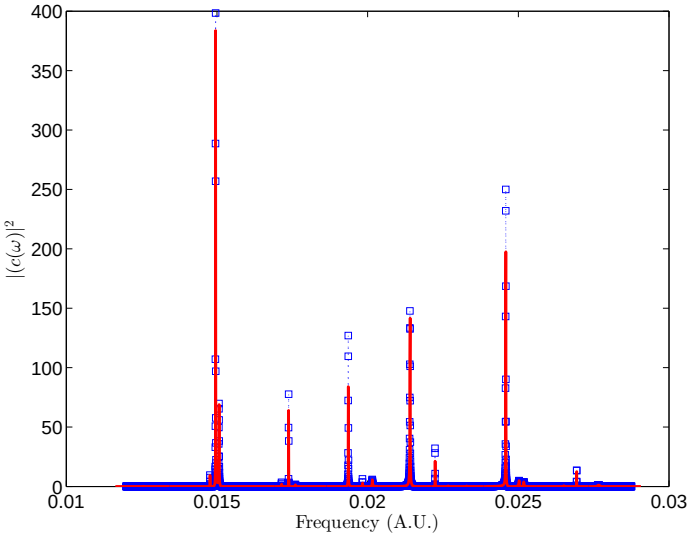


Figure 5.5: The plots of the projection of the scattering WDF (blue) onto frequency domain as compared to $|c(\omega)^2|$ respectively (red) for the $OH(v = 0) + CO \leftrightarrow OCO(v = 0) + H$ collision.

# VI. $M + Ng$ Scattering

With confidence that the code is working and with some insight into the scattering WDF, we now focus on producing scattering WDFs for $M + Ng$ collisions.

## 6.1 Theory

The Hamiltonian for the $M + Ng$ reaction is

$$\hat{H} = \frac{1}{2\mu}\hat{P}^2_{\vec{R}_\mu} + \hat{H}^0_{MNg}(\vec{r}_{N_M}, \vec{r}_{N_{Ng}}, \vec{R}) + \hat{V}^M_{ls}(\vec{r}_{N_M}, \vec{R}) \tag{6.1}$$

where $M$ is the alkali metal, $Ng$ is the noble gas, $\mu$ is the reduced mass, $\vec{R}_\mu$ is the coordinate vector from the origin to the center of mass of the two nuclei, $\vec{R}$ is the coordinate vector between the center of masses for each atom, $\vec{r}_N$ is the coordinate vector from the center of mass of the designated atom to the $n^{th}$ electron of the designated atom, $\hat{V}^M_{ls}$ is the spin-orbit potential for the alkali atom with quantum numbers $l$ and $s$ (the electronic angular momentum and spin values respectively), $\hat{P}_{\vec{R}_\mu}$ is the momentum of the reduced mass, and $\hat{H}^0_{MNg}(\vec{r}_{N_M}, \vec{r}_{N_{Ng}}, \vec{R}) = \hat{H}^0_M(\vec{r}_{N_M}) + \hat{H}^0_{Ng}(\vec{r}_{N_{Ng}}) + \hat{V}_{MNg}(\vec{r}_{N_M}, \vec{r}_{N_{Ng}}, \vec{R})$ contains the electronic Hamiltonians and the interaction potential. Note that the functional dependence of the first $N_M - 1$ electrons of alkali metal and the first $N_{Ng} - 1$ electrons of noble gas were dropped but still implied. The spin-orbit potential for the noble gas is zero because in the ground state, the total angular momentum for a noble gas is zero. The total angular momentum is zero because the shell is full of electrons [22]. The advantage of writing the Hamiltonian in the form of Eq. 6.1 is that the electrostatic potentials are grouped together which makes it easier to make the Born-Oppenheimer expansion.

Because of the interaction potential, the Hamiltonian in Eq. 6.1 is not separable [4, 5, 23]. In order to resolve this problem, the Born-Oppenheimer approximation is made. The Born-Oppenheimer approximation assumes that due to the mass of the nuclei compared to the mass of the electrons, the electrons will quickly settle into their eigenstates

every time the nuclei move. As a consequence, the separation distance, $\vec{R}$, between each nuclei is parametrized. The eigenvalues of the electronic Hamiltonian, $\hat{H}^0_{MNg}(\vec{r}_{N_M}, \vec{r}_{N_{Ng}}, \vec{R})$, are solved for each value of $\vec{R}$ [20]. In other words, the electronic Hamiltonian is completely diagonalized, and the diagonal entries, the eigenvalues, are plotted as a function of $\vec{R}$. The plot of the $i^{th}$ eigenvalue of the Hamiltonian forms a surface of potential energy values called the potential energy surface (PES) [8]. More specifically, these plots are refereed to as the adiabatic potential energy surfaces because the electronic Hamiltonian is diagonalized. A scattering event is simplified with the Born-approximation because the electronic dynamics is eliminated from the problem.

Unfortunately, the Born-Oppenheimer approximation does not allow coupling between the various PES. In order to account for this, a variation of the Born-Oppenheimer approximation, the group Born-Oppenheimer approximation, instead neglects non-coupled states, and the dimensionality of a coupling matrix used in the Born-Oppenheimer approximation reduces to the number of coupled states with the Born-Oppenheimer approximation being the limit in which there is a single state. The premise for this approximation arises from the fact that the coupling terms can be neglected when the adiabatic electronic energy levels are far apart; however, if the adiabatic electronic energy levels approach each other at a particular nuclear separation, then the coupling terms will be large. Because this work is interested in the application of scattering in a DPAL laser system, coupling will be assumed for the group of molecular states in the P-maniforld. The molecular states of interest are: $|^J_\Omega,^{\frac{3}{2}}_{\frac{3}{2}}>$, $|^J_\Omega,^{\frac{3}{2}}_{\frac{1}{2}}>$, $|^J_\Omega,^{\frac{3}{2}}_{-\frac{1}{2}}>$, $|^J_\Omega,^{\frac{3}{2}}_{-\frac{3}{2}}>$, $|^J_\Omega,^{\frac{1}{2}}_{\frac{1}{2}}>$, $|^J_\Omega,^{\frac{1}{2}}_{-\frac{1}{2}}>$ where $J$ is the total angular momentum which is the sum of the total electronic angular momentum $j$ and the internuclear angular momentum $L_\mu$ and $\Omega$ is the projection of $J$ onto the body-fixed z axis [8, 17]. The body-fixed states are represented as $|\vec{R},^{J}_{\Omega},^{j}_{m_j}>$; however, the dependence on $\vec{R}$ was dropped for notational simplicity. For these states, $\Omega = \pm\frac{3}{2}$ when $m_j = \pm\frac{3}{2}$ and $\Omega = \pm\frac{1}{2}$ when $m_j = \pm\frac{1}{2}$. Because, there are six electronic molecular states of interest, the Hamiltonian will consist of a set of

6$x$6 matrices for each value of $J$. We were interested in the body-fixed projections rather than the space-fixed projections because transforming into the body-fixed reference frame reduces the two body problem into a one dimensional problem since the internuclear vector $\vec{R}$ remains invariant [17]. If we neglect the coupling between the positive and negative z-axis projections in the body-fixed reference frame, the 6$x$6 matrix reduces to a 3$x$3 matrix where the $^2P_{\frac{3}{2}}$ manifold becomes two-fold degenerate.

The Hamiltonian represented in the body-fixed Born-Oppenheimer molecular basis [8, 9] is

$$\hat{H} = \frac{1}{2\mu}
\begin{array}{c}
\begin{matrix} \quad |^{J}_{\frac{3}{2},\frac{3}{2}}{}^{\frac{3}{2}}> & \quad |^{J}_{\frac{1}{2},\frac{1}{2}}{}^{\frac{3}{2}}> & \quad |^{J}_{\frac{1}{2},\frac{1}{2}}{}^{\frac{1}{2}}> \end{matrix} \\
\begin{pmatrix} \frac{d^2}{dR^2} & 0 & 0 \\ 0 & \frac{d^2}{dR^2} & 0 \\ 0 & 0 & \frac{d^2}{dR^2} \end{pmatrix}
\end{array} +$$

$$\begin{array}{c}
\begin{matrix} \quad |^{J}_{\frac{3}{2},\frac{3}{2}}{}^{\frac{3}{2}}> & \quad |^{J}_{\frac{1}{2},\frac{1}{2}}{}^{\frac{3}{2}}> & \quad |^{J}_{\frac{1}{2},\frac{1}{2}}{}^{\frac{1}{2}}> \end{matrix} \\
\begin{pmatrix} \Pi + \frac{a(R)}{2} & 0 & 0 \\ 0 & \frac{2\Sigma+\Pi}{3} + \frac{a(R)}{2} & \mp\frac{\sqrt{2}}{3}(\Sigma - \Pi) \\ 0 & \mp\frac{\sqrt{2}}{3}(\Sigma - \Pi) & \frac{\Sigma+2\Pi}{3} - a(R) \end{pmatrix}
\end{array} + \qquad (6.2)$$

$$\begin{array}{c}
\begin{matrix} \quad |^{J}_{\frac{3}{2},\frac{3}{2}}{}^{\frac{3}{2}}> & \quad |^{J}_{\frac{1}{2},\frac{1}{2}}{}^{\frac{3}{2}}> & \quad |^{J}_{\frac{1}{2},\frac{1}{2}}{}^{\frac{1}{2}}> \end{matrix} \\
\begin{pmatrix} \frac{J(J+1)-\frac{3}{4}}{2\mu R^2} & -\frac{[3(J-\frac{1}{2})(J+\frac{3}{2})]^{\frac{1}{2}}}{2\mu R^2} & 0 \\ -\frac{[3(J-\frac{1}{2})(J+\frac{3}{2})]^{\frac{1}{2}}}{2\mu R^2} & \frac{J(J+1)+\frac{13}{4}}{2\mu R^2} & 0 \\ 0 & 0 & \frac{J(J+1)+\frac{3}{4}}{2\mu R^2} \end{pmatrix}
\end{array}$$

where $a(R)$ is the spin-orbit split parameter of the alkali metal and where $\Pi$ and $\Sigma$ are the eigenvalues associated with the adiabatic electronic energy surfaces labelled $\Pi$ and $\Sigma$ respectively. Note that the $m_j = -\frac{3}{2}, -\frac{1}{2}$ values are decoupled from the $m_j = \frac{3}{2}, \frac{1}{2}$ values. With the full Hamiltonian represented in the Born-Oppenheimer molecular basis, the physics of the $M + Ng$ can be deduced. The first matrix of Eq. 6.2 contains the radial derivative coupling terms, which are neglected [8, 9, 18], so the radial derivative coupling

matrix simply contains the kinetic energy on the diagonal elements. The second matrix in Eq. 6.2 contains the spin-orbit coupling terms. This matrix contains both the electronic Hamiltonian and the spin-orbit potential. The presence of the spin-orbit potential forced the states with the same electronic angular momentum projected onto the internuclear axis but originating from different asymptotic curves to couple. The spin-orbit coupling, which is also known as radial coupling, couples the ${}^2P_{\frac{3}{2}}$ (the $|^{\frac{3}{2}}_{\omega}>$ states) and the ${}^2P_{\frac{1}{2}}$ (the $|^{\frac{1}{2}}_{\omega}>$ states). The spin-orbit coupling is the only source of probability transfer at this level of theory between the P-manifold split. This coupling factor depends upon the strength of the spin-orbit coupling function and the energy difference between the two states. If the energy of the system is less than the energy difference between ${}^2P_{\frac{3}{2}}$ and ${}^2P_{\frac{1}{2}}$, then there is low probability that a transition will occur.

Once there is a probability density function on the ${}^2P_{\frac{3}{2}}$ curve due to spin-orbit coupling, Coriolis coupling can occur on the two-fold degenerate ${}^2P_{\frac{3}{2}}$ manifold. The matrix containing the Coriolis coupling term will be referred to as the total angular momentum matrix reserving the term Coriolis coupling for the off diagonal matrix elements. The diagonal elements of this matrix has the same functional form as the effective potential in the hydrogen atom Hamiltonian, so the diagonal matrix elements will be referred to as the effective potential (or centrifugal barrier). The total angular momentum matrix results from the nuclear kinetic energy begin transformed into the body-fixed coordinate system. This transformation moves the dynamics of the molecule into a rotating non-inertial reference frame, and the use of a non-inertial reference frame creates a fictitious potential known as the centrifugal potential along the diagonal of the matrix [6]. This potential only appears in the body-fixed coordinate system and is purely a dynamical effect dependent on coordinates. The effect of rotating into the body-fixed reference frame creates an angular momentum dependent term in the Hamiltonian which couples the total electronic momentum to the nuclear angular momentum. This coupling term measures the rate at

which the molecular wave function rotates compared to the nuclear axis. If the molecular wave function rotates at the same rate as the nuclear axis, then the total angular momentum is the same as the electronic angular momentum, and no coupling occurs. On the other hand, if the energies are large enough, the nuclear axis rotates at a rate comparable to the rate at which the electrons relax into their adiabatic states. The molecule is no longer in an adiabatic state, and coupling between various PES occurs [8]. Coriolis coupling occurs between the $|^{\frac{3}{2}}_{\frac{3}{2}}>$ and the $|^{\frac{3}{2}}_{\frac{1}{2}}>$ states. It is possible then that the wavefunction gets trapped in the $^2P_{\frac{3}{2}}$ manifold due to Coriolis coupling. This prevents some of the wavefunction to scatter back down to the $^2P_{\frac{1}{2}}$ manifold. The strength of the Coriolis coupling depends upon the velocity at which the colliding partners interact. As the nuclear velocity increases, the rate at which the molecular axis rotates increases. At large enough energies the molecular wavefunction will not be able to keep up with the molecular axis, and a transition takes place that changes the electronic projection onto the molecular axis.

The Hamiltonian in Eq. 6.2 is in diabatic form. In order to have the Hamiltonian in adiabatic form, the electronic terms need to be diagonalized. A transformation matrix, $U_{so}$, is used to diagonalize the electronic terms [8]; however, this transformation matrix must also be applied to the kinetic operator. In this new basis, coupling terms are added to the kinetic energy operator that wasn't present in the Born-Oppenheimer molecular basis. These new coupling terms are the spin-orbit coupling physics in a different representation; therefore, the spin-orbit coupling is sometimes referred to as radial coupling (not to be confused with radial derivative coupling).

## 6.2 Results

For the $M+Ng$ systems, the correlation functions were previously calculated by Loper [9]. The Hamiltonian for these systems is defined by Eq. 6.2. Because coupling between the positive spin states with the negative spin states is small, the $-\frac{J+1}{\mu R^2}$ term in the Coriolis coupling component was assumed to be zero. As a result, the Coriolis coupling reduced to

a 3×3 matrix rather than a 6×6 matrix. The full Hamiltonian was also reduced to a 3 matrix from eliminating this coupling term. The initial state was assumed to be in the positive spin state. The Møller states were calculated using the asymptotic Hamiltonian and the $3 \times 3$ full Hamiltonian. Because the Hamiltonian is in the diabatic state, the propagation scheme in the split operator method had to change slightly. In order to for Eq. 3.16 to apply, the potential operator must act on a wavefunction in the adiabatic basis rather than the diabatic basis. Thus a transformation matrix must be applied to the wavefunction. After the potential operator acts on the transformed wavefunction and before the Fourier transform is taken, the wavefunction must be transformed back into the diabatic representation using the transpose conjugate of the transformation matrix. The same transformation must occur at the second potential operator in the split-operator propagation scheme.

Calculation of the Møller states was done in the same manner as the $H + H_2$ and $OH + CO$ problems. Because the full Hamiltonian depends upon the total angular momentum, a reactant Møller state was created for each value of $J$. As J increases, greater amounts of energy was required to reach the interaction potential, so the asymptotic region kept getting pushed back due to the centrifugal potential. The asymptotic region for all regions was therefore defined according to the start of the asymptotic region of the highest J value. For example, for the $K + He$ system, the asymptotic region for $J = 0.5$ was approximately 20 Bohr versus 400 Bohr for $J = 250.5$. The highest J value used was the value of J associated with the particle being unable to reach the interaction region for the a system corresponding to energies of $0 - 0.0075 E_H$[9]. For each system, the highest J-value was different, so each system had a different number of correlation functions. Because there are three states of interest for each value of $J$: $|^{J}_{\frac{3}{2}},^{\frac{3}{2}}_{\frac{3}{2}}>$, $|^{J}_{\frac{1}{2}},^{\frac{3}{2}}_{\frac{1}{2}}>$, and $|^{J}_{\frac{1}{2}},^{\frac{1}{2}}_{\frac{1}{2}}>$, three product Møller states for each value of $J$ were created on each surface. Not only was there a static product Møller state for each surface, the reactant Møller states were also propagated along each curve and correlated with each product Møller state. In other words, for each alkali

plus noble gas system, there were correlation functions computed for each of the reactant Møller states evolving on the three different PES overlapping with each of the three product Møller states as a function of total angular momentum.

Fig. 6.1 sumarizes the computational procedure along with the coupling terms present. Although all of the states belonging to the $^2P_{\frac{3}{2}}$ maniforld are at the same energy level in the asymptotic regime, they were artifically seperated in Fig. 6.1 in order to show which states leads to seperate adiabatic surfaces duing the collision. The adiabatic surfaces are shown in Fig. 6.2.

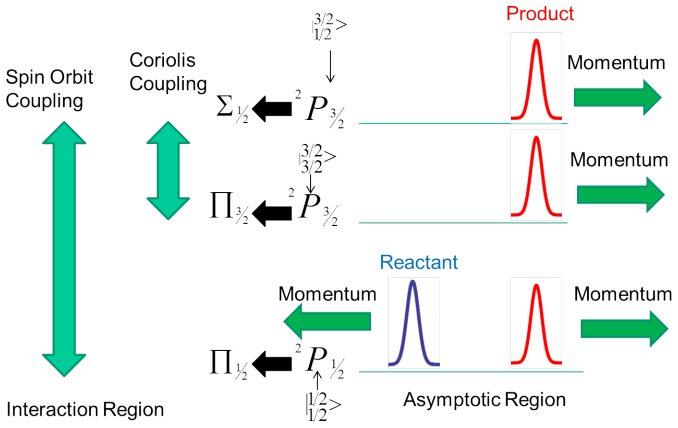


Figure 6.1: Summary of the $M+Ng$ collision. The states $|^J_{\frac{3}{2},\frac{3}{2}}{}^{,\frac{3}{2}}>$ and $|^J_{\frac{1}{2},\frac{1}{2}}{}^{,\frac{3}{2}}>$ belong to the $^2P_{\frac{3}{2}}$ manifold in the asymptotic regime while $|^J_{\frac{1}{2},\frac{1}{2}}{}^{,\frac{1}{2}}>$ belongs to the $^2P_{\frac{1}{2}}$ manifold. Although all of the states belonging to the $^2P_{\frac{3}{2}}$ maniforld are at the same energy level in the asymptotic regime, they were artifically seperated. Three product Møller states are placed on each of the adiabatic PES which are labeled as $\Pi_{\frac{1}{2}}$ , $\Pi_{\frac{3}{2}}$, and $\Sigma_{\frac{1}{2}}$. A reactant Møller can be placed on any adiabatic surface, but as an example, the reactant Møller state starts on the $\Pi_{\frac{1}{2}}$ surface. Radial coupling couples the $\Pi_{\frac{1}{2}}$ and $\Sigma_{\frac{1}{2}}$ surfaces when the reactant Møller state is propagated into the interaction region, and Coriolis coupling couples the $\Pi_{\frac{1}{2}}$ and $\Sigma_{\frac{1}{2}}$ surfaces.

Scattering WDFs were produced for the following systems: Ke+He, Ke+Ne, K+Ar, Rb+He, Rb+Ne, Rb+Ar, Cs+Ne, Cs+Ar. The same code that imported the correlation functions and produced the scattering WDFs for previous potentials was also used for the

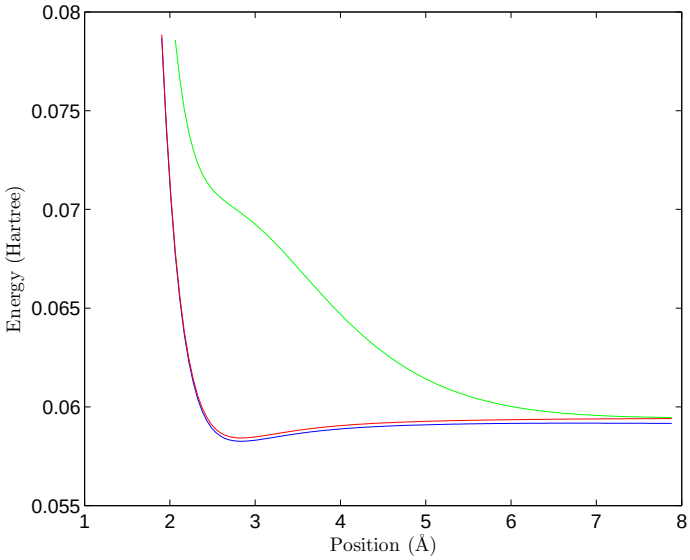


Figure 6.2: The adiabatic PES ($\Pi_{\frac{1}{2}}$ (blue), $\Pi_{\frac{3}{2}}$ (red), and $\Sigma_{\frac{1}{2}}$ (green) for the $K+He$ collision.

$M+Ng$ collisions. After the scattering WDFs were calculated, an analysis of the scattering WDFs was done. The parameters and grid sizes associated with the correlation function of each alkali plus noble gas studied are shown in Table 6.1.

Table 6.1: Alkali and Noble Gas Parameters

| meaning | $K+He$ | $K+Ne$ | $K+Ar$ | $Rb+He$ | $Rb+Ne$ | $Rb+Ar$ | $Cs+Ne$ | $Cs+Ar$ |
|---|---|---|---|---|---|---|---|---|
| time grid | 150000 | 125000 | 125000 | 100000 | 75000 | 125000 | 75000 | 125000 |
| tau grid | 65536 | 65536 | 65536 | 65536 | 65536 | 65536 | 65536 | 65536 |
| sampled | 2 | 2 | 2 | 2 | 1 | 2 | 1 | 2 |
| min time | 0 | 0 | 0 | 0 | 0 | 0 | 0 | 0 |
| max time | 2999980 | 4999960 | 4999960 | 1999980 | 5999920 | 4999960 | 5999920 | 4999960 |

Figs. 6.3-6.5 show the scattering WDFs for the $K+Ne$ system for the case when the reactant Møller state was on the $|^{\frac{1}{2}}_{\frac{1}{2}}>$ surface and correlated with product states on each surface at a total angular momentum value of $J = 100.5$. As we will see shortly,

the "reflection scattering WDF", which is the scattering WDF associated with the product Møller state on the same surface as the reactant Møller state, had the greatest amplitude and maintained the same structure as the total angular momentum increased. The structure of this scattering WDF consisted of closely spaced, negatively chirped, single peaked (or valley) bands. The bands alternate between positive and negative values. The scattering WDF for the correlation function between a reactant Møller state on the $|^{\frac{1}{2}}_{\frac{1}{2}}>$ surface and product Møller state on the $|^{\frac{3}{2}}_{\frac{1}{2}}>$ or the $|^{\frac{3}{2}}_{\frac{3}{2}}>$ surface also have a series of closely space bands with a negative chirp to their structure; however, unlike the scattering WDF for the $c^{\frac{1}{2},\frac{1}{2}}_{\frac{1}{2},\frac{1}{2}}(t)$, some of the bands consist of oscillating peaks and valleys inside them rather than being a single peak. If the square well potential provides insight into the meaning of these oscillating peaks and valleys that appear in the middle of the scattering WDF for the $M + Ng$ collisions, the appearance of the oscillating peaks and valleys in the band may signify multiple transmissions of probability at that surface depending upon the number of bands present with oscillating peaks of valleys. The reflection scattering WDF has a similar structure to the square well scattering WDF at low square well depths which had only a single transmission of probability through the square well with significant probability. The bands with oscillating peaks and valleys did not appear until the square well depth was deep enough such that any secondary transmissions (or reflections) had significant probability. This may apply that there were multiple transfers of relatively significant probability amplitude to the $|^{\frac{3}{2}}_{\frac{1}{2}}>$ or the $|^{\frac{3}{2}}_{\frac{3}{2}}>$ surfaces. As the total angular momentum changed, the structure of the scattering WDF may change; but the scattering WDF still had these basic features.

### *6.2.1 Detailed Balance.*

When the total angular momentum is equal to 1.5 atomic units, $J = 1.5$, the Coriolis coupling and effective potential are very small. The only coupling that occurs is the radial

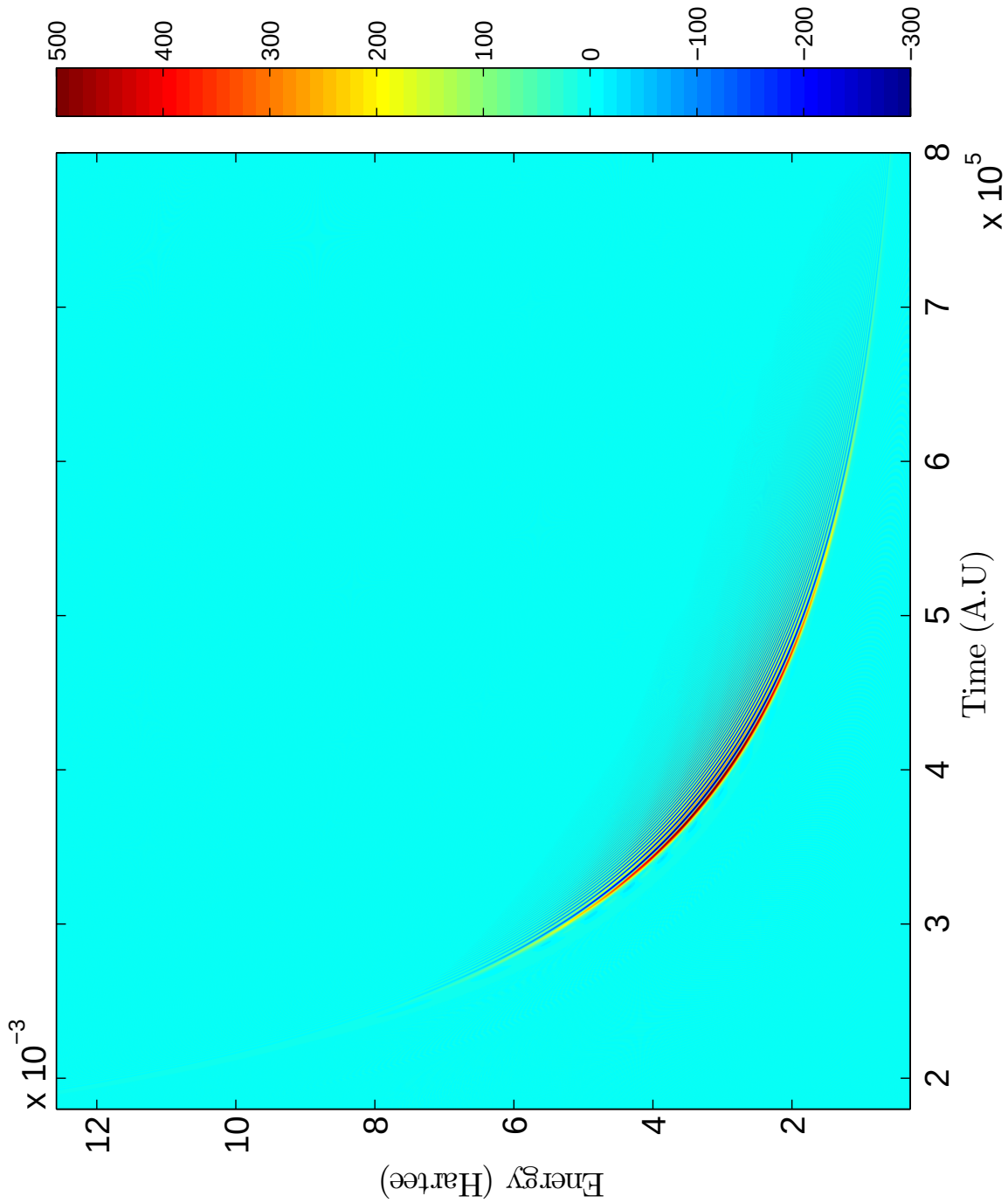


Figure 6.3: Scattering Wigner Distribution Function for K+Ne system with reactant Møller state in $|^{\frac{1}{2}}_{\frac{1}{2}}>$, product Møller state in $|^{\frac{1}{2}}_{\frac{1}{2}}>$, and $J = 100.5$

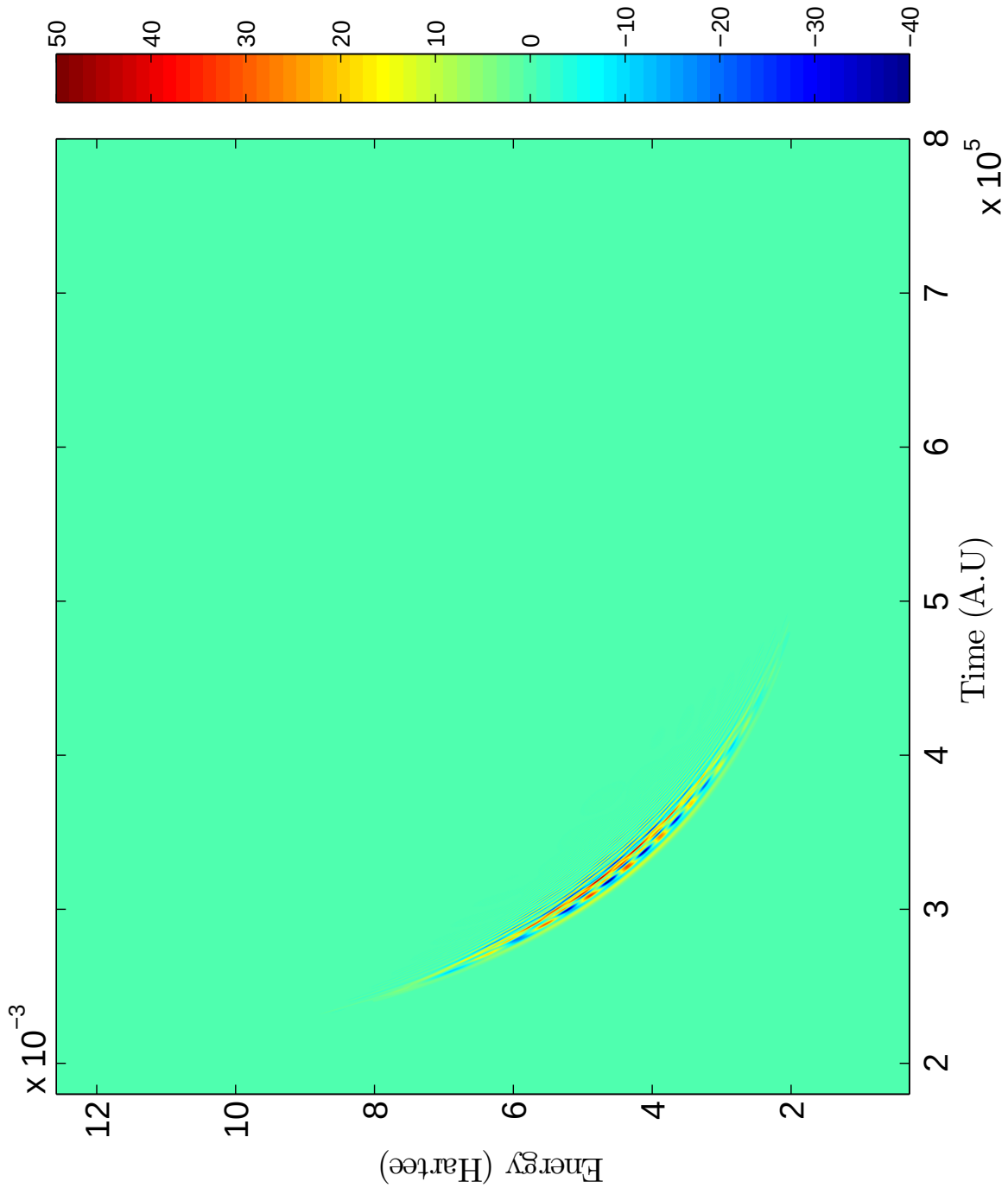


Figure 6.4: Scattering Wigner Distribution Function for K+Ne system with reactant Møller state in $|^{\frac{1}{2}}_{\frac{1}{2}}>$, product Møller state in $|^{\frac{3}{2}}_{\frac{1}{2}}>$, and $J = 100.5$

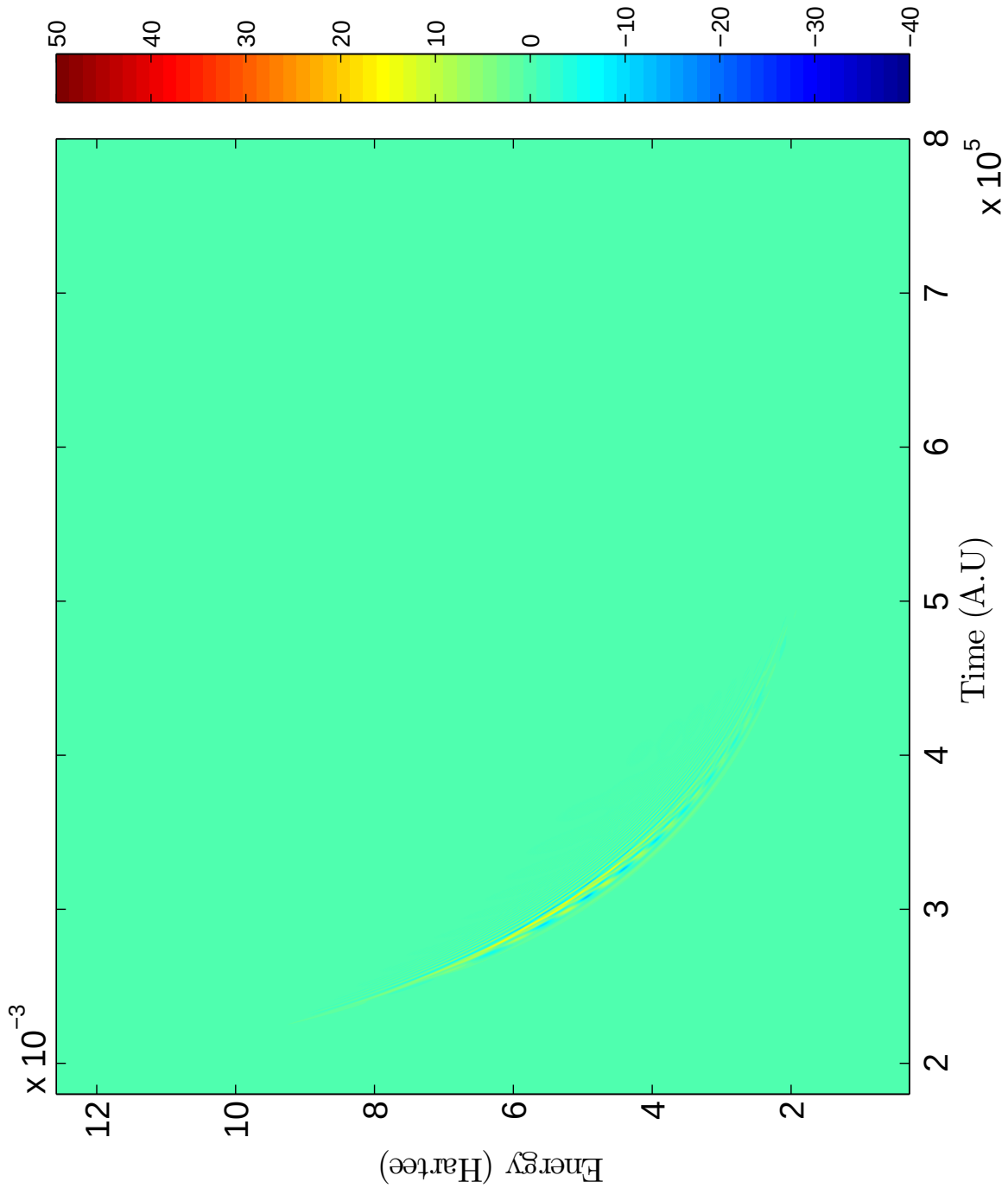


Figure 6.5: Scattering Wigner Distribution Function for K+Ne system with reactant Møller state in $|^{\frac{1}{2}}_{\frac{1}{2}}>$, product Møller state in $|^{\frac{3}{2}}_{\frac{3}{2}}>$, and $J = 100.5$

coupling, and if the reactant Møller state starts on either the $|^{\frac{1}{2}}_{\frac{1}{2}}>$ or the $|^{\frac{3}{2}}_{\frac{1}{2}}>$ PES, then the dynamics of probability transfer can be estimated by a two level system instead of three. According to the principle of detailed balance, the rate of probability transfer between the two surfaces is the same when the reactant Møller state starts on either the $|^{\frac{1}{2}}_{\frac{1}{2}}>$ or the $|^{\frac{3}{2}}_{\frac{1}{2}}>$ PES up to a proportionality constant governed by the difference in energy levels. The principle of detailed balance is shown below:

$$\frac{P_{ij}(E)}{P_{ji}(E)} = e^{-\frac{\Delta E}{KT}} \tag{6.3}$$

where $\Delta E$ is the difference in energy levels between the $|^{\frac{1}{2}}_{\frac{1}{2}}>$ and the $|^{\frac{3}{2}}_{\frac{1}{2}}>$ surfaces, $K$ is the Boltzmann constant, $T$ is the temperature, and $P_{ij}$ is the integrated projection of the scattering WDF at energy $E$ with the reactant Møller state starting on surface $i$ and ending on surface $j$. Figs. 6.6-6.11 demonstrate this idea. Notice that no detail of the WDF can be seen on the $|^{\frac{3}{2}}_{\frac{3}{2}}>$ in this scale, but the WDF can be seen on both the $|^{\frac{1}{2}}_{\frac{1}{2}}>$ and the $|^{\frac{3}{2}}_{\frac{1}{2}}>$ surface. In Fig. 6.6, the reactant Møller state started on the $|^{\frac{1}{2}}_{\frac{1}{2}}>$ surface of $K + Ne$, so most of the probability reflected back on the $|^{\frac{1}{2}}_{\frac{1}{2}}>$ surface while about a tenth of the probability was coupled via radial coupling to the $|^{\frac{3}{2}}_{\frac{1}{2}}>$ surface as seen by the amplitudes of the WDF for each surface. Now Fig. 6.7 shows the WDFs for the $K + Ne$ system when the reactant Møller state starts on the $|^{\frac{3}{2}}_{\frac{1}{2}}>$ surface. As the figure shows, most of the probability is reflected back on the $|^{\frac{3}{2}}_{\frac{1}{2}}>$ surface while about a tenth of the probability is transferred to the $|^{\frac{1}{2}}_{\frac{1}{2}}>$ surface via radial coupling.

When the WDF associated with $|^{\frac{1}{2}}_{\frac{1}{2}}>$ product Møller state in Fig. 6.6 is compared with the $|^{\frac{3}{2}}_{\frac{1}{2}}>$ surface in Fig. 6.7, there is a lot of similarity between the scattering WDFs. The similarity between Fig 6.8 and Fig 6.9 is consistent with the principle of detailed balance. Since $P_{ij}(E)$ differes from $P_{ji}(E)$, this suggests that the scattering WDFs differ by a constant amplitude factor, $e^{-\frac{\Delta E}{KT}}$. Further analysis must be done in order to determine if the difference in amplitude is $e^{-\frac{\Delta E}{KT}}$. When the WDF associated with $|^{\frac{3}{2}}_{\frac{1}{2}}>$ product Møller state in Fig. 6.8 is compared with the $|^{\frac{1}{2}}_{\frac{1}{2}}>$ surface in Fig. 6.9, the similarities are also consistent with the

principle of detailed balance. The $Cs$+$Ne$ collision between the $|^{\frac{3}{2}}_{\frac{1}{2}}>$ and $|^{\frac{3}{2}}_{\frac{3}{2}}>$ surface is also consistent with the principle of detailed balance since the large spin-obit split of $Cs + Ne$ causes the radial coupling to be insignificant creating a two-level system. An example of this is shown for $Cs + Ne$ at $J = 150.5$ in Fig. 6.12-Fig. 6.17. Figs. 6.6-6.17 suggest that the principle of detailed balance is not only satisfied for the integrated projection of the scattering WDF at energy $E$ for a two level system but throughout the entire collision. Again further analysis must be done to verify this claim.

### *6.2.2 High Total Angular Momentum Values.*

At high values of total angular Momentum, the effective potential becomes so large that the radial (spin-orbit) coupling is essentially turned off as seen in Eq. 6.2. The effective potential, which are the diagonal elements of the angular momentum dependent matrix in Eq. 6.2, shifts the adiabatic PES to higher values of internuclear separation distances, $R$. Because the spin-orbit coupling function is independent of total angular momentum, the spin-orbit coupling function remains the same which radially couples the $|^{\frac{1}{2}}_{\frac{1}{2}}>$ and the $|^{\frac{3}{2}}_{\frac{1}{2}}>$ surfaces localized at small values of internuclear separation distances (between 5-10 Bohr approximately). When the effective potential shifts the PES to higher values of $R$, only high energy components of the wave-packet will penetrate deep enough into the PES and experience the spin-orbit coupling effects while the low energy components will never experience this coupling effect.

If the reactant Møller state starts on the $|^{\frac{1}{2}}_{\frac{1}{2}}>$ surface, then the scattering WDF should decrease in amplitude for the $|^{\frac{3}{2}}_{\frac{1}{2}}>$ and the $|^{\frac{3}{2}}_{\frac{3}{2}}>$ surfaces. The radial Coupling gets turned off for most values of energy being studied, so most of the probability is reflected back on the $|^{\frac{1}{2}}_{\frac{1}{2}}>$ surface before the effects from spin-orbit coupling can be felt. Because very little probability is transferred to the $|^{\frac{3}{2}}_{\frac{1}{2}}>$ surface, there is very little probability to be transferred to the $|^{\frac{3}{2}}_{\frac{3}{2}}>$ surface via Coriolis coupling. Figs. 6.18-6.24 show that as $J$ increases, the

amplitude of the scattering WDF decreases for the $|^{\frac{3}{2}}_{\frac{1}{2}}>$ and the $|^{\frac{3}{2}}_{\frac{3}{2}}>$ surfaces when the reactant Møller state starts on the $|^{\frac{1}{2}}_{\frac{1}{2}}>$ surface of $K + Ne$.

The scale used in Fig. 6.23 shows that the scattering WDF is zero for the $|^{\frac{3}{2}}_{\frac{1}{2}}>$ and the $|^{\frac{3}{2}}_{\frac{3}{2}}>$ surfaces; but, when the scale is changed to 0.3 which is approximately $\frac{1}{100}$ of the original scattering WDF amplitude on the $|^{\frac{3}{2}}_{\frac{1}{2}}>$ surface when the effective potential and Coriolis coupling were turned off ($J = 1.5$), the scattering WDF can be seen as shown in Fig. 6.24. Also, one can observe the scattering WDF shift to higher energy levels as $J$ increases for the $|^{\frac{3}{2}}_{\frac{1}{2}}>$ and the $|^{\frac{3}{2}}_{\frac{3}{2}}>$ surfaces in Fig. 6.25-Fig. 6.30.

If the reactant Møller state starts on either the $|^{\frac{3}{2}}_{\frac{1}{2}}>$ or the $|^{\frac{3}{2}}_{\frac{3}{2}}>$ surface, the scattering WDF should decrease in amplitude for the $|^{\frac{1}{2}}_{\frac{1}{2}}>$ surface for the same reasons mentioned above as shown in Figs. 6.31-6.36. The radial coupling term is turned off, and the probability is only transferred between the $|^{\frac{3}{2}}_{\frac{1}{2}}>$ and the $|^{\frac{3}{2}}_{\frac{3}{2}}>$ surfaces (the Coriolis coupled surfaces) as shown in Figs. 6.37-6.48. At low values of $J$, the Coriolis coupling is weak, so there isn't much probability that flows between the $|^{\frac{3}{2}}_{\frac{1}{2}}>$ and the $|^{\frac{3}{2}}_{\frac{3}{2}}>$ surfaces regardless of where the reactant Møller state starts. As $J$ increases, the strength of the Coriolis coupling increases which increases the amplitude of the scattering WDF on the $|^{\frac{3}{2}}_{\frac{1}{2}}>$ surface if the reactant Møller state started on the $|^{\frac{3}{2}}_{\frac{3}{2}}>$ surface or the $|^{\frac{3}{2}}_{\frac{3}{2}}>$ surface if the reactant Møller state started on the $|^{\frac{3}{2}}_{\frac{1}{2}}>$ surface. For high values of $J$, radial coupling is turned off at large J, so most of the probability (all but a fraction of a percent) exists on the $|^{\frac{3}{2}}_{\frac{1}{2}}>$ and the $|^{\frac{3}{2}}_{\frac{3}{2}}>$ surfaces. The amplitude of the scattering WDF for these surfaces are on the same order of magnitude for high values of $J$. Similarly, the structure of the scattering WDFs are almost the same for high values of $J$ for the $|^{\frac{3}{2}}_{\frac{1}{2}}>$ and the $|^{\frac{3}{2}}_{\frac{3}{2}}>$ surfaces. This suggests that the probability transfer between the $|^{\frac{3}{2}}_{\frac{1}{2}}>$ and the $|^{\frac{3}{2}}_{\frac{3}{2}}>$ surfaces reaches some sort of equilibrium for large values of $J$.

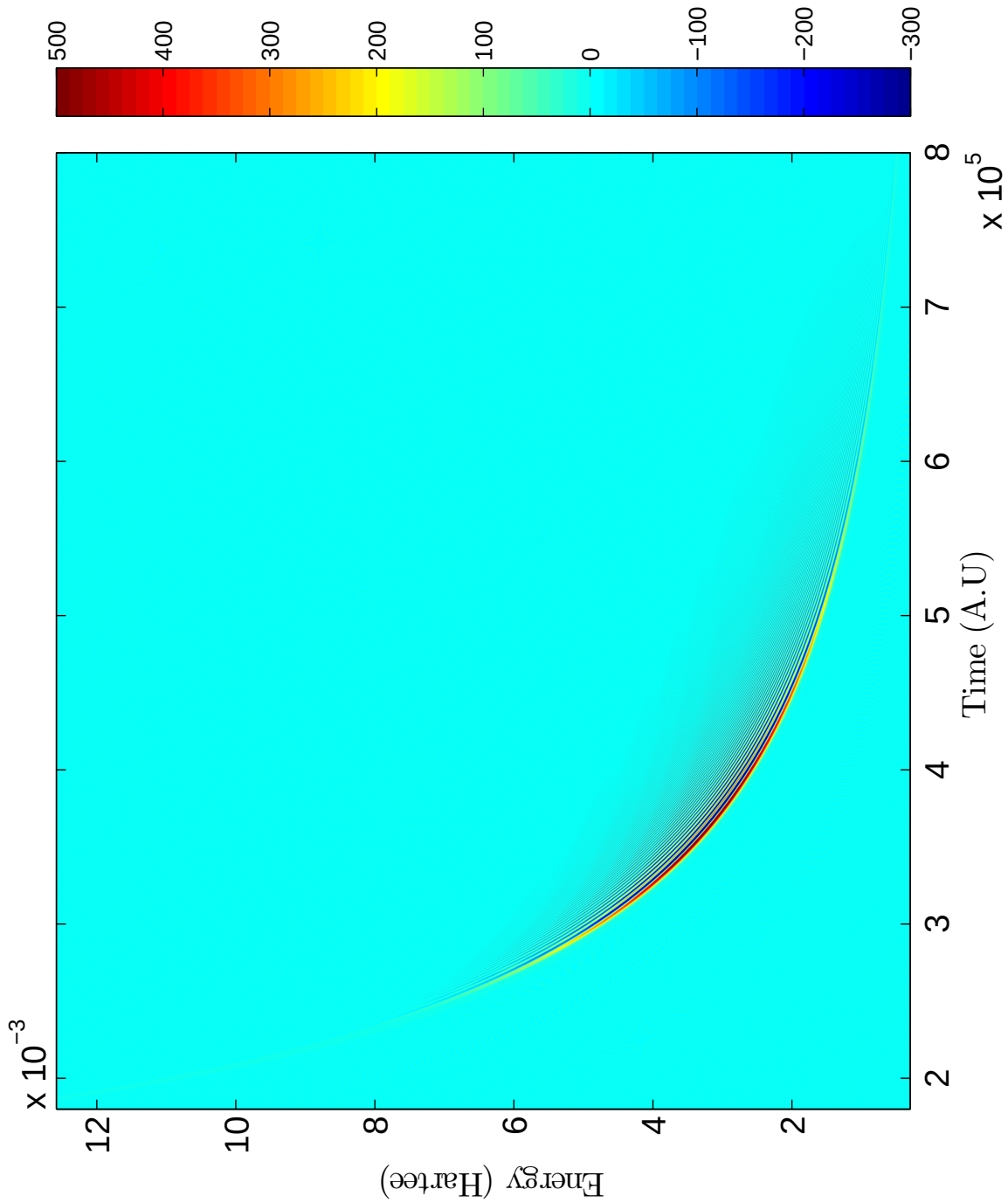


Figure 6.6: Scattering Wigner Distribution Function for K+Ne system with reactant Møller state in $|^{\frac{1}{2}}_{\frac{1}{2}}>$, product Møller state in $|^{\frac{1}{2}}_{\frac{1}{2}}>$, and $J = 1.5$

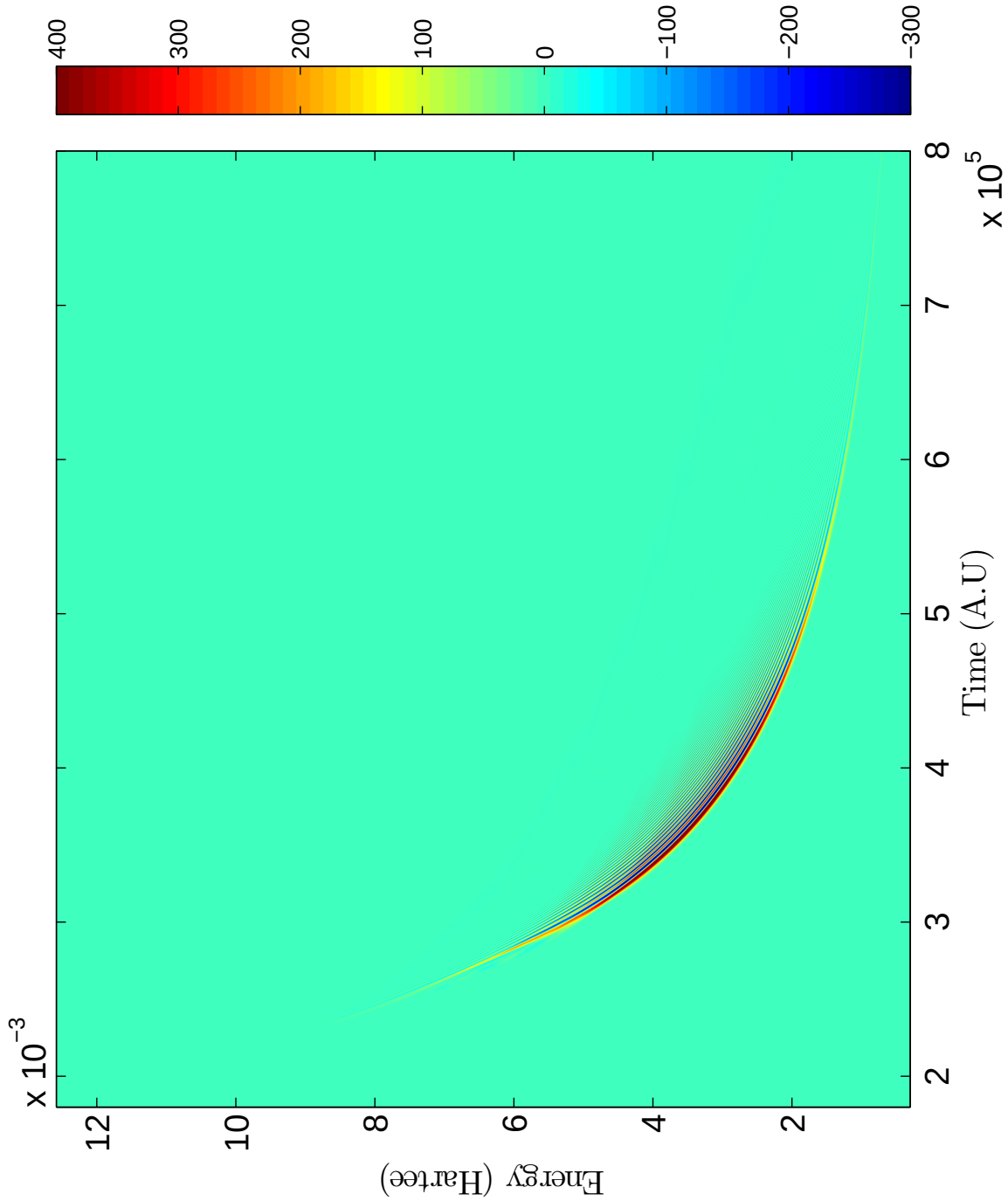


Figure 6.7: Scattering Wigner Distribution Function for K+Ne system with reactant Møller state in $|^{\frac{3}{2}}_{\frac{1}{2}}>$, product Møller state in $|^{\frac{3}{2}}_{\frac{1}{2}}>$, and $J = 1.5$

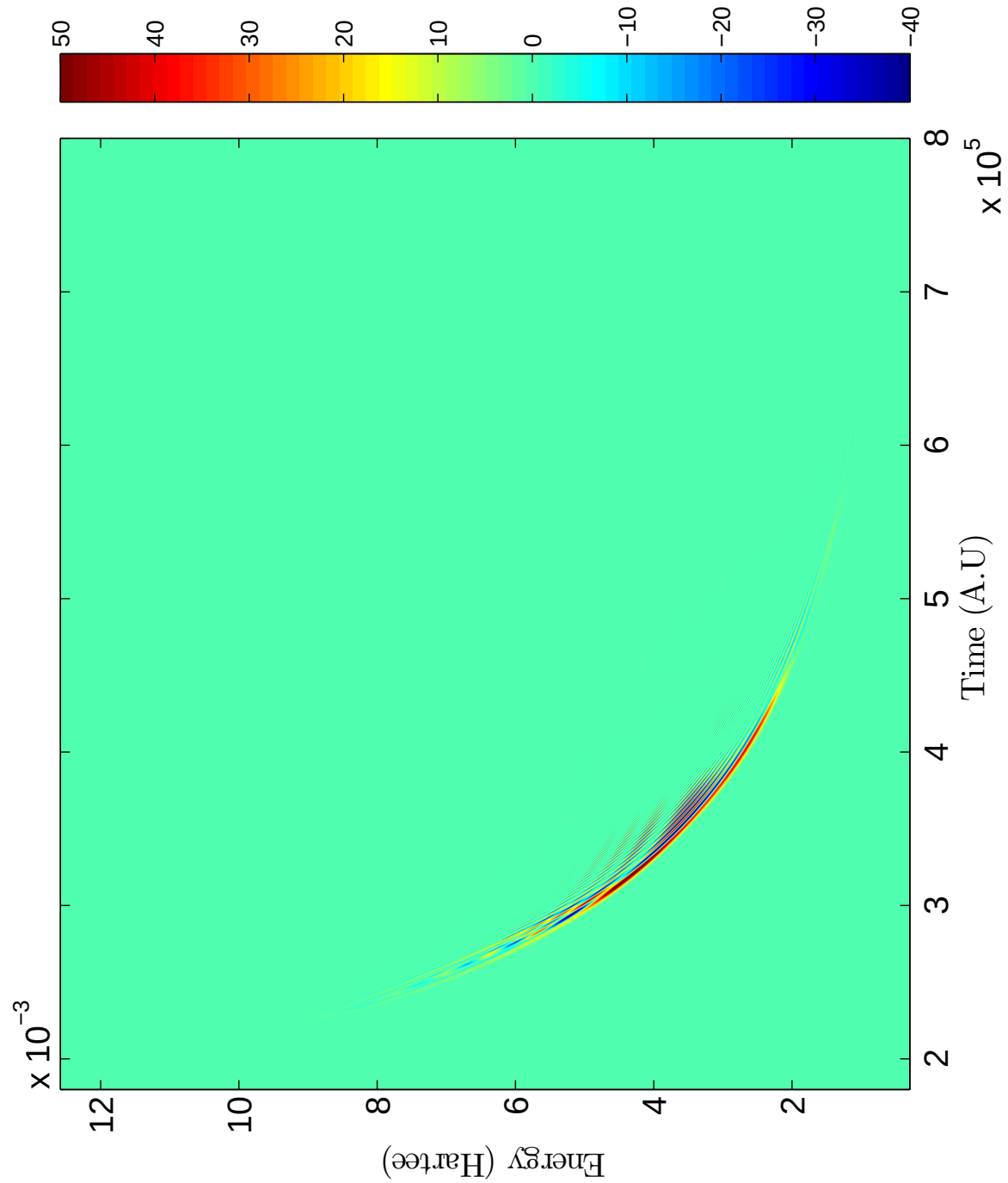


Figure 6.8: Scattering Wigner Distribution Function for K+Ne system with reactant Møller state in $|^{\frac{1}{2}}_{\frac{1}{2}}>$, product Møller state in $|^{\frac{3}{2}}_{\frac{1}{2}}>$, and $J = 1.5$

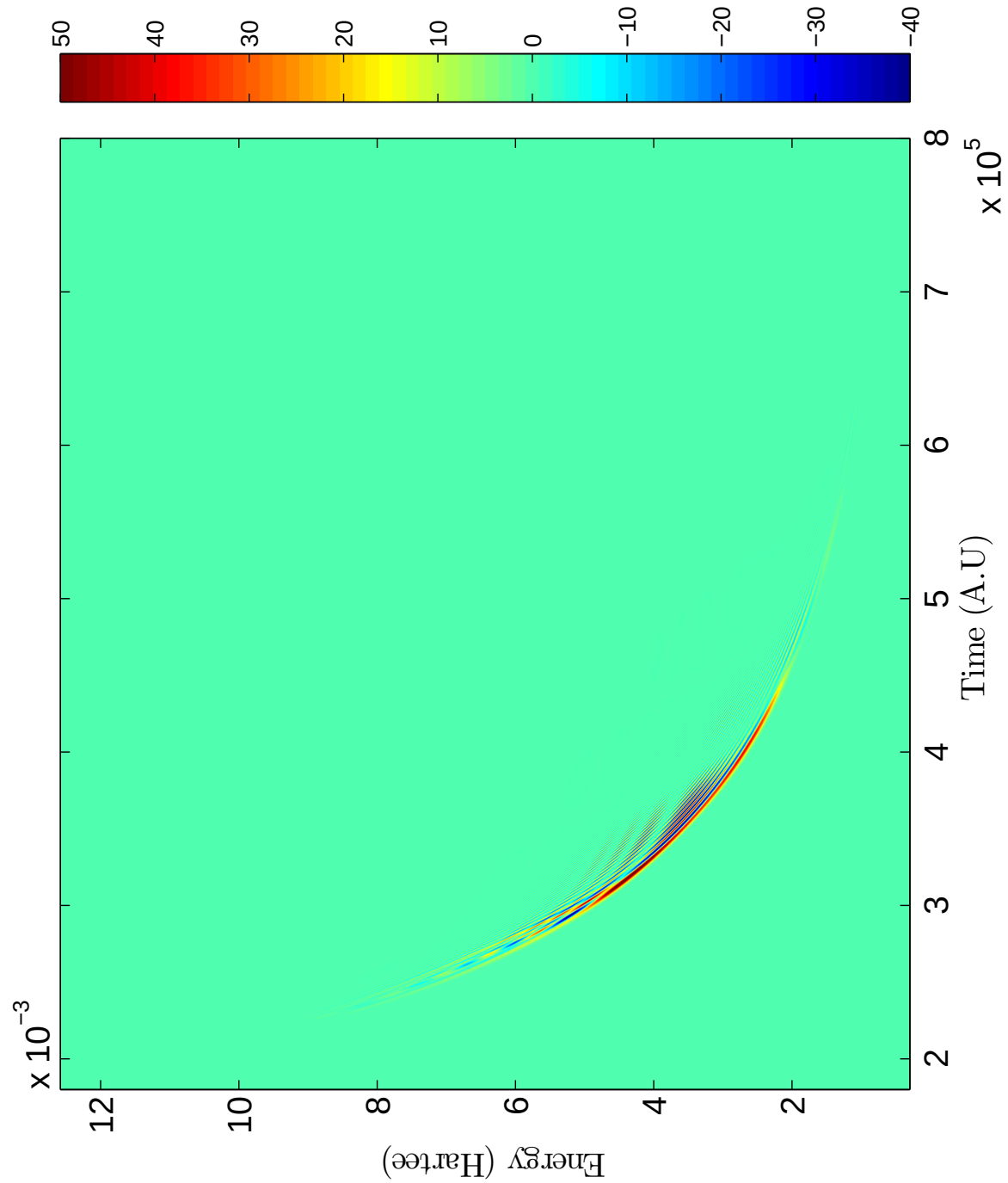


Figure 6.9: Scattering Wigner Distribution Function for K+Ne system with reactant Møller state in $|^{\frac{3}{2}}_{\frac{1}{2}}>$, product Møller state in $|^{\frac{1}{2}}_{\frac{1}{2}}>$, and $J = 1.5$

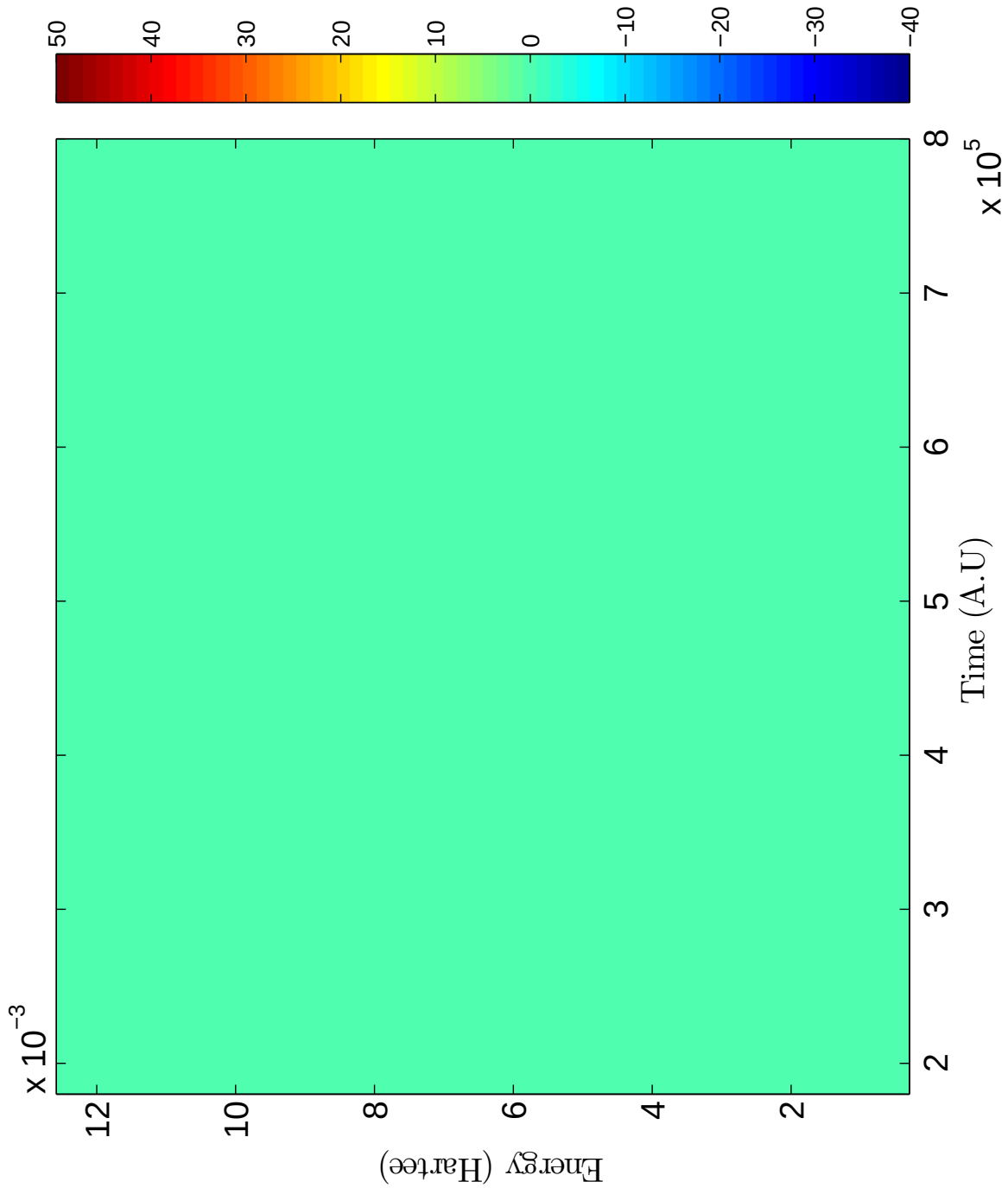


Figure 6.10: Scattering Wigner Distribution Function for K+Ne system with reactant Møller state in $|^{\frac{1}{2}}_{\frac{1}{2}}>$, product Møller state in $|^{\frac{3}{2}}_{\frac{3}{2}}>$, and $J = 1.5$. Note that the scale is the same as Fig. 6.8. The purpose of this is to show that collision reduces to a two level system at low values of $J$.

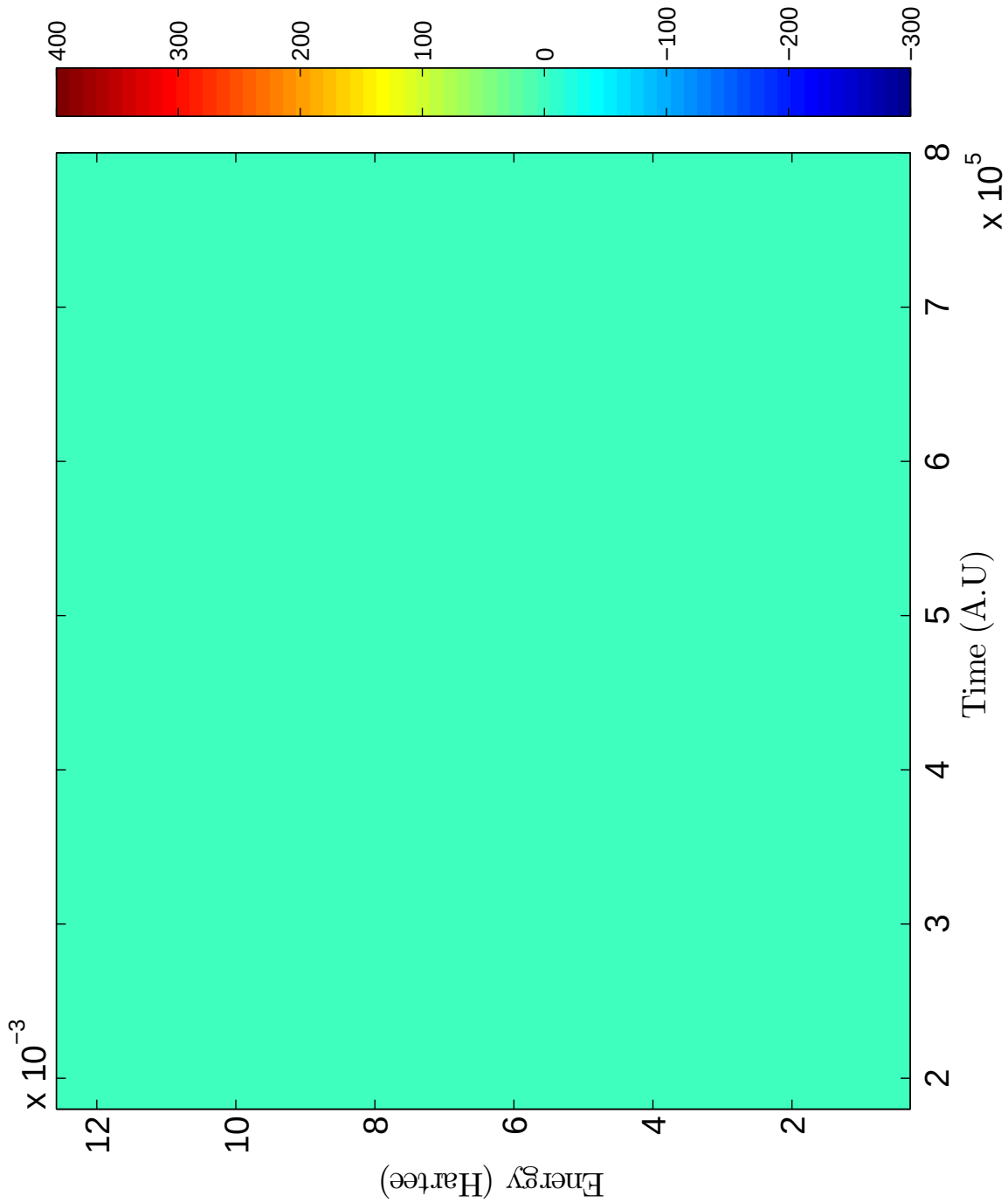


Figure 6.11: Scattering Wigner Distribution Function for K+Ne system with reactant Møller state in $|^{\frac{3}{2}}_{\frac{1}{2}}>$, product Møller state in $|^{\frac{3}{2}}_{\frac{3}{2}}>$, and $J = 1.5$. Note that the scale is the same as Fig. 6.8. The purpose of this is to show that collision reduces to a two level system at low values of $J$.

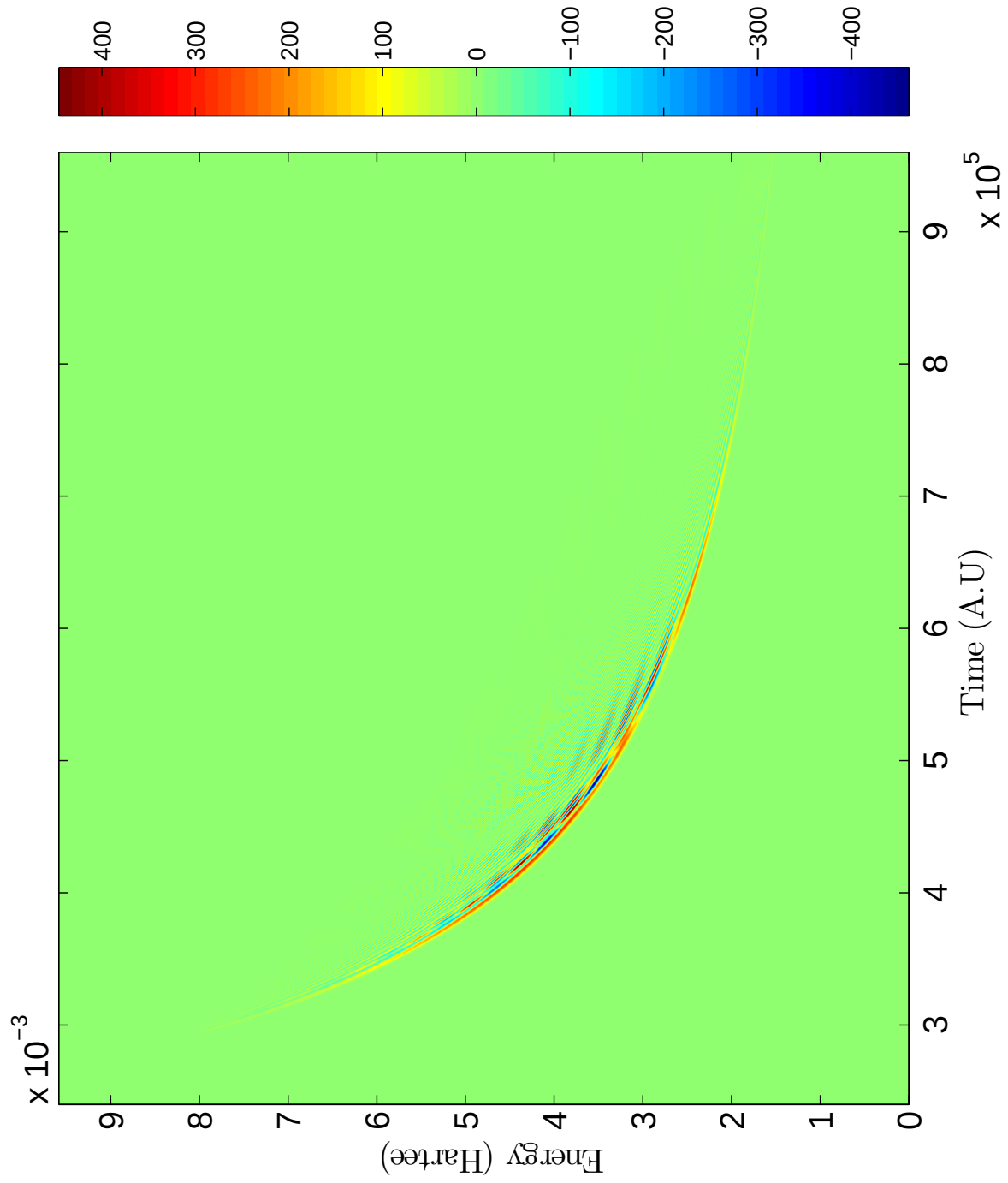


Figure 6.12: Scattering Wigner Distribution Function for Cs+Ne system with reactant Møller state in $|^{\frac{3}{2}}_{\frac{1}{2}}>$, product Møller state in $|^{\frac{3}{2}}_{\frac{1}{2}}>$, and $J = 150.5$

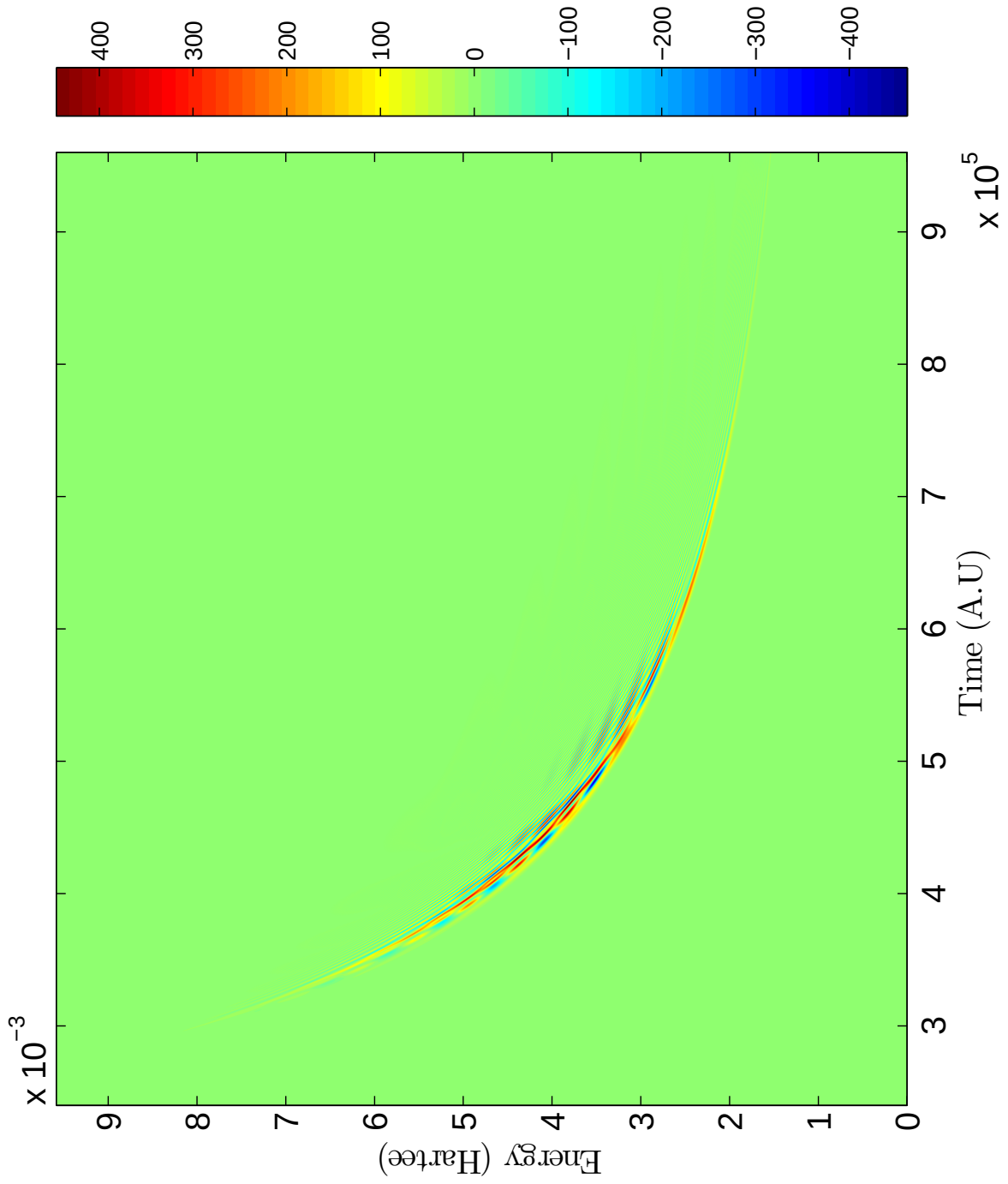


Figure 6.13: Scattering Wigner Distribution Function for Cs+Ne system with reactant Møller state in $|\frac{3}{2}\frac{3}{2}>$, product Møller state in $|\frac{3}{2}\frac{3}{2}>$, and $J = 150.5$

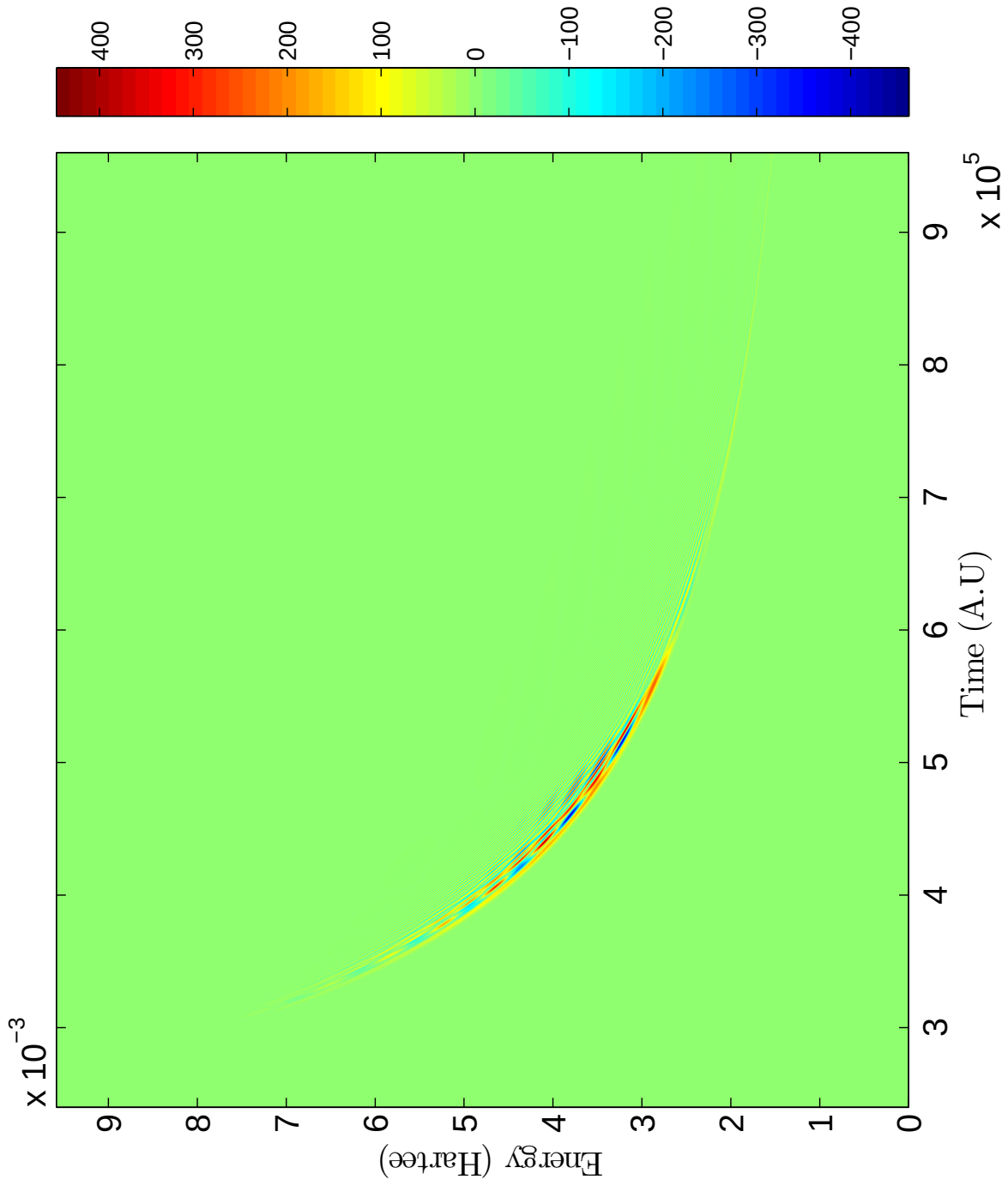


Figure 6.14: Scattering Wigner Distribution Function for Cs+Ne system with reactant Møller state in $|^{\frac{3}{2}}_{\frac{1}{2}}>$, product Møller state in $|^{\frac{3}{2}}_{\frac{3}{2}}>$, and $J = 150.5$

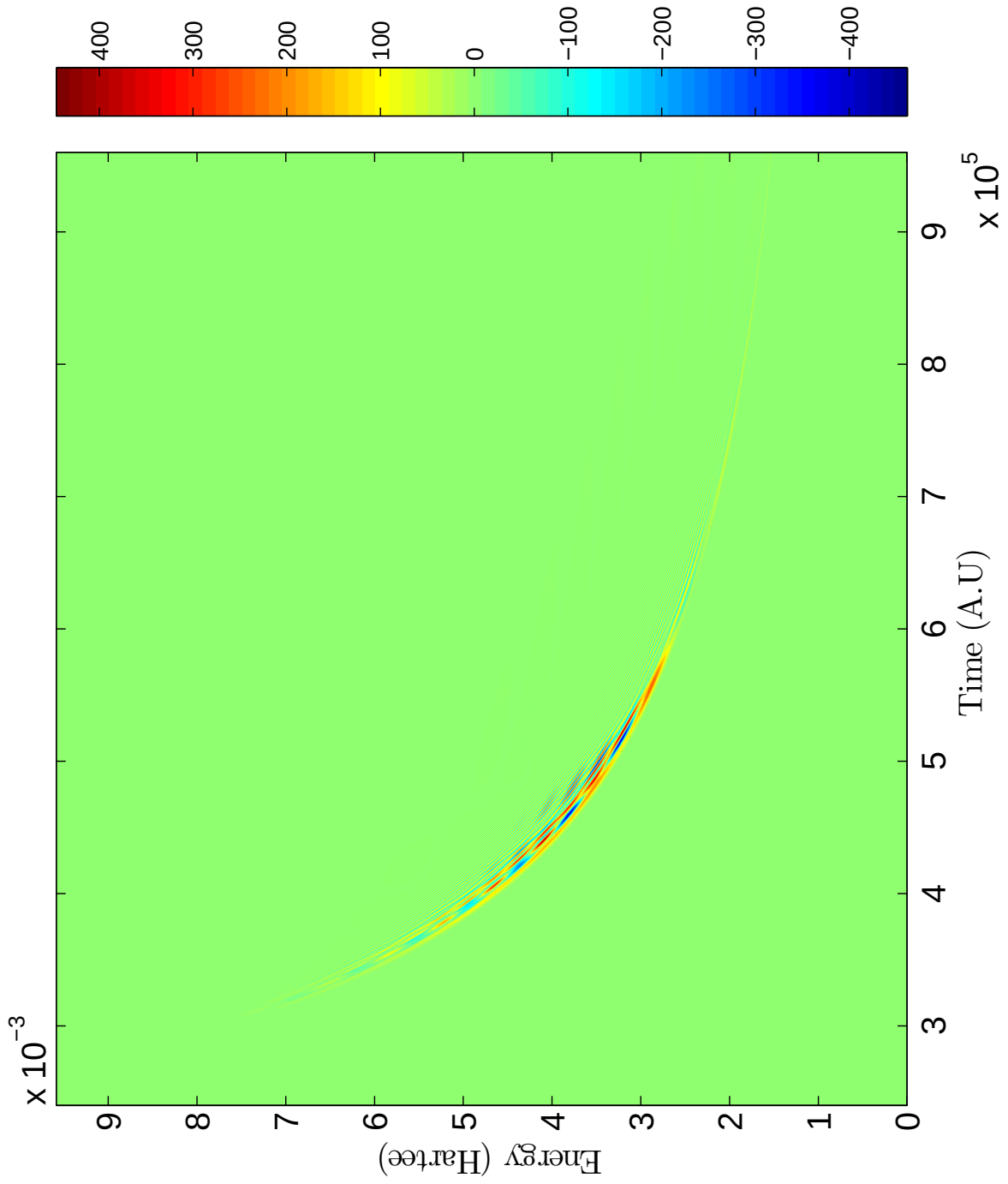


Figure 6.15: Scattering Wigner Distribution Function for Cs+Ne system with reactant Møller state in $|\frac{3}{2}\frac{3}{2}>$, product Møller state in $|\frac{3}{2}\frac{1}{2}>$, and $J = 150.5$

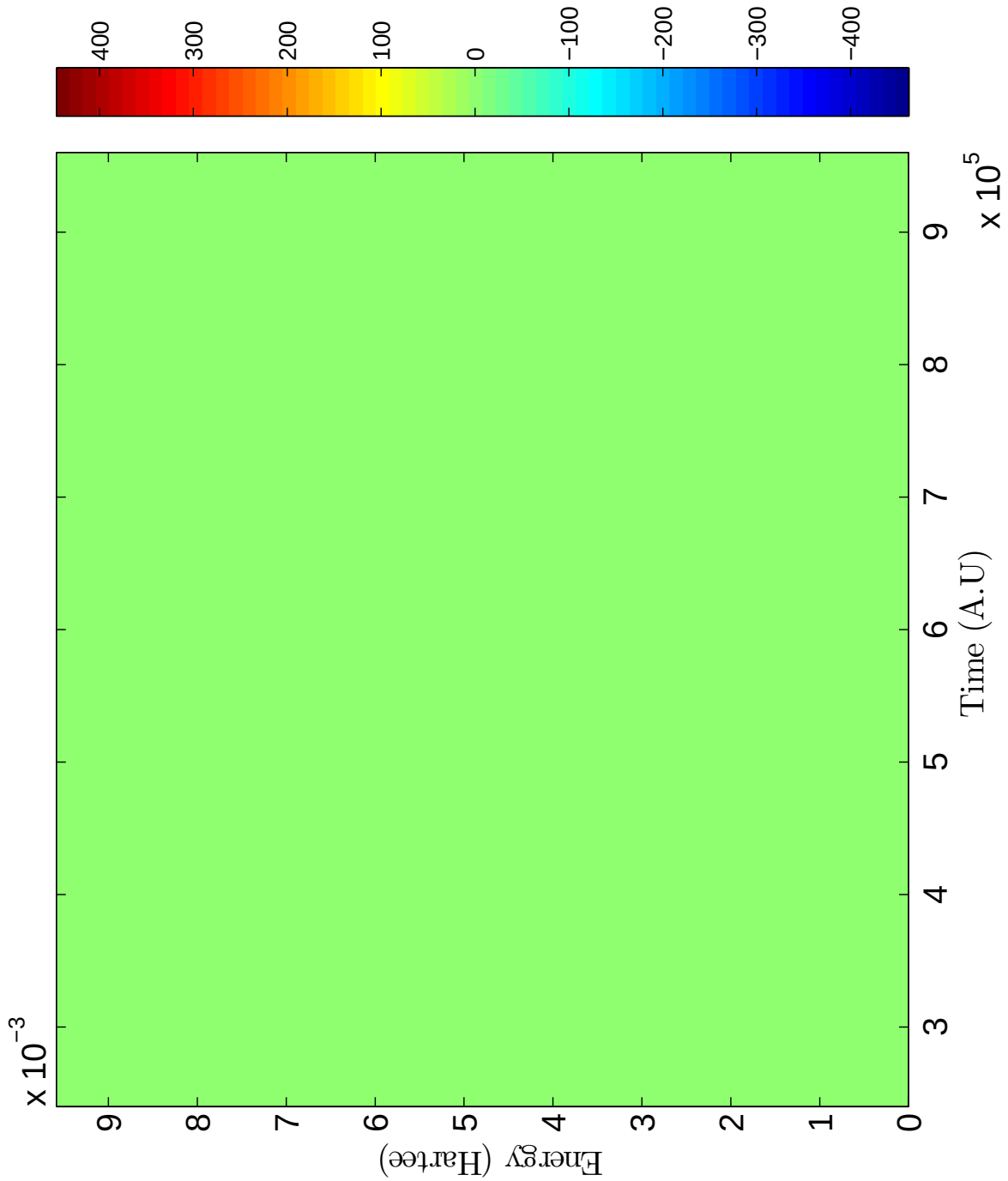


Figure 6.16: Scattering Wigner Distribution Function for Cs+Ne system with reactant Møller state in $|^{\frac{3}{2}}_{\frac{1}{2}}>$, product Møller state in $|^{\frac{1}{2}}_{\frac{1}{2}}>$, and $J = 150.5$. Note that the scale is the same as Fig. 6.112. The purpose of this is to show that collision reduces to a two level system at low values of $J$.

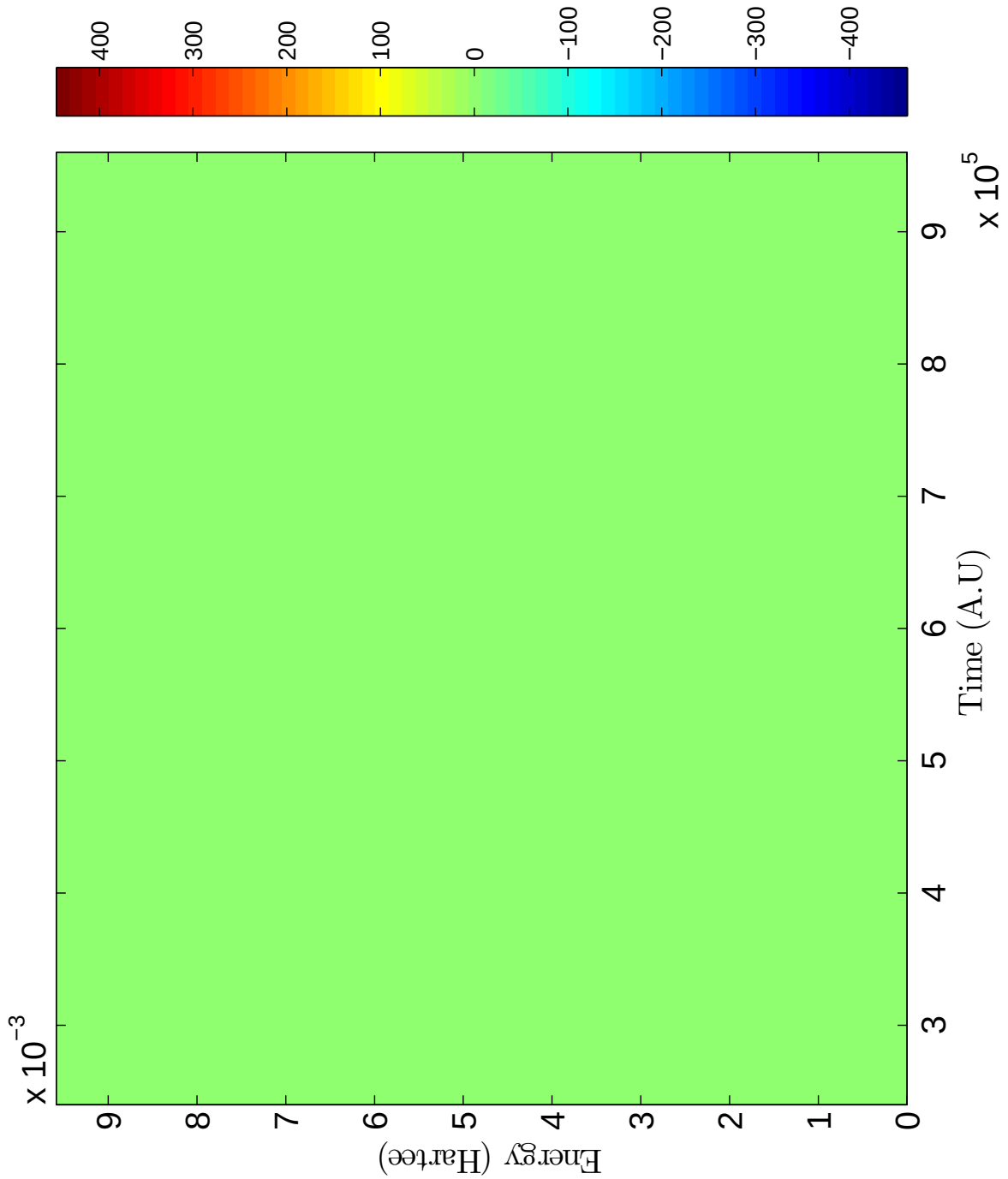


Figure 6.17: Scattering Wigner Distribution Function for Cs+Ne system with reactant Møller state in $|^{\frac{3}{2}}_{\frac{3}{2}}>$, product Møller state in $|^{\frac{1}{2}}_{\frac{1}{2}}>$, and $J = 150.5$. Note that the scale is the same as Fig. 6.112. The purpose of this is to show that collision reduces to a two level system at low values of $J$.

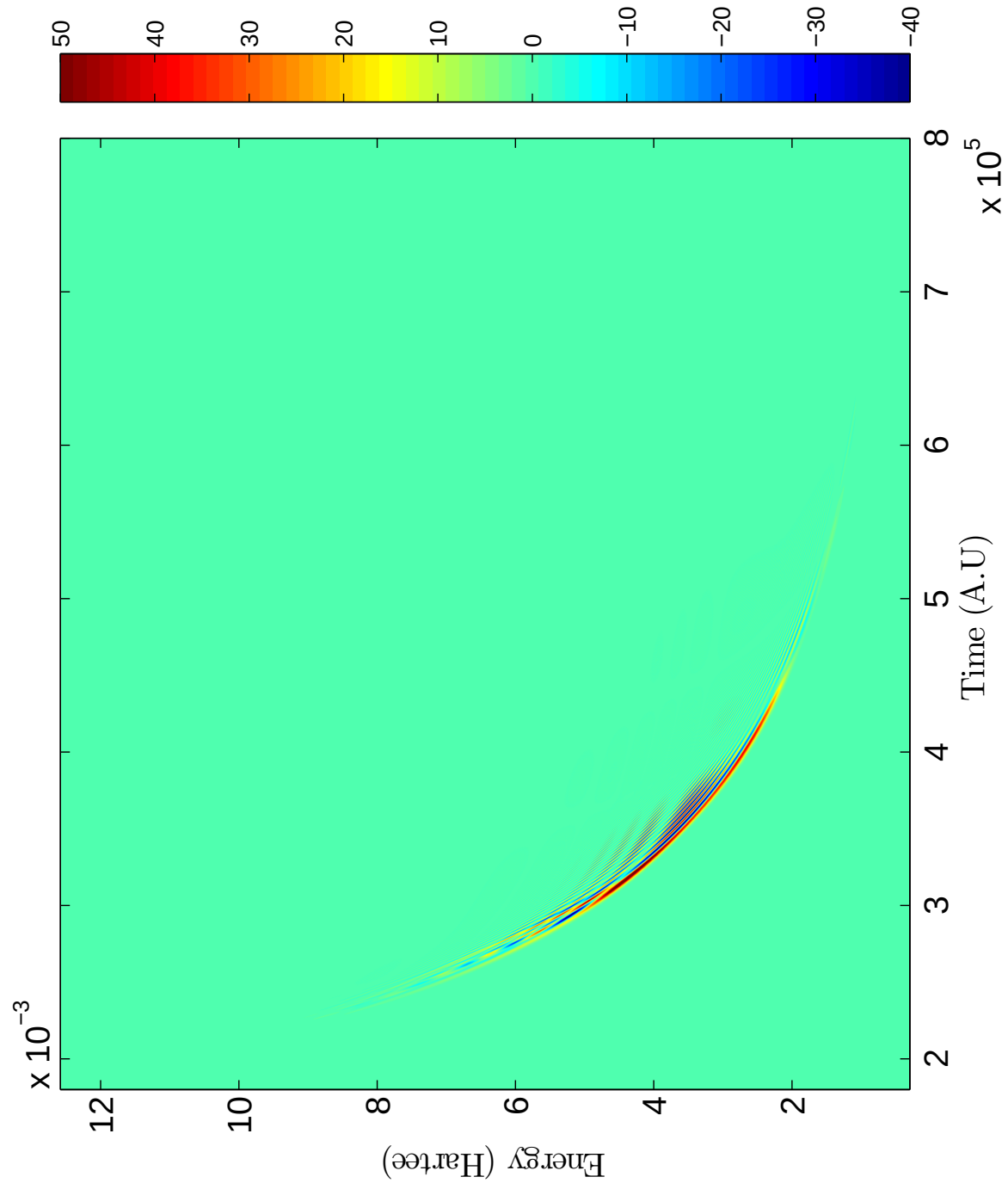


Figure 6.18: Scattering Wigner Distribution Function for K+Ne system with reactant Møller state in $|^{\frac{1}{2}}_{\frac{1}{2}}>$, product Møller state in $|^{\frac{3}{2}}_{\frac{1}{2}}>$, and $J = 1.5$

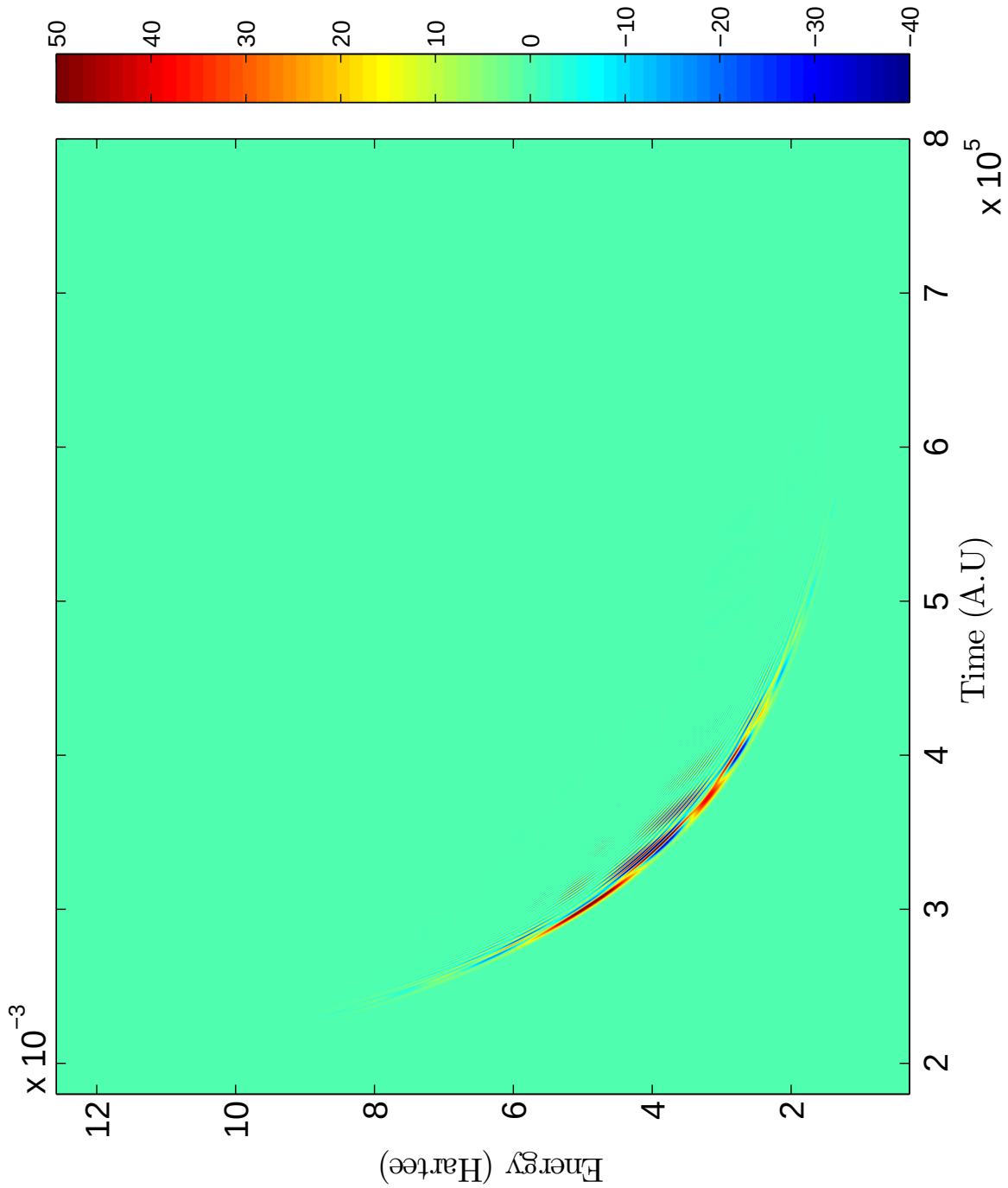


Figure 6.19: Scattering Wigner Distribution Function for K+Ne system with reactant Møller state in $|^{\frac{1}{2}}_{\frac{1}{2}}>$, product Møller state in $|^{\frac{3}{2}}_{\frac{1}{2}}>$, and $J = 50.5$. Note that the scale is the same as Fig. 6.18. The purpose of this is to observe the diminishing amplitude of the scattering WDF as the $J$ increases.

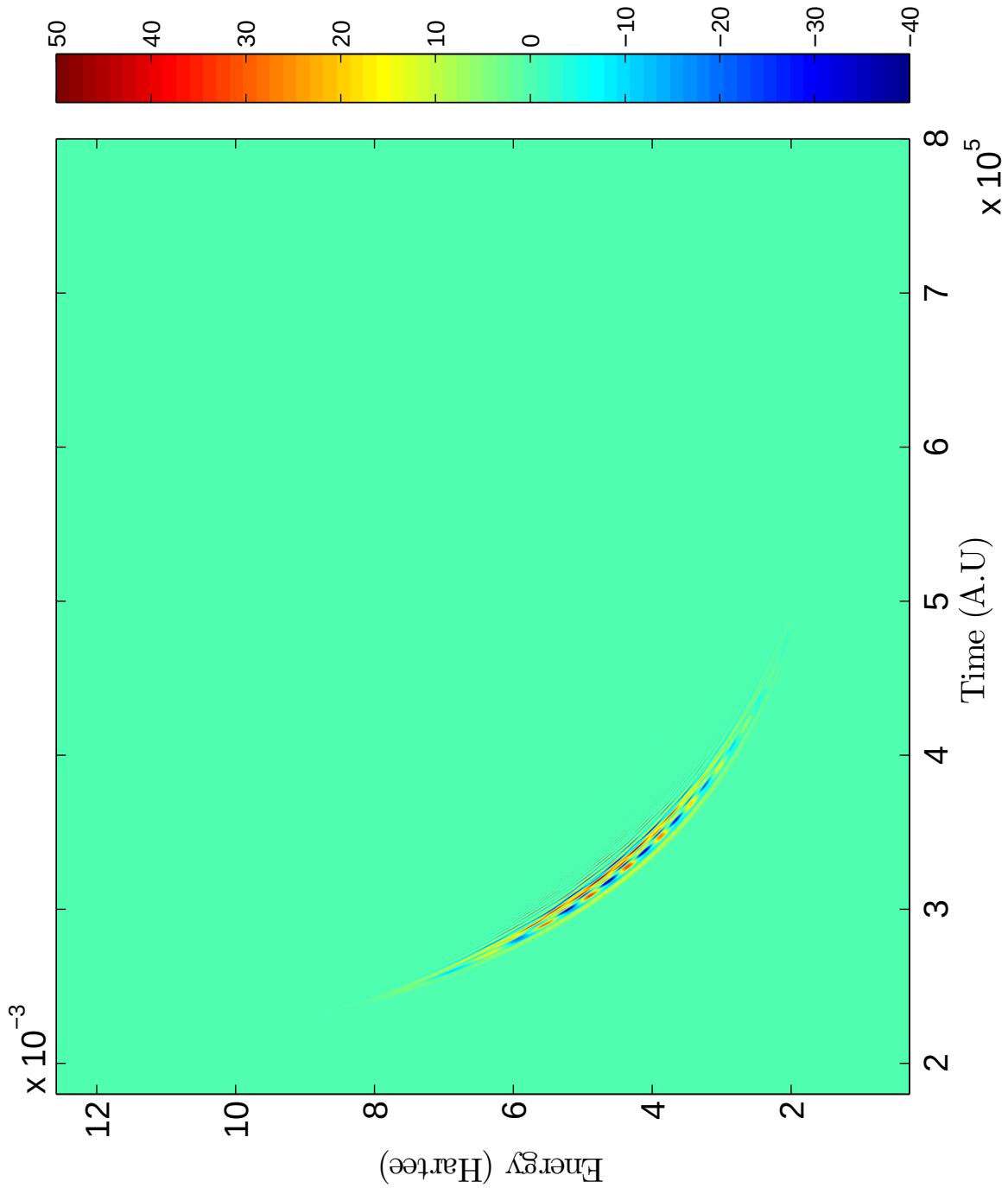


Figure 6.20: Scattering Wigner Distribution Function for K+Ne system with reactant Møller state in $|^{\frac{1}{2}}_{\frac{1}{2}}>$, product Møller state in $|^{\frac{3}{2}}_{\frac{1}{2}}>$, and $J = 100.5$. Note that the scale is the same as Fig. 6.18. The purpose of this is to observe the diminishing amplitude of the scattering WDF as the $J$ increases.

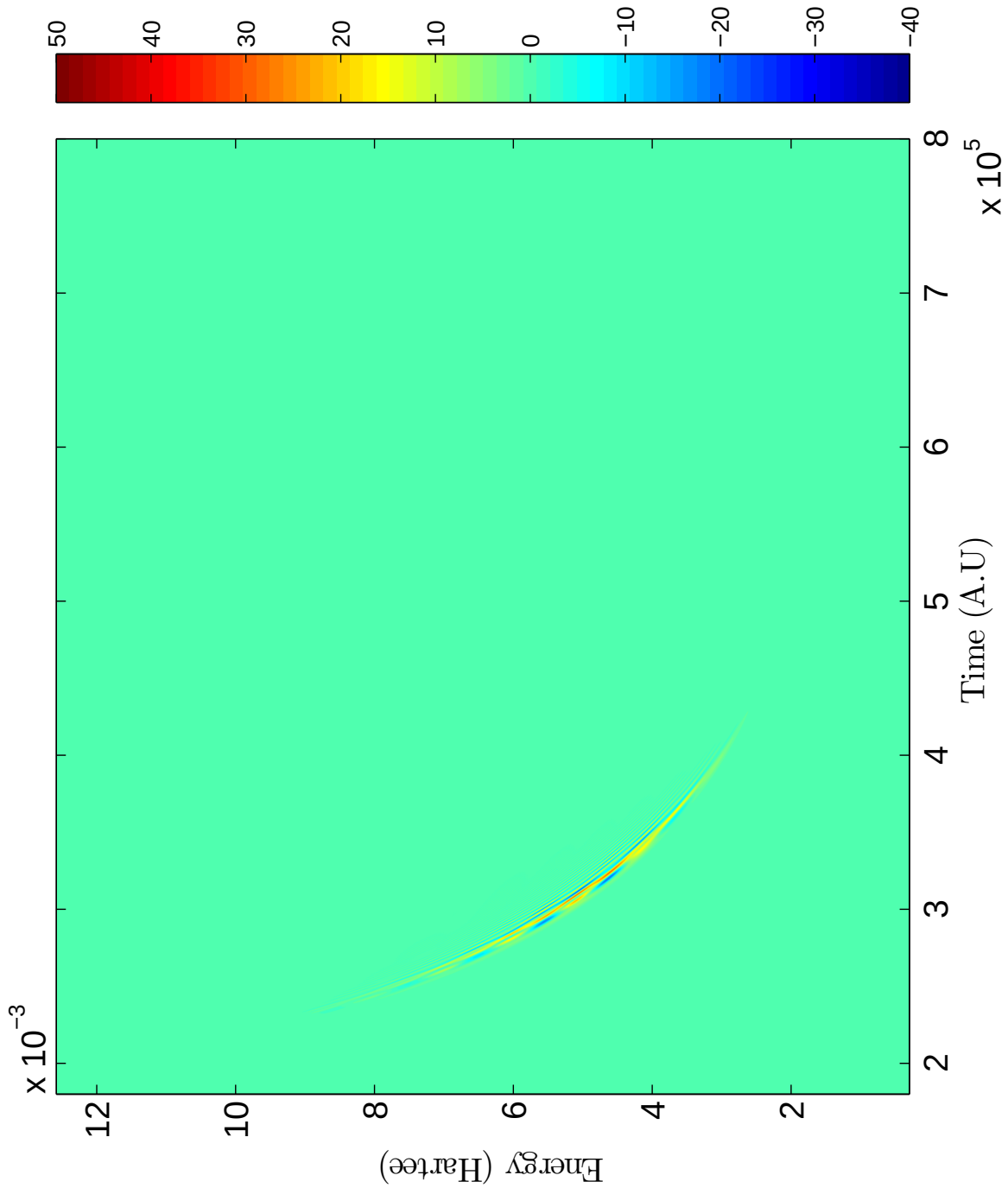


Figure 6.21: Scattering Wigner Distribution Function for K+Ne system with reactant Møller state in $|^{\frac{1}{2}}_{\frac{1}{2}}>$, product Møller state in $|^{\frac{3}{2}}_{\frac{1}{2}}>$, and $J = 150.5$. Note that the scale is the same as Fig. 6.18. The purpose of this is to observe the diminishing amplitude of the scattering WDF as the $J$ increases.

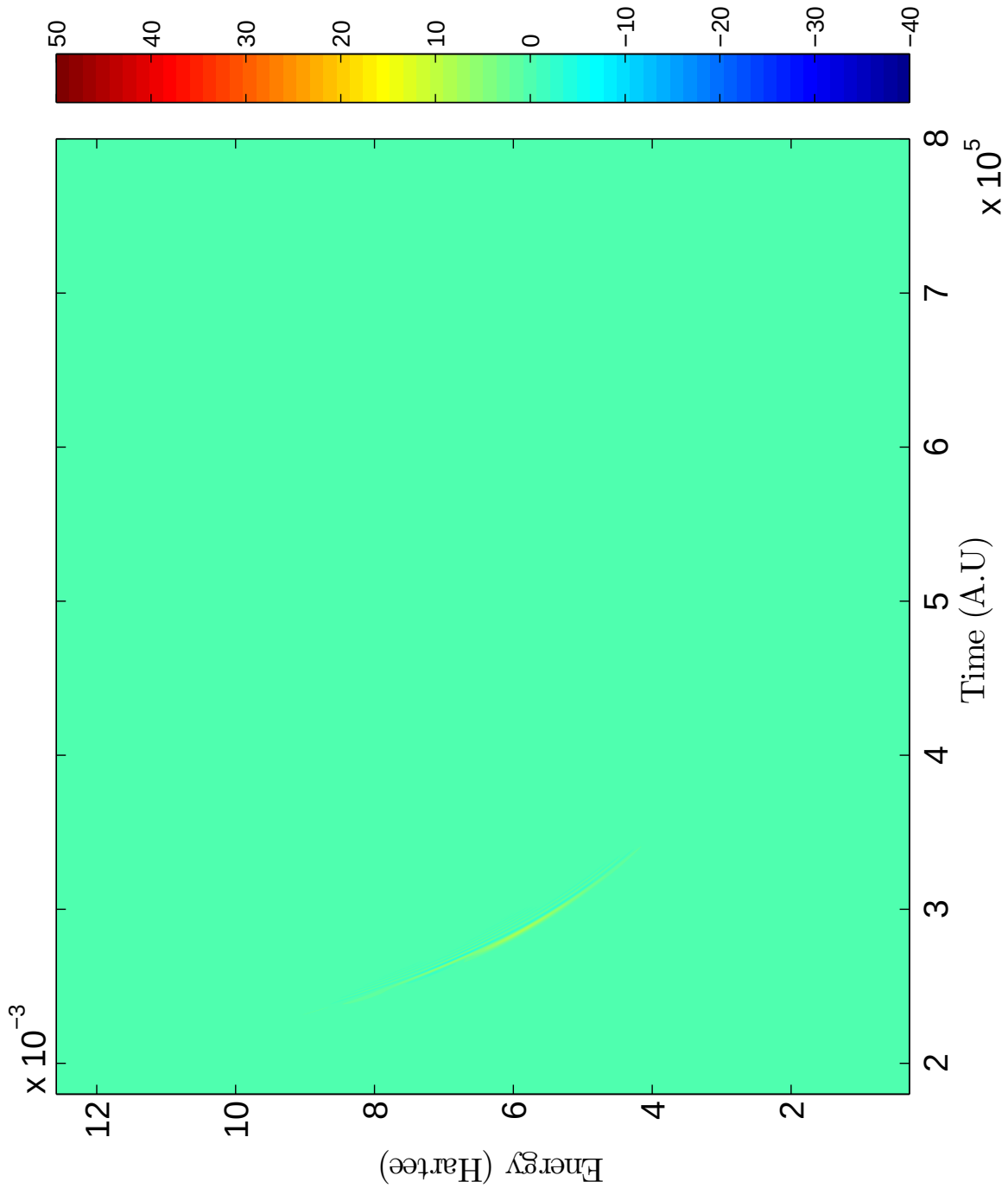


Figure 6.22: Scattering Wigner Distribution Function for K+Ne system with reactant Møller state in $|^{\frac{1}{2}}_{\frac{1}{2}}>$, product Møller state in $|^{\frac{3}{2}}_{\frac{1}{2}}>$, and $J = 200.5$. Note that the scale is the same as Fig. 6.18. The purpose of this is to observe the diminishing amplitude of the scattering WDF as the $J$ increases.

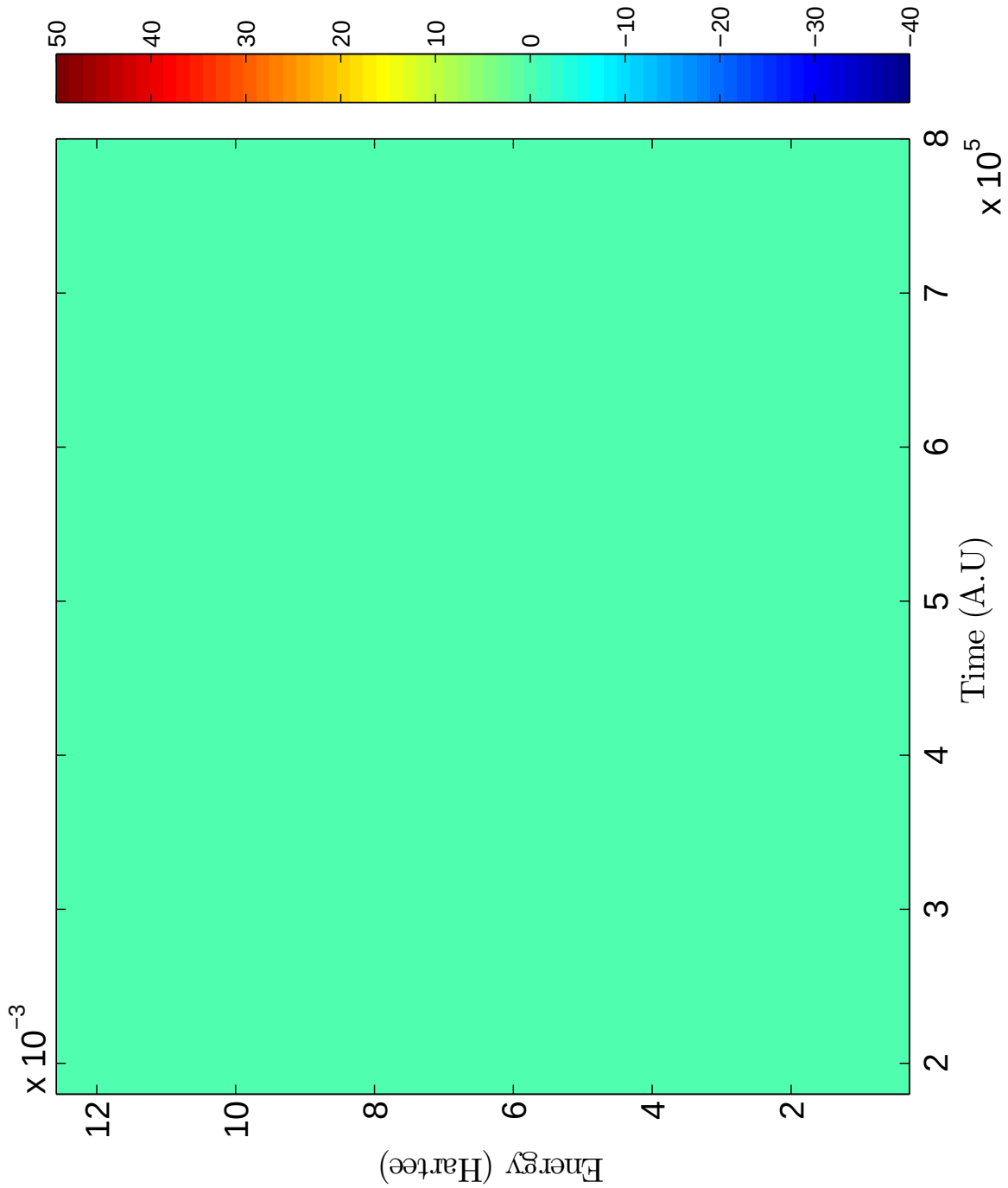


Figure 6.23: Scattering Wigner Distribution Function for K+Ne system with reactant Møller state in $|^{\frac{1}{2}}_{\frac{1}{2}}>$, product Møller state in $|^{\frac{3}{2}}_{\frac{1}{2}}>$, and $J = 250.5$. Note that the scale is the same as Fig. 6.18. The purpose of this is to observe the diminishing amplitude of the scattering WDF as the $J$ increases.

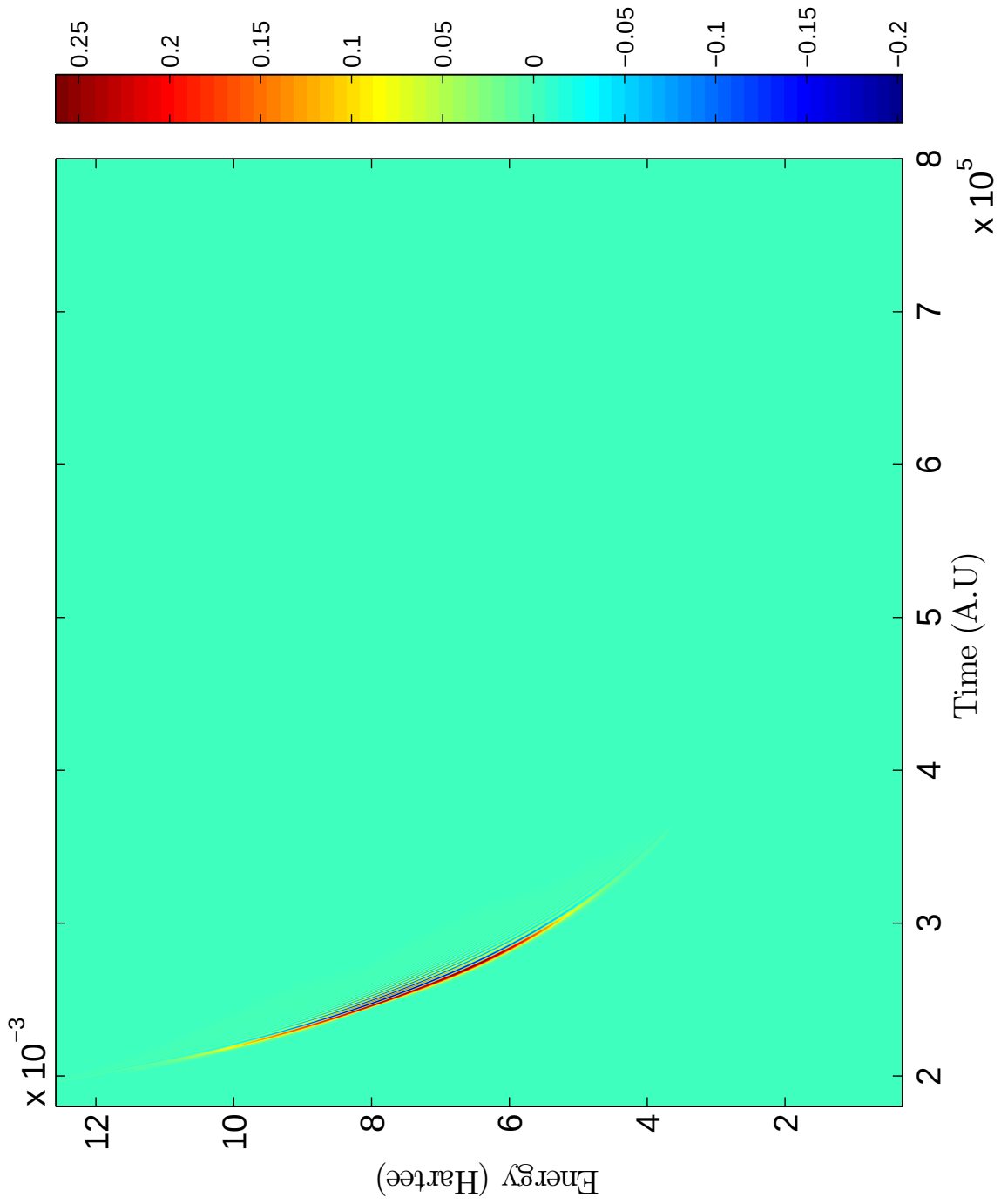


Figure 6.24: Scattering Wigner Distribution Function for K+Ne system with reactant Møller state in $|^{\frac{1}{2}}_{\frac{1}{2}}>$, product Møller state in $|^{\frac{3}{2}}_{\frac{1}{2}}>$, and $J = 250.5$. The scale for this figure is different than the scale used in Fig. 6.18. The scale is based on the maximum and minimum value of the scattering WDF to show that the amplitude exists.

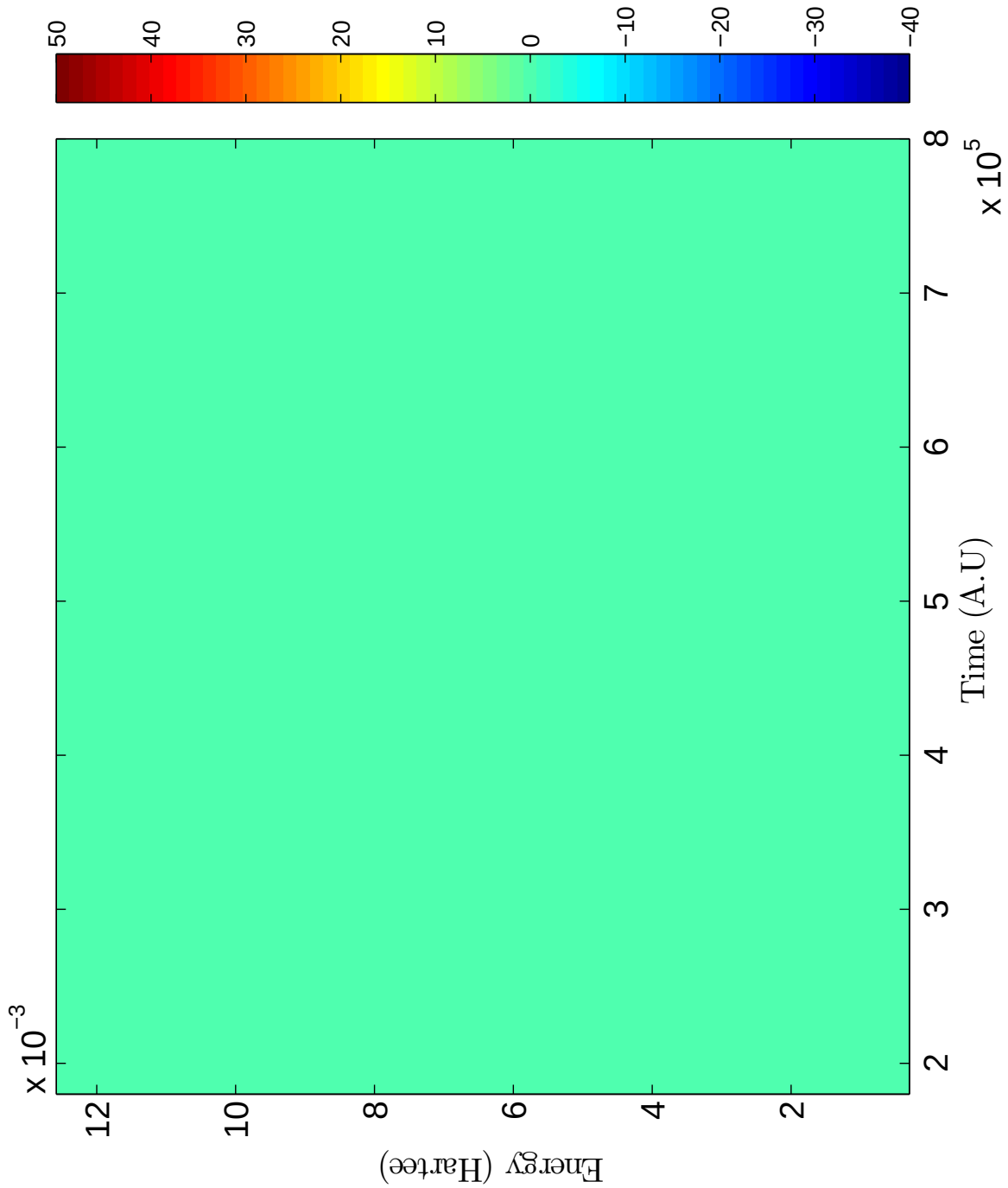


Figure 6.25: Scattering Wigner Distribution Function for K+Ne system with reactant Møller state in $|^{\frac{1}{2}}_{\frac{1}{2}}>$, product Møller state in $|^{\frac{3}{2}}_{\frac{3}{2}}>$, and $J = 1.5$

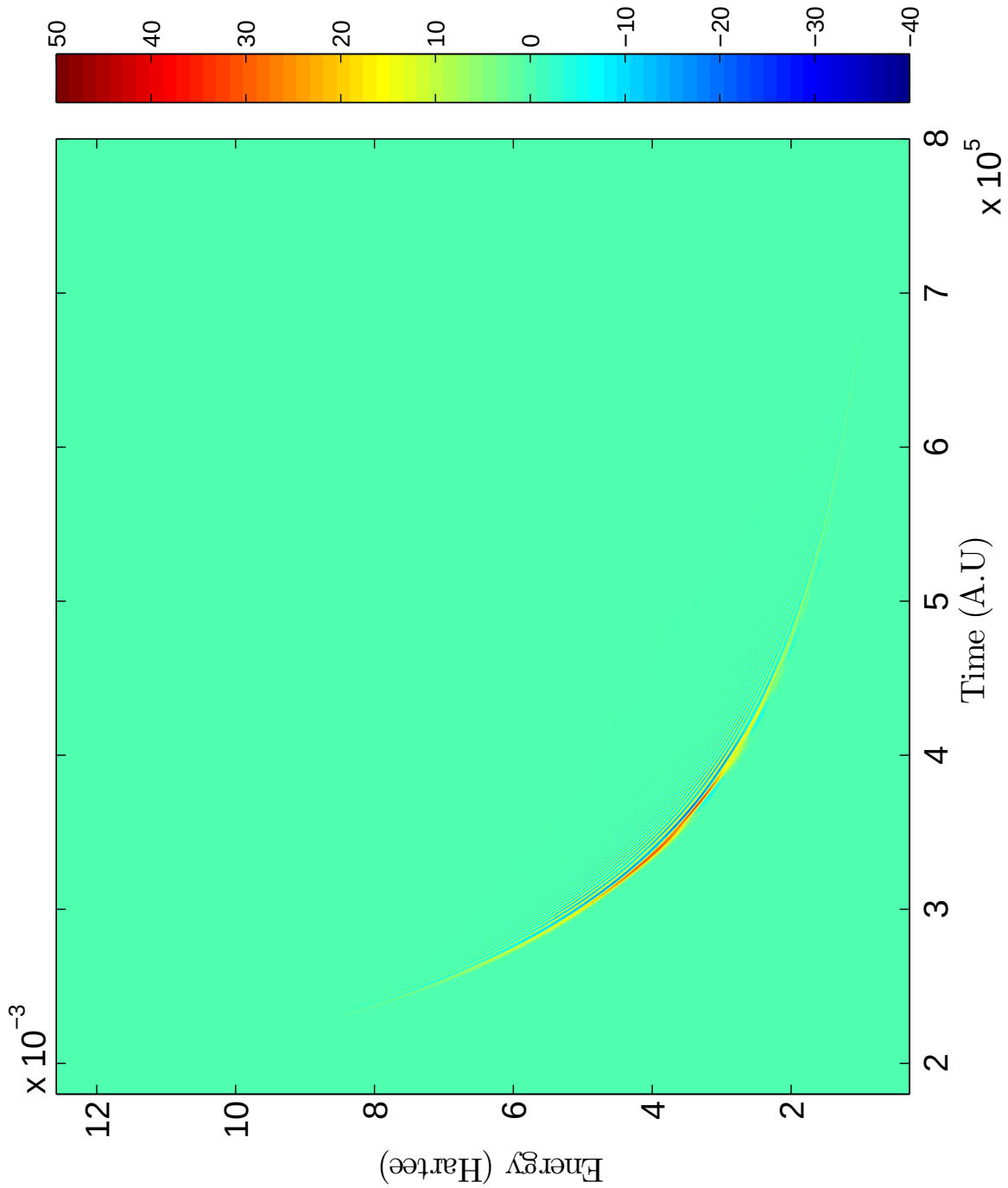


Figure 6.26: Scattering Wigner Distribution Function for K+Ne system with reactant Møller state in $|^{\frac{1}{2}}_{\frac{1}{2}}>$, product Møller state in $|^{\frac{3}{2}}_{\frac{3}{2}}>$, and $J = 50.5$. Note that the scale is the same as Fig. 6.25. The purpose of this is to observe the diminishing amplitude of the scattering WDF as the $J$ increases.

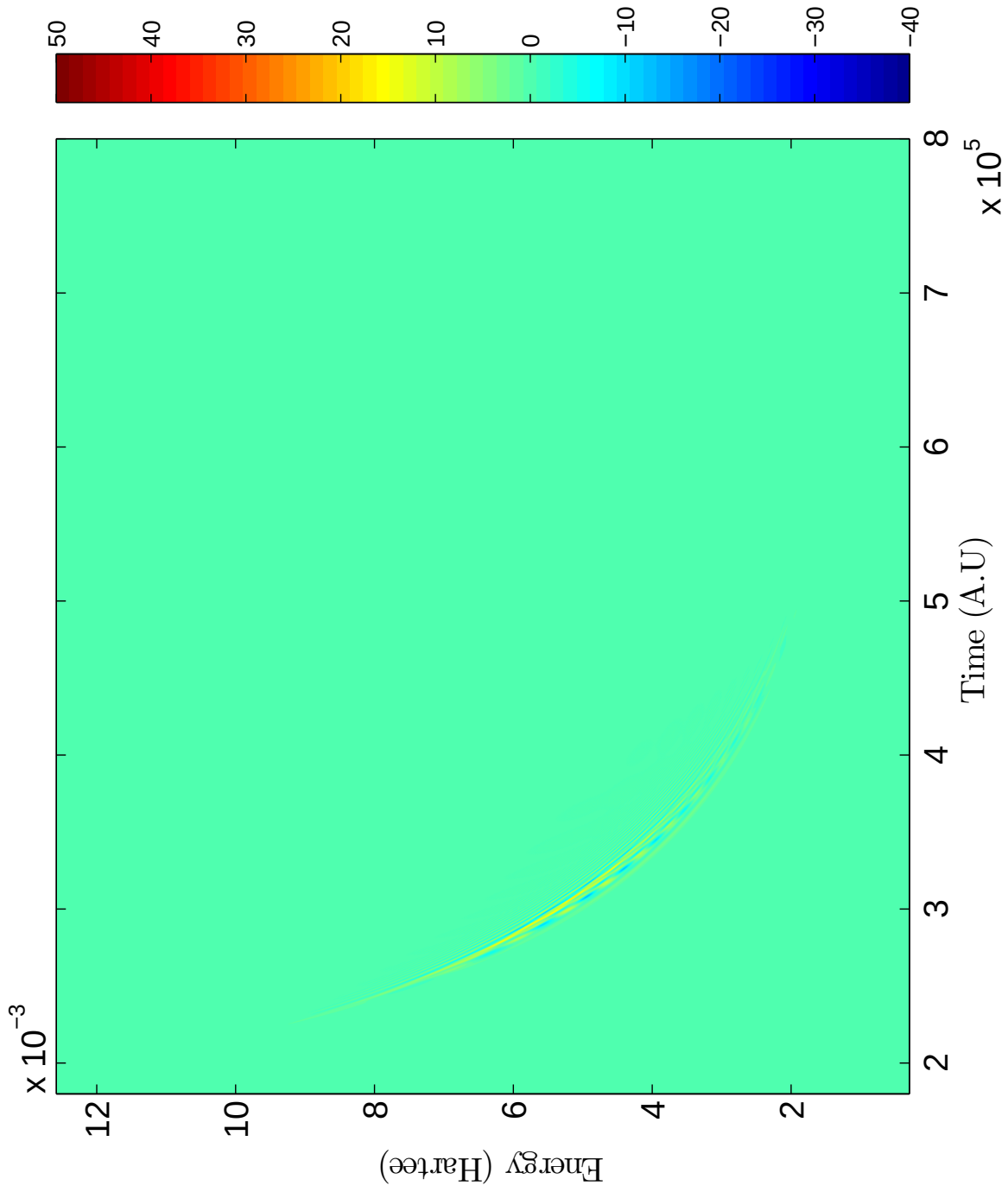


Figure 6.27: Scattering Wigner Distribution Function for K+Ne system with reactant Møller state in $|^{\frac{1}{2}}_{\frac{1}{2}}>$, product Møller state in $|^{\frac{3}{2}}_{\frac{3}{2}}>$, and $J = 100.5$. Note that the scale is the same as Fig. 6.25. The purpose of this is to observe the diminishing amplitude of the scattering WDF as the $J$ increases.

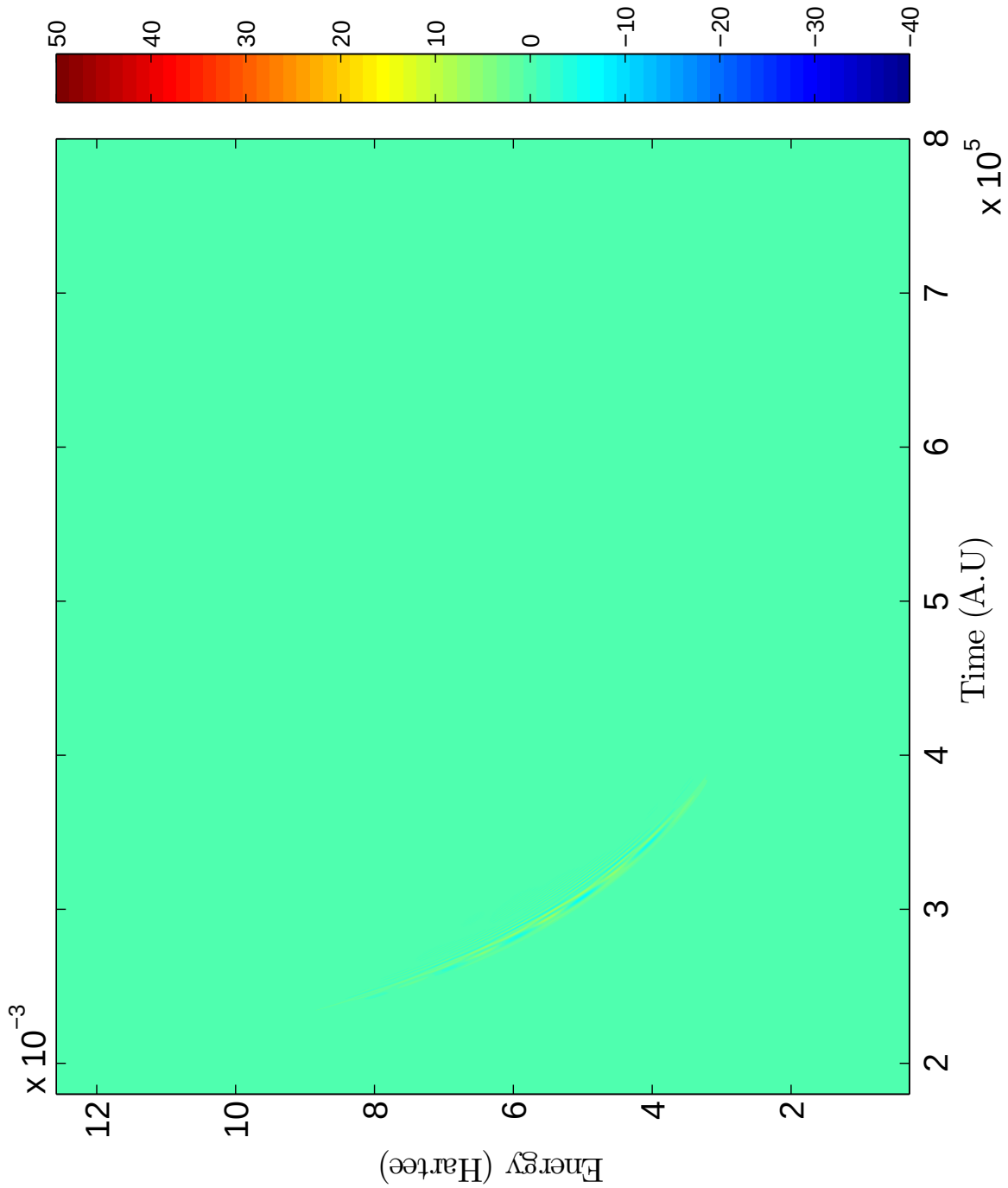


Figure 6.28: Scattering Wigner Distribution Function for K+Ne system with reactant Møller state in $|^{\frac{1}{2}}_{\frac{1}{2}}>$, product Møller state in $|^{\frac{3}{2}}_{\frac{3}{2}}>$, and $J = 150.5$. Note that the scale is the same as Fig. 6.25. The purpose of this is to observe the diminishing amplitude of the scattering WDF as the $J$ increases.

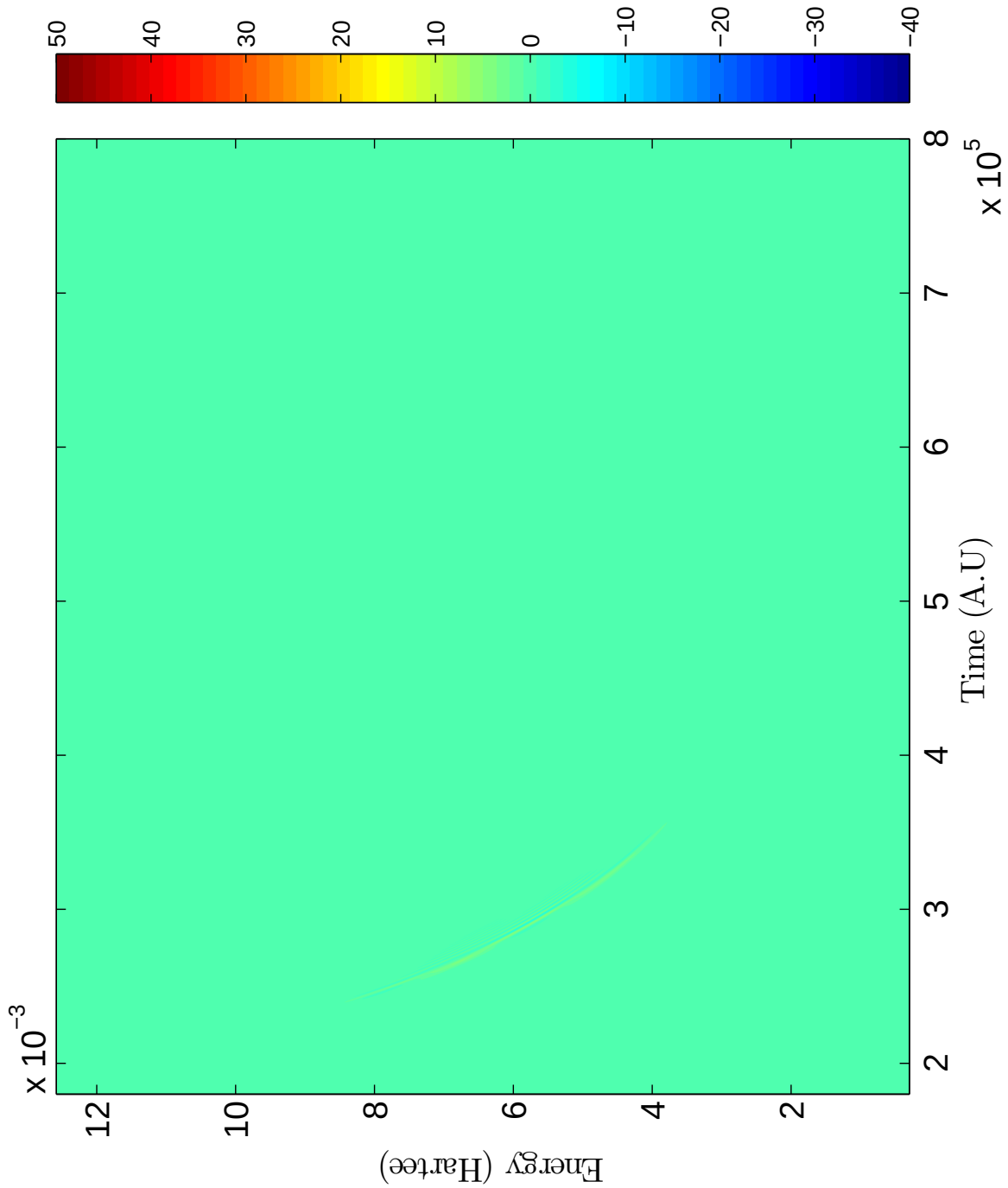


Figure 6.29: Scattering Wigner Distribution Function for K+Ne system with reactant Møller state in $|^{\frac{1}{2}}_{\frac{1}{2}}>$, product Møller state in $|^{\frac{3}{2}}_{\frac{3}{2}}>$, and $J = 200.5$. Note that the scale is the same as Fig. 6.25. The purpose of this is to observe the diminishing amplitude of the scattering WDF as the $J$ increases.

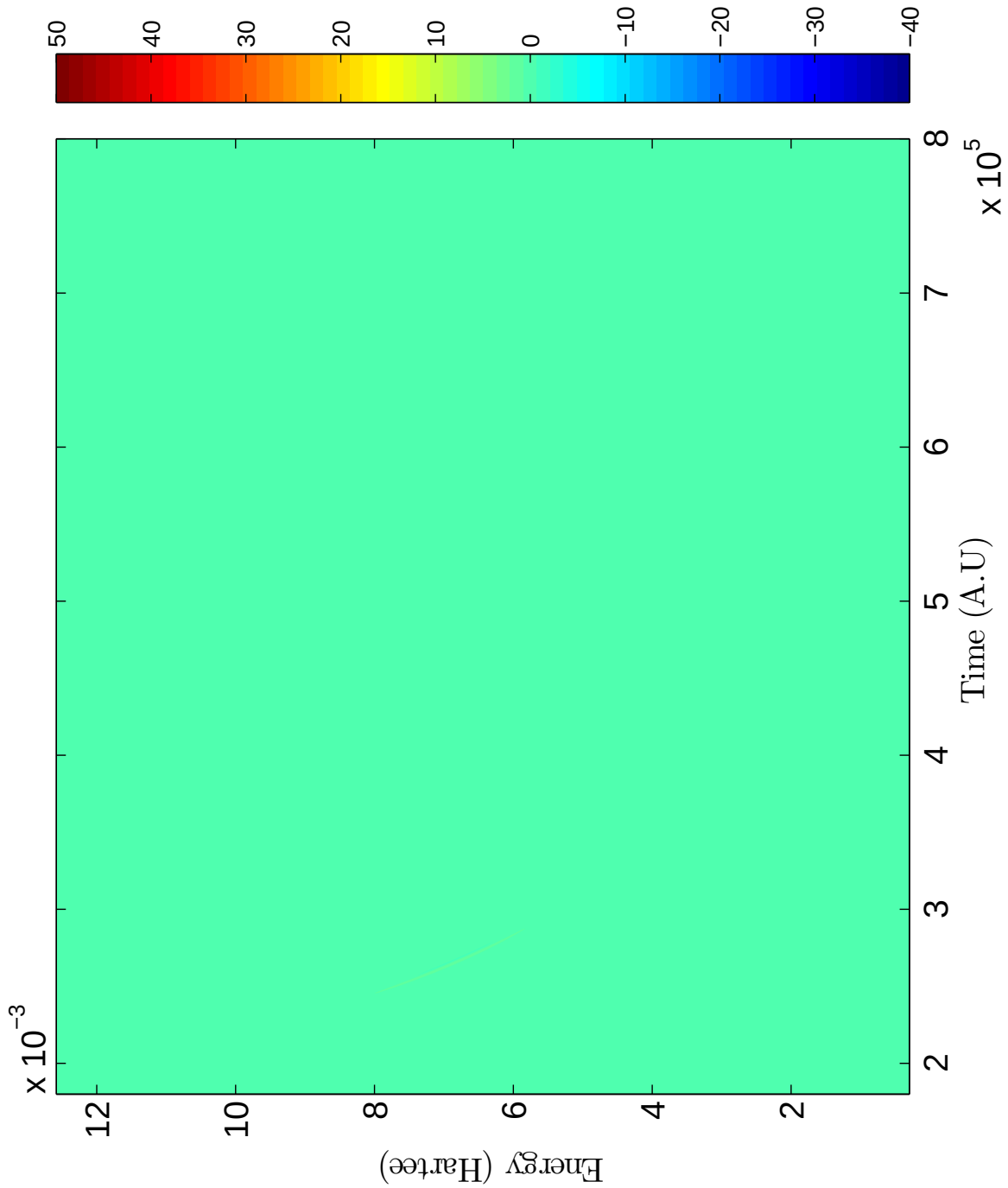


Figure 6.30: Scattering Wigner Distribution Function for K+Ne system with reactant Møller state in $|^{\frac{1}{2}}_{\frac{1}{2}}>$, product Møller state in $|^{\frac{3}{2}}_{\frac{3}{2}}>$, and $J = 250.5$. Note that the scale is the same as Fig. 6.25. The purpose of this is to observe the diminishing amplitude of the scattering WDF as the $J$ increases.

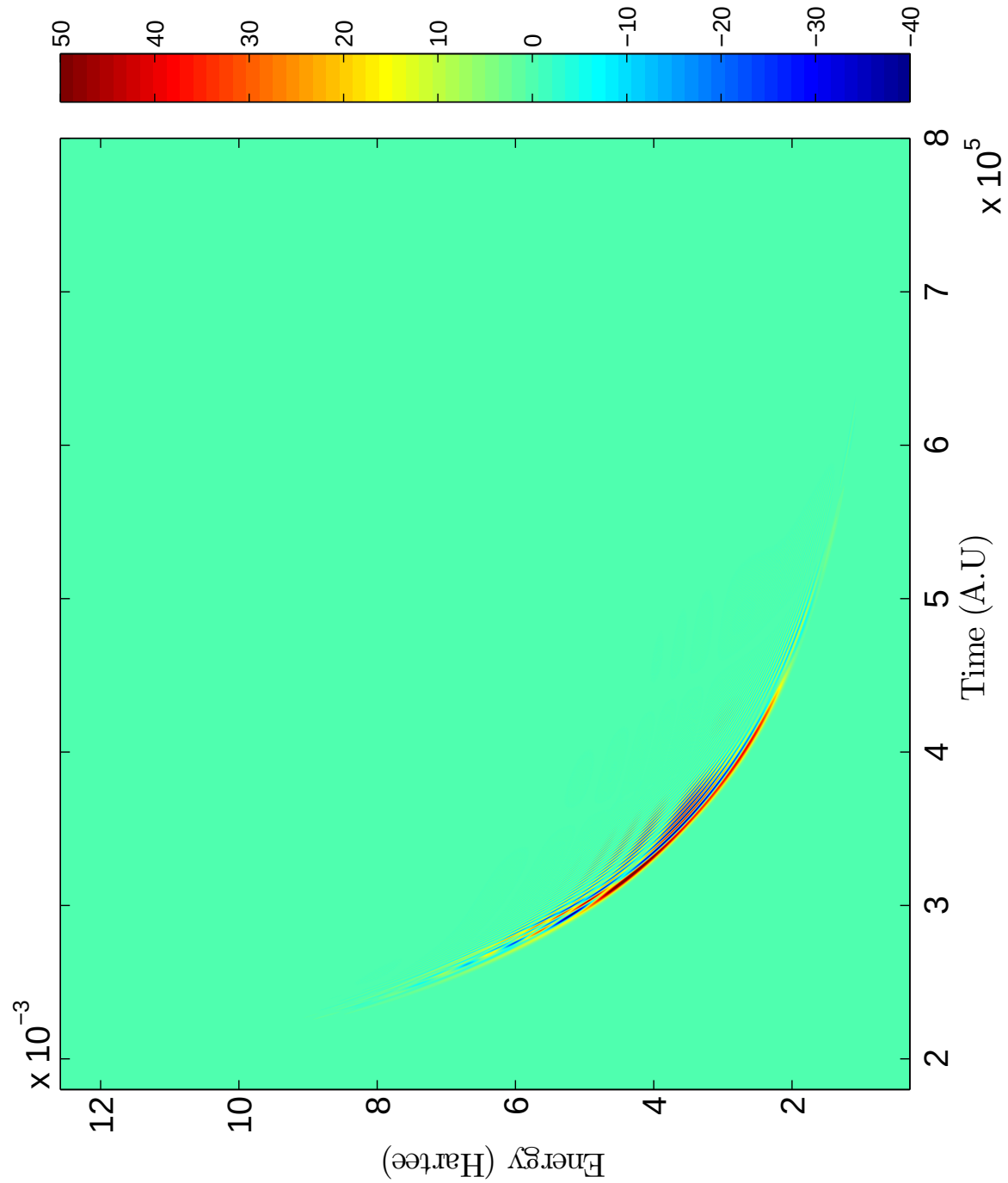


Figure 6.31: Scattering Wigner Distribution Function for K+Ne system with reactant Møller state in $|^{\frac{3}{2}}_{\frac{1}{2}}>$, product Møller state in $|^{\frac{1}{2}}_{\frac{1}{2}}>$, and $J = 0.5$

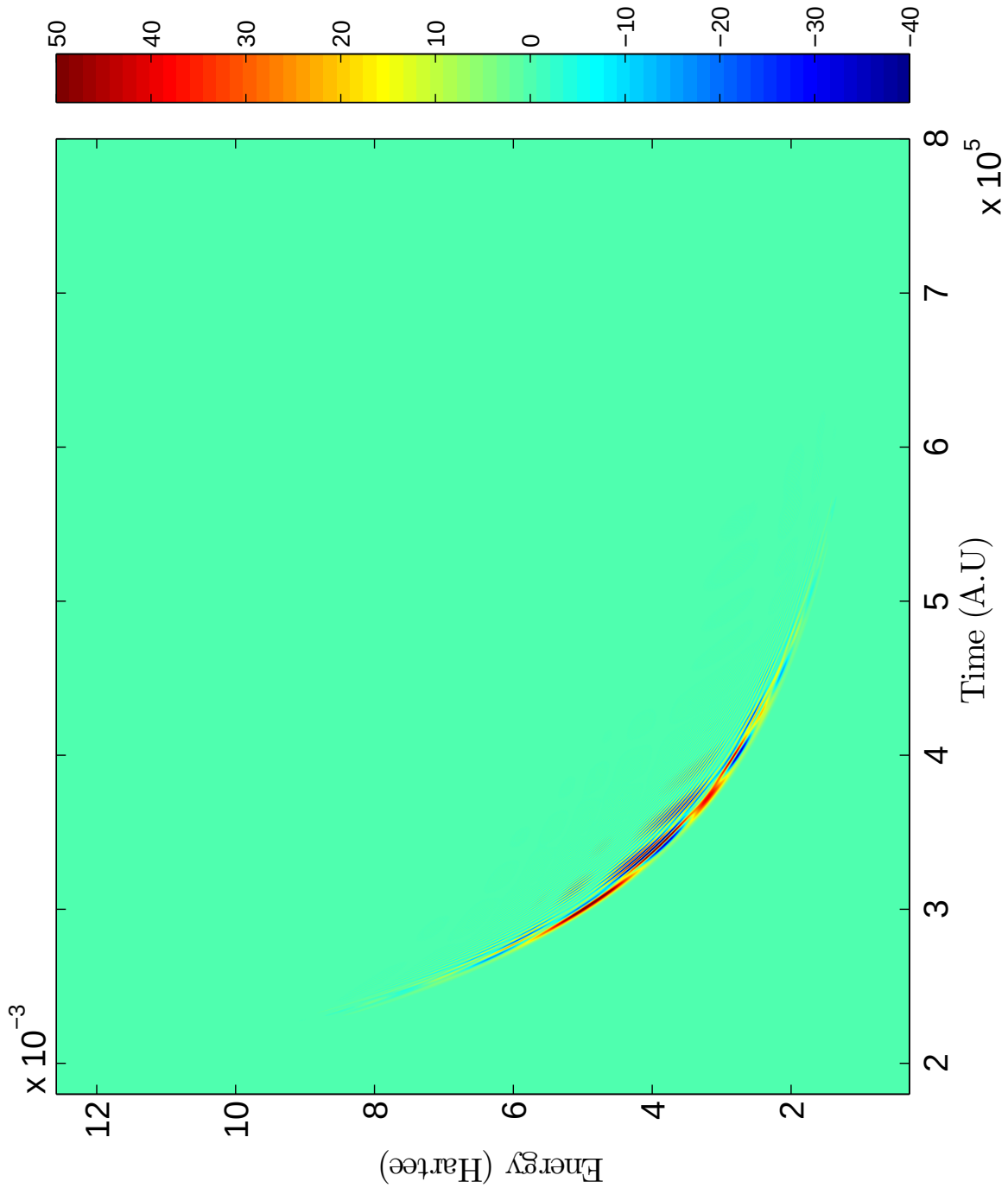


Figure 6.32: Scattering Wigner Distribution Function for K+Ne system with reactant Møller state in $|^{\frac{3}{2}}_{\frac{1}{2}}>$, product Møller state in $|^{\frac{1}{2}}_{\frac{1}{2}}>$, and $J = 50.5$. Note that the scale is the same as Fig. 6.31. The purpose of this is to observe the diminishing amplitude of the scattering WDF as the $J$ increases.

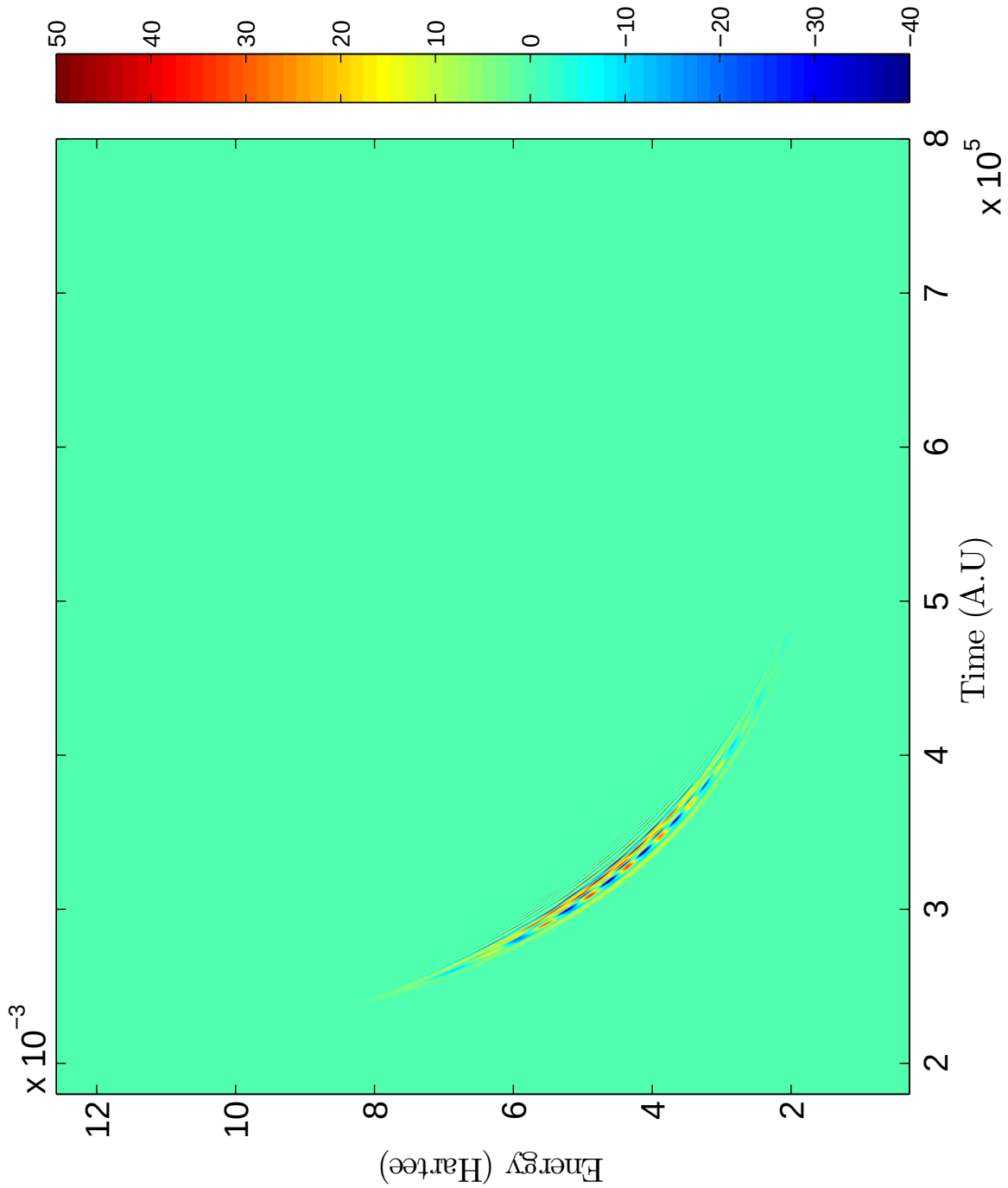


Figure 6.33: Scattering Wigner Distribution Function for K+Ne system with reactant Møller state in $|^{\frac{3}{2}}_{\frac{1}{2}}>$, product Møller state in $|^{\frac{1}{2}}_{\frac{1}{2}}>$, and $J = 100.5$. Note that the scale is the same as Fig. 6.31. The purpose of this is to observe the diminishing amplitude of the scattering WDF as the $J$ increases.

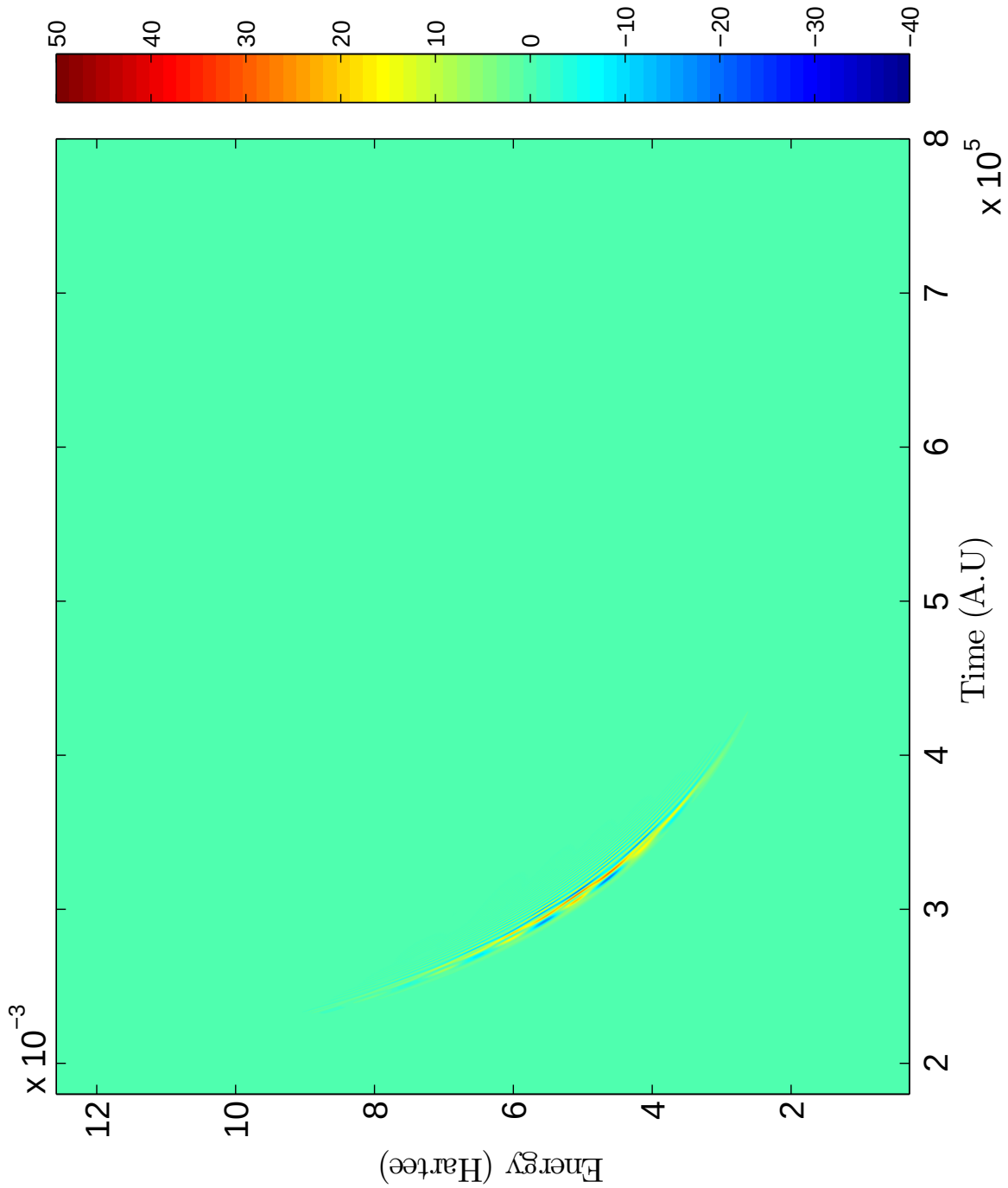


Figure 6.34: Scattering Wigner Distribution Function for K+Ne system with reactant Møller state in $|^{\frac{3}{2}}_{\frac{1}{2}}>$, product Møller state in $|^{\frac{1}{2}}_{\frac{1}{2}}>$, and $J = 150.5$. Note that the scale is the same as Fig. 6.31. The purpose of this is to observe the diminishing amplitude of the scattering WDF as the $J$ increases.

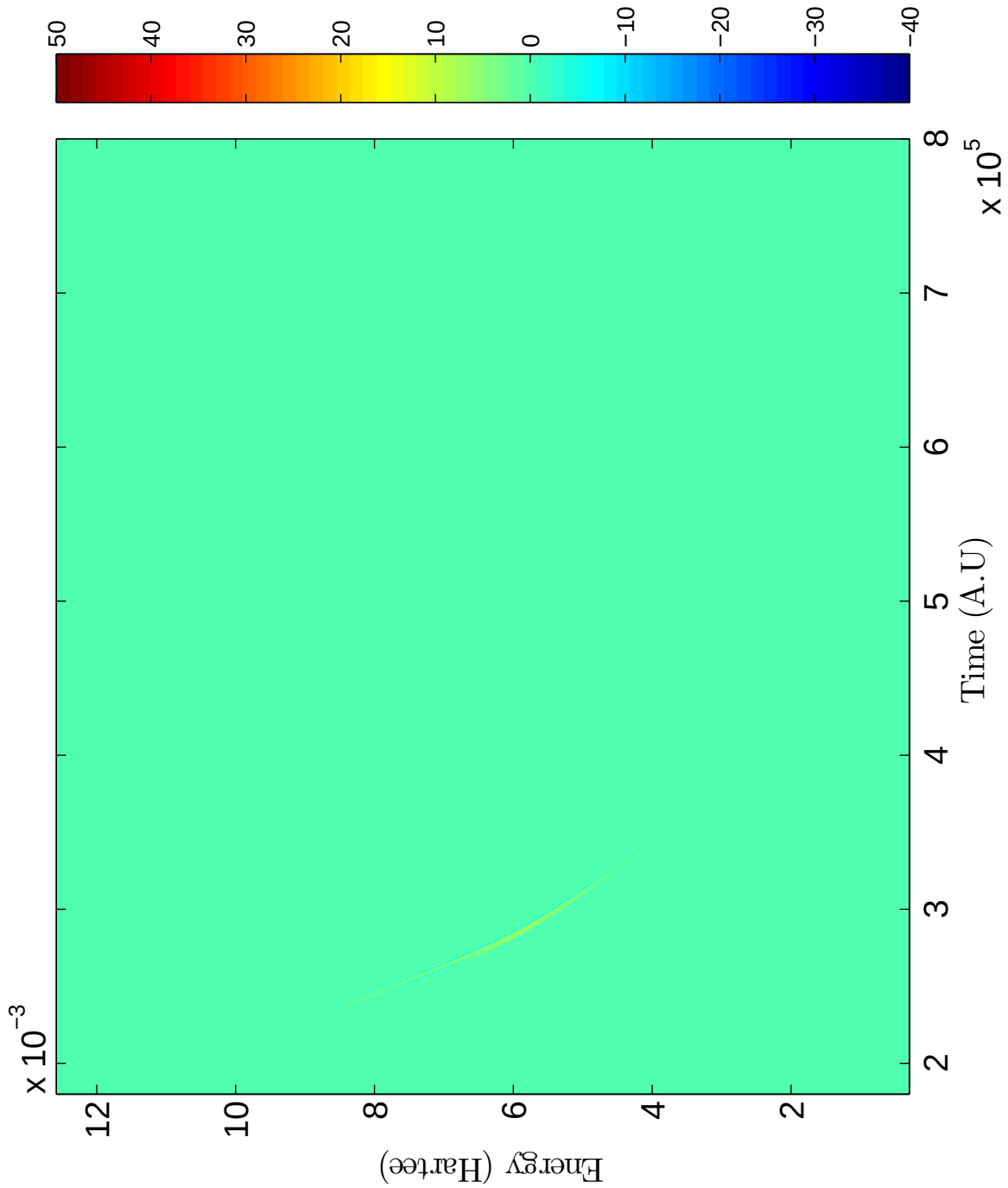


Figure 6.35: Scattering Wigner Distribution Function for K+Ne system with reactant Møller state in $|^{\frac{3}{2}}_{\frac{1}{2}}>$, product Møller state in $|^{\frac{1}{2}}_{\frac{1}{2}}>$, and $J = 200.5$. Note that the scale is the same as Fig. 6.31. The purpose of this is to observe the diminishing amplitude of the scattering WDF as the $J$ increases.

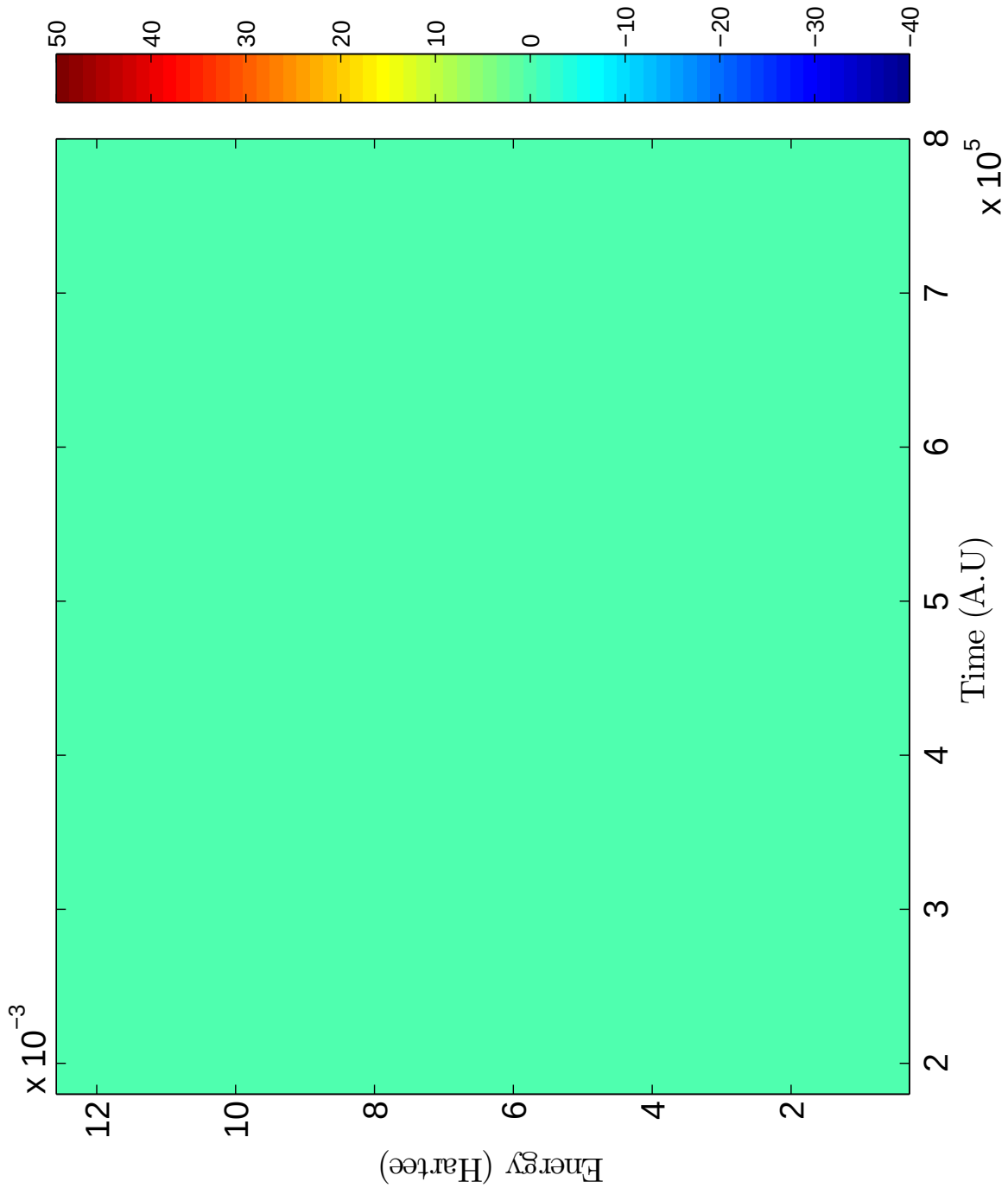


Figure 6.36: Scattering Wigner Distribution Function for K+Ne system with reactant Møller state in $|^{\frac{3}{2}}_{\frac{1}{2}}>$, product Møller state in $|^{\frac{1}{2}}_{\frac{1}{2}}>$, and $J = 250.5$. Note that the scale is the same as Fig. 6.31. The purpose of this is to observe the diminishing amplitude of the scattering WDF as the $J$ increases.

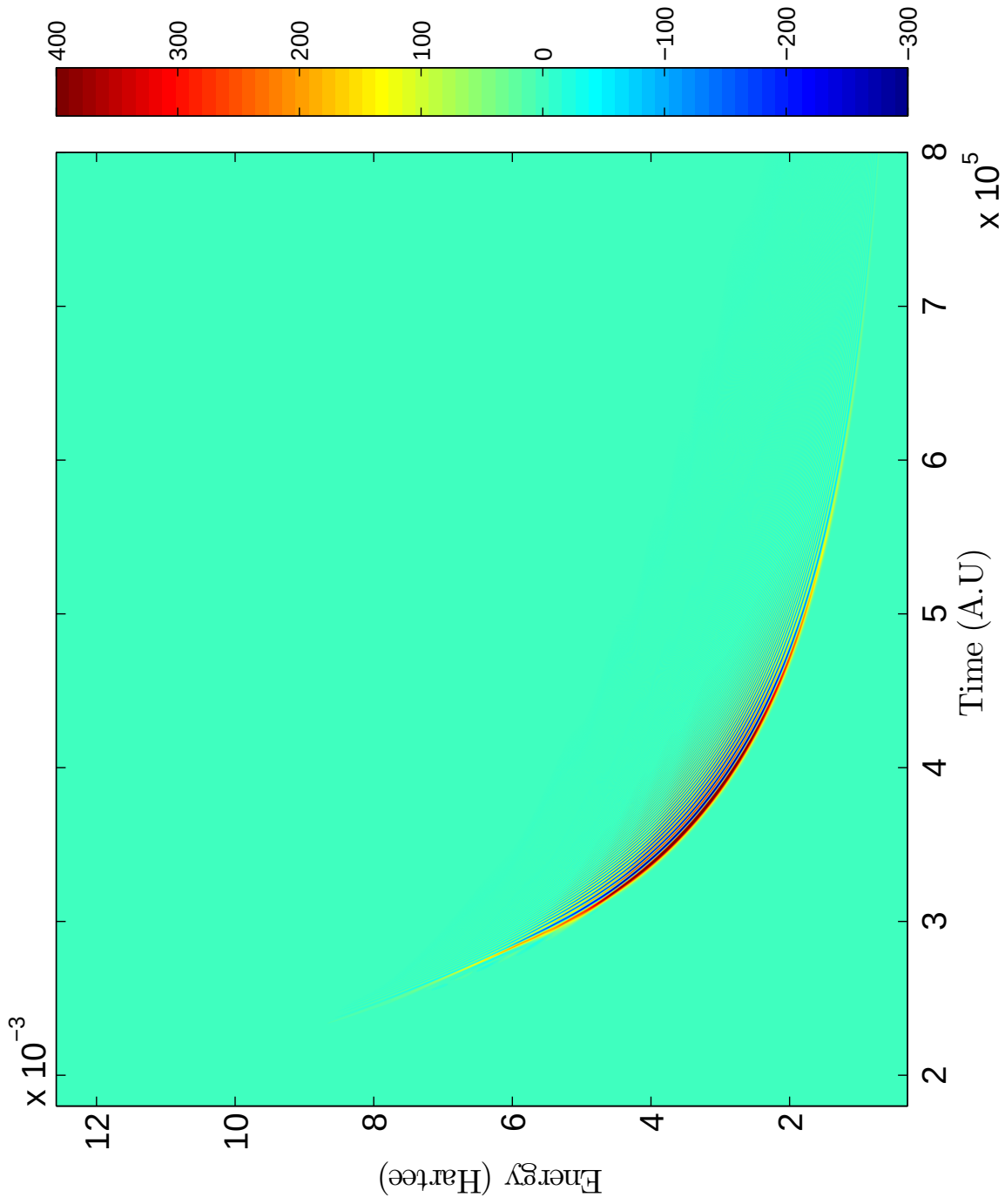


Figure 6.37: Scattering Wigner Distribution Function for K+Ne system with reactant Møller state in $|^{\frac{3}{2}}_{\frac{1}{2}}>$, product Møller state in $|^{\frac{3}{2}}_{\frac{1}{2}}>$, and $J = 0.5$

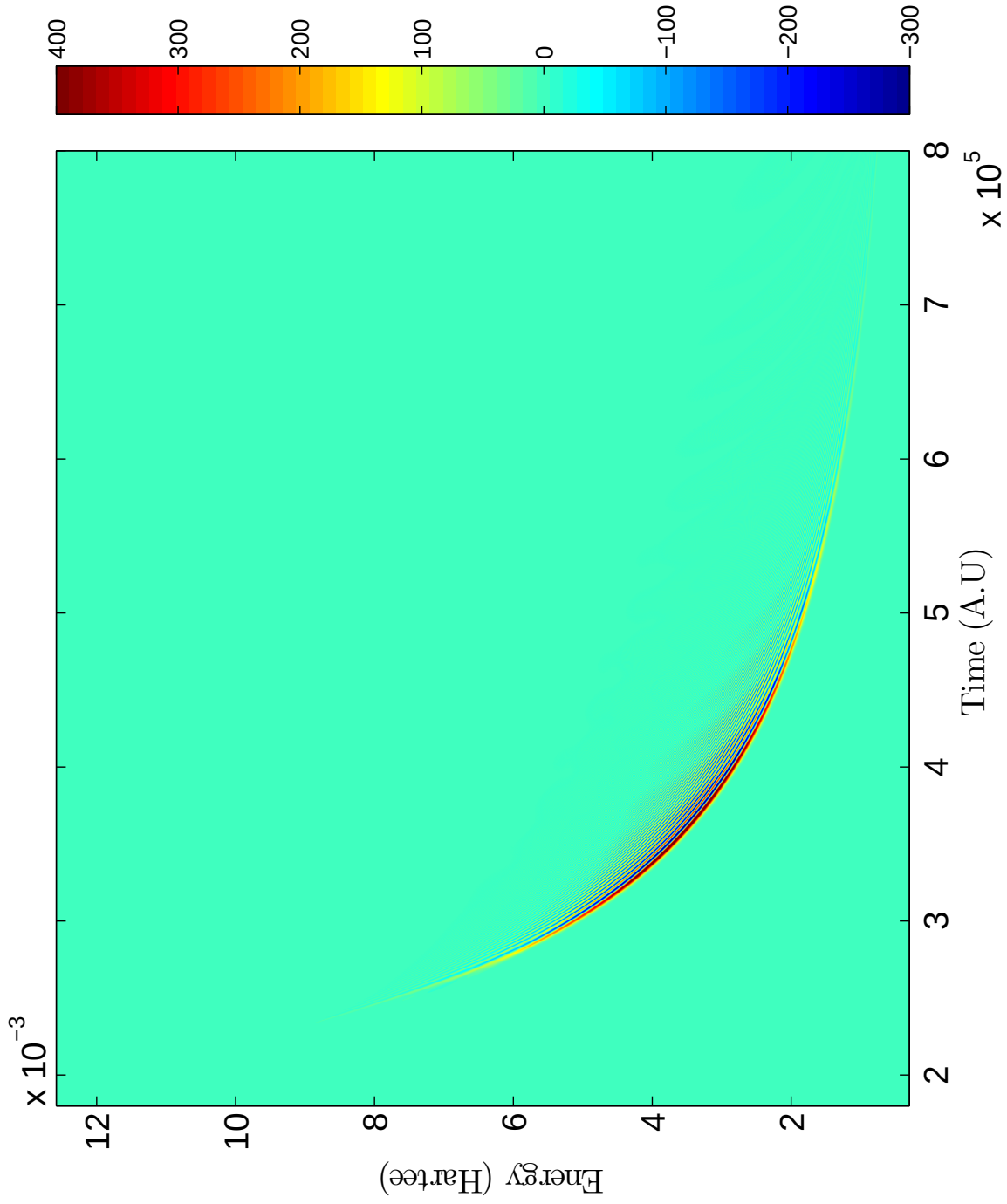


Figure 6.38: Scattering Wigner Distribution Function for K+Ne system with reactant Møller state in $|^{\frac{3}{2}}_{\frac{1}{2}}>$, product Møller state in $|^{\frac{3}{2}}_{\frac{1}{2}}>$, and $J = 50.5$

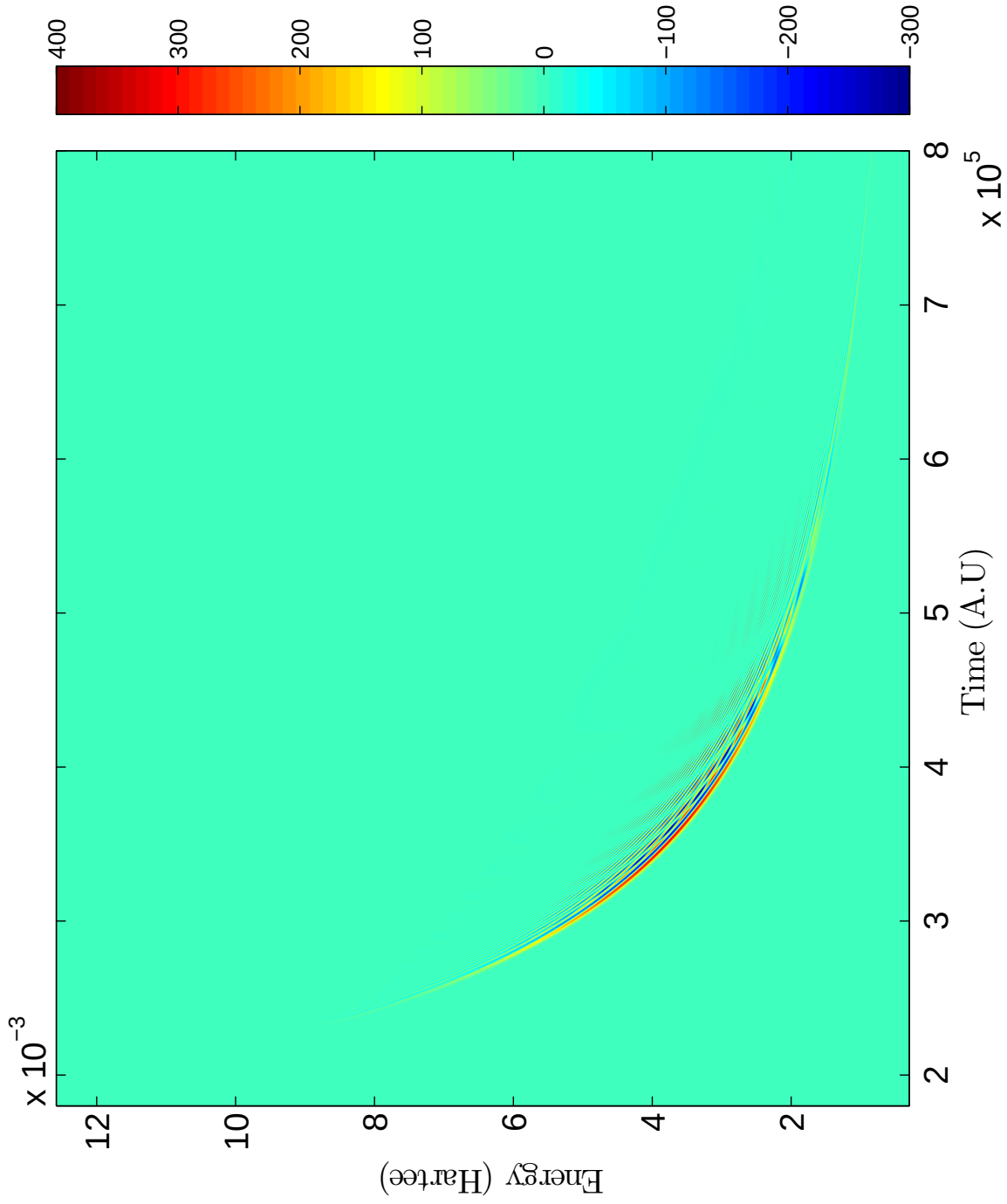


Figure 6.39: Scattering Wigner Distribution Function for K+Ne system with reactant Møller state in $|^{\frac{3}{2}}_{\frac{1}{2}}>$, product Møller state in $|^{\frac{3}{2}}_{\frac{1}{2}}>$, and $J = 100.5$

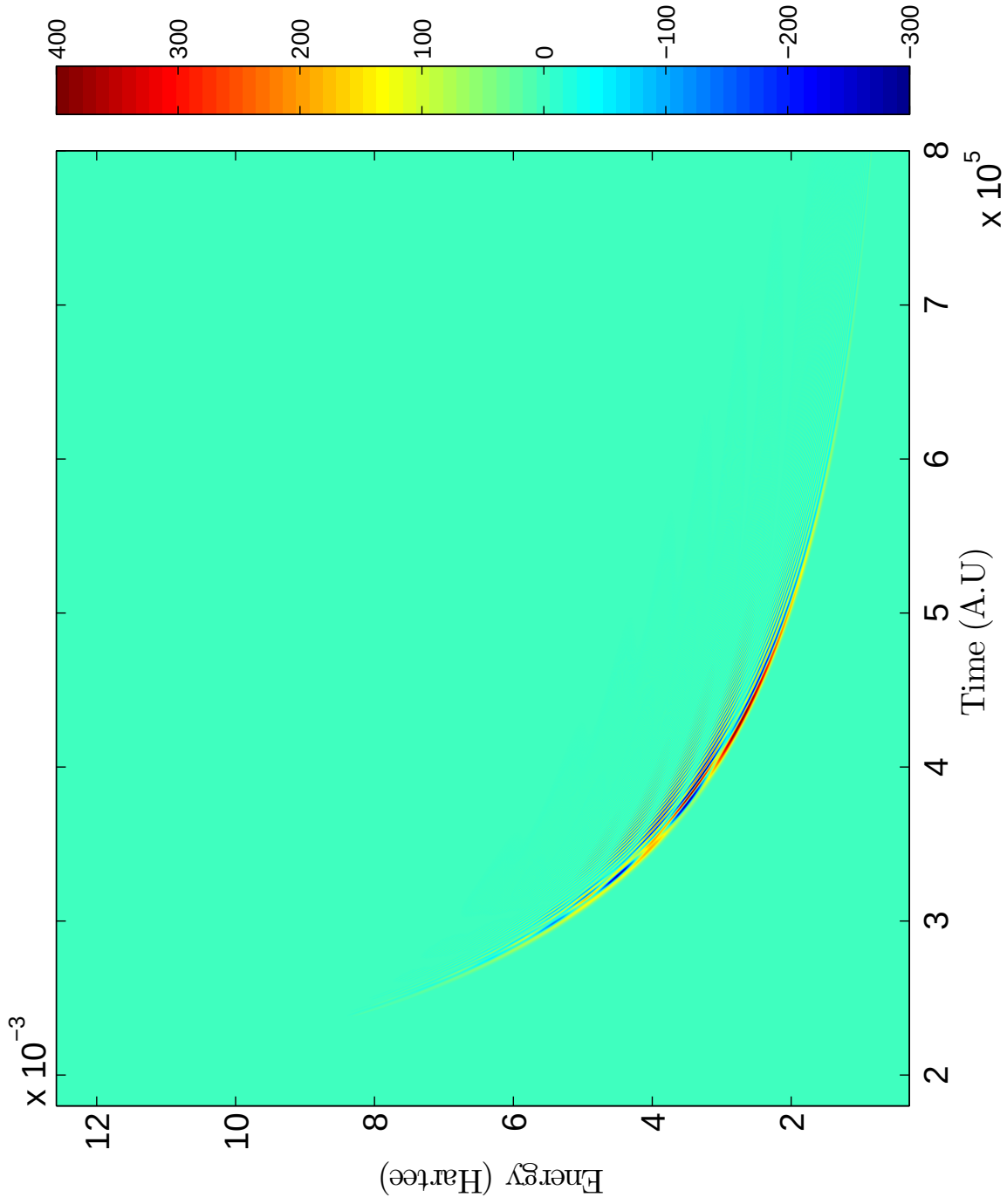


Figure 6.40: Scattering Wigner Distribution Function for K+Ne system with reactant Møller state in $|^{\frac{3}{2}}_{\frac{1}{2}}>$, product Møller state in $|^{\frac{3}{2}}_{\frac{1}{2}}>$, and $J = 150.5$

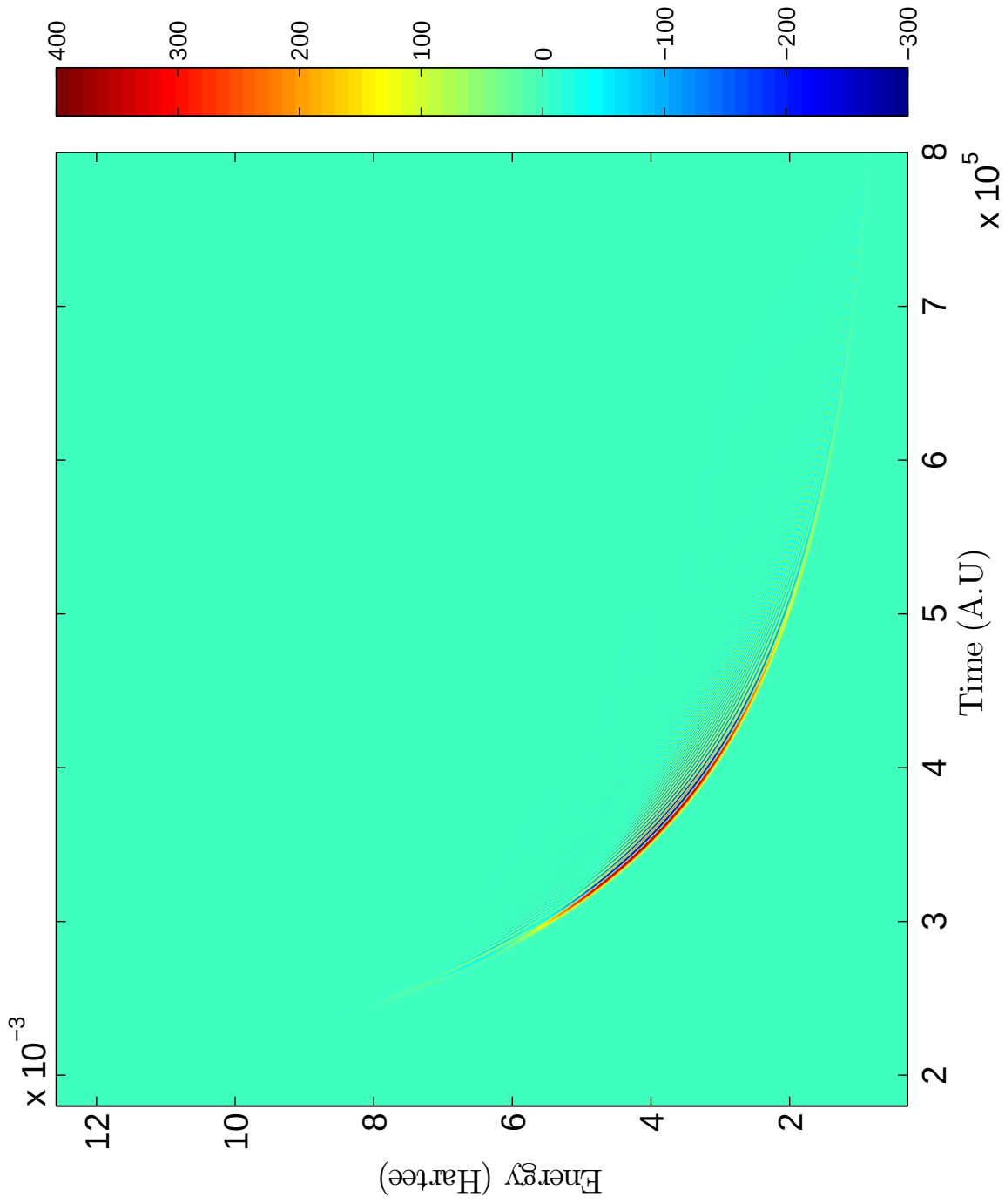


Figure 6.41: Scattering Wigner Distribution Function for K+Ne system with reactant Møller state in $|^{\frac{3}{2}}_{\frac{1}{2}}>$, product Møller state in $|^{\frac{3}{2}}_{\frac{1}{2}}>$, and $J = 200.5$

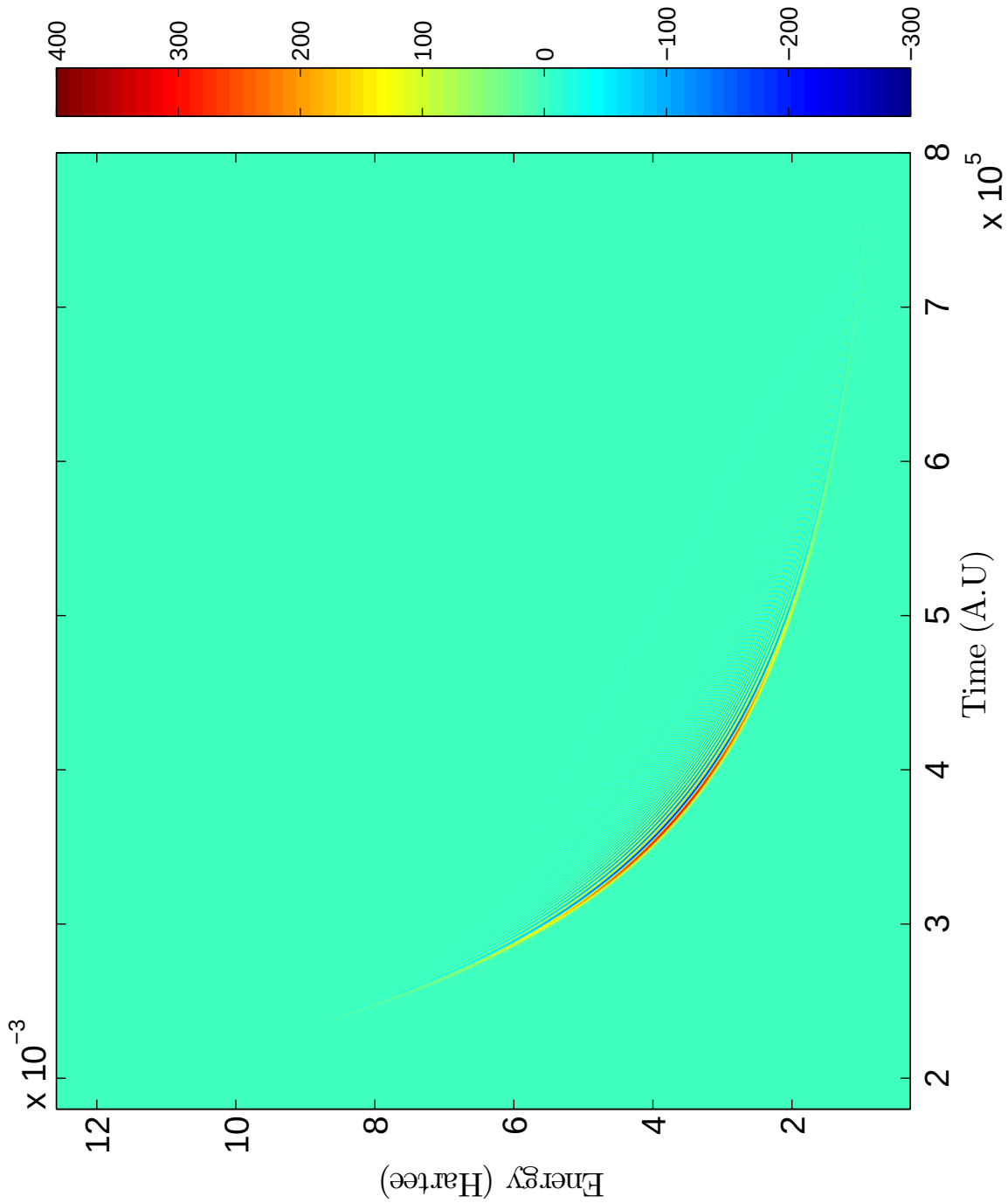


Figure 6.42: Scattering Wigner Distribution Function for K+Ne system with reactant Møller state in $|^{\frac{3}{2}}_{\frac{1}{2}}>$, product Møller state in $|^{\frac{3}{2}}_{\frac{1}{2}}>$, and $J = 250.5$

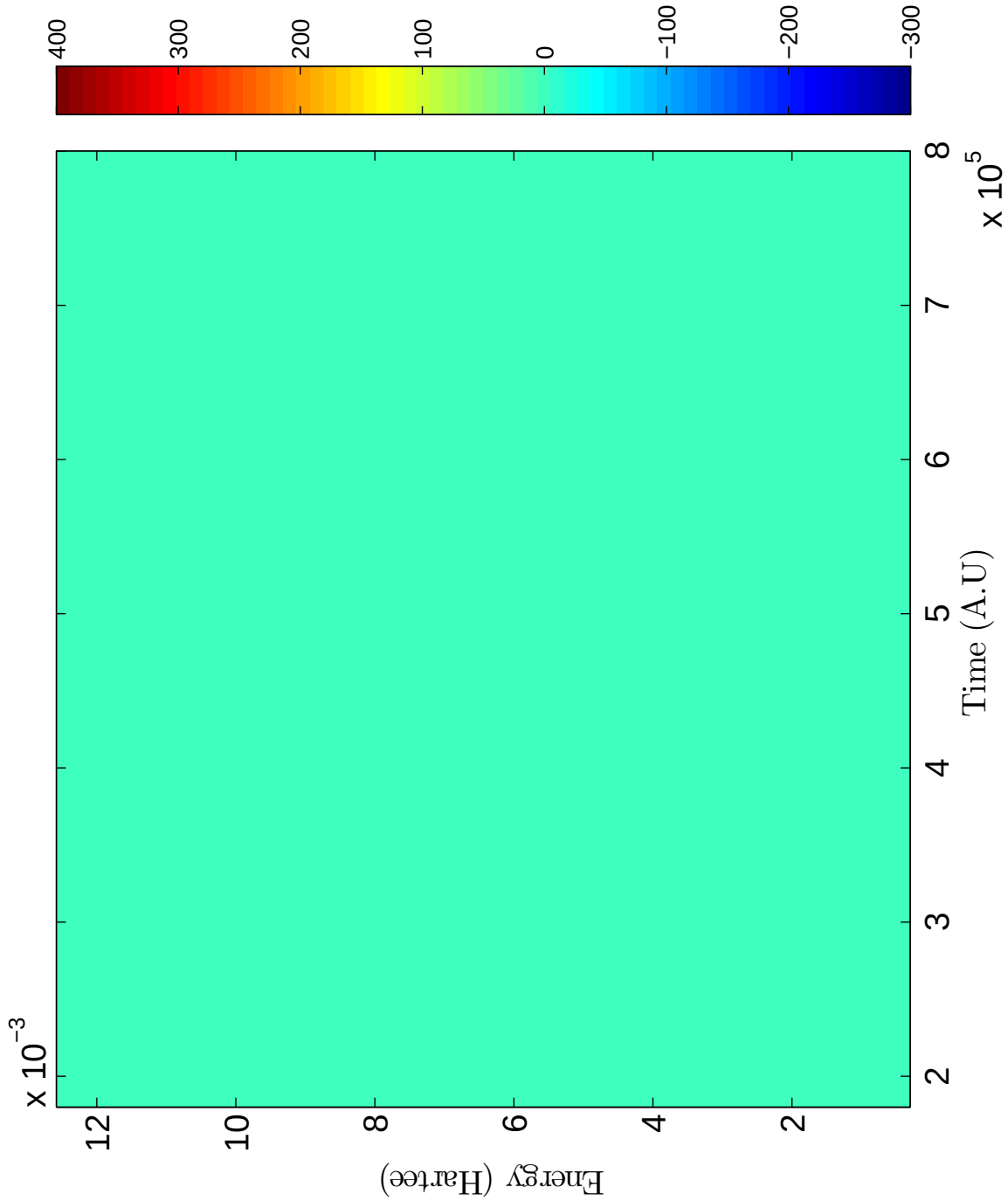


Figure 6.43: Scattering Wigner Distribution Function for K+Ne system with reactant Møller state in $|^{\frac{3}{2}}_{\frac{1}{2}}>$, product Møller state in $|^{\frac{3}{2}}_{\frac{3}{2}}>$, and $J = 0.5$. Note that the scale is the same as Fig. 6.37. The purpose of this is to observe the increasing amplitude of the scattering WDF as $J$ increases and to show how the amplitude of the scattering WDFs for the $|^{\frac{3}{2}}_{\frac{1}{2}}>$ and the $|^{\frac{3}{2}}_{\frac{3}{2}}>$ surfaces approach each other for high $J$.

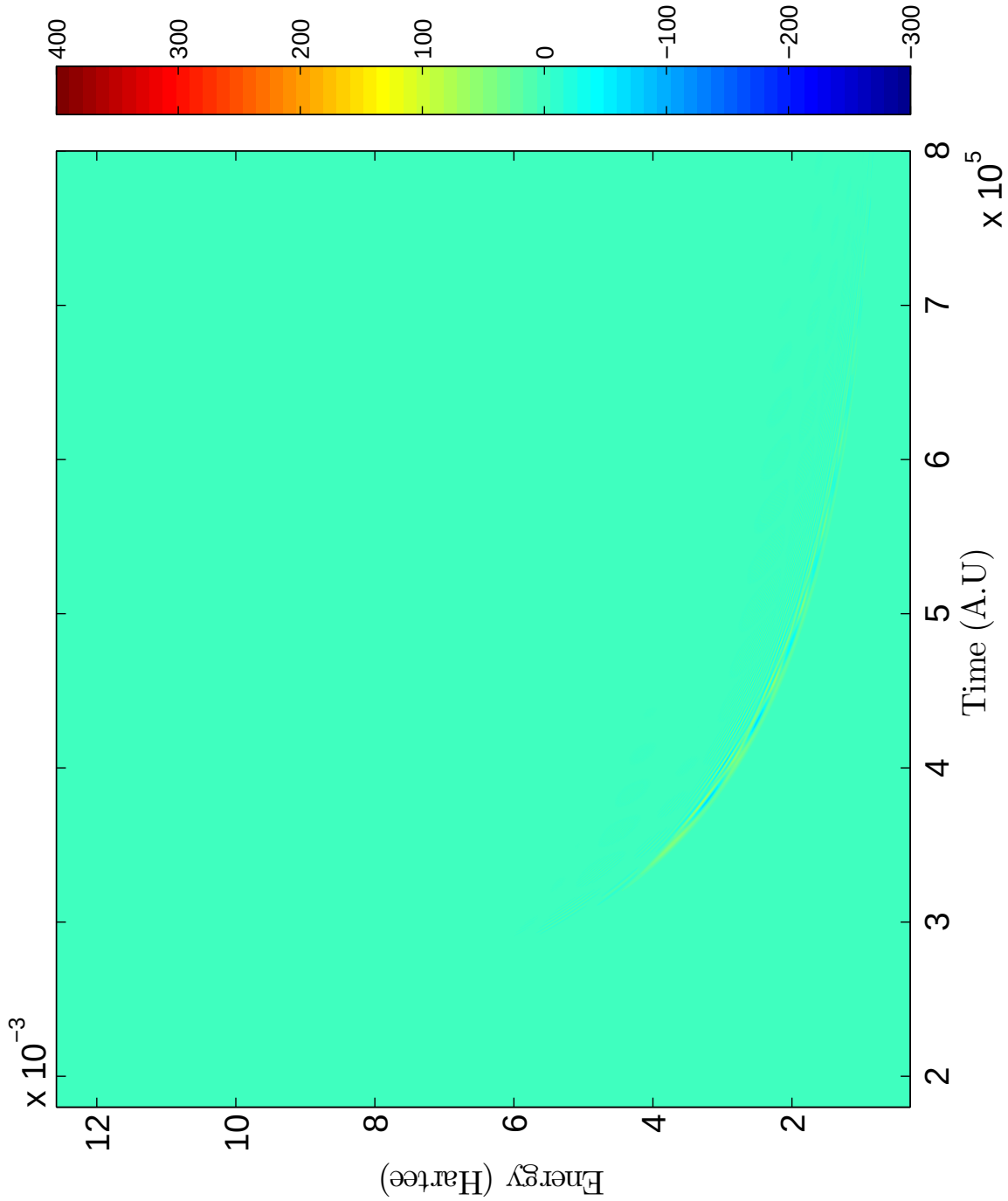


Figure 6.44: Scattering Wigner Distribution Function for K+Ne system with reactant Møller state in $|^{\frac{3}{2}}_{\frac{1}{2}}>$, product Møller state in $|^{\frac{3}{2}}_{\frac{3}{2}}>$, and $J = 50.5$. Note that the scale is the same as Fig. 6.37. The purpose of this is to observe the increasing amplitude of the scattering WDF as $J$ increases and to show how the amplitude of the scattering WDFs for the $|^{\frac{3}{2}}_{\frac{1}{2}}>$ and the $|^{\frac{3}{2}}_{\frac{3}{2}}>$ surfaces approach each other for high $J$.

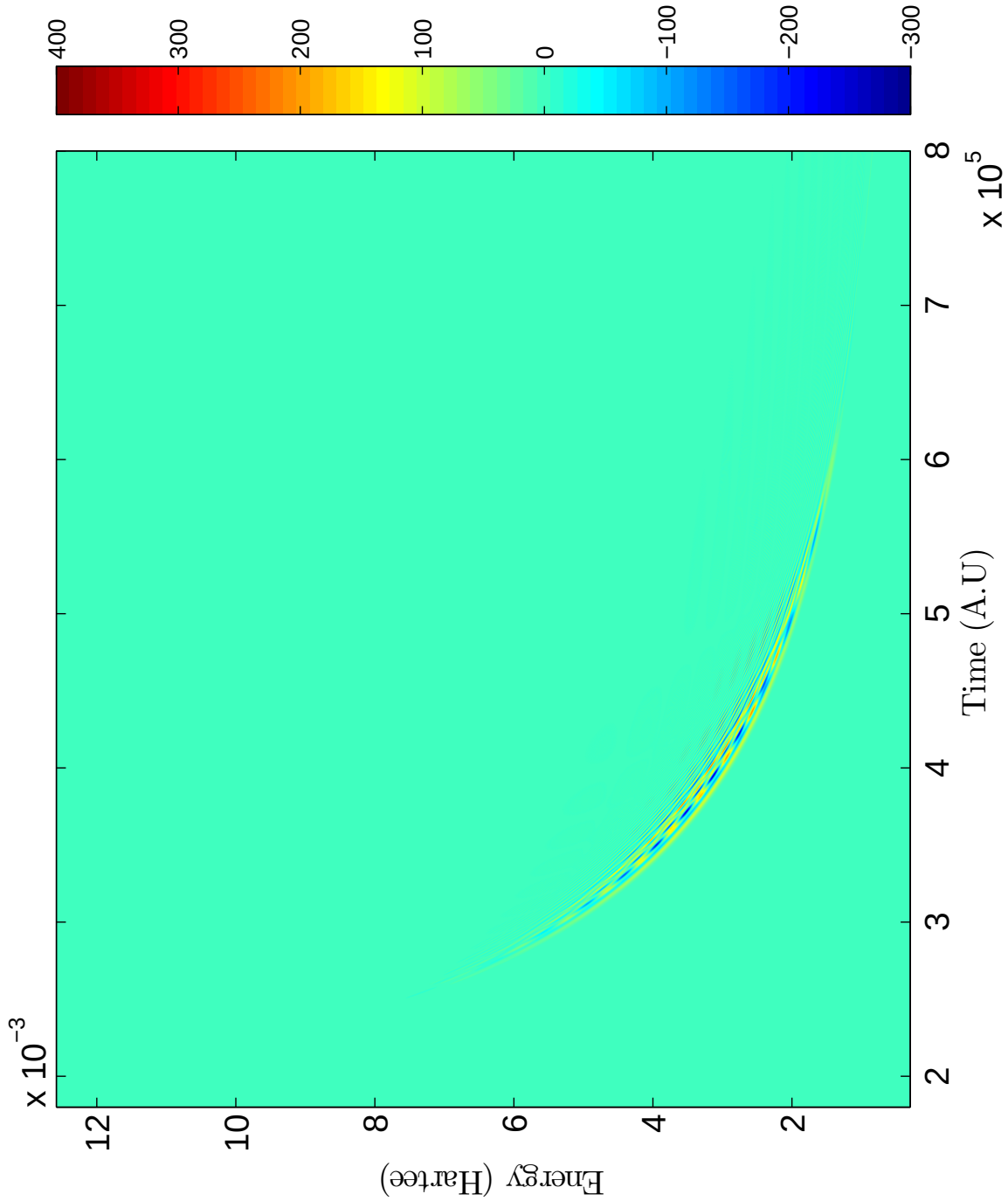


Figure 6.45: Scattering Wigner Distribution Function for K+Ne system with reactant Møller state in $|^{\frac{3}{2}}_{\frac{1}{2}}>$, product Møller state in $|^{\frac{3}{2}}_{\frac{3}{2}}>$, and $J = 100.5$. Note that the scale is the same as Fig. 6.37. The purpose of this is to observe the increasing amplitude of the scattering WDF as $J$ increases and to show how the amplitude of the scattering WDFs for the $|^{\frac{3}{2}}_{\frac{1}{2}}>$ and the $|^{\frac{3}{2}}_{\frac{3}{2}}>$ surfaces approach each other for high $J$.

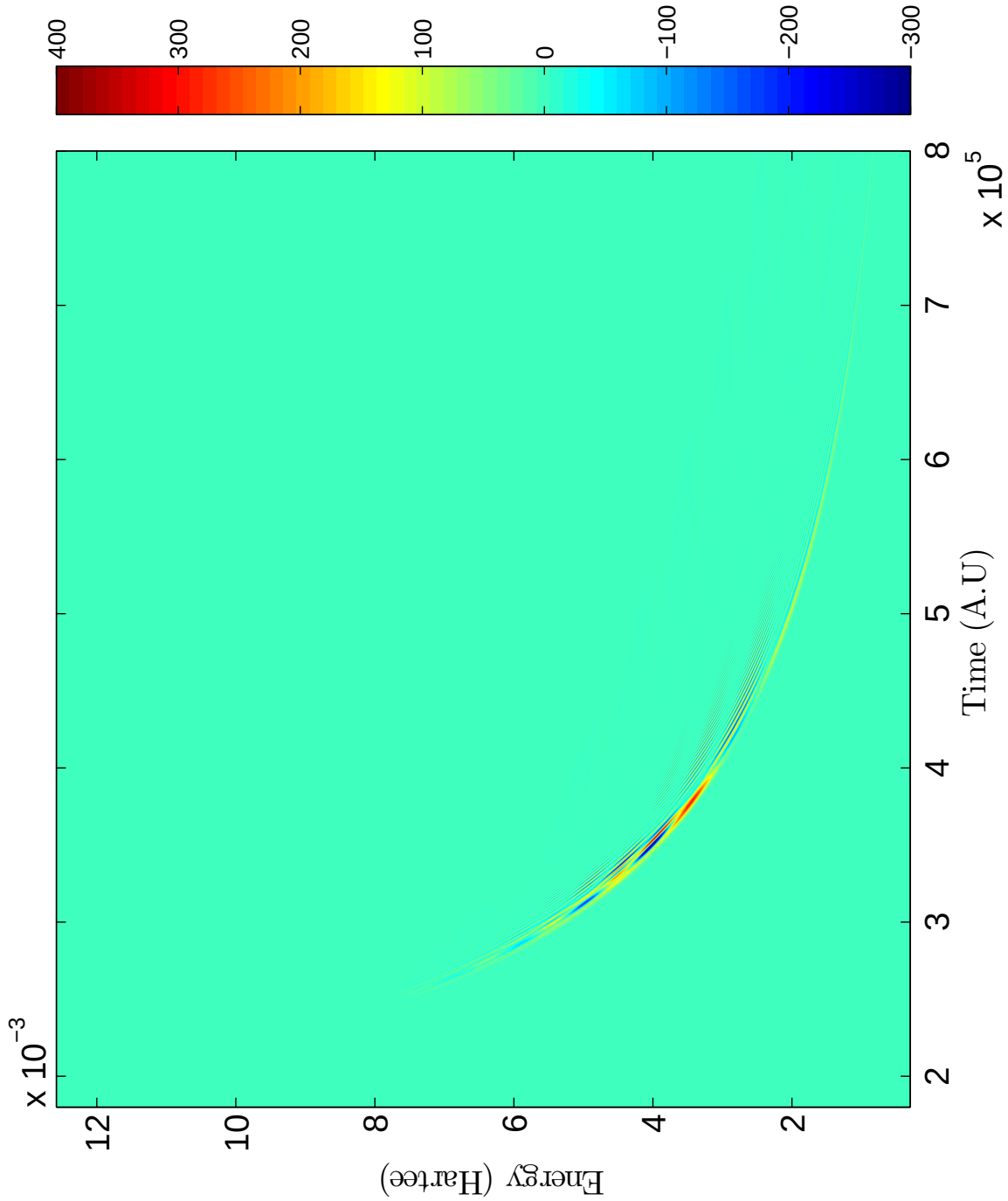


Figure 6.46: Scattering Wigner Distribution Function for K+Ne system with reactant Møller state in $|^{\frac{3}{2}}_{\frac{1}{2}}>$, product Møller state in $|^{\frac{3}{2}}_{\frac{3}{2}}>$, and $J = 150.5$. Note that the scale is the same as Fig. 6.37. The purpose of this is to observe the increasing amplitude of the scattering WDF as $J$ increases and to show how the amplitude of the scattering WDFs for the $|^{\frac{3}{2}}_{\frac{1}{2}}>$ and the $|^{\frac{3}{2}}_{\frac{3}{2}}>$ surfaces approach each other for high $J$.

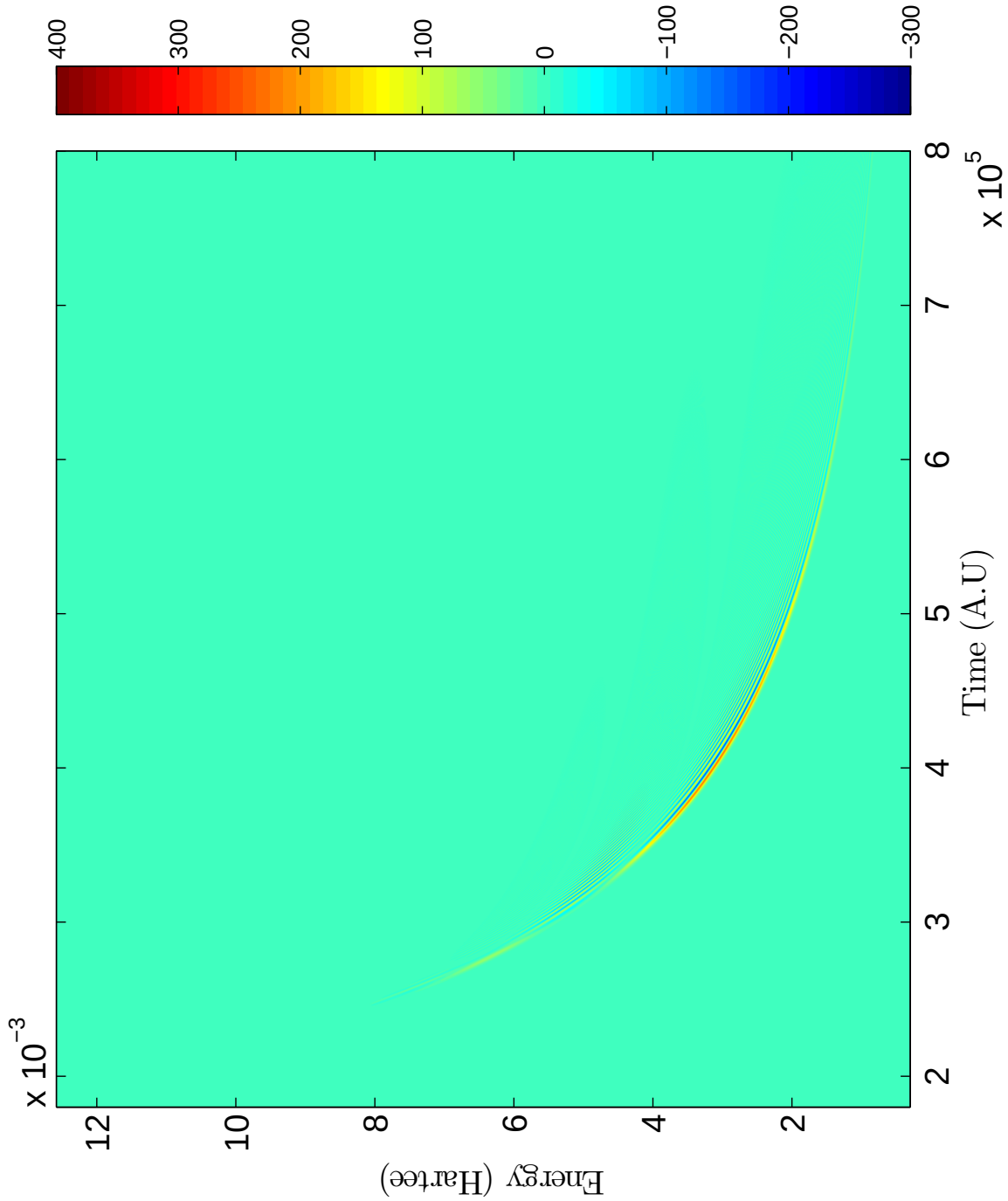


Figure 6.47: Scattering Wigner Distribution Function for K+Ne system with reactant Møller state in $|^{\frac{3}{2}}_{\frac{1}{2}}>$, product Møller state in $|^{\frac{3}{2}}_{\frac{3}{2}}>$, and $J = 200.5$. Note that the scale is the same as Fig. 6.37. The purpose of this is to observe the increasing amplitude of the scattering WDF as $J$ increases and to show how the amplitude of the scattering WDFs for the $|^{\frac{3}{2}}_{\frac{1}{2}}>$ and the $|^{\frac{3}{2}}_{\frac{3}{2}}>$ surfaces approach each other for high $J$.

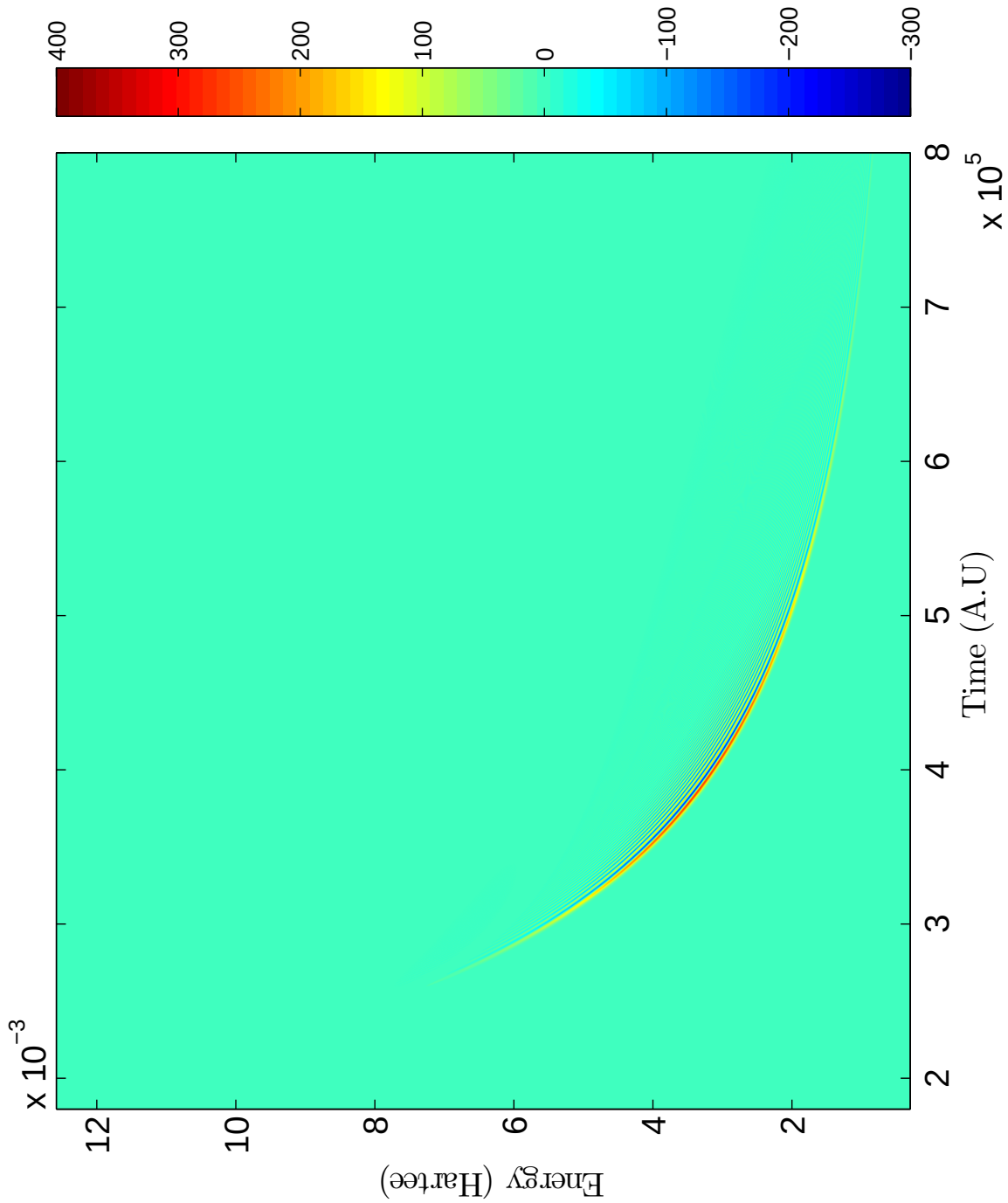


Figure 6.48: Scattering Wigner Distribution Function for K+Ne system with reactant Møller state in $|^{\frac{3}{2}}_{\frac{1}{2}}>$, product Møller state in $|^{\frac{3}{2}}_{\frac{3}{2}}>$, and $J = 250.5$. Note that the scale is the same as Fig. 6.37. The purpose of this is to observe the increasing amplitude of the scattering WDF as $J$ increases and to show how the amplitude of the scattering WDFs for the $|^{\frac{3}{2}}_{\frac{1}{2}}>$ and the $|^{\frac{3}{2}}_{\frac{3}{2}}>$ surfaces approach each other for high $J$.

### *6.2.3 Angular Momentum Study.*

Scattering WDFs were produced for the Potassium plus noble gas collisions in steps of $\Delta J = 5.0$ starting from $J = 5.5$ to $J = 250.5$ ($J = 1.5$ is also included) with the reactant state starting in the $|^{\frac{1}{2}}_{\frac{1}{2}}>$ surface. The purpose of this study was to see how the total angular momentum impacted probability transfer between the various surfaces. As mentioned in the square well problem, the sum of all the values of the scattering WDF along an energy slice multiplied by a normalization factor is the probability of transmitting on that surface. The normalization factor is shown in Eq. 2.10 and is independent of the value of $J$. Although the maximum and minimum values of the scattering WDF along the energy slice are only two contributions to the sum, their difference provides the largest contribution to the sum. As discussed in the square well problems, for a given peak there is an associated valley on the same order of magnitude with the same peak width, so they cancel each other out in the sum. The largest peak and the largest valley have the greatest difference in their magnitude and do not necessarily cancel each other out, so the difference between the largest peak and valley can be used to approximate the sum of the scattering WDF values along a particular energy slice. Furthermore, the maximum and minimum values for a given energy slice are approximately the same for a range of energy values (multiple energy slices), so we can use the maximum and minimum values of the scattering WDF to compare the relative flow of probabilities at various total angular momentum among the various potential energy surfaces. Because we are concerned with the change in probability transfer as $J$ changes, we simply looked at the maximum value of the scattering WDF instead of the difference between the maximum and minimum value of the scattering WDF as shown in Fig. 6.49.

When the reactant Møller state starts on the $|^{\frac{1}{2}}_{\frac{1}{2}}>$ surface, there is very little probability on the $|^{\frac{3}{2}}_{\frac{3}{2}}>$ for low values of $J$, and the maximum value of the scattering WDF associated with the product Møller state on the $|^{\frac{3}{2}}_{\frac{3}{2}}>$ surface is very near zero for low values of $J$. As

the Coriolis coupling becomes stronger as $J$ increases, the maximum value of the scattering WDF for the $|^{\frac{3}{2}}_{\frac{3}{2}}>$ surface increases. The maximum value of the scattering WDF peaks and decreases for even higher $J$ until the maximum value for the scattering WDF becomes zero for very high $J$. The maximum value of the scattering WDF peaks and decreases to zero due to the effects of the effective potential which reduces the amount of probability that can be radially coupled. The maximum value of the scattering WDF associated with the product Møller state on the $|^{\frac{3}{2}}_{\frac{1}{2}}>$ surface is more complicated due to the interplay between Coriolis and radial coupling at that surface. When the Coriolis coupling is turned off at low values of $J$, radial coupling is the only source of probability to the $|^{\frac{3}{2}}_{\frac{1}{2}}>$ surface, so unlike the $|^{\frac{3}{2}}_{\frac{3}{2}}>$ surface scattering WDF, the maximum value of the scattering WDF is non-zero at low values of $J$. As $J$ increases, the strength of the Coriolis coupling increases and some of the probability is transferred to the $|^{\frac{3}{2}}_{\frac{3}{2}}>$ surface. At $J = 60.5$, the effective potential overpowers the Coriolis coupling (since the probability transfer to the $|^{\frac{3}{2}}_{\frac{1}{2}}>$ surface decreases with increasing effective potential), and the maximum value of the scattering WDF associated with the product Møller state on the $|^{\frac{3}{2}}_{\frac{1}{2}}>$ surface drops to zero at the same rate as the $|^{\frac{3}{2}}_{\frac{3}{2}}>$ surface

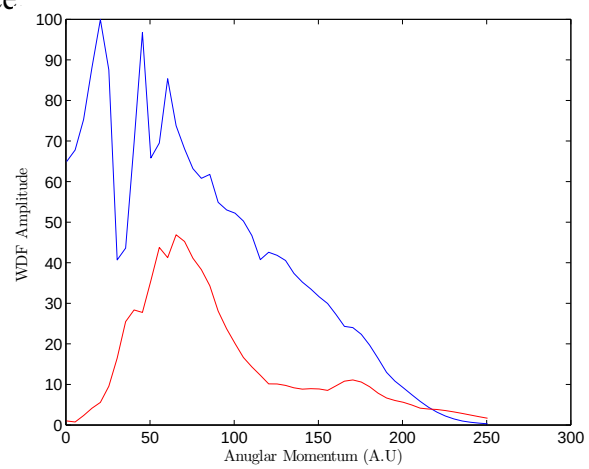


Figure 6.49: The maximum value of the scattering Wigner Distribution Function for K+Ne system with reactant Møller state in $|^{\frac{1}{2}}_{\frac{1}{2}}>$, product Møller state in $|^{\frac{3}{2}}_{\frac{1}{2}}>$ (Blue), and product Møller state $|^{\frac{3}{2}}_{\frac{3}{2}}>$ (Red). The maximum value was sampled for every $\Delta J = 5$ ranging from $J = 5.5$ to $J = 250.5$ (including $J = 1.5$.

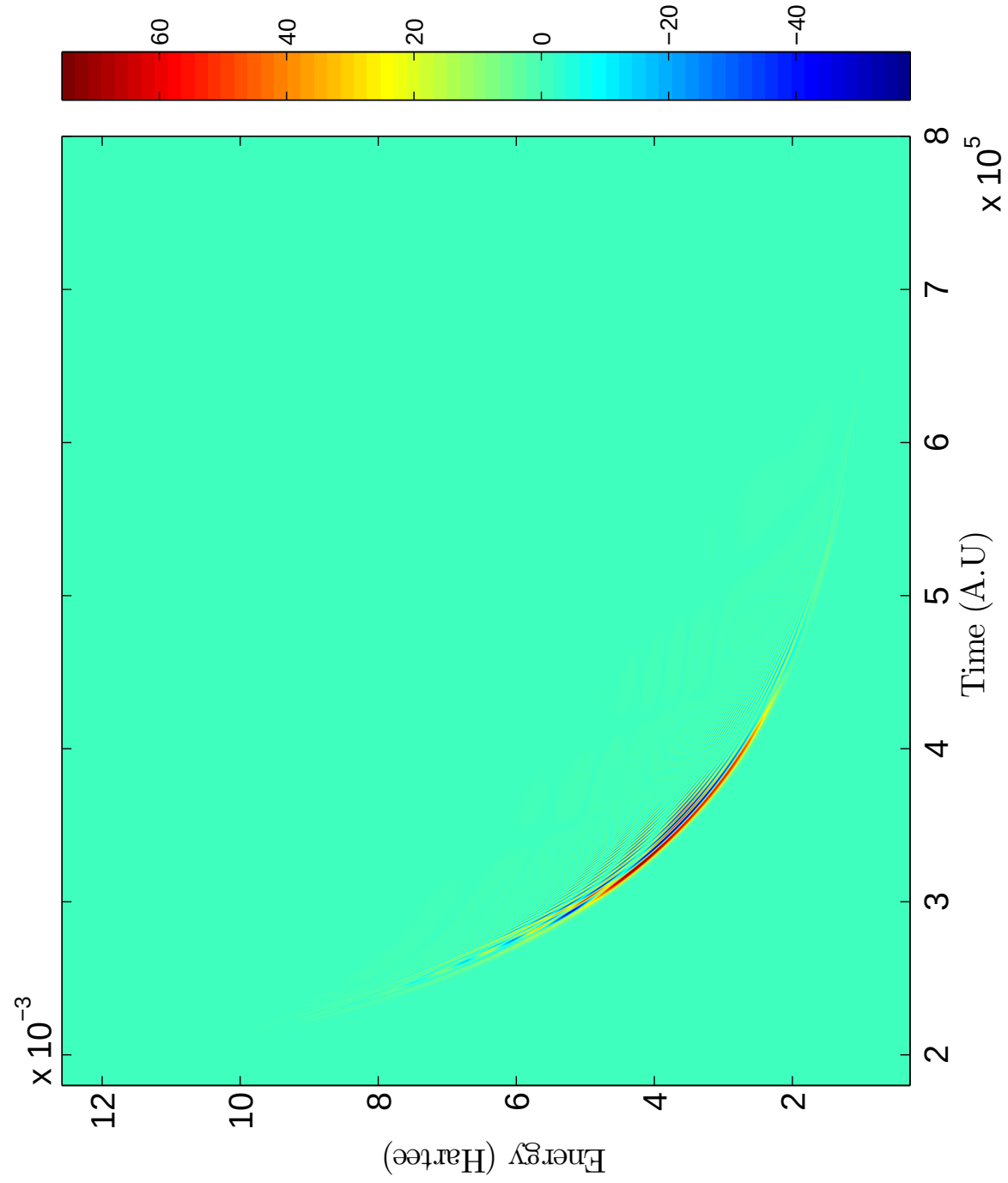


Figure 6.50: Scattering Wigner Distribution Function for K+Ne system with reactant Møller state in $|^{\frac{1}{2}}_{\frac{1}{2}}>$, product Møller state in $|^{\frac{3}{2}}_{\frac{1}{2}}>$, and $J = 10.5$

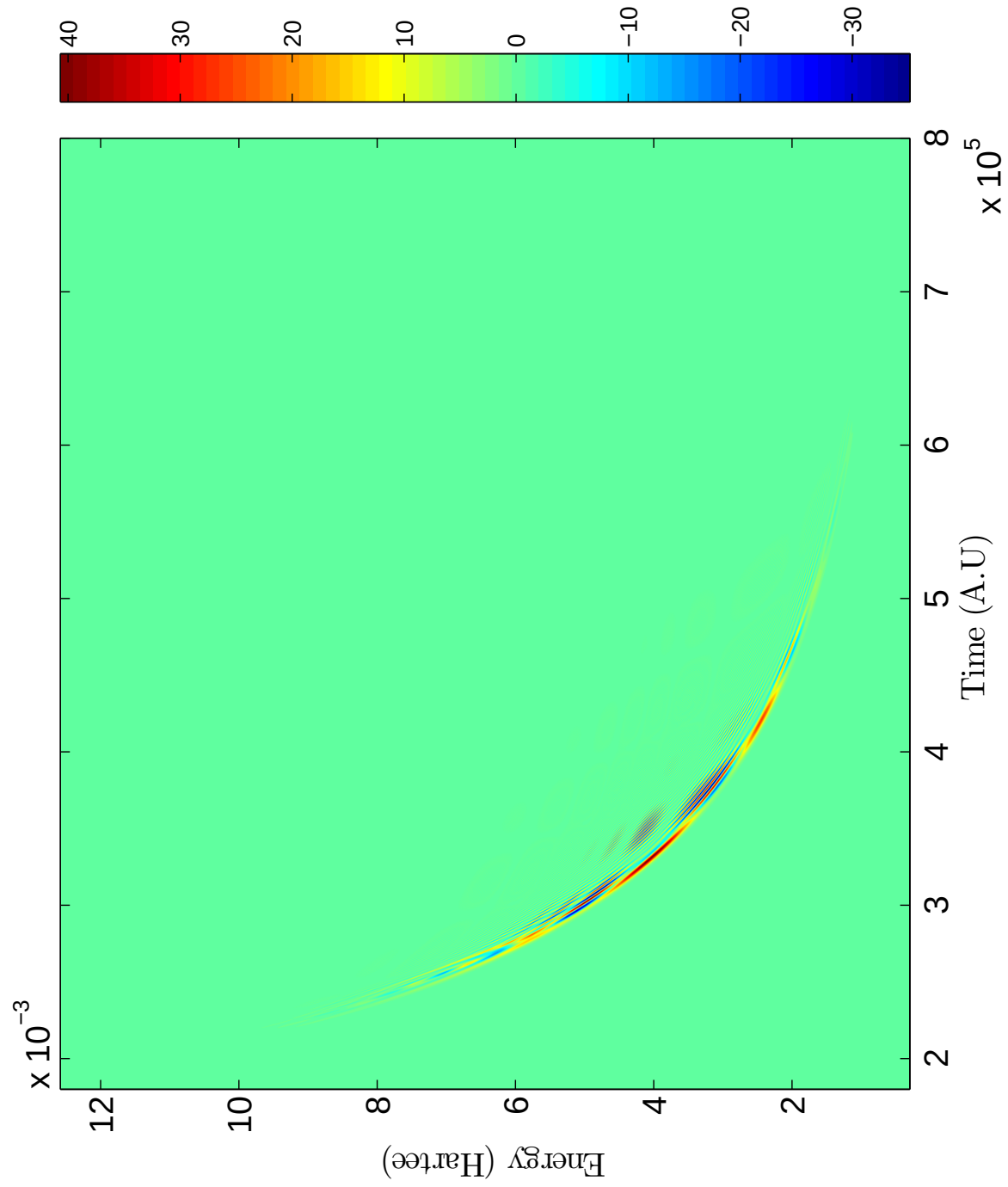


Figure 6.51: Scattering Wigner Distribution Function for K+Ne system with reactant Møller state in $|^{\frac{1}{2}}_{\frac{1}{2}}>$, product Møller state in $|^{\frac{3}{2}}_{\frac{1}{2}}>$, and $J = 30.5$

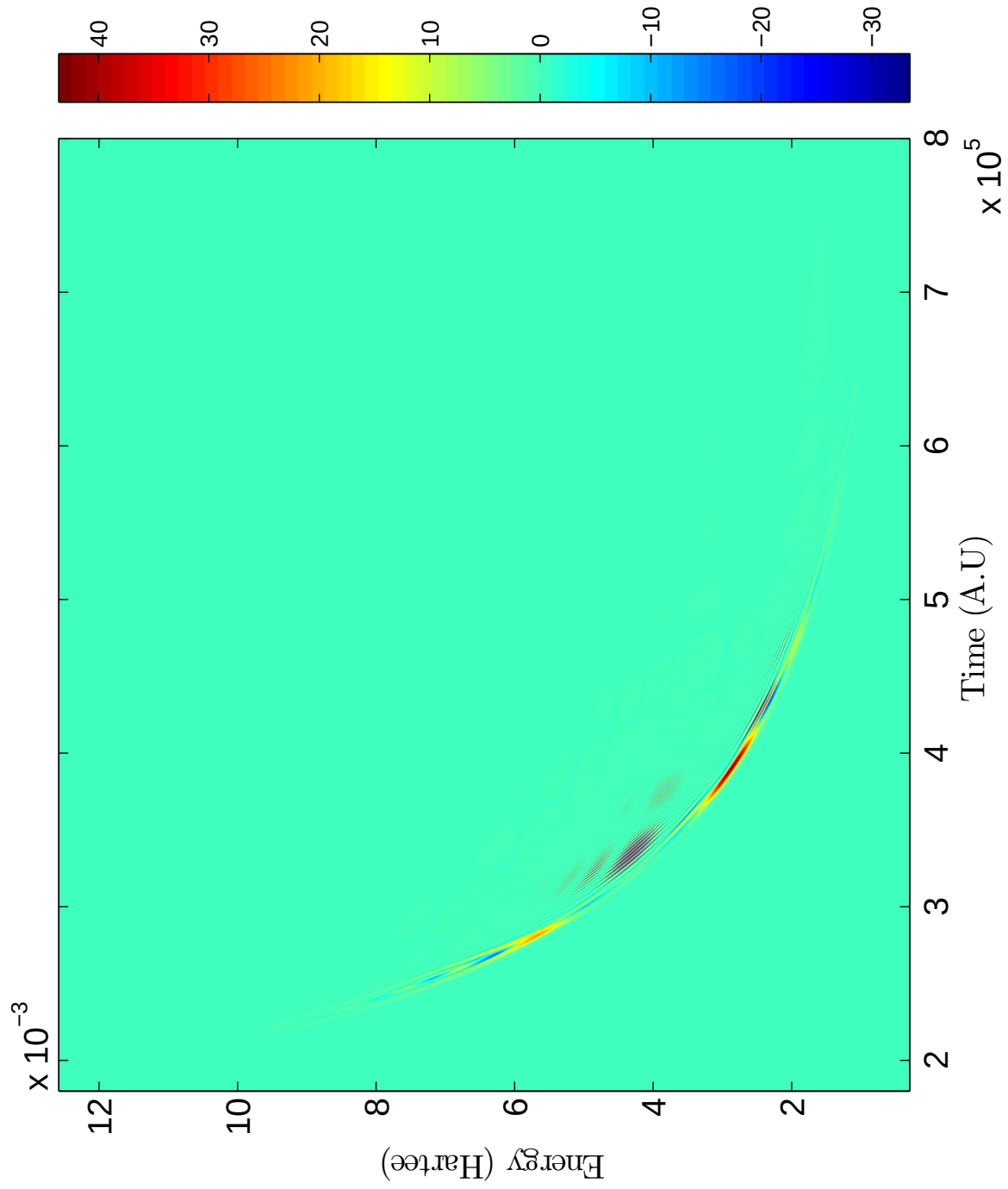


Figure 6.52: Scattering Wigner Distribution Function for K+Ne system with reactant Møller state in $|^{\frac{1}{2}}_{\frac{1}{2}}>$, product Møller state in $|^{\frac{3}{2}}_{\frac{1}{2}}>$, and $J = 35.5$

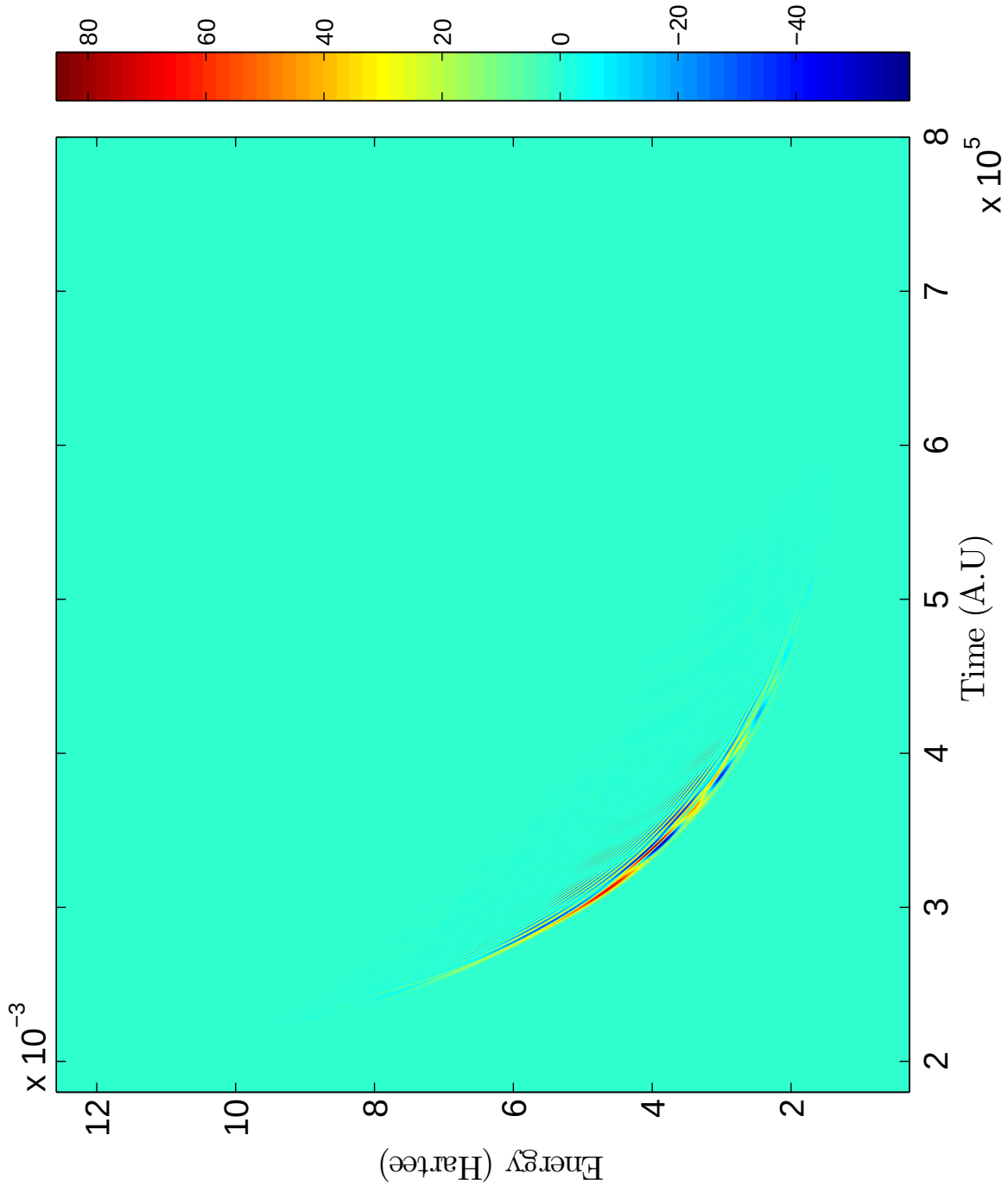


Figure 6.53: Scattering Wigner Distribution Function for K+Ne system with reactant Møller state in $|^{\frac{1}{2}}_{\frac{1}{2}}>$, product Møller state in $|^{\frac{3}{2}}_{\frac{1}{2}}>$, and $J = 60.5$

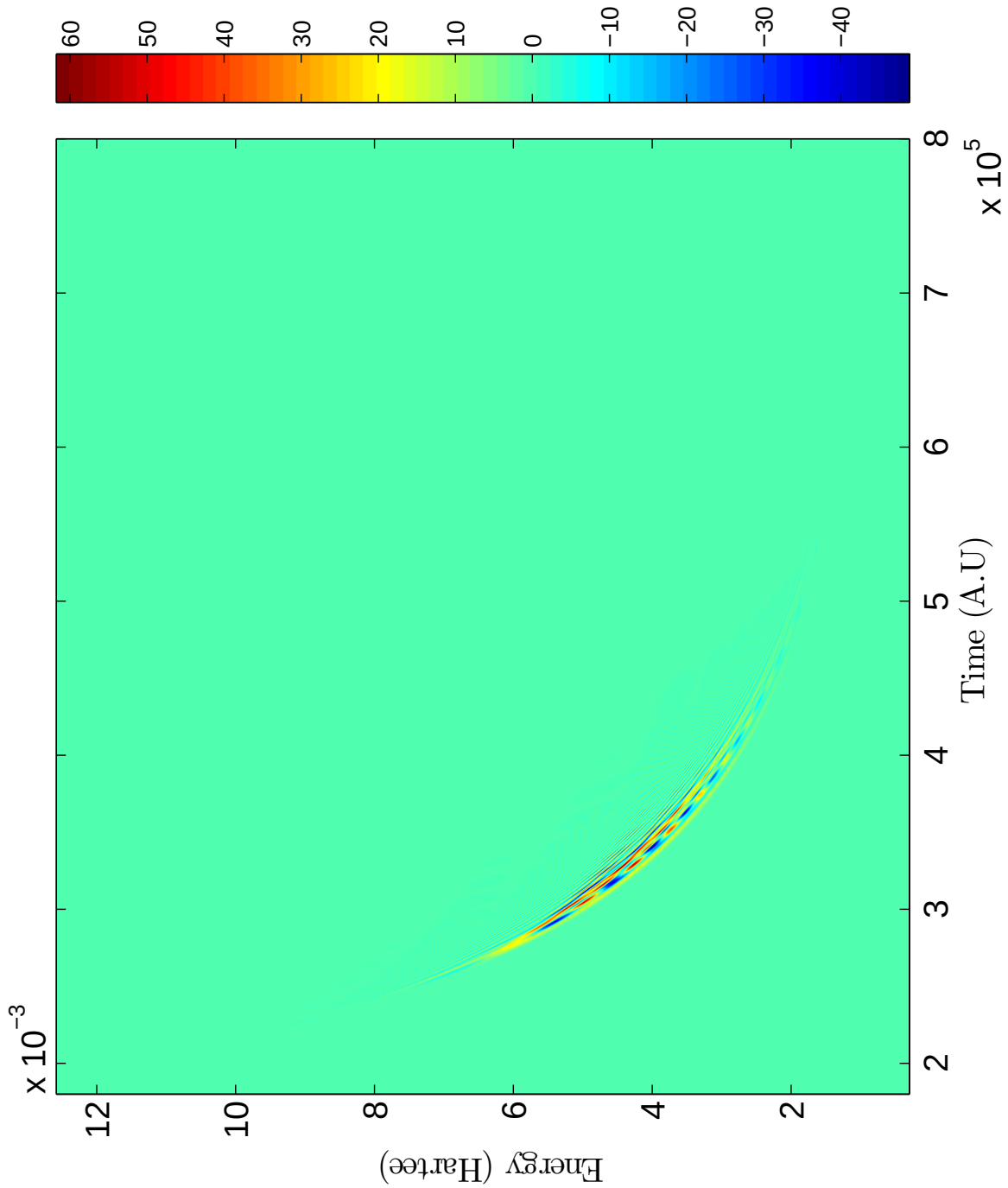


Figure 6.54: Scattering Wigner Distribution Function for K+Ne system with reactant Møller state in $|^{\frac{1}{2}}_{\frac{1}{2}}>$, product Møller state in $|^{\frac{3}{2}}_{\frac{1}{2}}>$, and $J = 85.5$

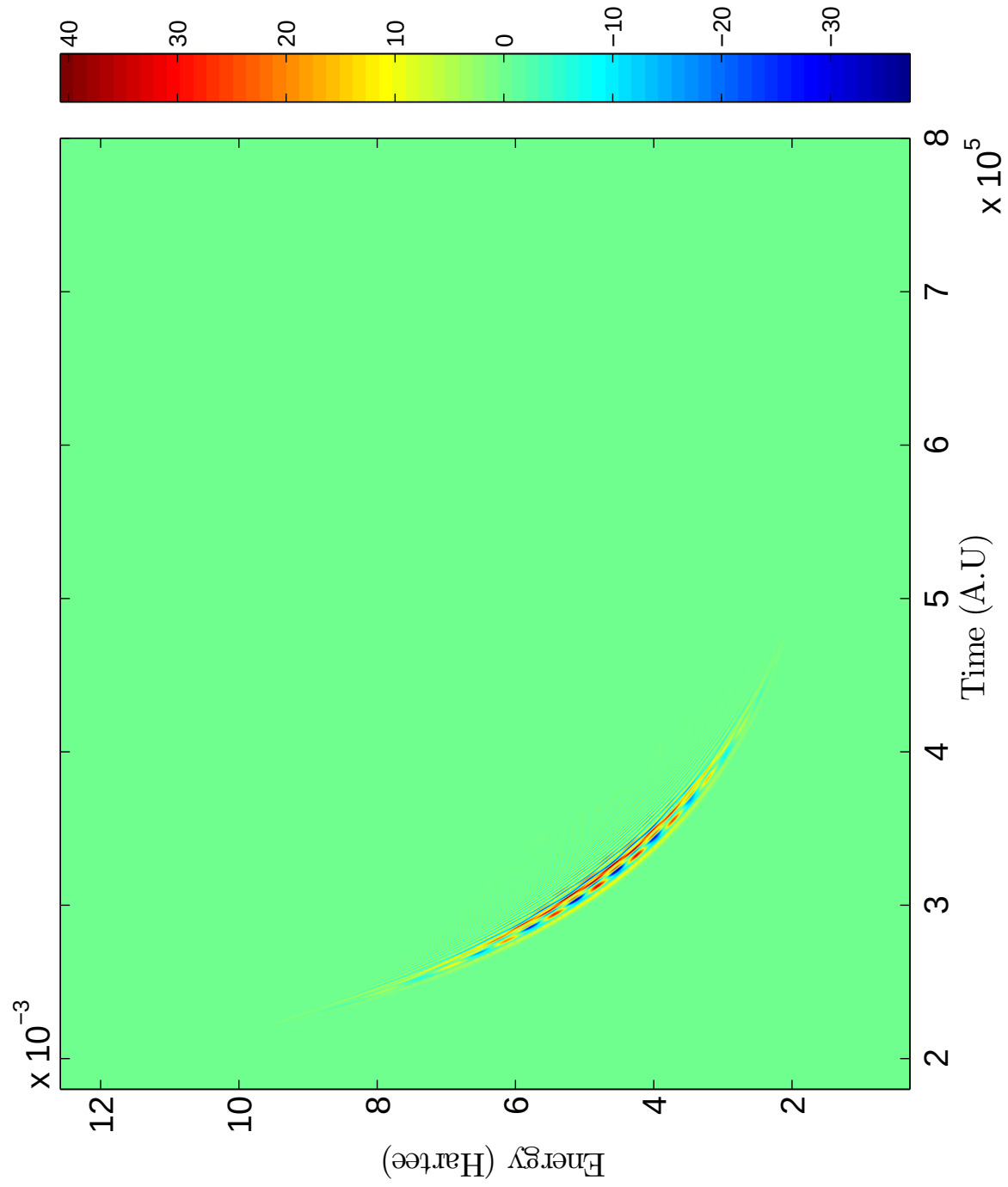


Figure 6.55: Scattering Wigner Distribution Function for K+Ne system with reactant Møller state in $|^{\frac{1}{2}}_{\frac{1}{2}}>$, product Møller state in $|^{\frac{3}{2}}_{\frac{1}{2}}>$, and $J = 115.5$

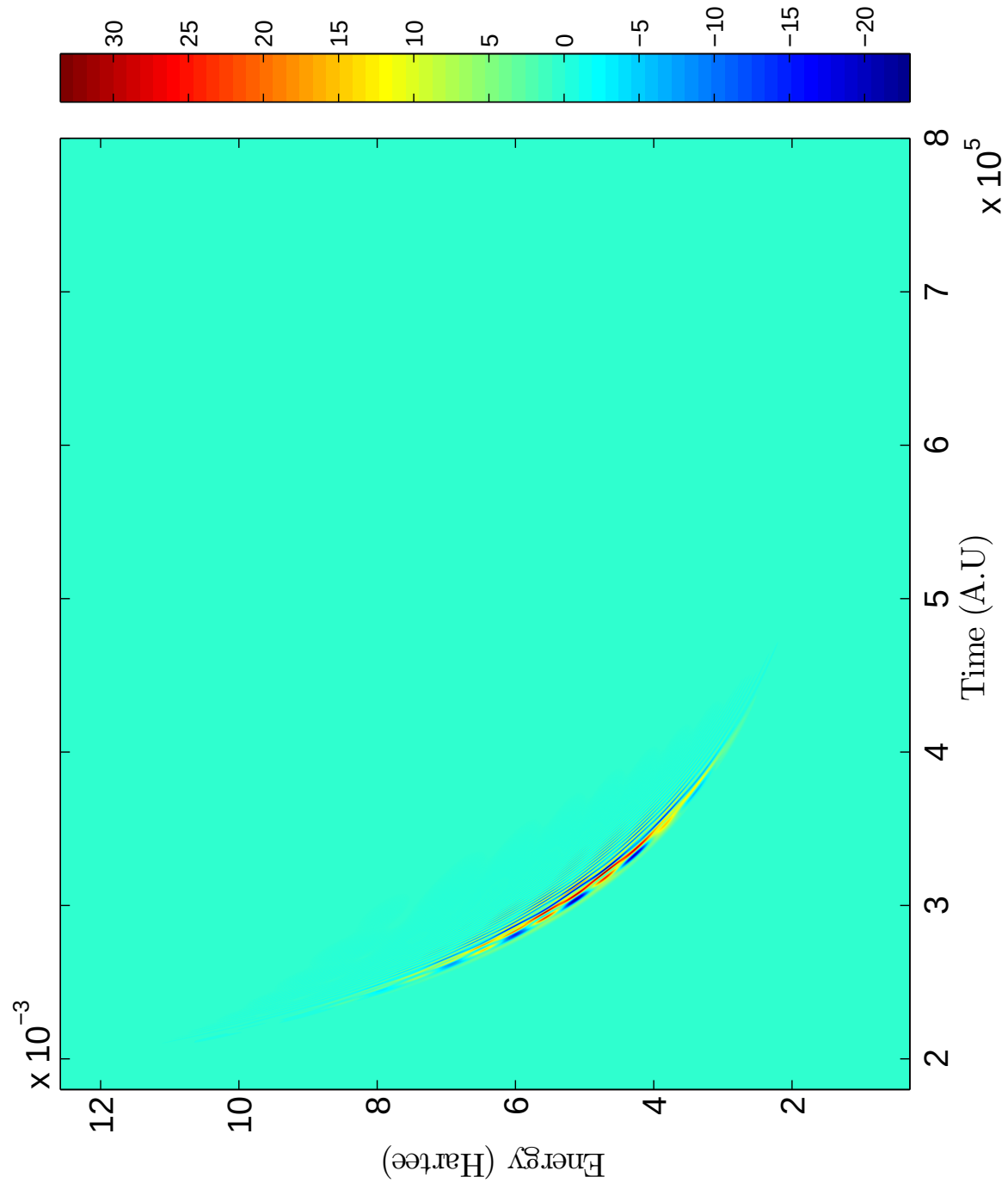


Figure 6.56: Scattering Wigner Distribution Function for K+Ne system with reactant Møller state in $|^{\frac{1}{2}}_{\frac{1}{2}}>$, product Møller state in $|^{\frac{3}{2}}_{\frac{1}{2}}>$, and $J = 145.5$

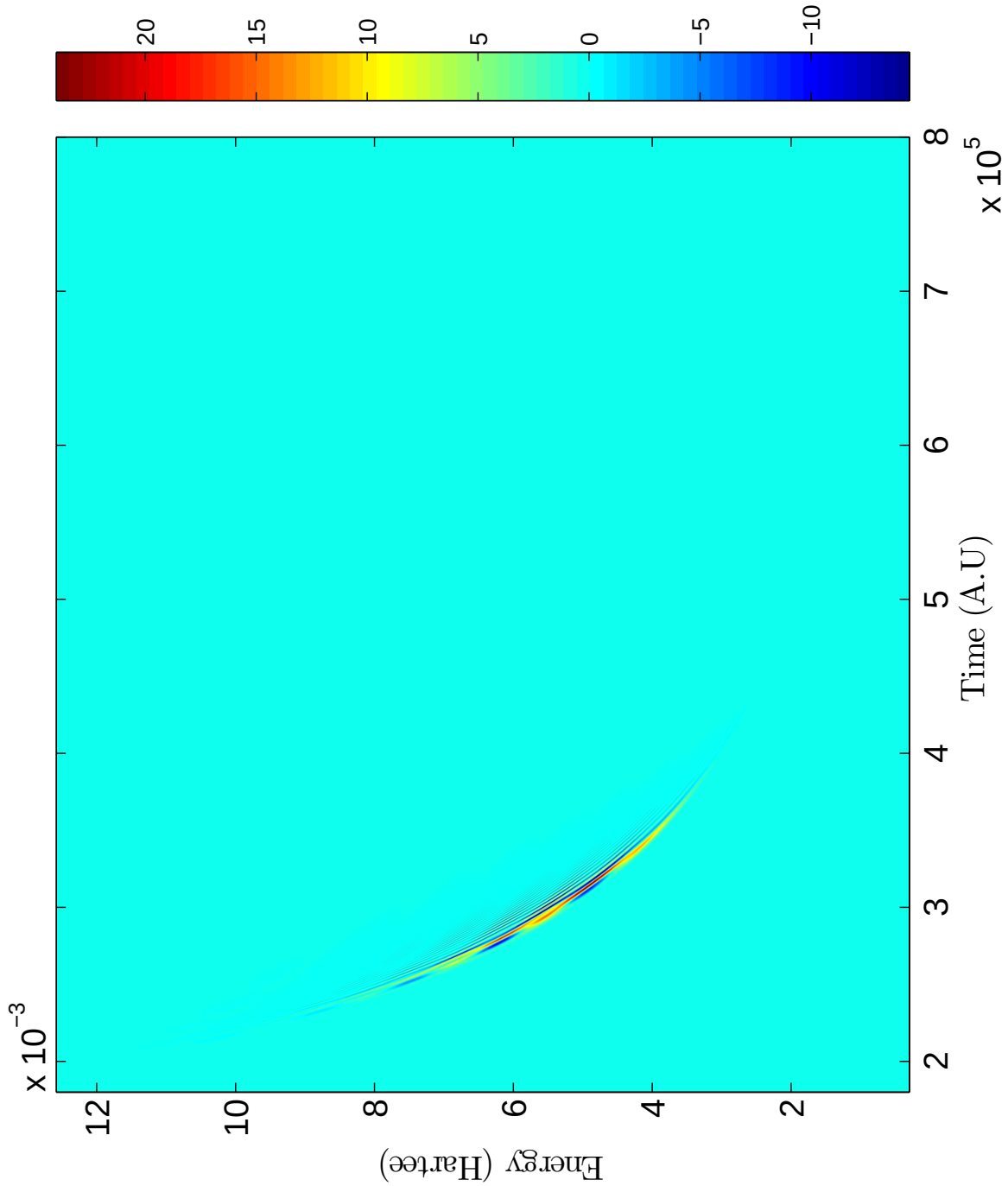


Figure 6.57: Scattering Wigner Distribution Function for K+Ne system with reactant Møller state in $|^{\frac{1}{2}}_{\frac{1}{2}}>$, product Møller state in $|^{\frac{3}{2}}_{\frac{1}{2}}>$, and $J = 170.5$

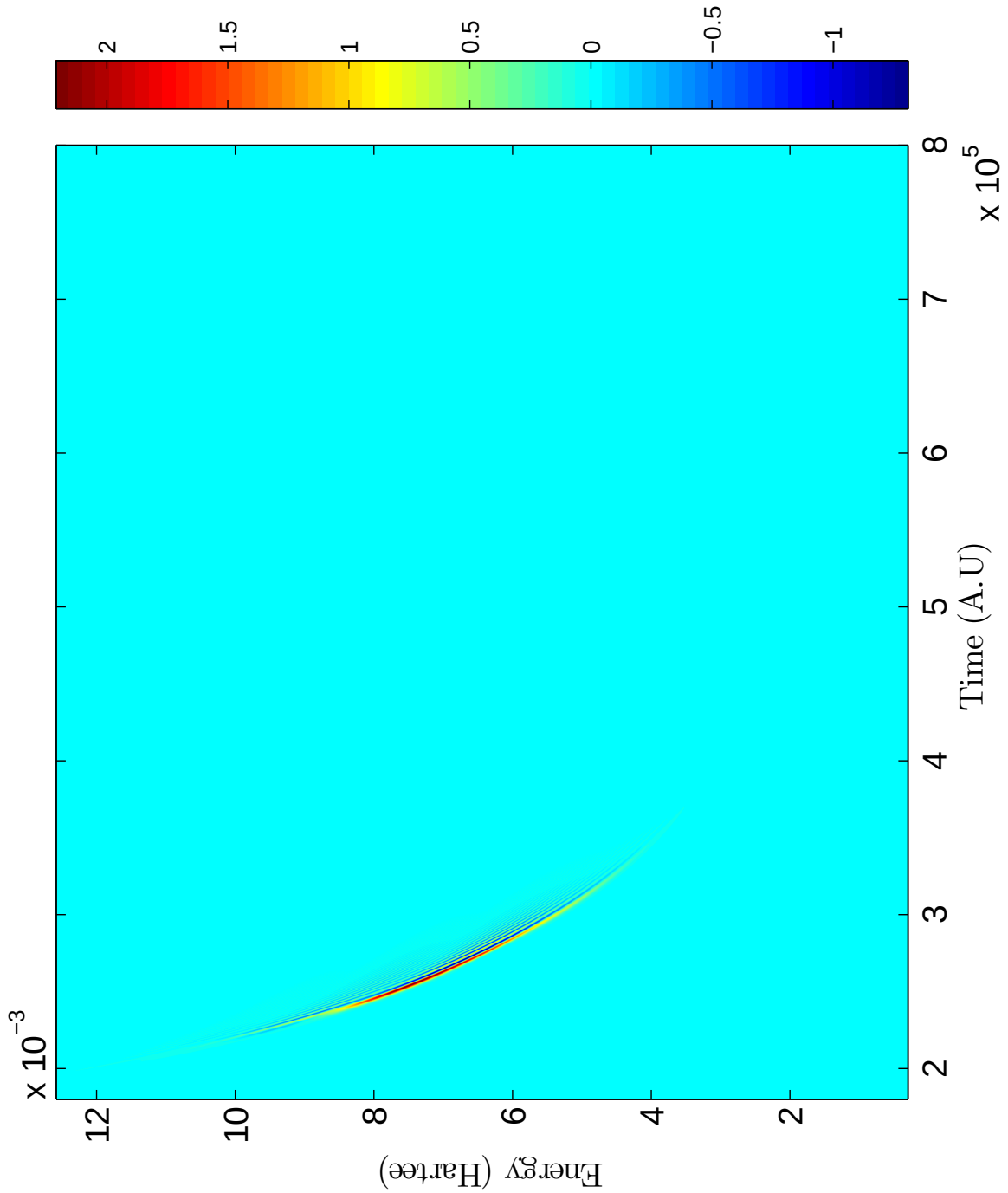


Figure 6.58: Scattering Wigner Distribution Function for K+Ne system with reactant Møller state in $|^{\frac{1}{2}}_{\frac{1}{2}}>$, product Møller state in $|^{\frac{3}{2}}_{\frac{1}{2}}>$, and $J = 225.5$

An interesting feature that occurs on the $|^{\frac{3}{2}}_{\frac{1}{2}}>$ surface in Fig. 6.49 is the appearance of a sharp dip in the maximum value of the scattering WDF at $J = 30.5$. This sharp dip is followed by one smaller dip at $J = 50.5$. These dips do not correspond to a peak on the $|^{\frac{3}{2}}_{\frac{3}{2}}>$ surface in Fig. 6.49; but, this dip does follow a similar occurrence in the change in the structure of the scattering WDF. As shown in Figs. 6.50-6.58, the number of oscillating peaks and valleys that appear in the middle of the structure of the scattering WDF increases as $J$ increases. When the effective potential begins to turn off the radial coupling, the number of oscillating peaks and valleys that appear in the middle of the scattering WDF begins to decrease. By $J = 225.5$, there are no more oscillating peaks and valleys just like at low values of $J$. After the dip found in Fig. 6.49, the number of oscillating peaks and valleys in the scattering WDF decrease. At $J = 35.5$ which is located in the dip, the scattering WDF seems to have split in half as shown in Fig. 6.52. Further investigation of the oscillating peaks and valleys in the scattering WDF reveals that not only do the number of oscillating peaks and valleys increase (decrease), the number of bands of oscillating peaks and valleys increase (decrease) perhaps suggesting multiple transfers of probability between surfaces.

### *6.2.4 Noble Gases.*

If the noble gas collision partner is changed while the alkali metal remains constant, the angular momentum matrix in Eq. 6.2 will be affected. The radial coupling will be unaffected because the noble gas does not contribute to spin-orbit potential. As the mass of the noble gas increases, the reduced mass increases, and the effective potential and the Coriolis coupling terms in the angular momentum matrix decrease in magnitude for a given value of $J$. As a result, higher $J$ values are needed in order to achieve the same Coriolis coupling and effective potential strengths seen in the lighter noble gas partners such as Helium. Figs. 6.59-6.70 demonstrate this concept. The amplitude of the scattering WDF for $K + He$ drops a couple orders of magnitude by the time $J = 105.5$ for the $|^{\frac{3}{2}}_{\frac{1}{2}}>$ and the

$|^{\frac{3}{2}}_{\frac{3}{2}}>$ surface if the reactant Møller state starts on the $|^{\frac{1}{2}}_{\frac{1}{2}}>$ surface; however, the amplitude of the scattering WDF for $K + Ar$ is on the same order of magnitude for the product Møller state on the $|^{\frac{3}{2}}_{\frac{1}{2}}>$ surface for $J = 105.5$ as compared to the scattering WDF amplitude for $J = 1.5$ The amplitude of the scattering WDF for the product Møller state on the $|^{\frac{3}{2}}_{\frac{3}{2}}>$ surface peaked at around $J = 105.5$ as compared to the amplitude of the scattering WDF at $J = 1.5$. In fact, the amplitude of the scattering WDF for these surfaces for the $K + Ar$ collision drops a couple orders of magnitude when $J = 275.5$ which is approximately 3 times the total angular momentum value than the $K + He$ system.

Figs. 6.71-6.73 are the plots of the maximum value of the scattering WDF as a function of $J$ for the $K + He$, $K + Ne$, and $K + Ar$ systems respectively when the reactant Møller state starts on the $|^{\frac{1}{2}}_{\frac{1}{2}}>$ surface. As the noble gas increases in mass, the difference in the order of magnitudes of the $|^{\frac{3}{2}}_{\frac{1}{2}}>$ and $|^{\frac{3}{2}}_{\frac{1}{2}}>$ surfaces increases. For example, for $K + He$ the maximum value of the scattering WDF for the $|^{\frac{3}{2}}_{\frac{3}{2}}>$ is comparable to the maximum value of the $|^{\frac{3}{2}}_{\frac{3}{2}}>$ WDF; however, for $K + Ne$ and $K + Ar$ this is never true. The maximum value of the scattering WDF for the $|^{\frac{3}{2}}_{\frac{3}{2}}>$ surface never reaches the same order of magnitude as the $|^{\frac{3}{2}}_{\frac{1}{2}}>$ surface for $K + Ne$. The difference between the relative order of magnitudes between these two surfaces is slightly greater for the $K + Ar$ system. The figures also reveal that the dip found in Fig. 6.49 for the study of the peak amplitude of the scattering WDF as a function of $J$ increases in depth as the noble gas becomes heavier.

When the reactant Møller state starts on the $|^{\frac{3}{2}}_{\frac{1}{2}}>$ or the $|^{\frac{3}{2}}_{\frac{3}{2}}>$ surfaces for these noble gas collisions, radial coupling is turned off at high values of $J$ due to the effective potential as shown in Figs. 6.74-6.89. The amplitude of the scattering WDF for the product state on the $|^{\frac{1}{2}}_{\frac{1}{2}}>$ surface decays to zero, and there is no probability transfer to the $|^{\frac{1}{2}}_{\frac{1}{2}}>$ state. As the mass of the noble gas increases the $J$ value at which radial coupling is turned off changes. This implies that the amplitude of the scattering WDF for this surface remains significant for larger values of $J$.

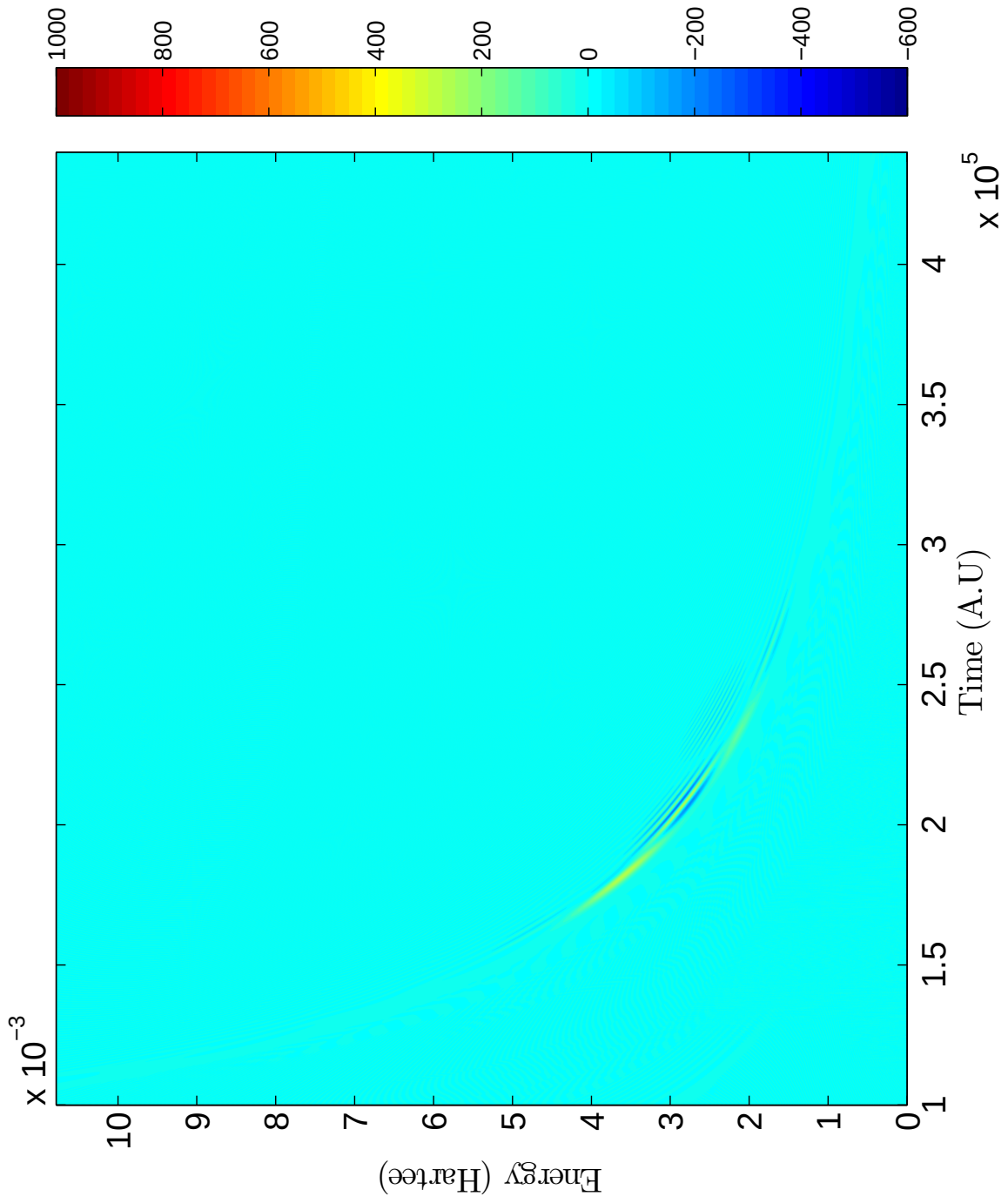


Figure 6.59: Scattering Wigner Distribution Function for K+He system with reactant Møller state in $|^{\frac{1}{2}}_{\frac{1}{2}}>$, product Møller state in $|^{\frac{3}{2}}_{\frac{1}{2}}>$, and $J = 1.5$

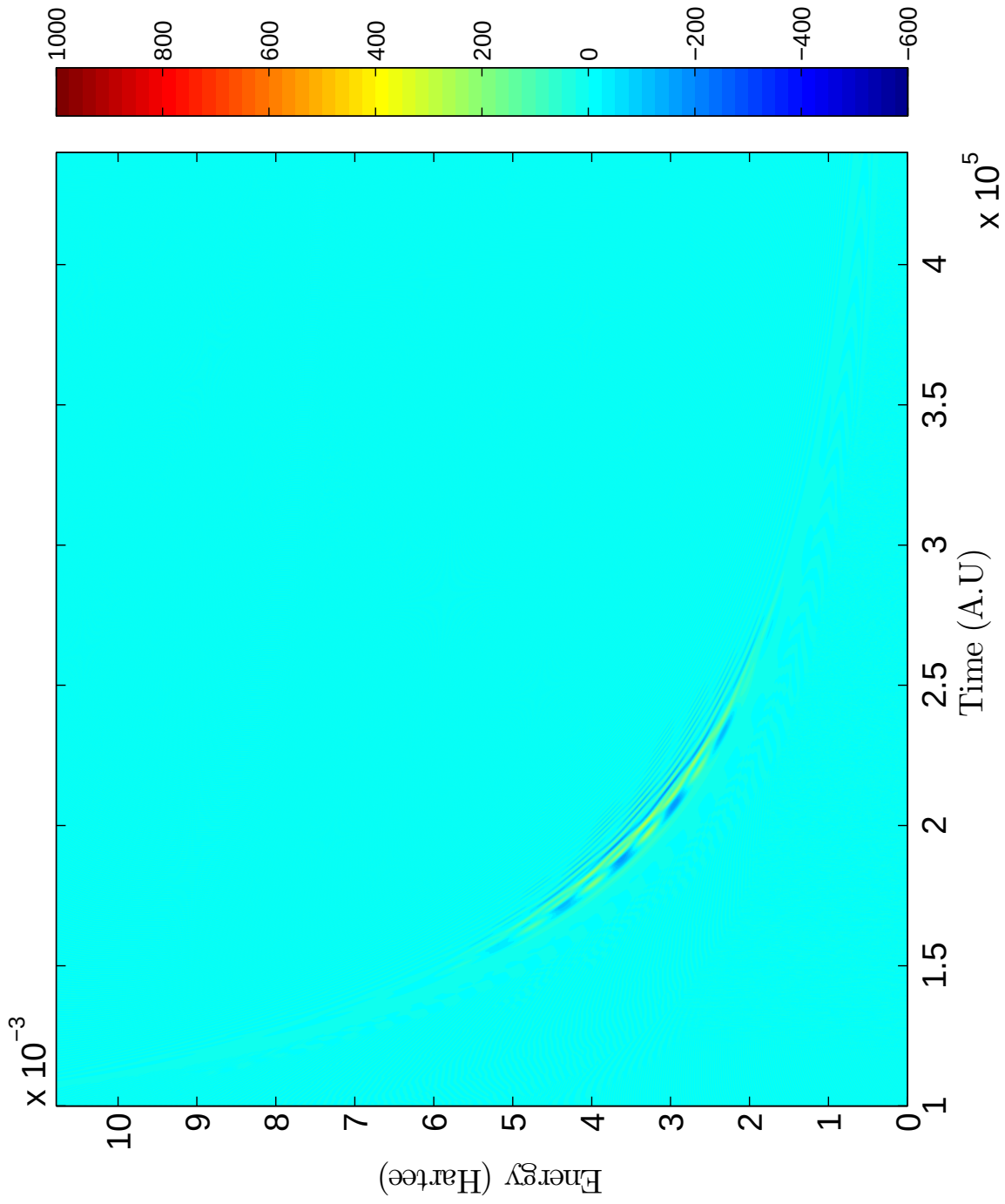


Figure 6.60: Scattering Wigner Distribution Function for K+He system with reactant Møller state in $|^{\frac{1}{2}}_{\frac{1}{2}}>$, product Møller state in $|^{\frac{3}{2}}_{\frac{1}{2}}>$, and $J = 50.5$

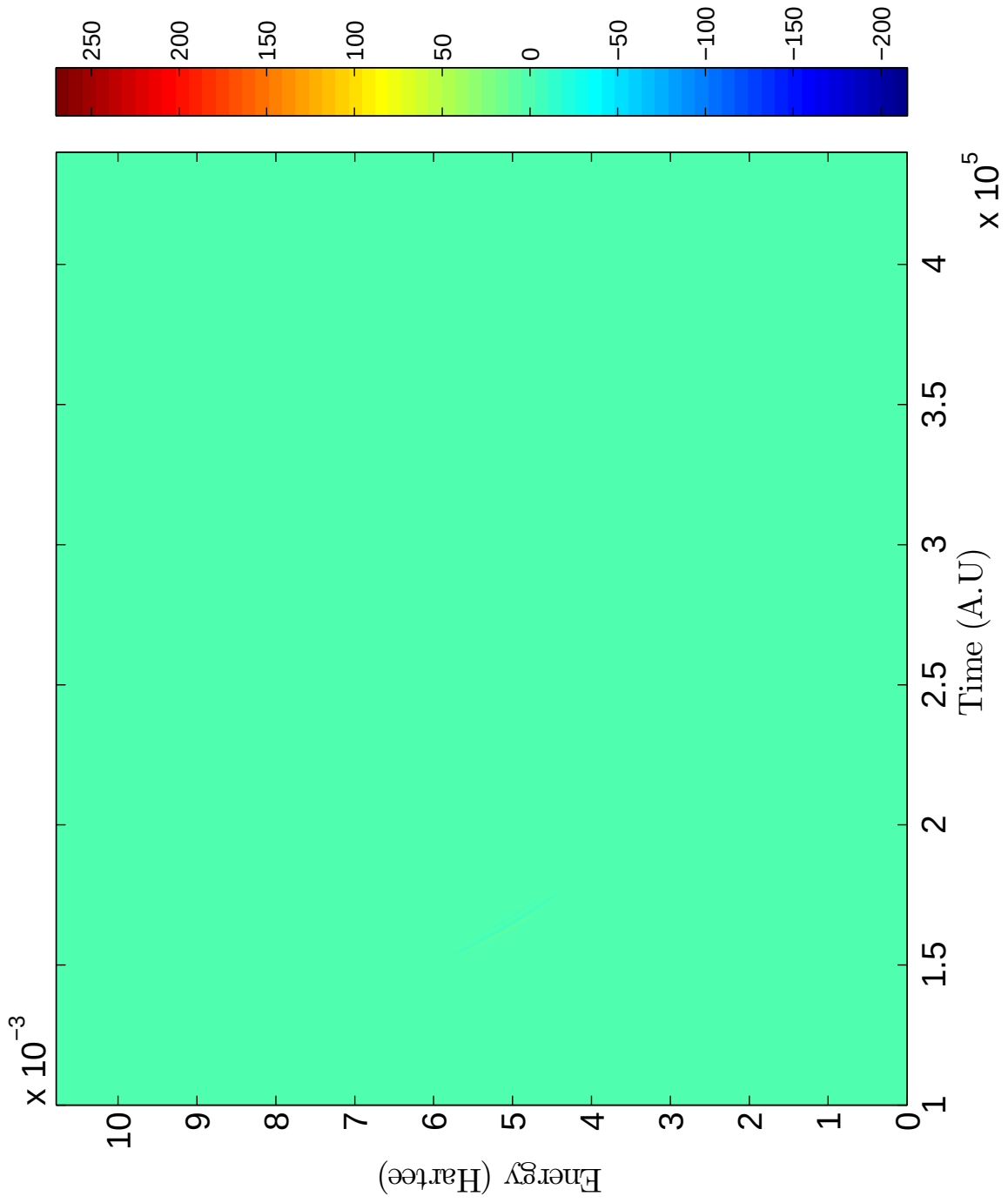


Figure 6.61: Scattering Wigner Distribution Function for K+He system with reactant Møller state in $|^{\frac{1}{2}}_{\frac{1}{2}}>$, product Møller state in $|^{\frac{3}{2}}_{\frac{1}{2}}>$, and $J = 100.5$

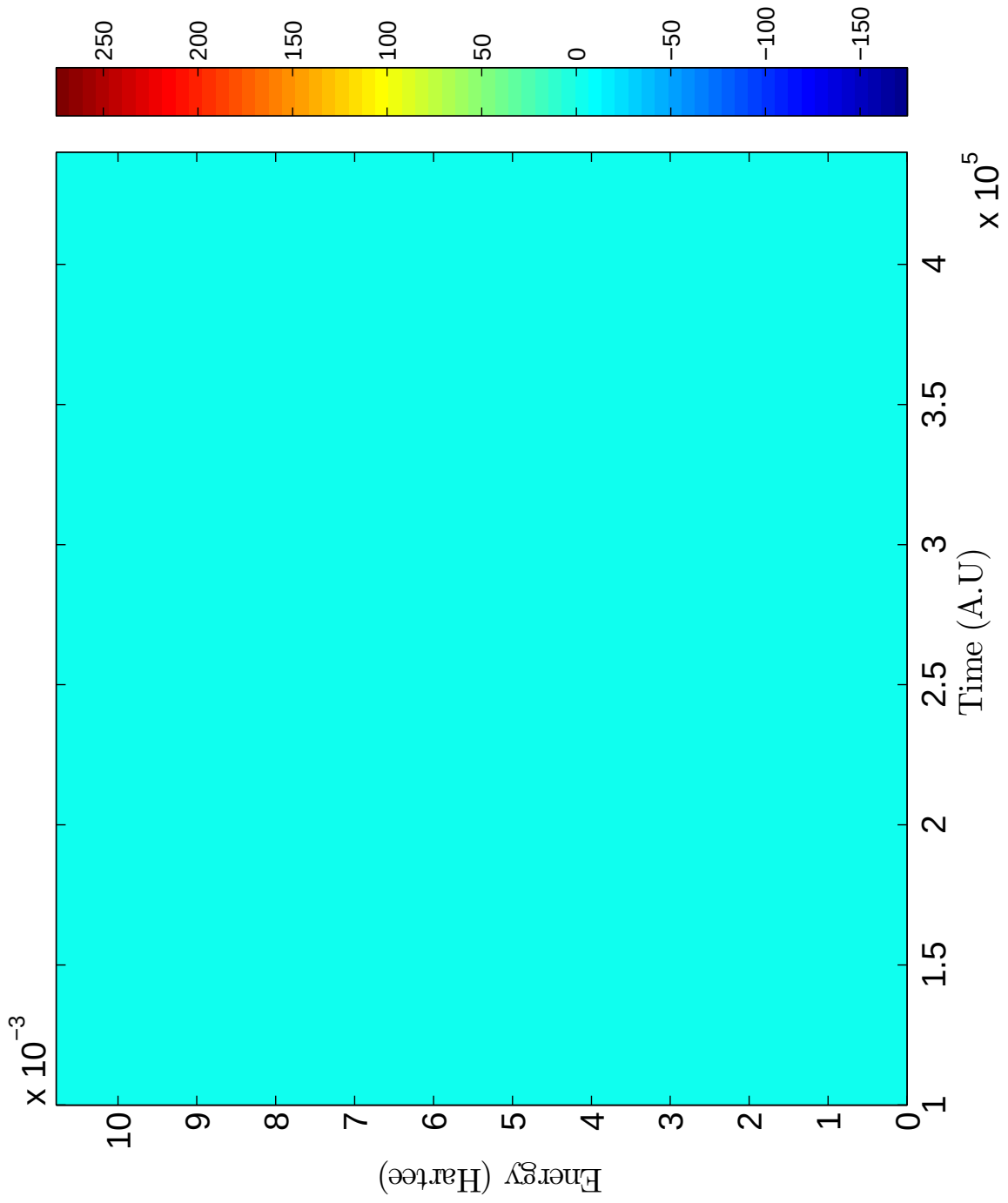


Figure 6.62: Scattering Wigner Distribution Function for K+He system with reactant Møller state in $|^{\frac{1}{2}}_{\frac{1}{2}}>$, product Møller state in $|^{\frac{3}{2}}_{\frac{3}{2}}>$, and $J = 1.5$

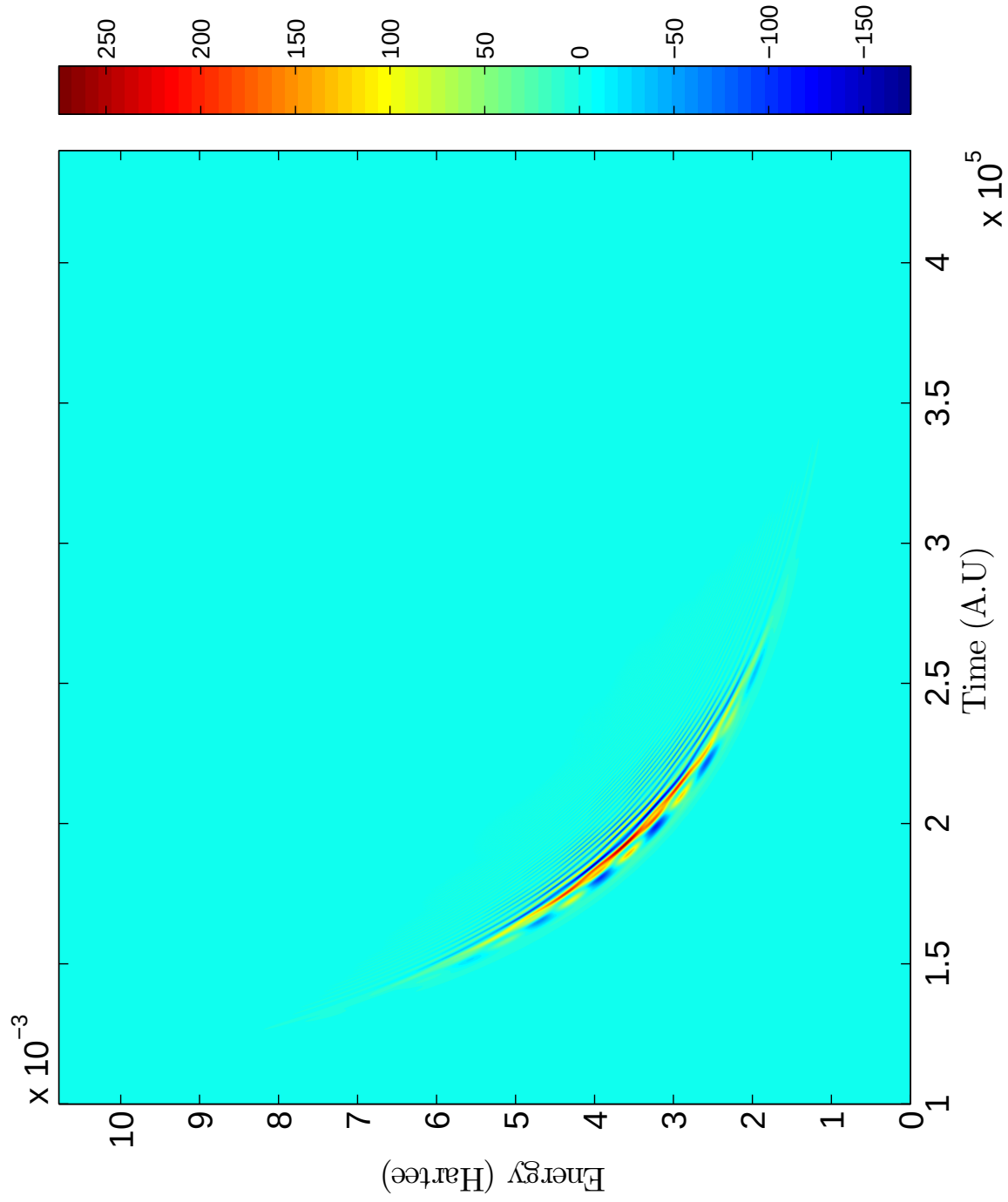


Figure 6.63: Scattering Wigner Distribution Function for K+He system with reactant Møller state in $|^{\frac{1}{2}}_{\frac{1}{2}}>$, product Møller state in $|^{\frac{3}{2}}_{\frac{3}{2}}>$, and $J = 50.5$

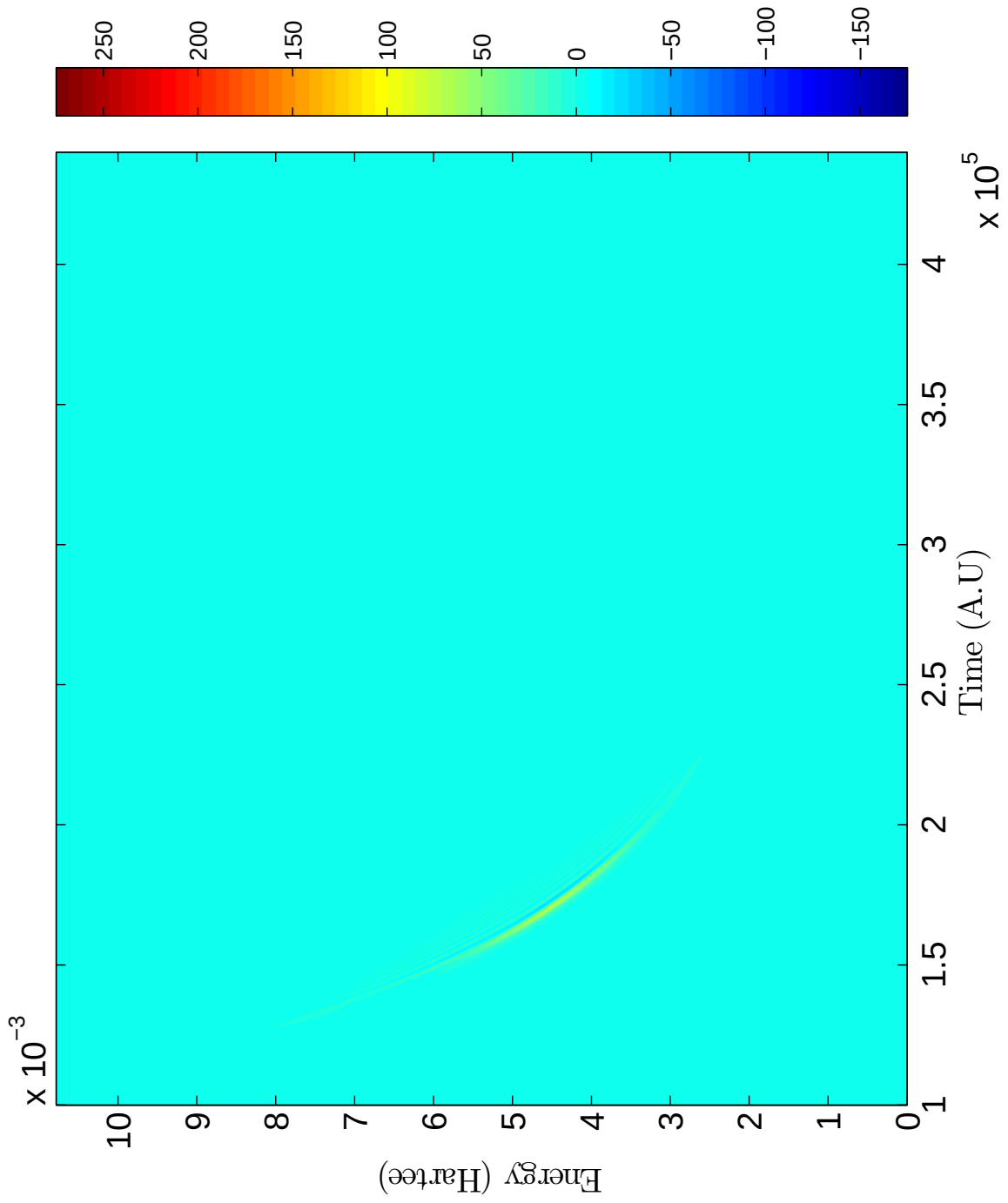


Figure 6.64: Scattering Wigner Distribution Function for K+He system with reactant Møller state in $|^{\frac{1}{2}}_{\frac{1}{2}}>$, product Møller state in $|^{\frac{3}{2}}_{\frac{3}{2}}>$, and $J = 100.5$

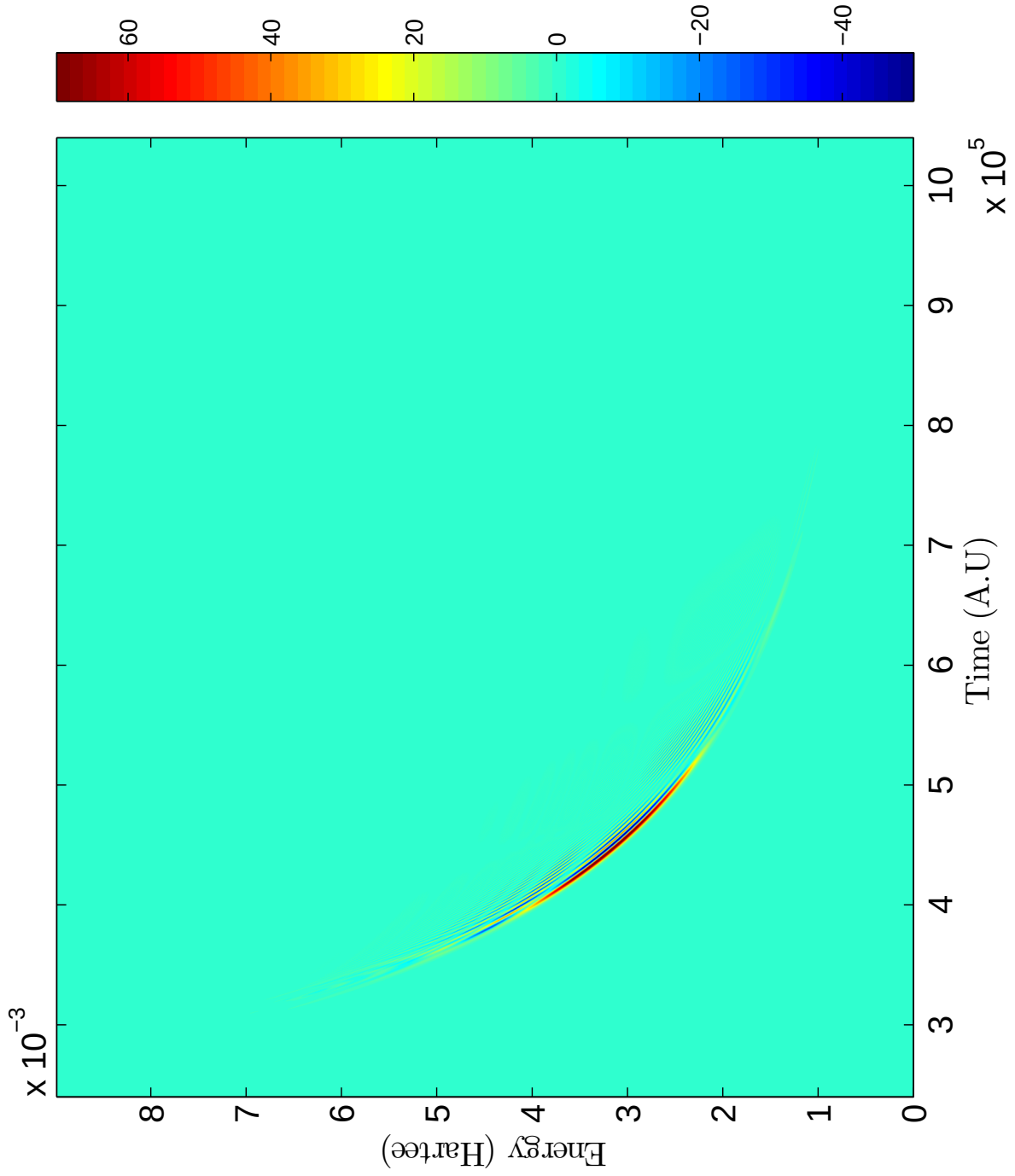


Figure 6.65: Scattering Wigner Distribution Function for K+Ar system with reactant Møller state in $|^{\frac{1}{2}}_{\frac{1}{2}}>$, product Møller state in $|^{\frac{3}{2}}_{\frac{1}{2}}>$, and $J = 1.5$

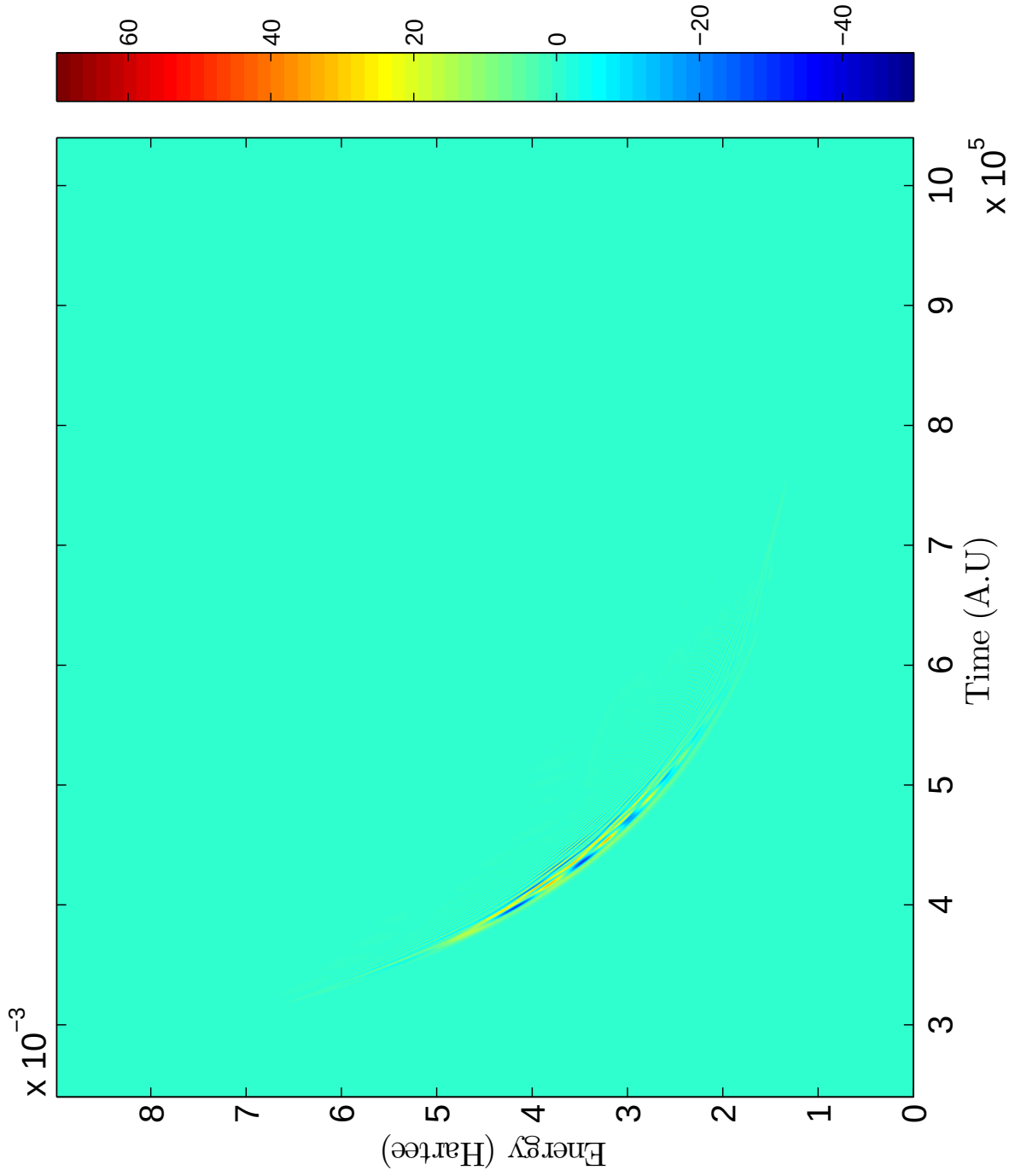


Figure 6.66: Scattering Wigner Distribution Function for K+Ar system with reactant Møller state in $|^{\frac{1}{2}}_{\frac{1}{2}}>$, product Møller state in $|^{\frac{3}{2}}_{\frac{1}{2}}>$, and $J = 100.5$

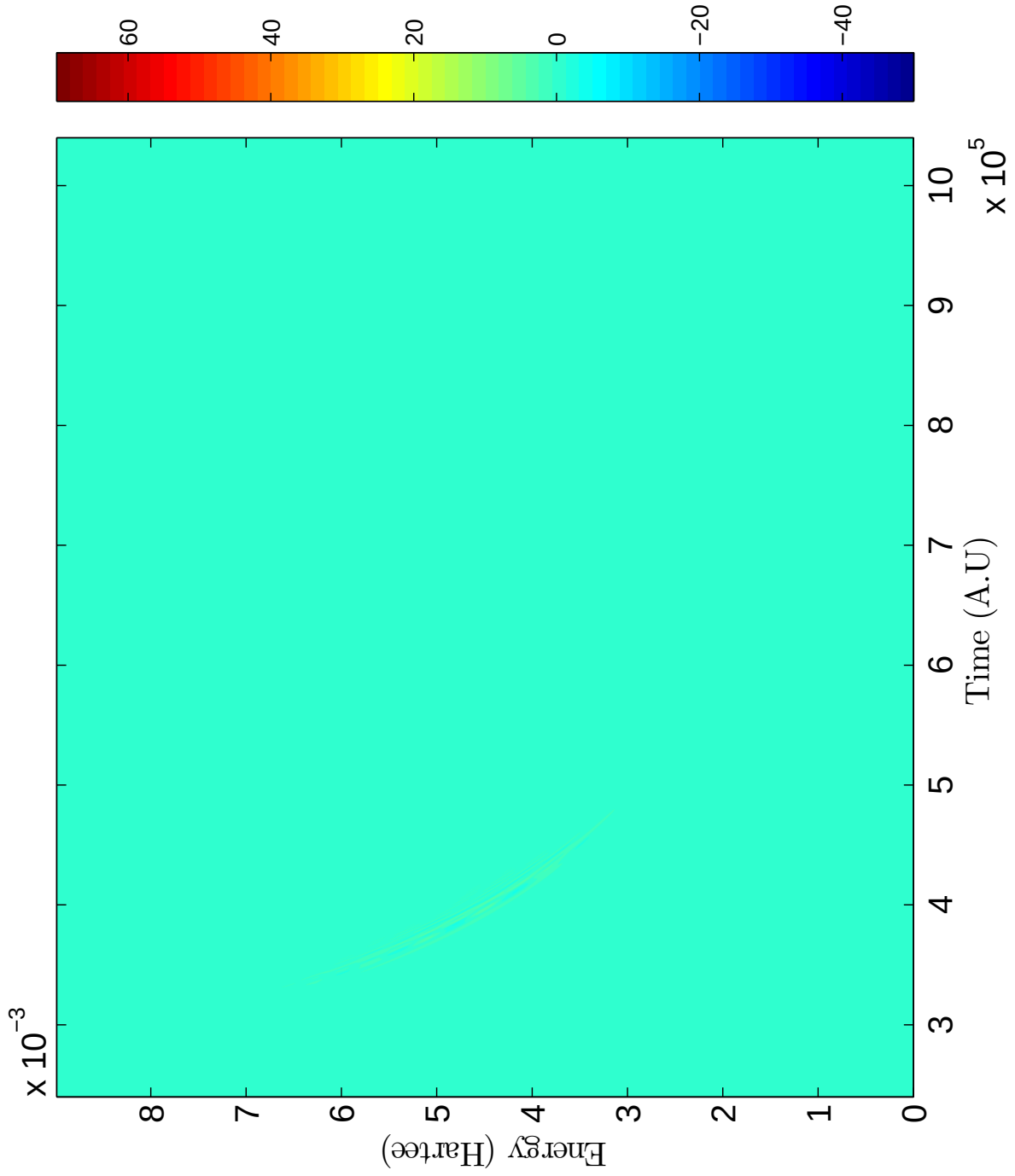


Figure 6.67: Scattering Wigner Distribution Function for K+Ar system with reactant Møller state in $|^{\frac{1}{2}}_{\frac{1}{2}}>$, product Møller state in $|^{\frac{3}{2}}_{\frac{1}{2}}>$, and $J = 200.5$

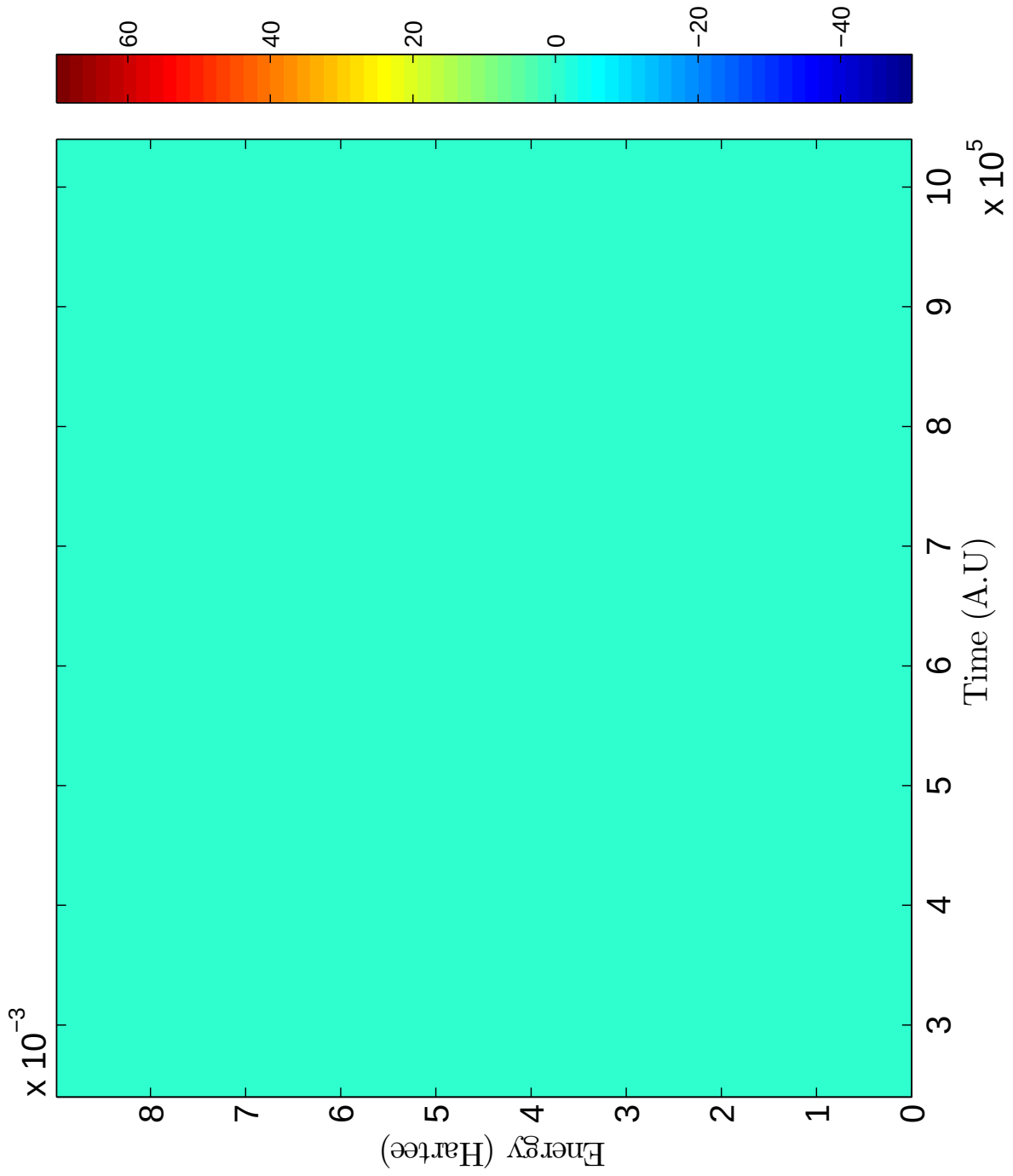


Figure 6.68: Scattering Wigner Distribution Function for K+Ar system with reactant Møller state in $|^{\frac{1}{2}}_{\frac{1}{2}}>$, product Møller state in $|^{\frac{3}{2}}_{\frac{3}{2}}>$, and $J = 1.5$

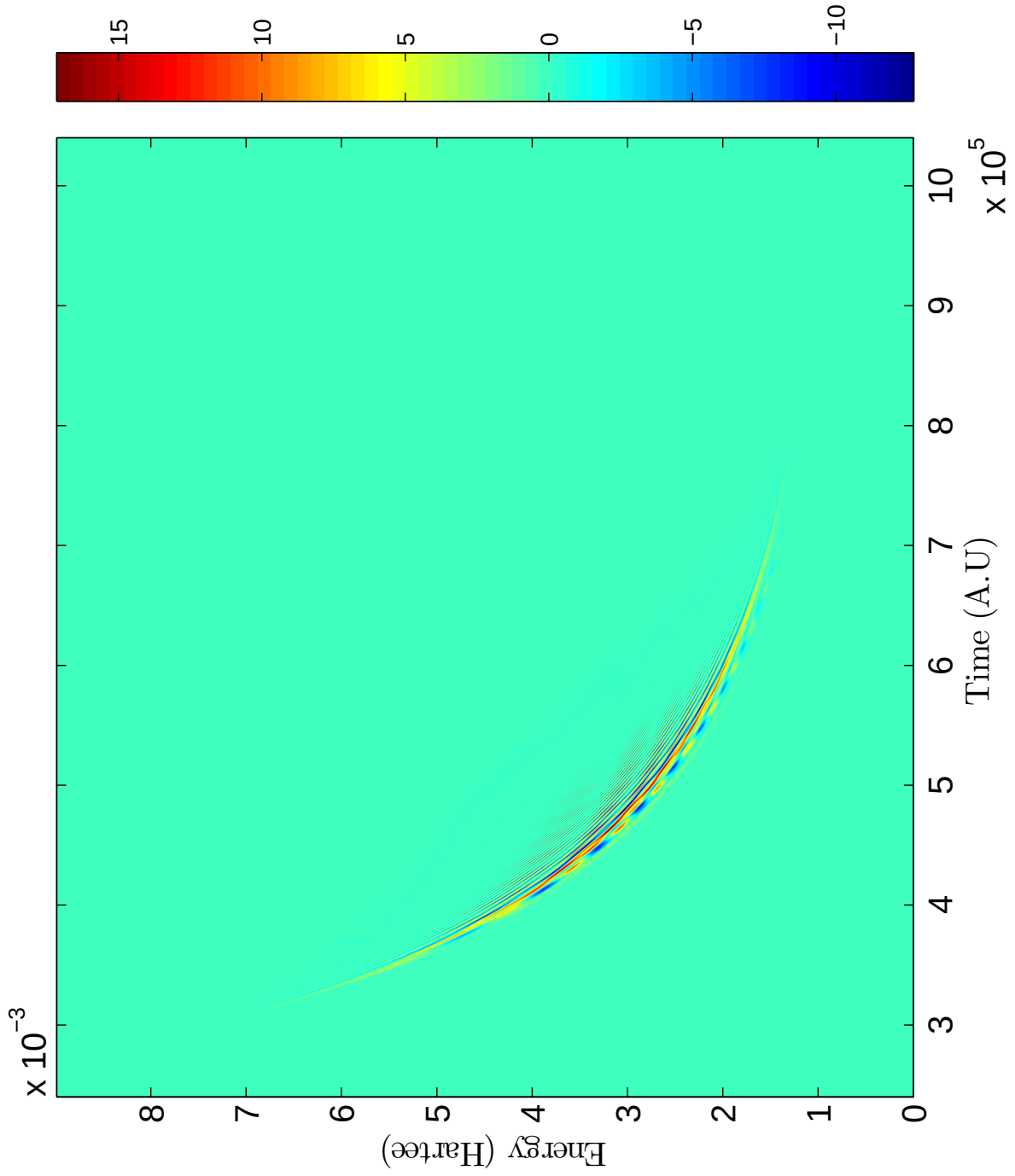


Figure 6.69: Scattering Wigner Distribution Function for K+Ar system with reactant Møller state in $|^{\frac{1}{2}}_{\frac{1}{2}}>$, product Møller state in $|^{\frac{3}{2}}_{\frac{3}{2}}>$, and $J = 100.5$

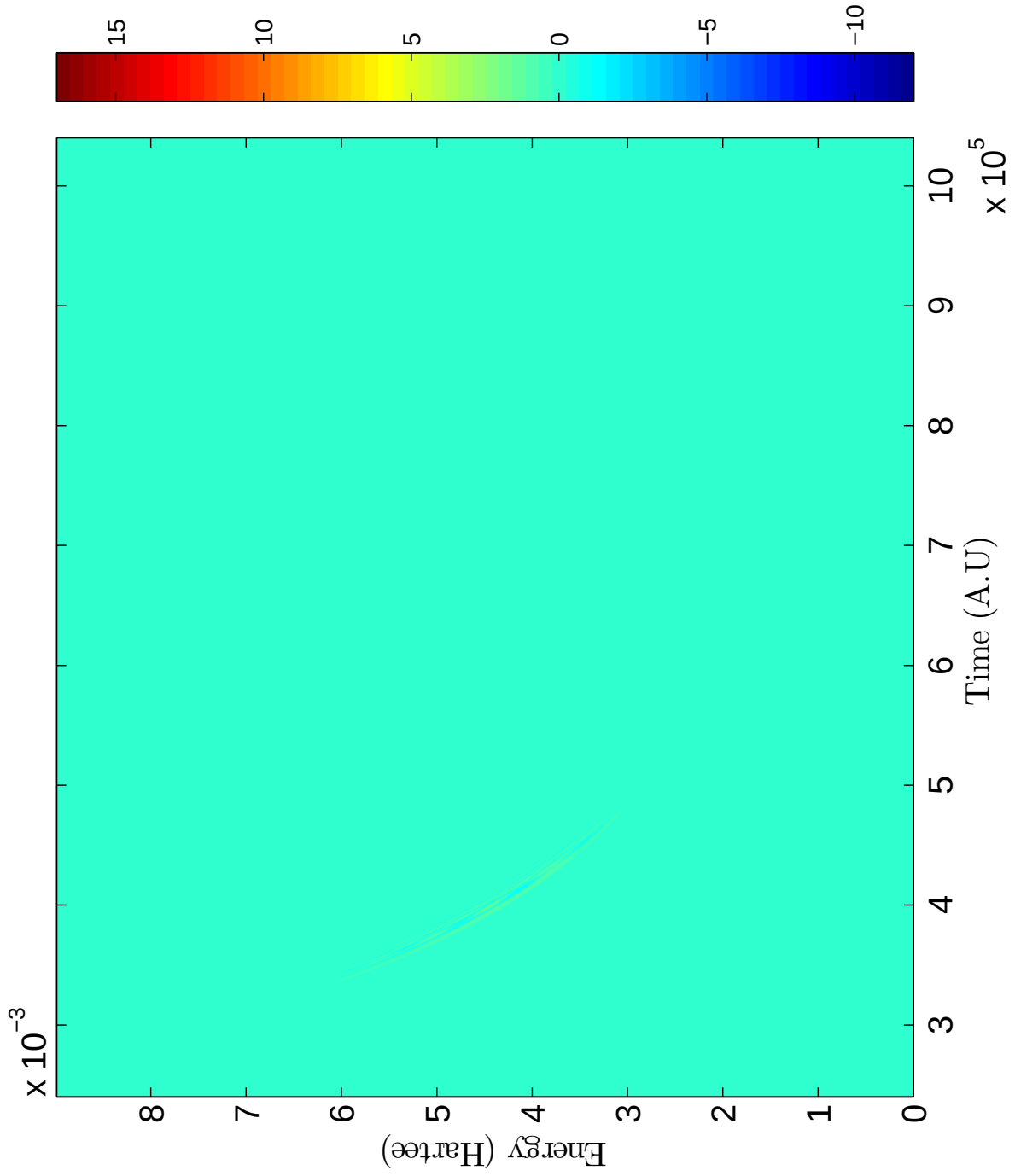


Figure 6.70: Scattering Wigner Distribution Function for K+Ar system with reactant Møller state in $|^{\frac{1}{2}}_{\frac{1}{2}}>$, product Møller state in $|^{\frac{3}{2}}_{\frac{3}{2}}>$, and $J = 200.5$

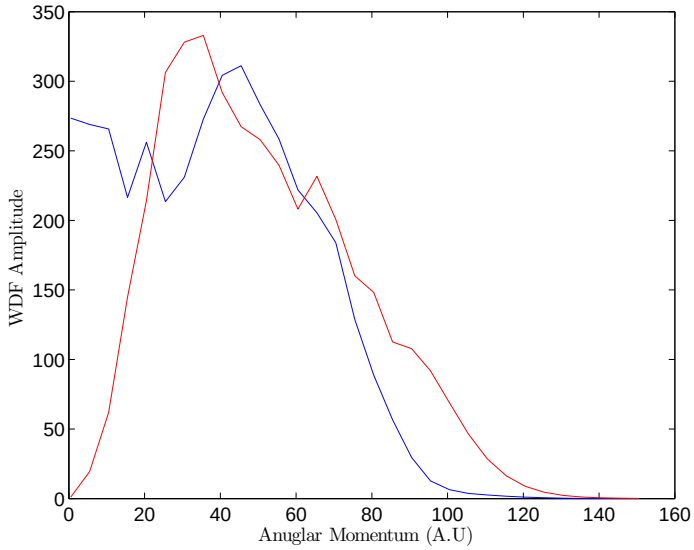


Figure 6.71: The maximum value of the scattering Wigner Distribution Function for K+He system with reactant Møller state in $|^{\frac{1}{2}}_{\frac{1}{2}}>$, product Møller state in $|^{\frac{3}{2}}_{\frac{1}{2}}>$ (Blue), and product Møller state $|^{\frac{3}{2}}_{\frac{3}{2}}>$ (Red). The maximum value was sampled for every $\Delta J = 5$ ranging from $J = 5.5$ to $J = 250.5$ (including $J = 1.5$).

If the reactant Møller state starts on the $|^{\frac{3}{2}}_{\frac{3}{2}}>$ surface, there has to be Coriolis coupling to the $|^{\frac{3}{2}}_{\frac{1}{2}}>$ surface before there can be radial coupling to the $|^{\frac{1}{2}}_{\frac{1}{2}}>$ surface. By the $J$ value that Coriolis coupling is high enough to allow for significant probability to be radially coupled to the $|^{\frac{1}{2}}_{\frac{1}{2}}>$, the effective potential begins to reduce the amount of probability going to the $|^{\frac{1}{2}}_{\frac{1}{2}}>$. As shown in Figs. 6.87-6.89, the amplitude of the scattering WDF for the product Møller state on the $|^{\frac{1}{2}}_{\frac{1}{2}}>$ surface remains lower for a wider range of $J$ values. On the other hand, if the reactant Møller state starts on the $|^{\frac{3}{2}}_{\frac{1}{2}}>$ surface, probability can be transferred to the $|^{\frac{1}{2}}_{\frac{1}{2}}>$ via radial coupling at low values of $J$. Although the effective potential eventually causes the probability transfer to the $|^{\frac{1}{2}}_{\frac{1}{2}}>$ to turn off, the amount of probability going to the $|^{\frac{1}{2}}_{\frac{1}{2}}>$ surface is significant compared to the total probability. For this reason, approximately half the states pumped into the $^2P_{\frac{3}{2}}$ do not contribute to the relaxation of alkali metals to the $^2P_{\frac{1}{2}}$ where lasing occurs.

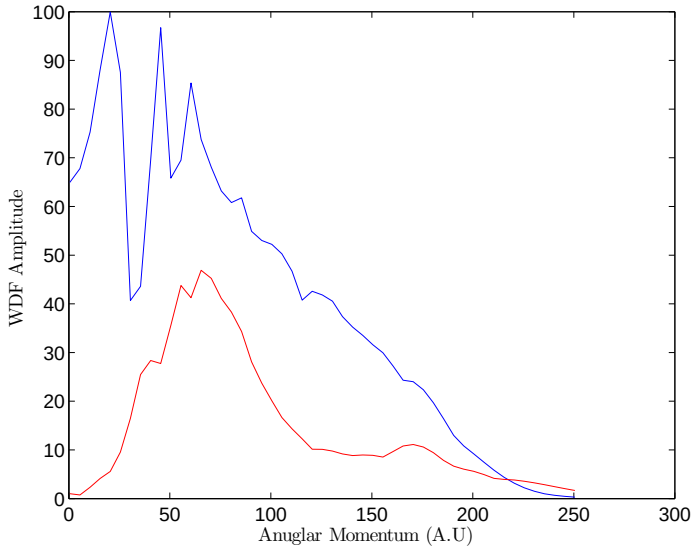


Figure 6.72: The maximum value of the scattering Wigner Distribution Function for K+Ne system with reactant Møller state in $|^{\frac{1}{2}}_{\frac{1}{2}}>$, product Møller state in $|^{\frac{3}{2}}_{\frac{1}{2}}>$ (Blue), and product Møller state $|^{\frac{3}{2}}_{\frac{3}{2}}>$ (Red). The maximum value was sampled for every $\Delta J = 5$ ranging from $J = 5.5$ to $J = 250.5$ (including $J = 1.5$). Note that this is the same plot shown in Fig. 6.49. This plot is shown again as a matter of convenience for the reader.

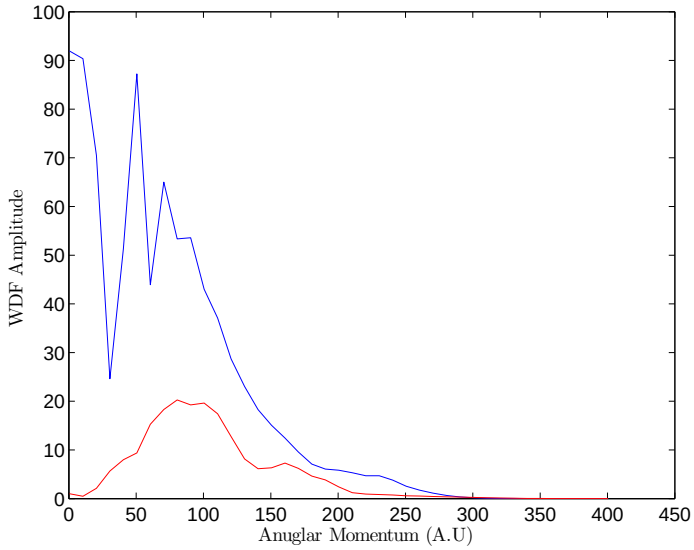


Figure 6.73: The maximum value of the scattering Wigner Distribution Function for K+Ar system with reactant Møller state in $|^{\frac{1}{2}}_{\frac{1}{2}}>$, product Møller state in $|^{\frac{3}{2}}_{\frac{1}{2}}>$ (Blue), and product Møller state $|^{\frac{3}{2}}_{\frac{3}{2}}>$ (Red). The maximum value was sampled for every $\Delta J = 5$ ranging from $J = 5.5$ to $J = 250.5$ (including $J = 1.5$).

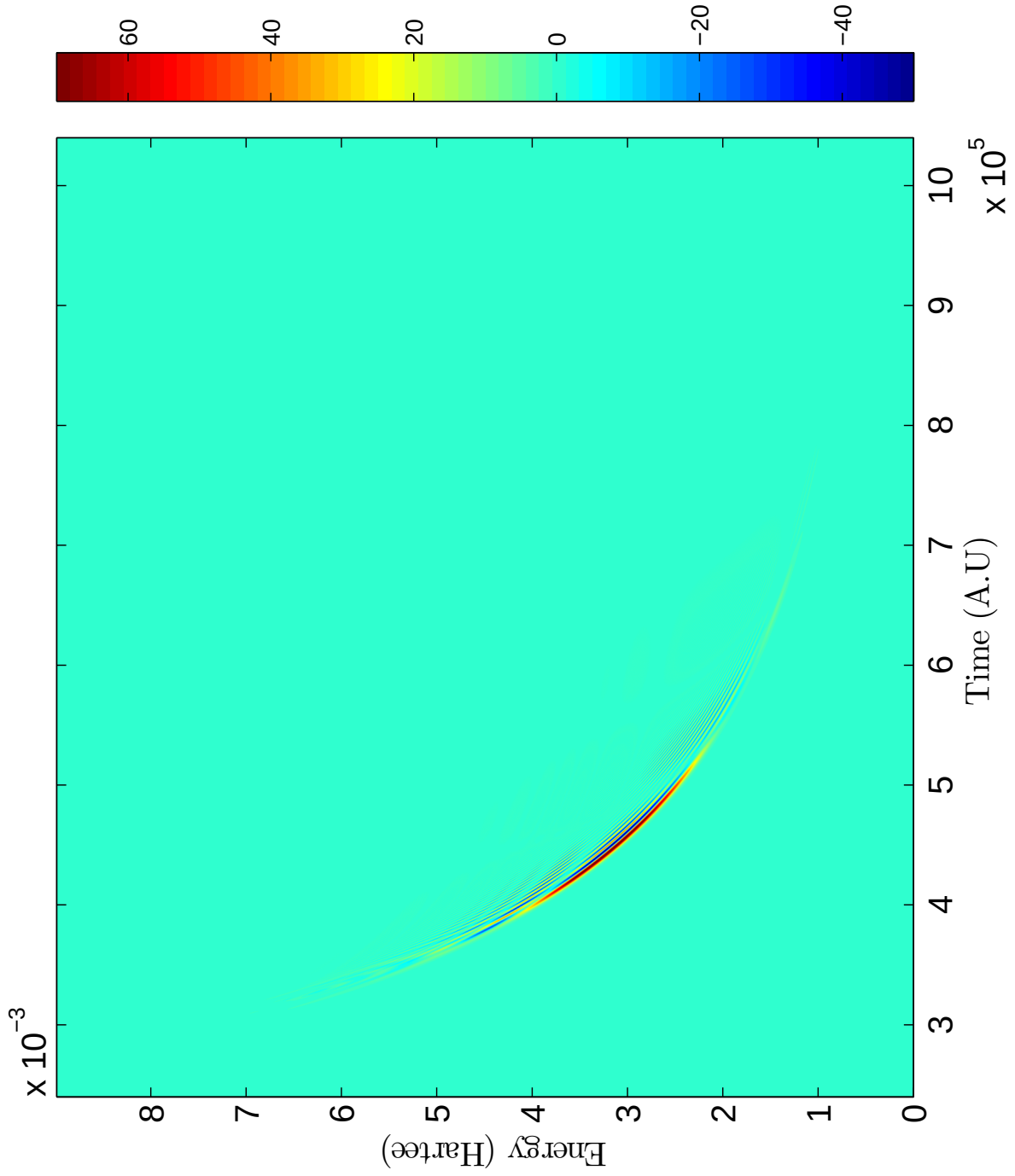


Figure 6.74: Scattering Wigner Distribution Function for K+Ar system with reactant Møller state in $|^{\frac{3}{2}}_{\frac{1}{2}}>$, product Møller state in $|^{\frac{1}{2}}_{\frac{1}{2}}>$, and $J = 1.5$

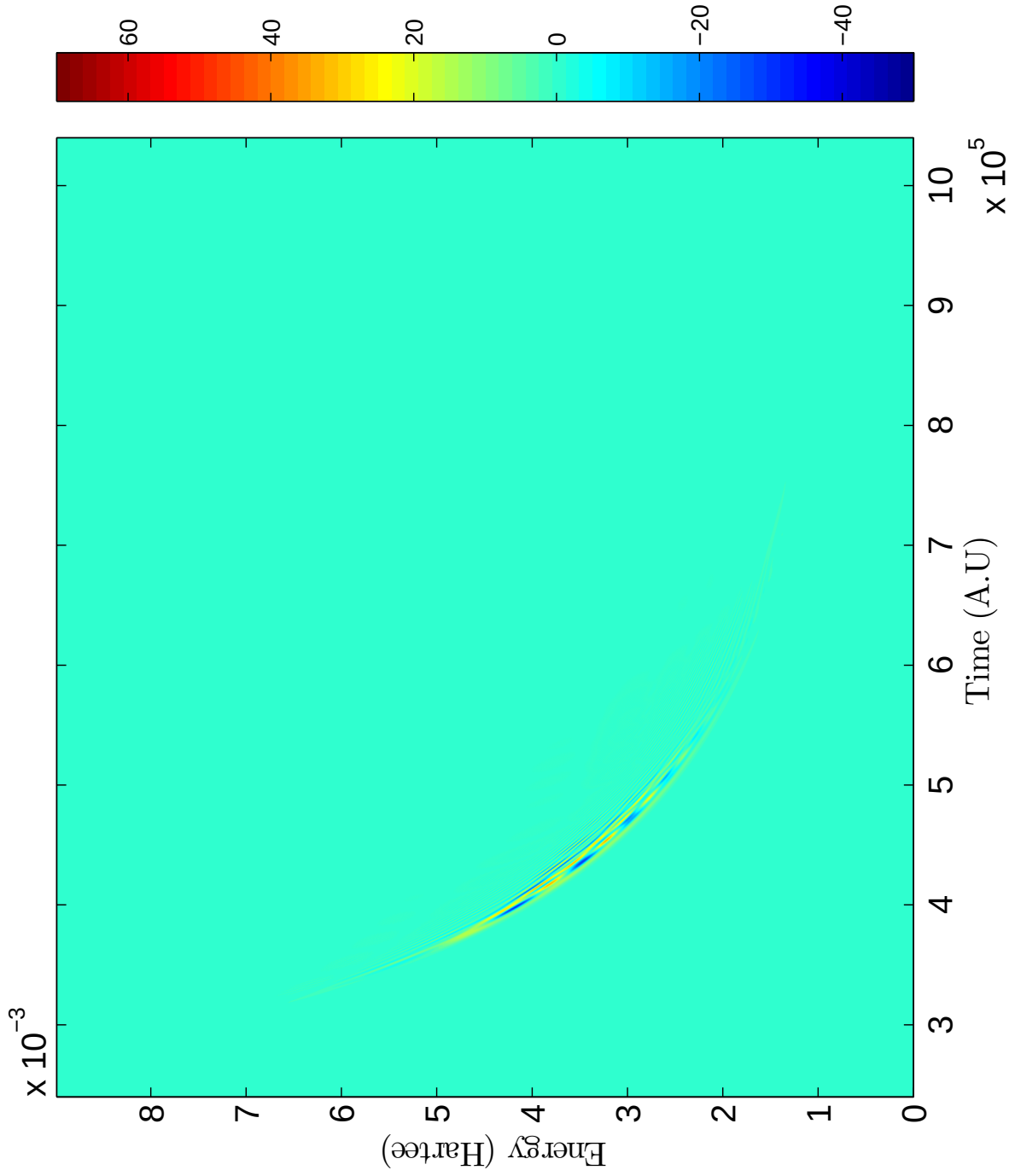


Figure 6.75: Scattering Wigner Distribution Function for K+Ar system with reactant Møller state in $|^{\frac{3}{2}}_{\frac{1}{2}}>$, product Møller state in $|^{\frac{1}{2}}_{\frac{1}{2}}>$, and $J = 100.5$

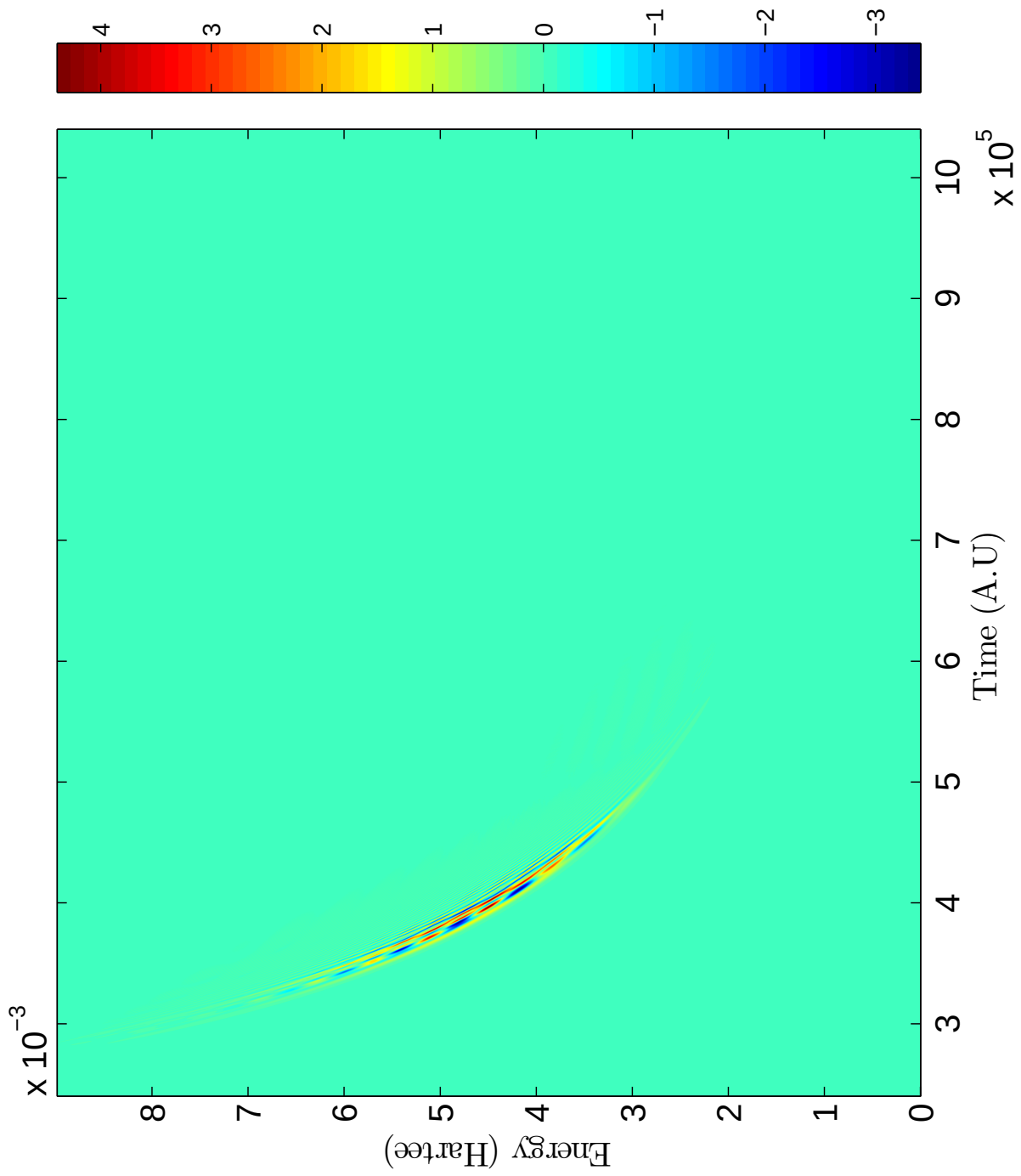


Figure 6.76: Scattering Wigner Distribution Function for K+Ar system with reactant Møller state in $|^{\frac{3}{2}}_{\frac{1}{2}}>$, product Møller state in $|^{\frac{1}{2}}_{\frac{1}{2}}>$, and $J = 200.5$. The scale for this figure is different than the scale used in Fig. 6.74. The scale is based on the maximum and minimum value of the scattering WDF to show that the amplitude exists.

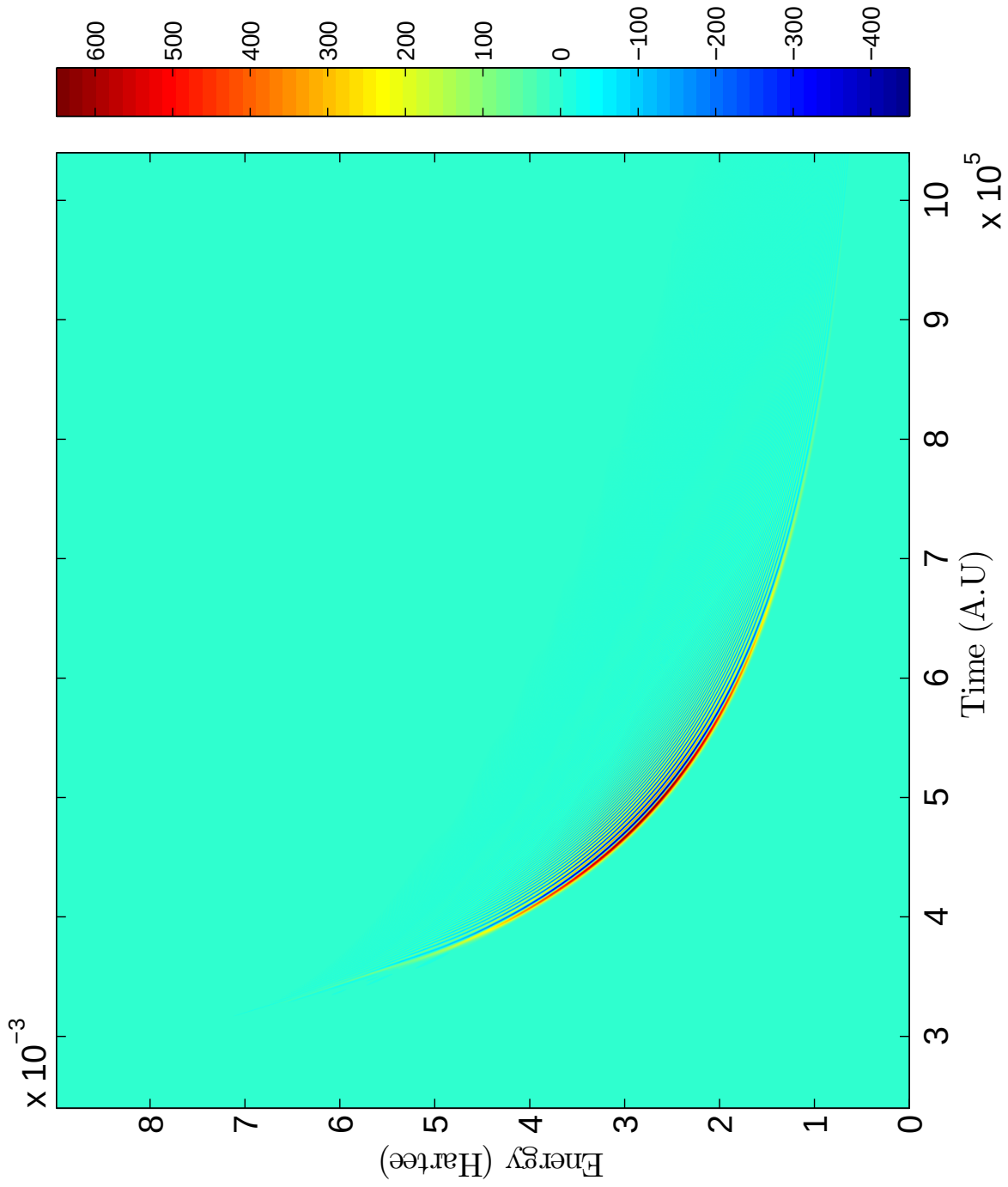


Figure 6.77: Scattering Wigner Distribution Function for K+Ar system with reactant Møller state in $|^{\frac{3}{2}}_{\frac{1}{2}}>$, product Møller state in $|^{\frac{3}{2}}_{\frac{1}{2}}>$, and $J = 1.5$

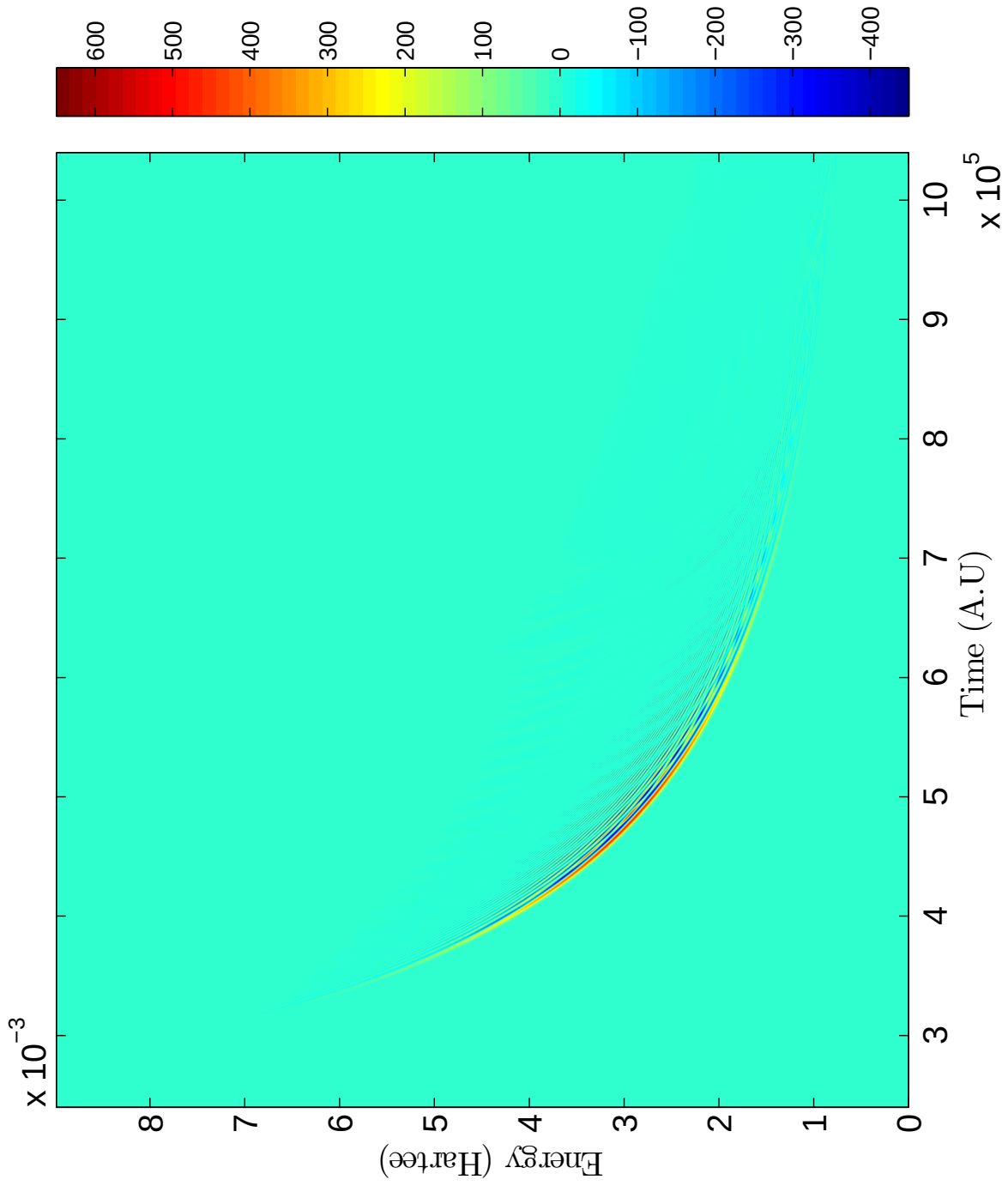


Figure 6.78: Scattering Wigner Distribution Function for K+Ar system with reactant Møller state in $|^{\frac{3}{2}}_{\frac{1}{2}}>$, product Møller state in $|^{\frac{3}{2}}_{\frac{1}{2}}>$, and $J = 100.5$

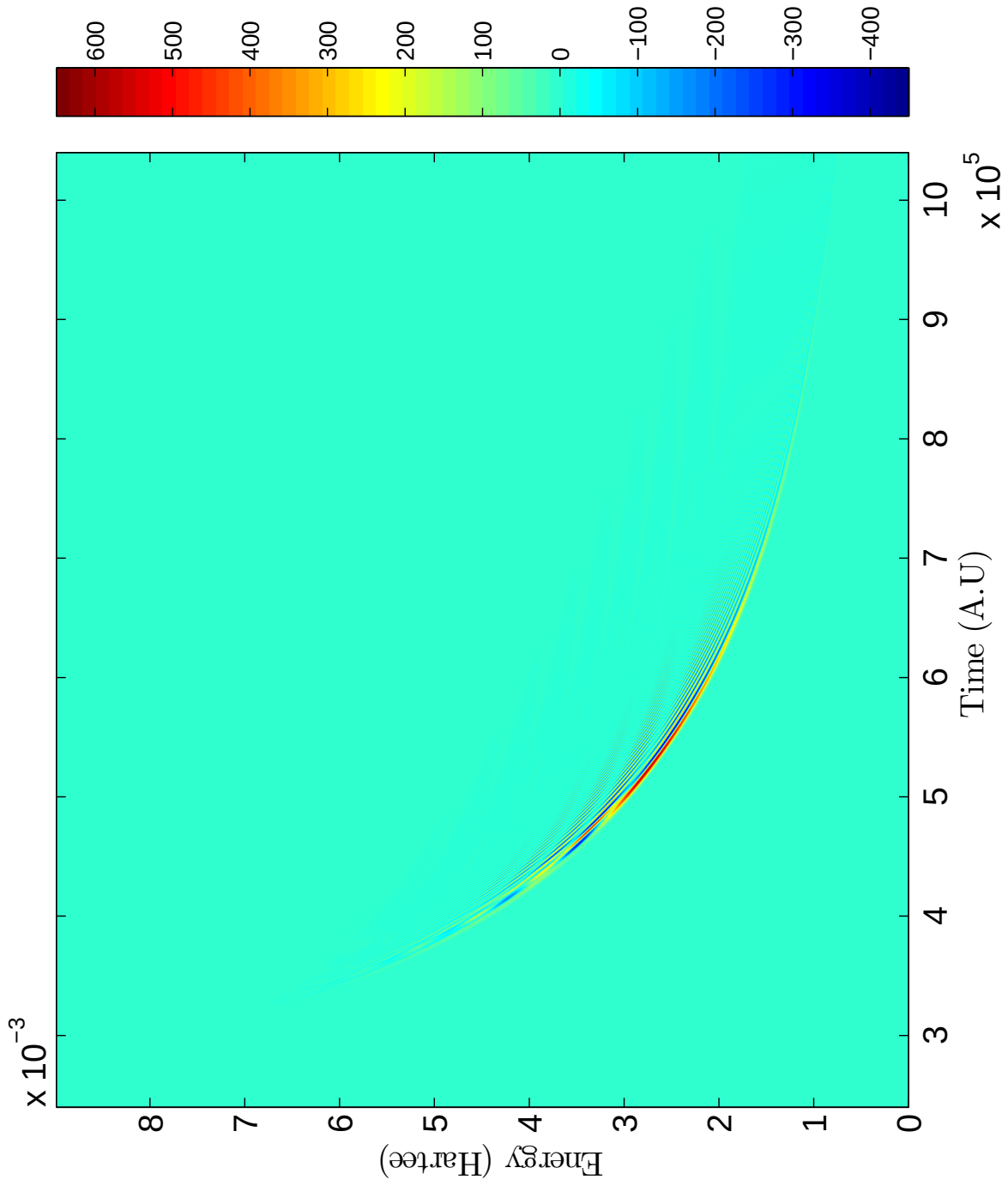


Figure 6.79: Scattering Wigner Distribution Function for K+Ar system with reactant Møller state in $|^{\frac{3}{2}}_{\frac{1}{2}}>$, product Møller state in $|^{\frac{3}{2}}_{\frac{1}{2}}>$, and $J = 200.5$

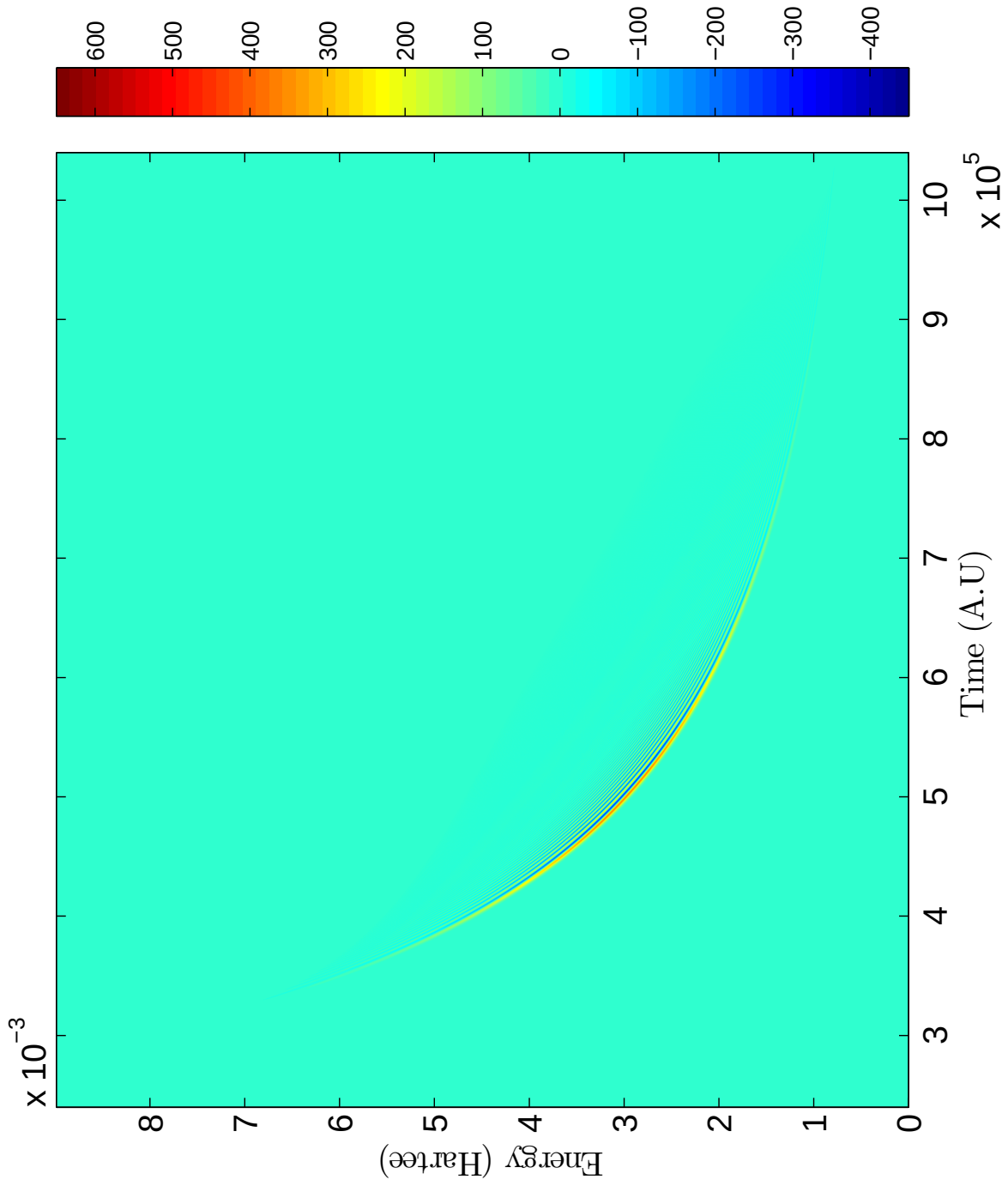


Figure 6.80: Scattering Wigner Distribution Function for K+Ar system with reactant Møller state in $|^{\frac{3}{2}}_{\frac{1}{2}}>$, product Møller state in $|^{\frac{3}{2}}_{\frac{1}{2}}>$, and $J = 300.5$

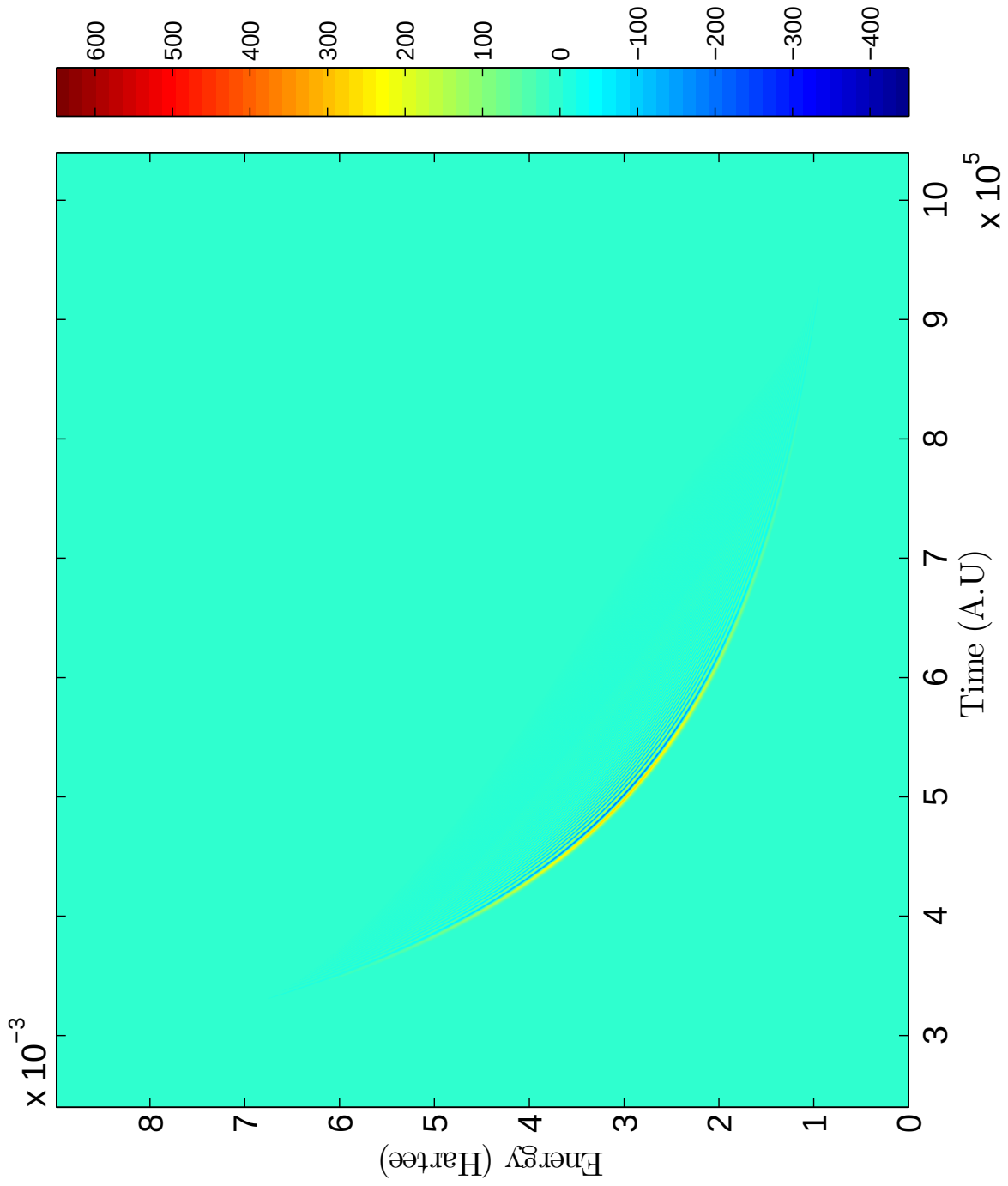


Figure 6.81: Scattering Wigner Distribution Function for K+Ar system with reactant Møller state in $|^{\frac{3}{2}}_{\frac{1}{2}}>$, product Møller state in $|^{\frac{3}{2}}_{\frac{1}{2}}>$, and $J = 400.5$

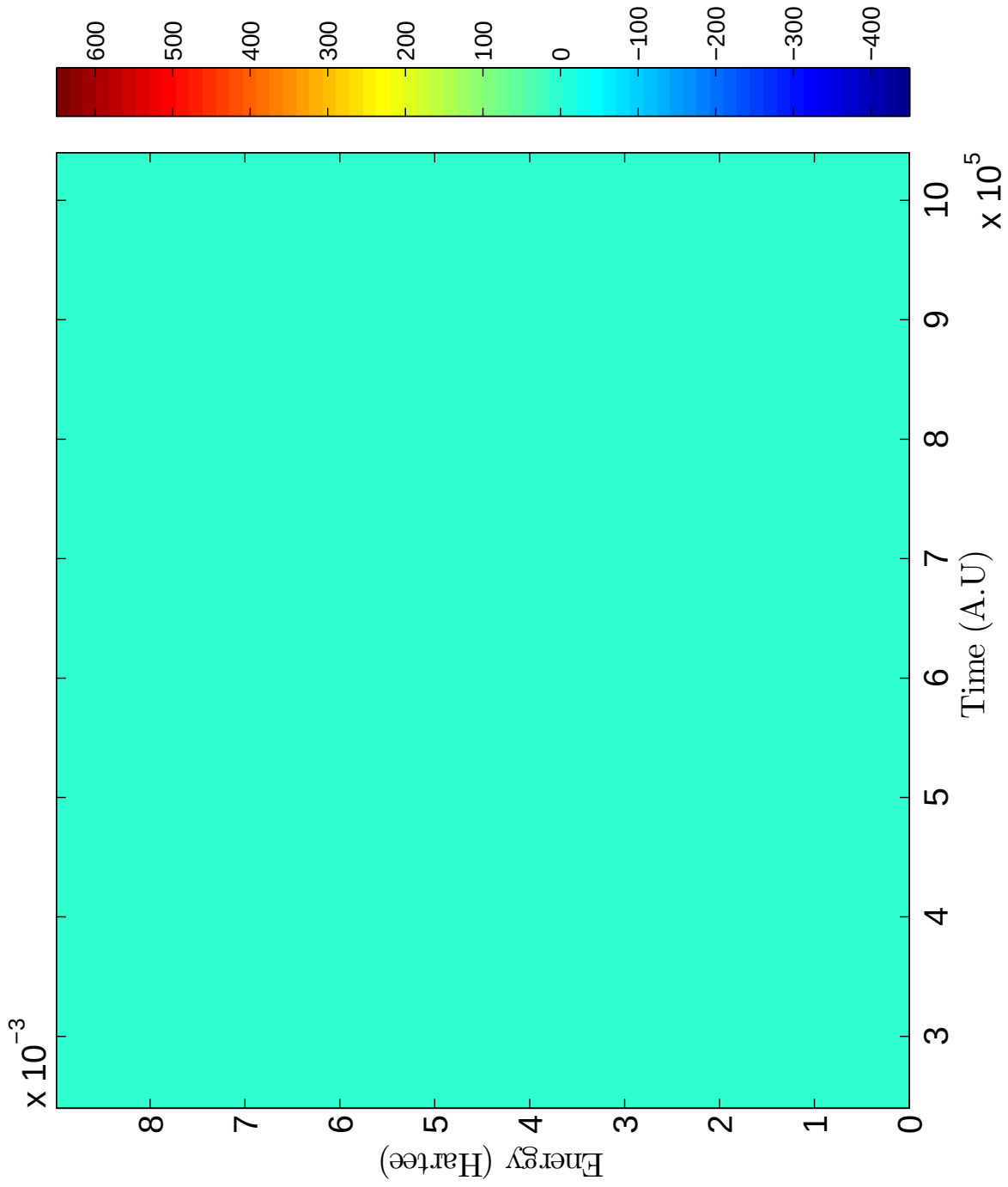


Figure 6.82: Scattering Wigner Distribution Function for K+Ar system with reactant Møller state in $|^{\frac{3}{2}}_{\frac{1}{2}}>$, product Møller state in $|^{\frac{3}{2}}_{\frac{3}{2}}>$, and $J = 1.5$

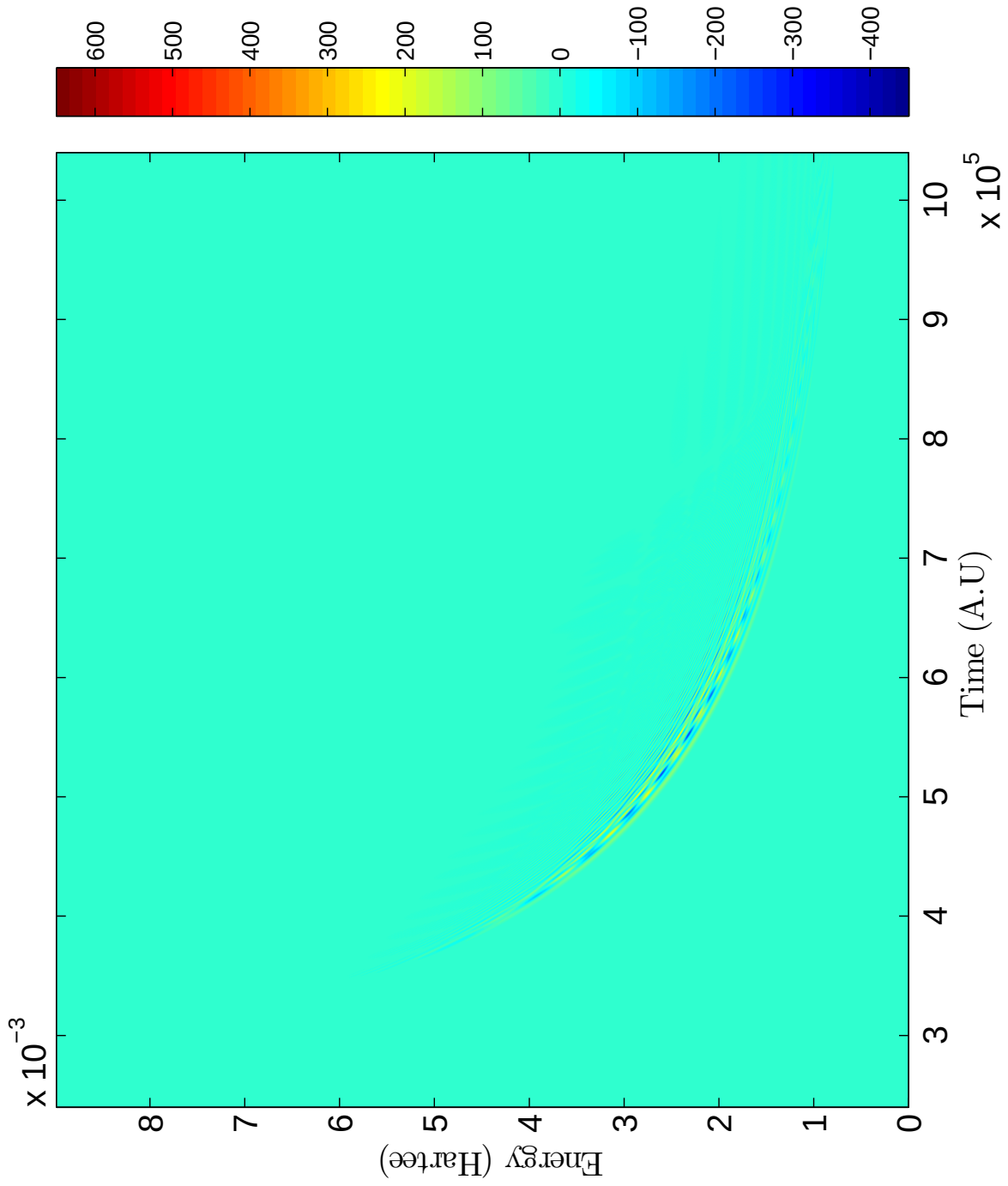


Figure 6.83: Scattering Wigner Distribution Function for K+Ar system with reactant Møller state in $|^{\frac{3}{2}}_{\frac{1}{2}}>$, product Møller state in $|^{\frac{3}{2}}_{\frac{3}{2}}>$, and $J = 100.5$

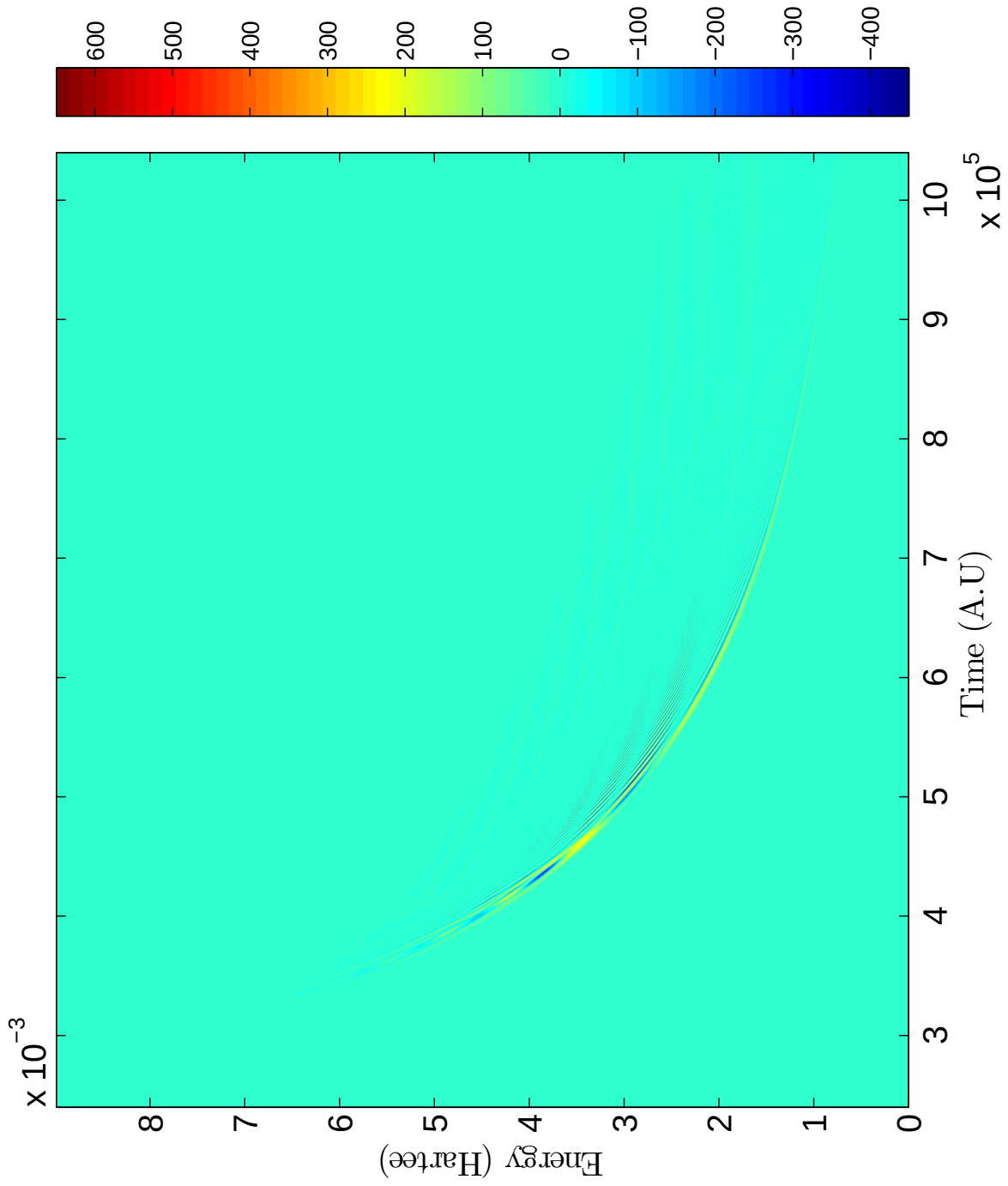


Figure 6.84: Scattering Wigner Distribution Function for K+Ar system with reactant Møller state in $|^{\frac{3}{2}}_{\frac{1}{2}}>$, product Møller state in $|^{\frac{3}{2}}_{\frac{3}{2}}>$, and $J = 200.5$

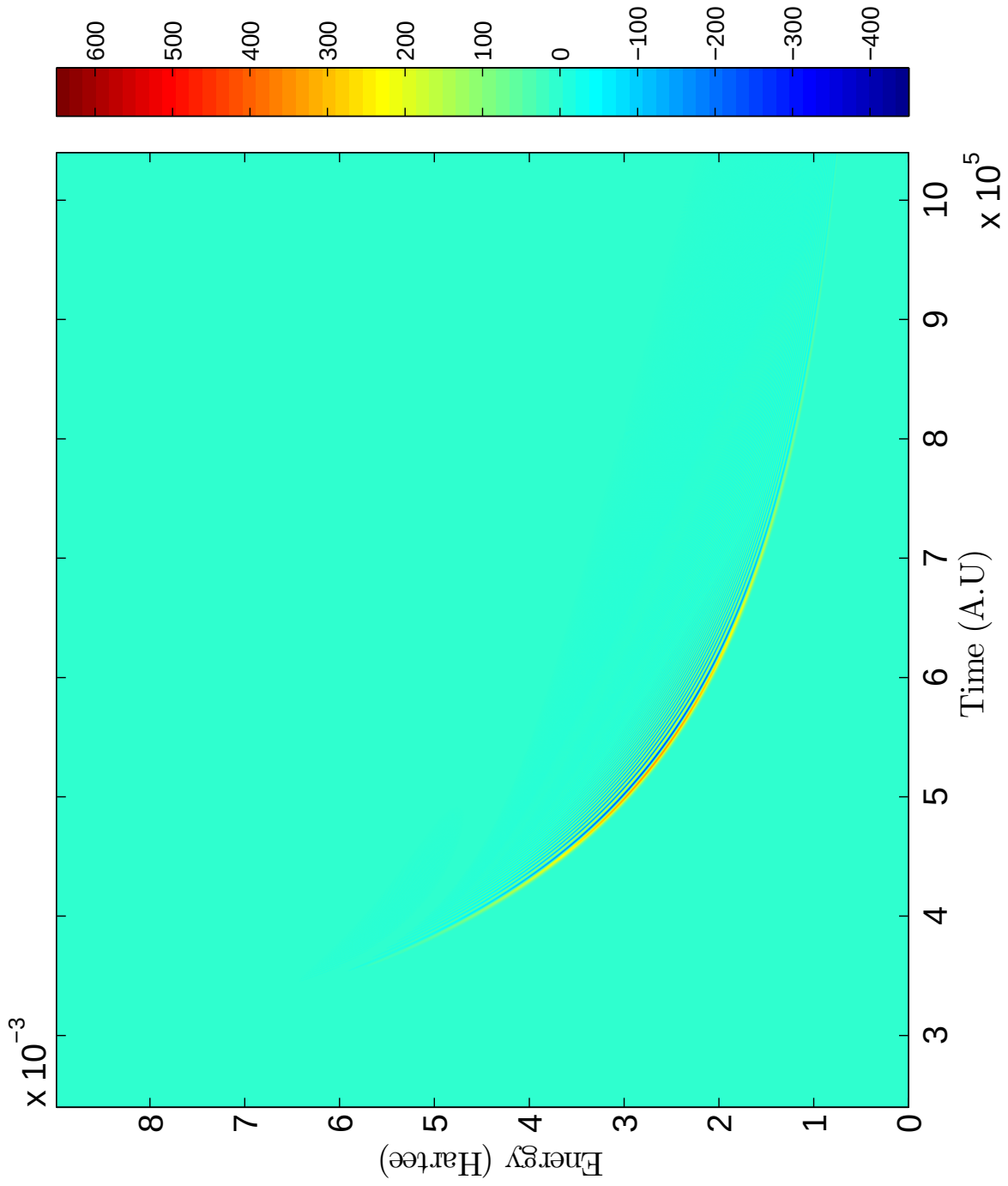


Figure 6.85: Scattering Wigner Distribution Function for K+Ar system with reactant Møller state in $|^{\frac{3}{2}}_{\frac{1}{2}}>$, product Møller state in $|^{\frac{3}{2}}_{\frac{3}{2}}>$, and $J = 300.5$

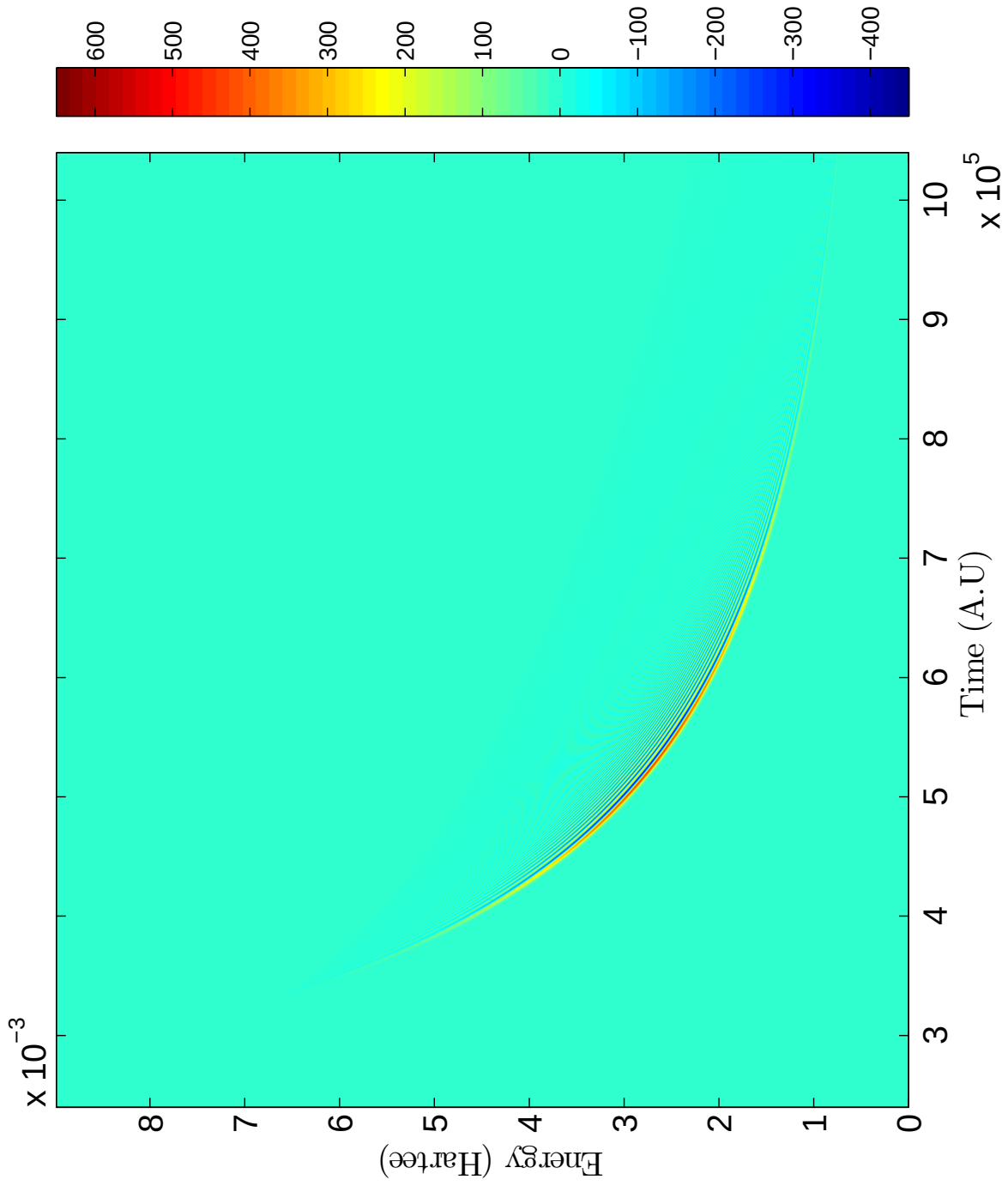


Figure 6.86: Scattering Wigner Distribution Function for K+Ar system with reactant Møller state in $|^{\frac{3}{2}}_{\frac{1}{2}}>$, product Møller state in $|^{\frac{3}{2}}_{\frac{3}{2}}>$, and $J = 400.5$

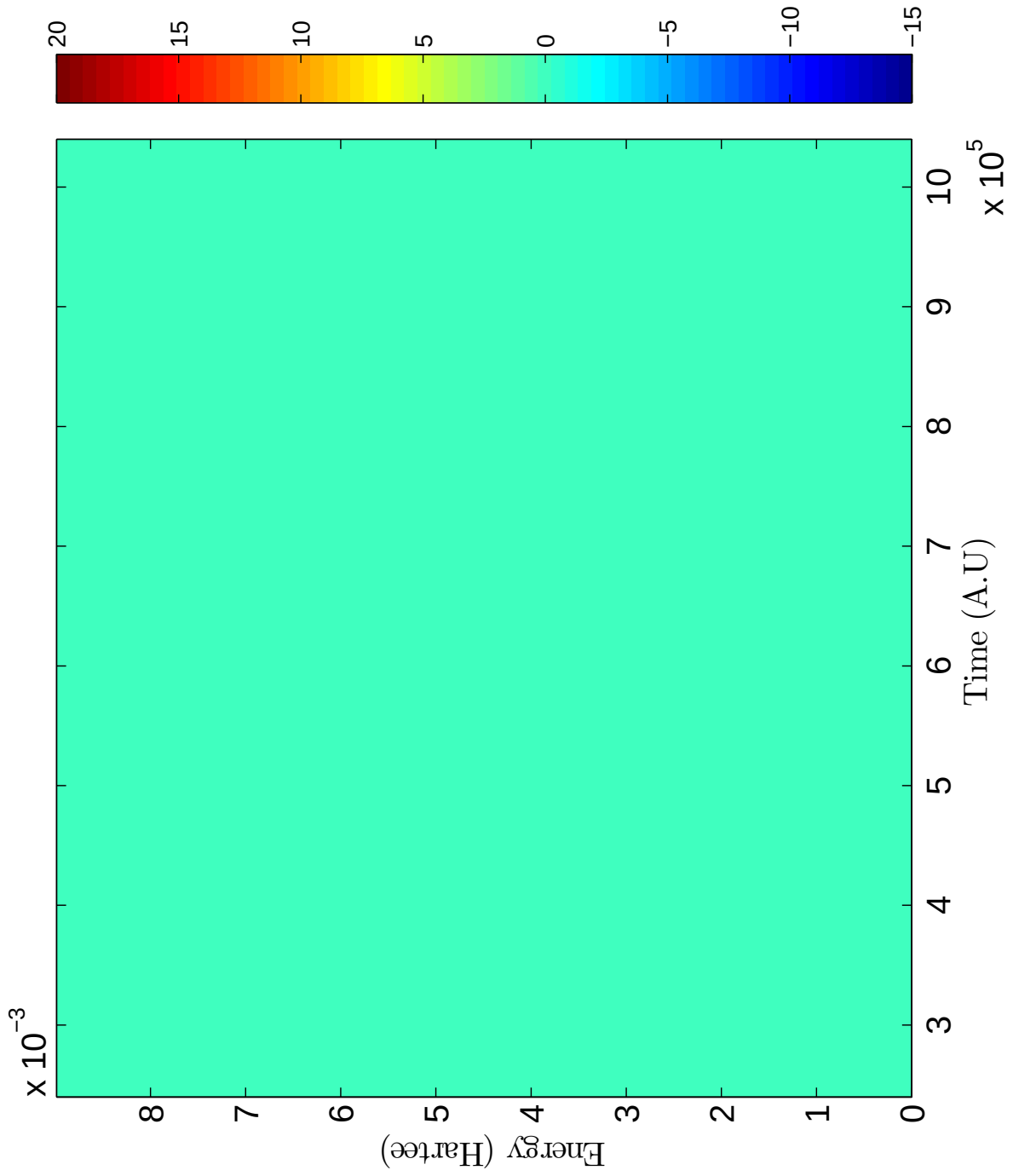


Figure 6.87: Scattering Wigner Distribution Function for K+Ar system with reactant Møller state in $|^{\frac{3}{2}}_{\frac{3}{2}}>$, product Møller state in $|^{\frac{1}{2}}_{\frac{1}{2}}>$, and $J = 1.5$

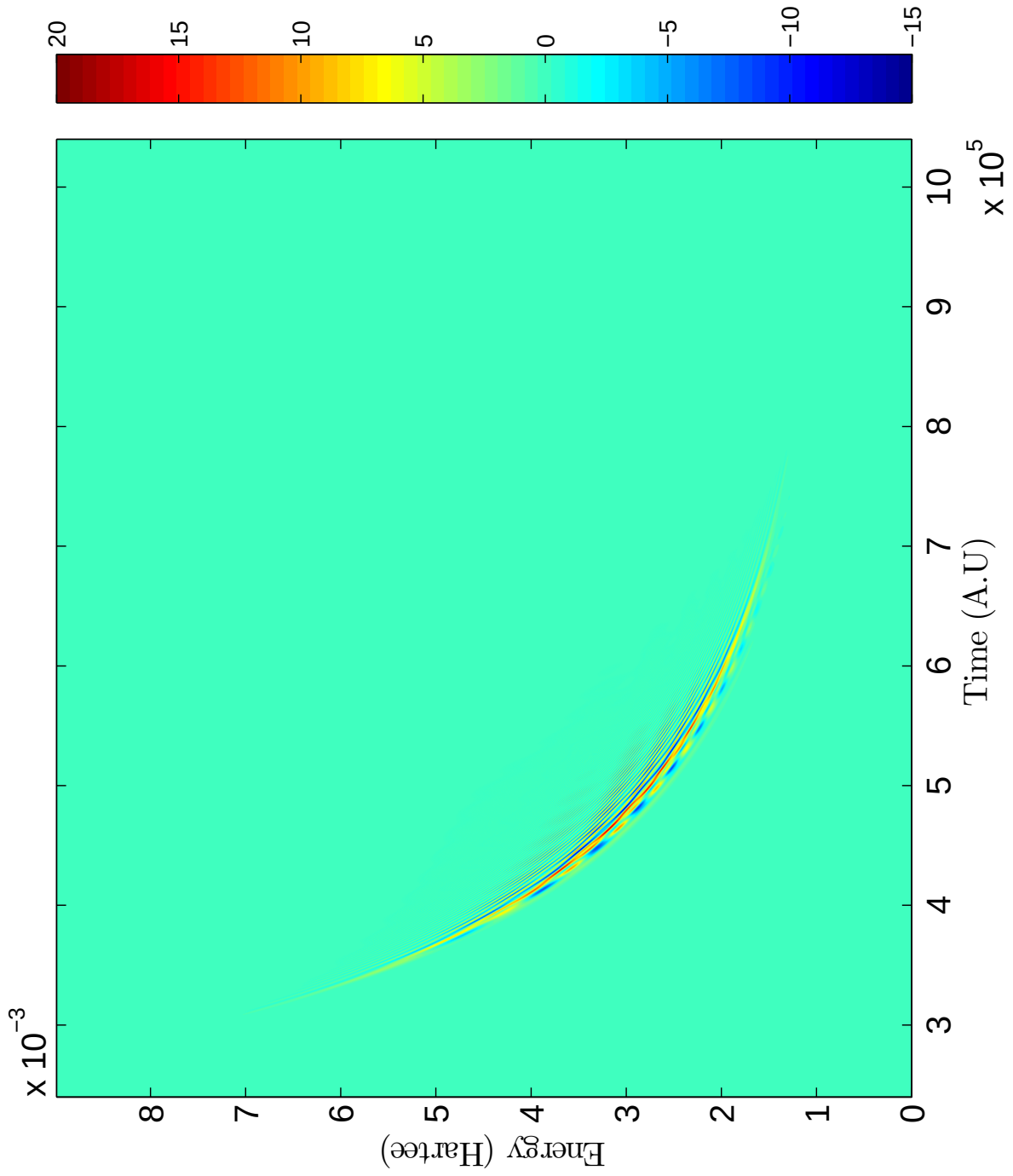


Figure 6.88: Scattering Wigner Distribution Function for K+Ar system with reactant Møller state in $|^{\frac{3}{2}}_{\frac{3}{2}}>$, product Møller state in $|^{\frac{1}{2}}_{\frac{1}{2}}>$, and $J = 100.5$

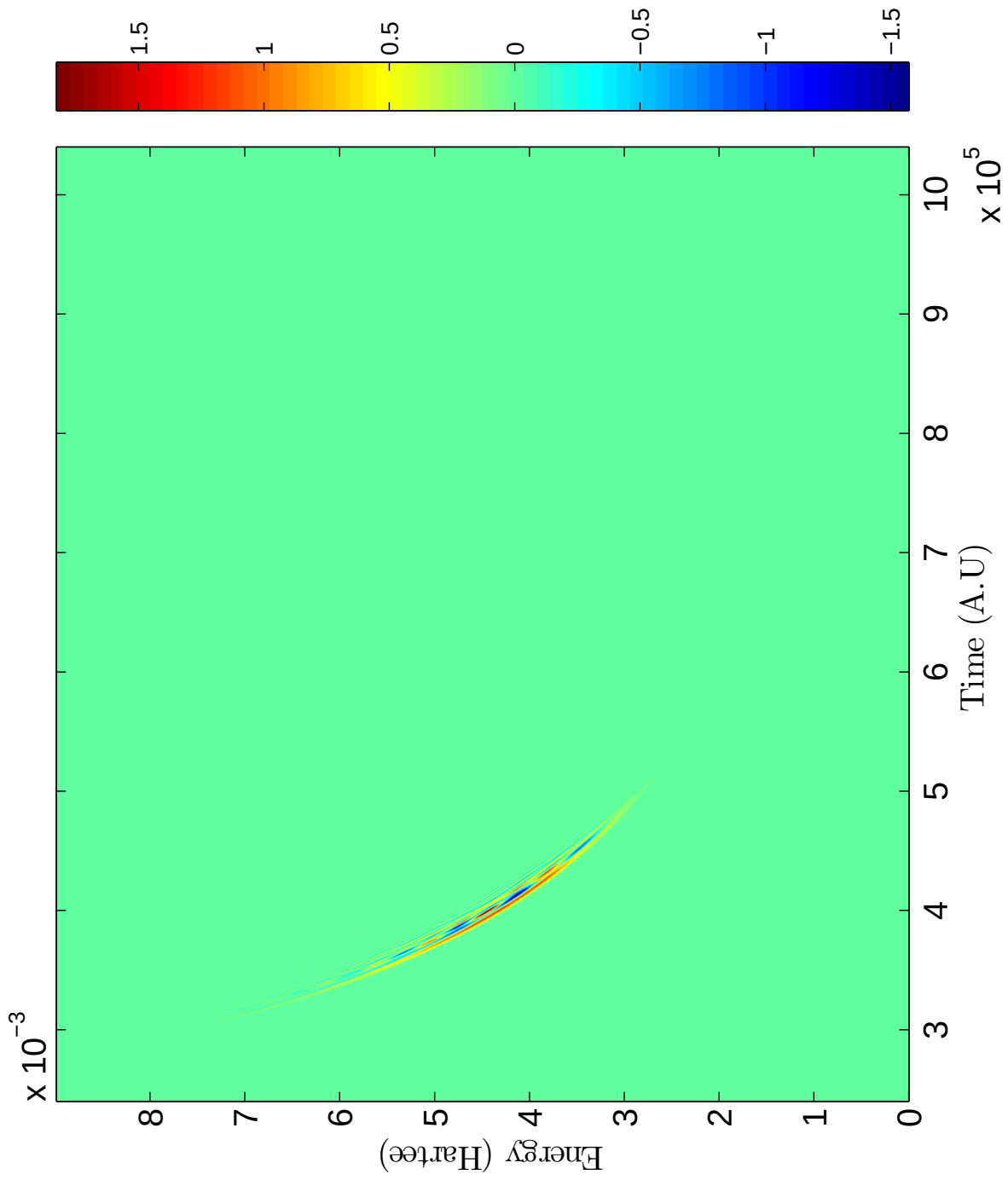


Figure 6.89: Scattering Wigner Distribution Function for K+Ar system with reactant Møller state in $|\frac{3}{2}\frac{3}{2}>$, product Møller state in $|\frac{1}{2}\frac{1}{2}>$, and $J = 200.5$. The scale for this figure is different than the scale used in Fig. 6.87. The scale is based on the maximum and minimum value of the scattering WDF to show that the amplitude exists.

### *6.2.5 Alkali Metals.*

If the alkali atom is changed while the noble gas atom remains the same, the angular momentum matrix in Eq. 6.2 will be affected. The difference in the various alkali metals is the spin-orbit split. As the alkali metal increases in mass, the spin-orbit split grows larger. A larger spin-orbit spliting means that higher energies are needed to achieve the transition from the $|^{\frac{1}{2}}_{\frac{1}{2}}>$ to the $|^{\frac{3}{2}}_{\frac{1}{2}}>$ surfaces. In effect, the probability of making the transition decreases. This implies that the transfer of probability between the $|^{\frac{1}{2}}_{\frac{1}{2}}>$ and $|^{\frac{3}{2}}_{\frac{1}{2}}>$ surfaces decreases since the strength of the radial coupling decreases. Figs. 6.31-6.48 and Figs. 6.90-6.120 show the scattering WDF for the $K + Ne$, $Rb + Ne$, and $Cs + Ne$ systems over a range of $\Delta J = 50$ from $J = 50.5$ to $J = 250.5$ ($J = 1.5$ is included) with the reactant Møller state starting on the $|^{\frac{3}{2}}_{\frac{1}{2}}>$ surface. For the $K + Ne$ system, the spin-orbit split is relatively small, so the radial coupling is relatively strong. As such we see that there is significant probability on all three surfaces for the certain values of $J$. The $Rb + Ne$ system has a larger spin-orbit split, so the probability of making a transition to the $|^{\frac{1}{2}}_{\frac{1}{2}}>$ exists but smaller than the $K + Ne$ case. The amplitude of the scattering WDF for $K + Ne$ for the $|^{\frac{1}{2}}_{\frac{1}{2}}>$ surface at $J = 1.5$ is approximately $\frac{1}{10}$ of the amplitude of the scattering WDF for the $|^{\frac{3}{2}}_{\frac{1}{2}}>$ surface at $J = 1.5$. In comparison, the change in the order of magnitude between these two surfaces for $Rb + Ne$ at $J = 1.5$ is $\frac{1}{1000000}$. The spin-orbit split for $Cs$ is much larger, so the radial coupling term is very weak. For this reason, the change in the order of magnitude in the scattering WDF between these surfaces for $Cs + Ne$ is $10^{-}10$. With such a drastic change in the amplitude of the scattering WDF between the two surfaces for $Cs + Ne$, we can assume that there is almost no radial Coupling for $Cs$. For the purpose of the DPAL, this is detrimental to optimizing the output power of the laser; however, for purposes of studying a two level system that only explores Coriolis coupling, this can be beneficial.

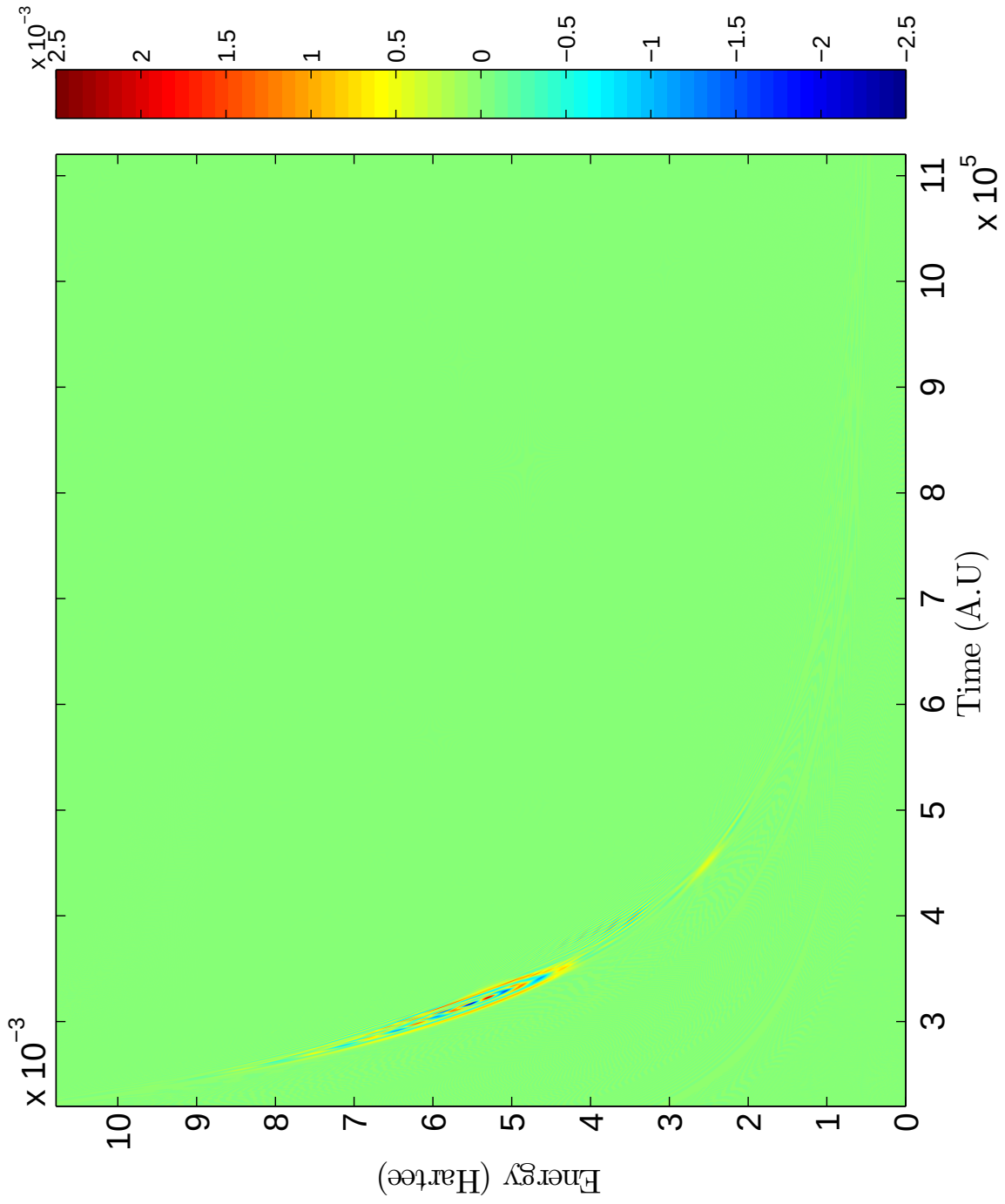


Figure 6.90: Scattering Wigner Distribution Function for Rb+Ne system with reactant Møller state in $|^{\frac{3}{2}}_{\frac{1}{2}}>$, product Møller state in $|^{\frac{1}{2}}_{\frac{1}{2}}>$, and $J = 1.5$

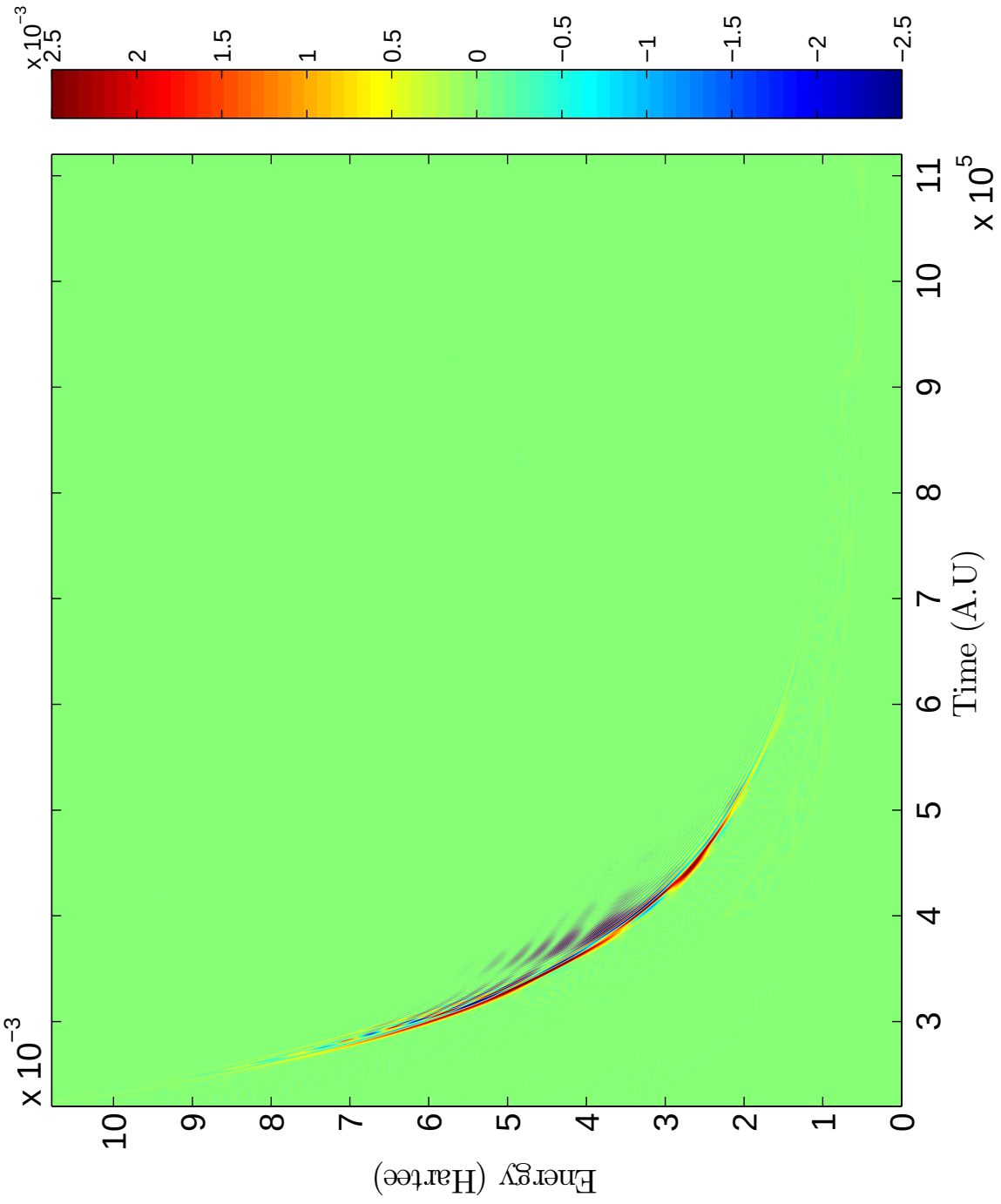


Figure 6.91: Scattering Wigner Distribution Function for Rb+Ne system with reactant Møller state in $|^{\frac{3}{2}}_{\frac{1}{2}}>$, product Møller state in $|^{\frac{1}{2}}_{\frac{1}{2}}>$, and $J = 50.5$

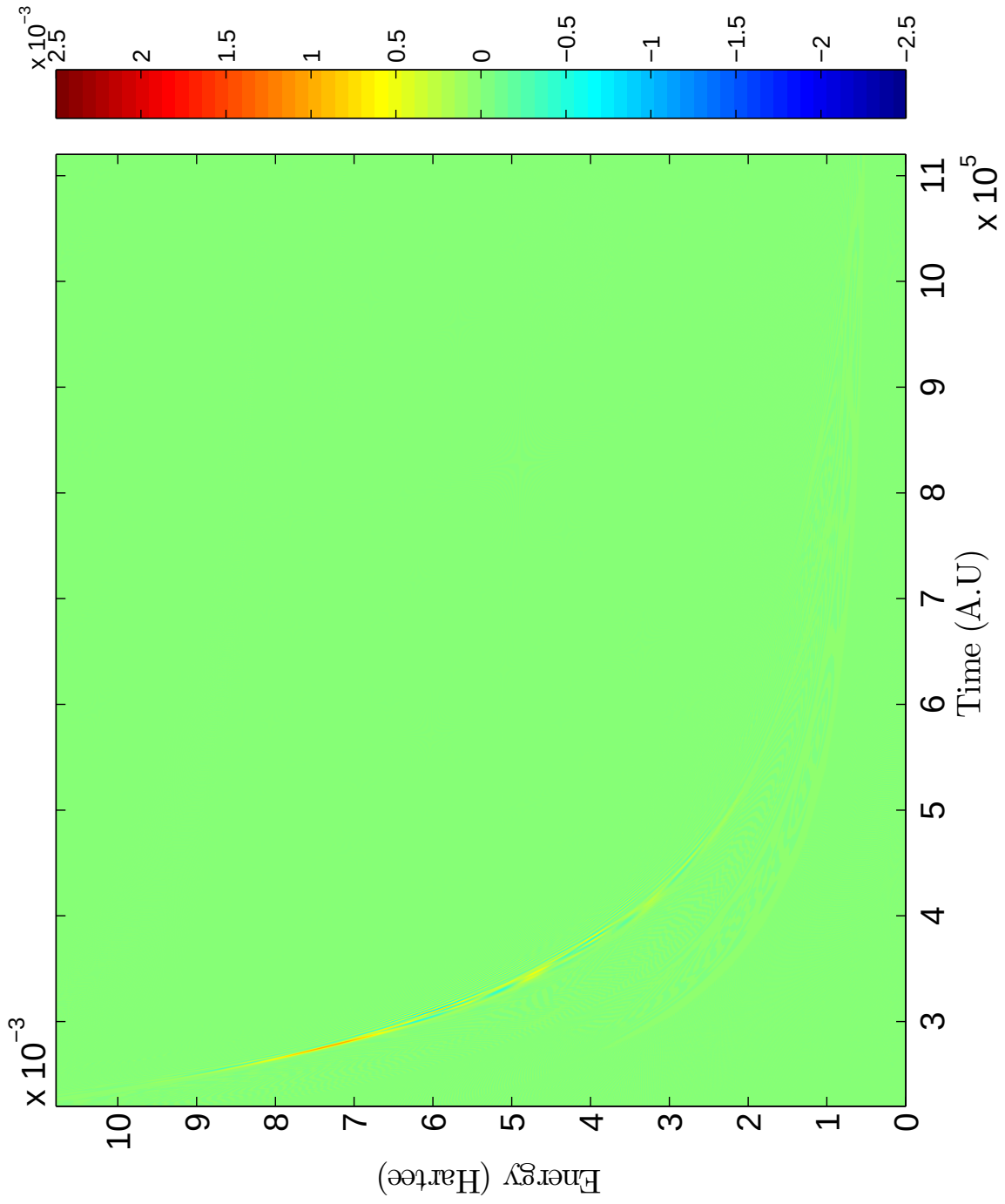


Figure 6.92: Scattering Wigner Distribution Function for Rb+Ne system with reactant Møller state in $|^{\frac{3}{2}}_{\frac{1}{2}}>$, product Møller state in $|^{\frac{1}{2}}_{\frac{1}{2}}>$, and $J = 100.5$

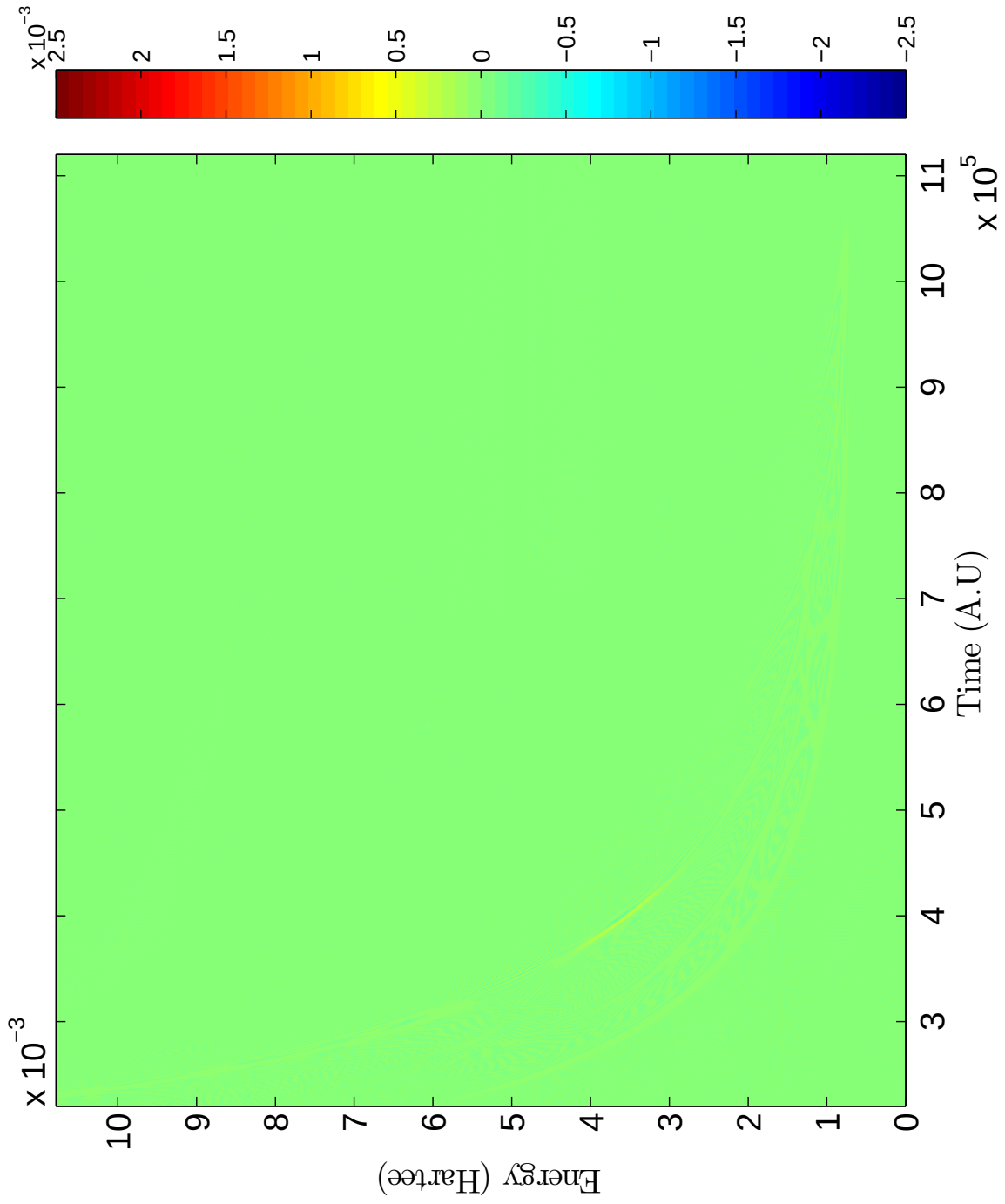


Figure 6.93: Scattering Wigner Distribution Function for Rb+Ne system with reactant Møller state in $|^{\frac{3}{2}}_{\frac{1}{2}}>$, product Møller state in $|^{\frac{1}{2}}_{\frac{1}{2}}>$, and $J = 150.5$

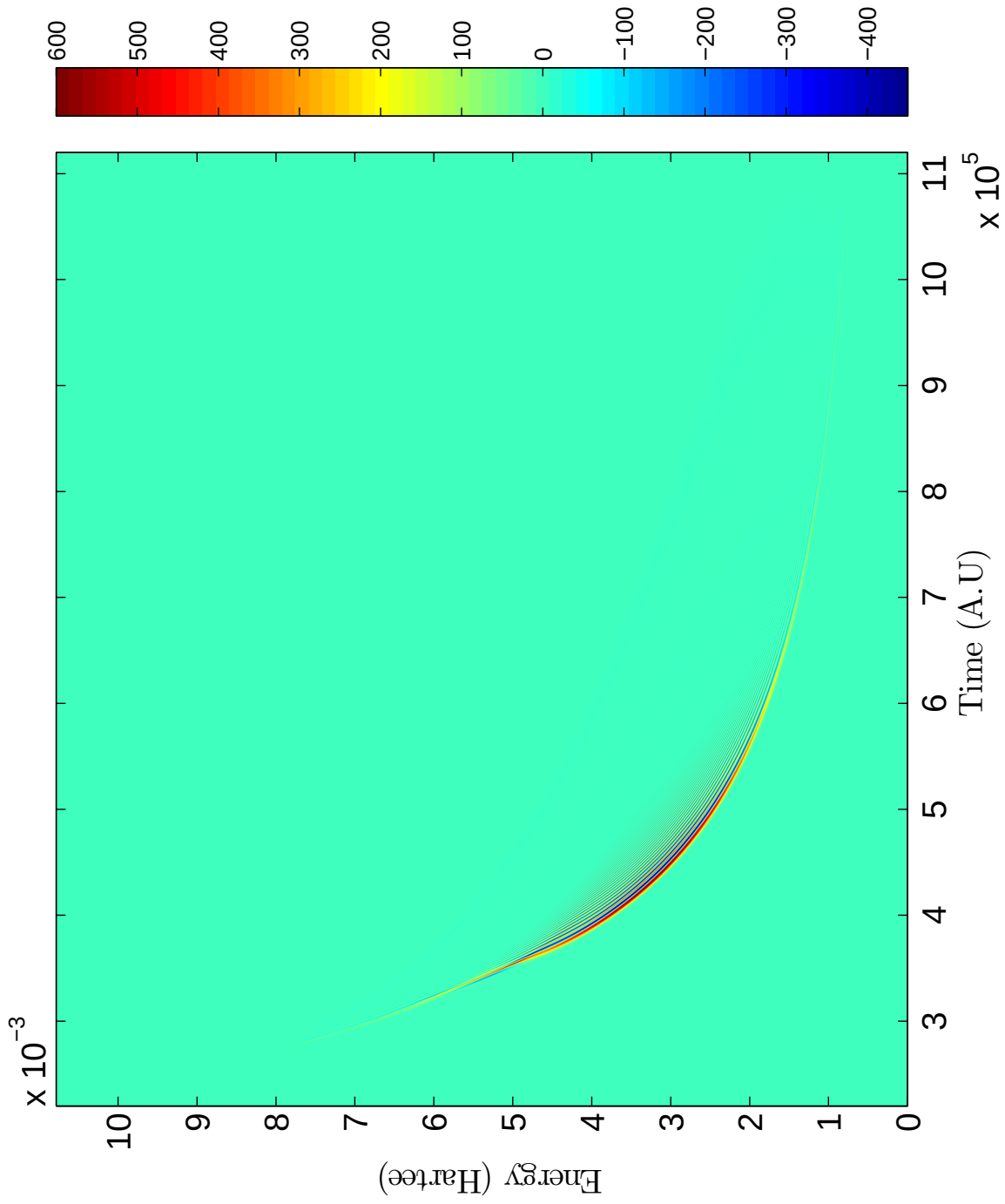


Figure 6.94: Scattering Wigner Distribution Function for Rb+Ne system with reactant Møller state in $|^{\frac{3}{2}}_{\frac{1}{2}}>$, product Møller state in $|^{\frac{3}{2}}_{\frac{1}{2}}>$, and $J = 1.5$

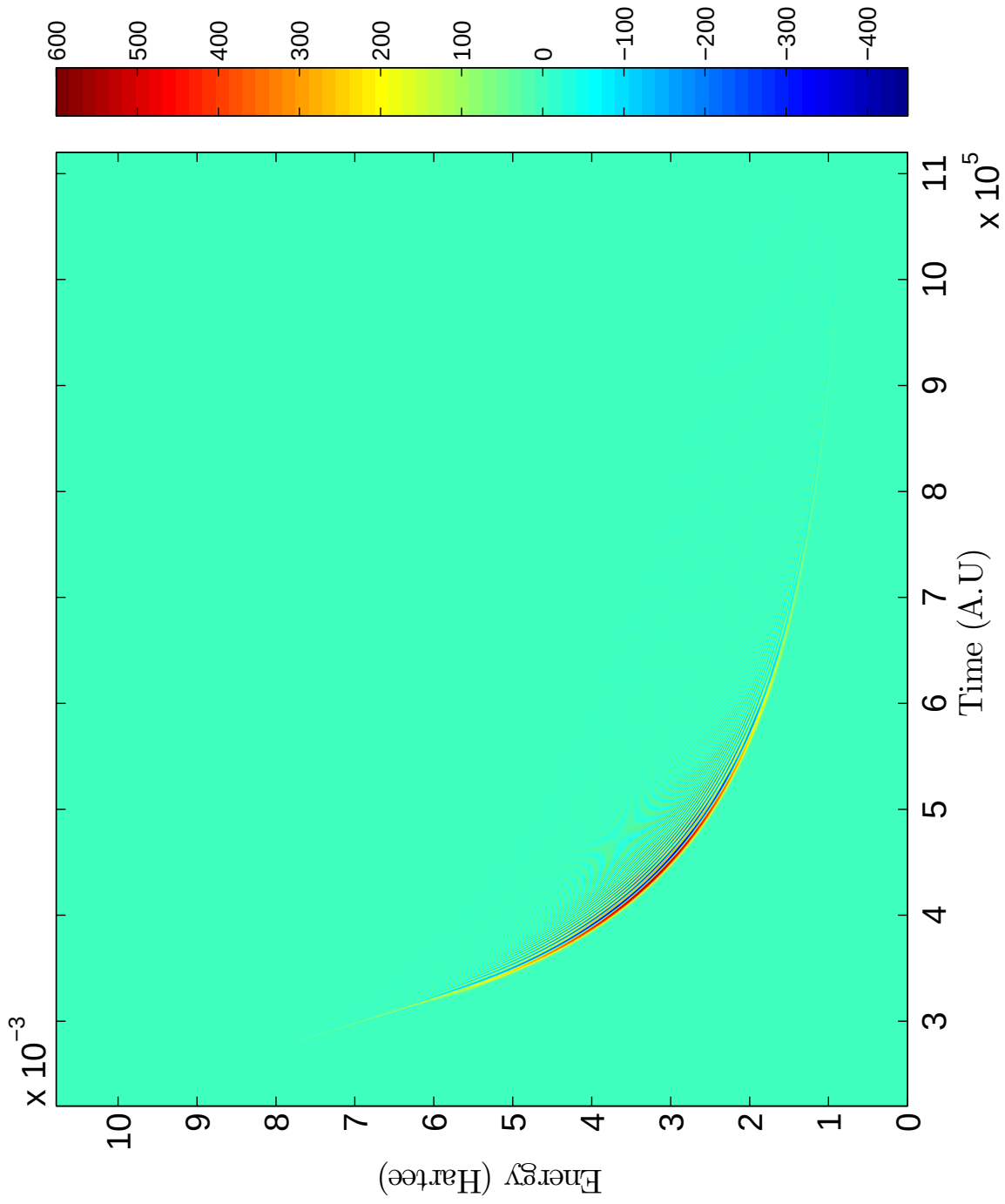


Figure 6.95: Scattering Wigner Distribution Function for Rb+Ne system with reactant Møller state in $|^{\frac{3}{2}}_{\frac{1}{2}}>$, product Møller state in $|^{\frac{3}{2}}_{\frac{1}{2}}>$, and $J = 50.5$

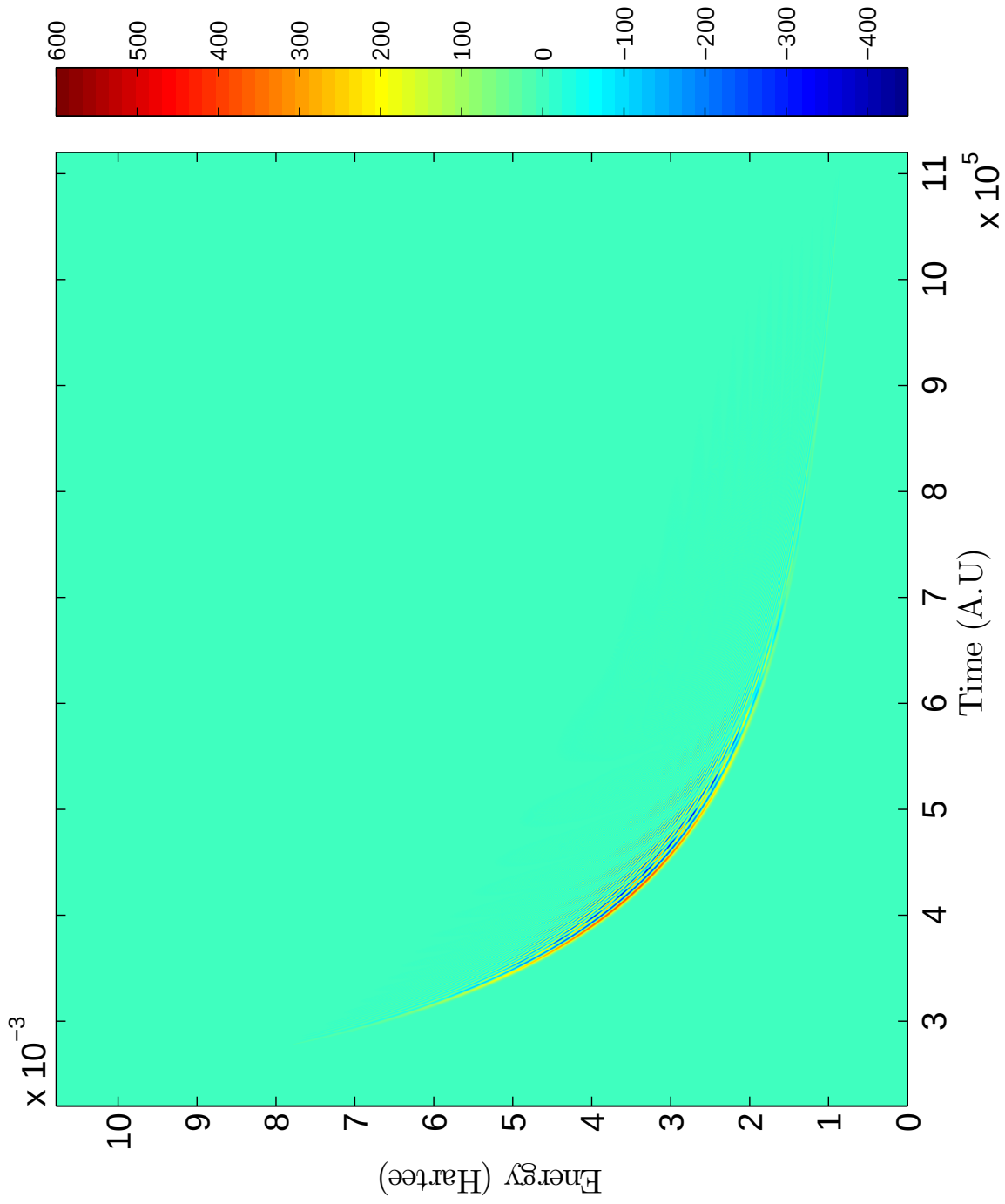


Figure 6.96: Scattering Wigner Distribution Function for Rb+Ne system with reactant Møller state in $|^{\frac{3}{2}}_{\frac{1}{2}}>$, product Møller state in $|^{\frac{3}{2}}_{\frac{1}{2}}>$, and $J = 100.5$

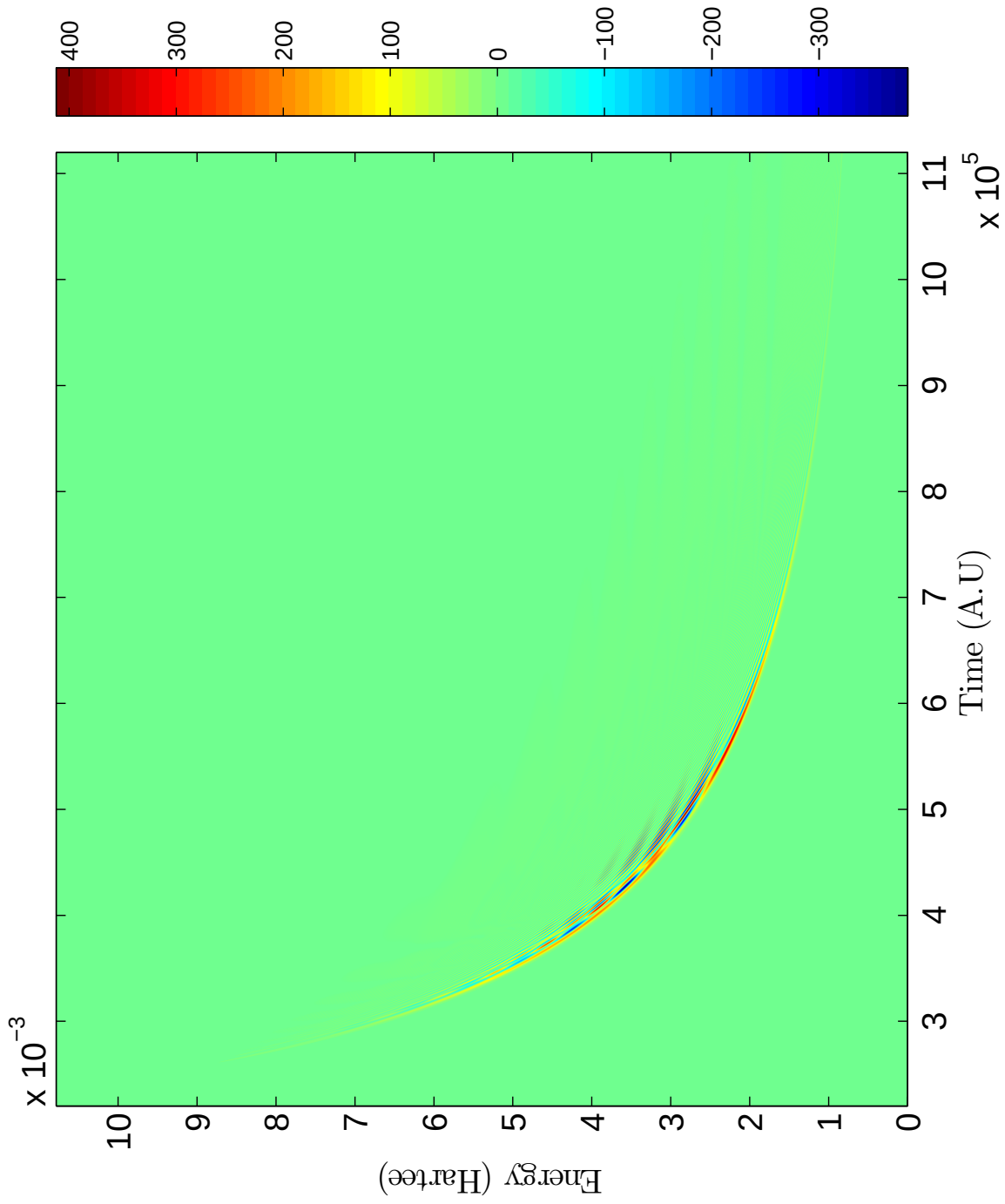


Figure 6.97: Scattering Wigner Distribution Function for Rb+Ne system with reactant Møller state in $|^{\frac{3}{2}}_{\frac{1}{2}}>$, product Møller state in $|^{\frac{3}{2}}_{\frac{1}{2}}>$, and $J = 150.5$

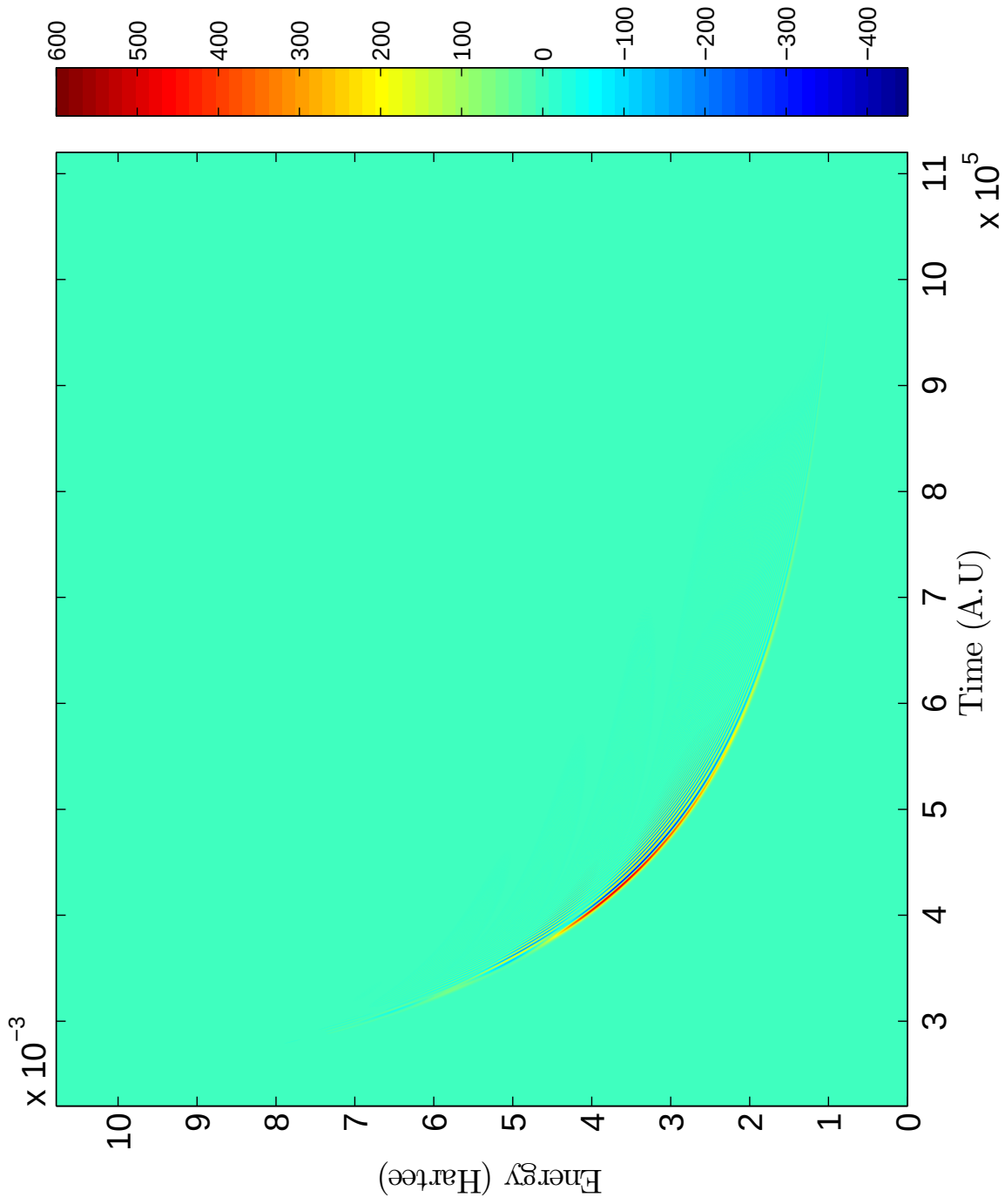


Figure 6.98: Scattering Wigner Distribution Function for Rb+Ne system with reactant Møller state in $|^{\frac{3}{2}}_{\frac{1}{2}}>$, product Møller state in $|^{\frac{3}{2}}_{\frac{1}{2}}>$, and $J = 200.5$

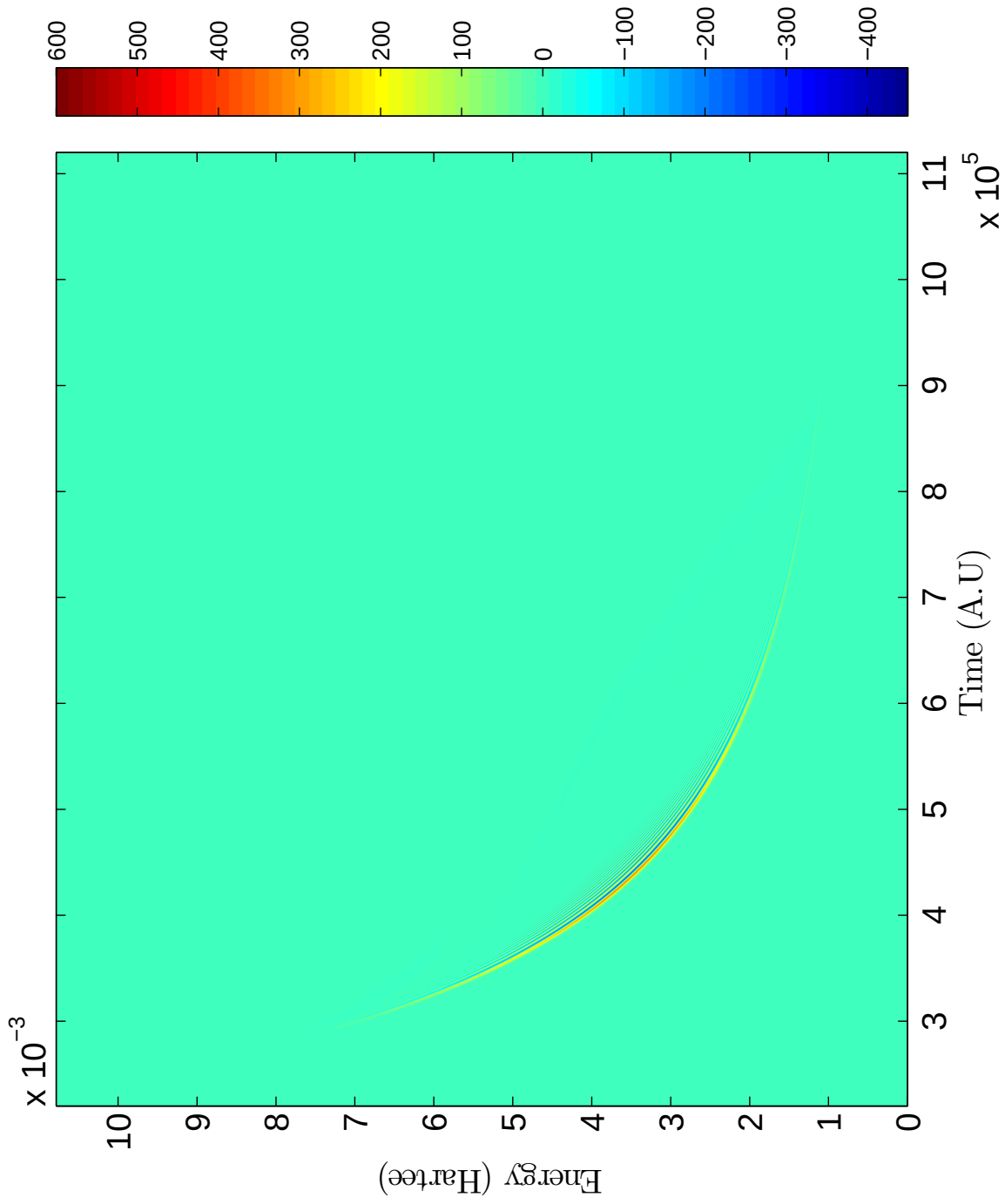


Figure 6.99: Scattering Wigner Distribution Function for Rb+Ne system with reactant Møller state in $|^{\frac{3}{2}}_{\frac{1}{2}}>$, product Møller state in $|^{\frac{3}{2}}_{\frac{1}{2}}>$, and $J = 250.5$

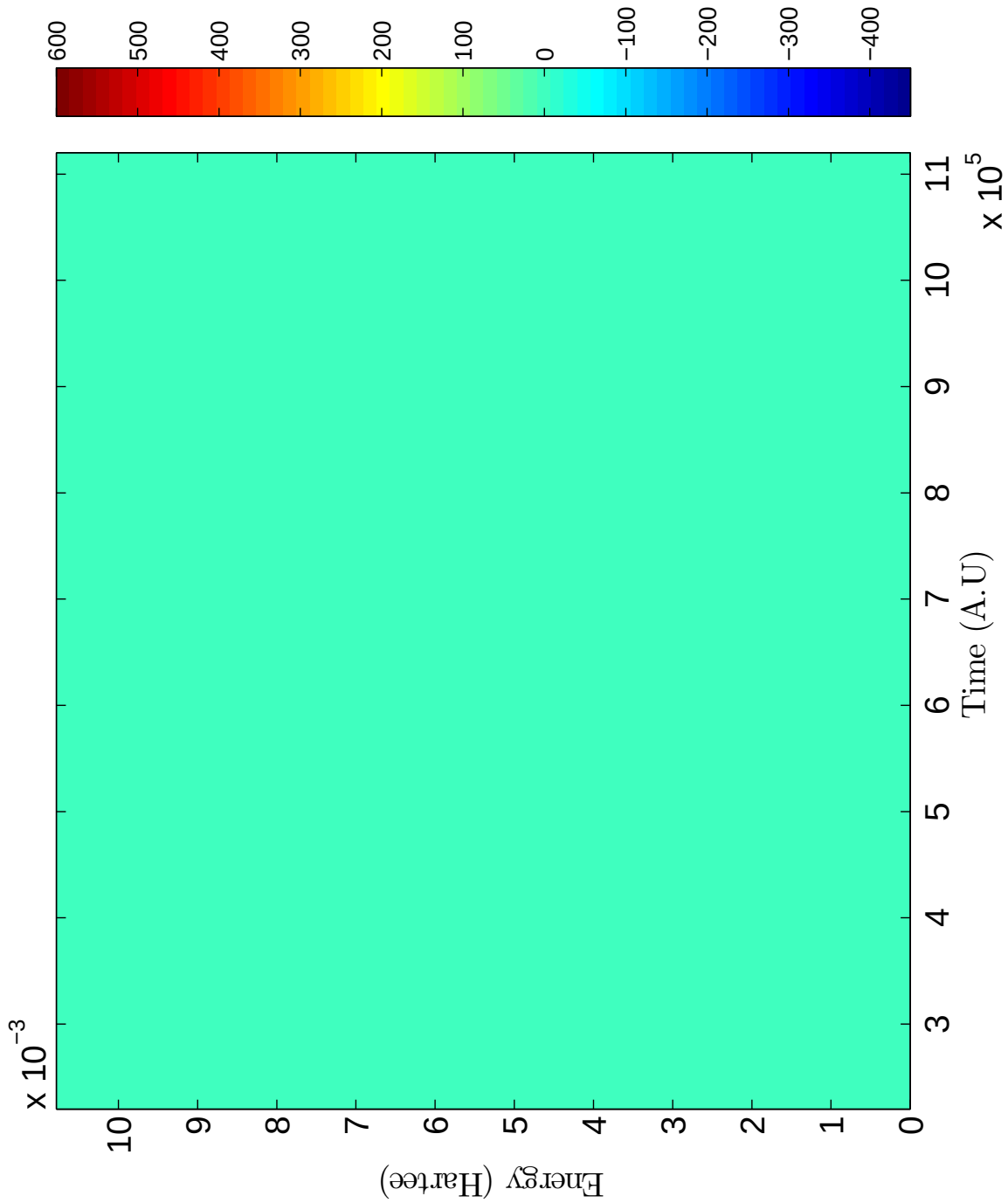


Figure 6.100: Scattering Wigner Distribution Function for Rb+Ne system with reactant Møller state in $|^{\frac{3}{2}}_{\frac{1}{2}}>$, product Møller state in $|^{\frac{3}{2}}_{\frac{3}{2}}>$, and $J = 1.5$

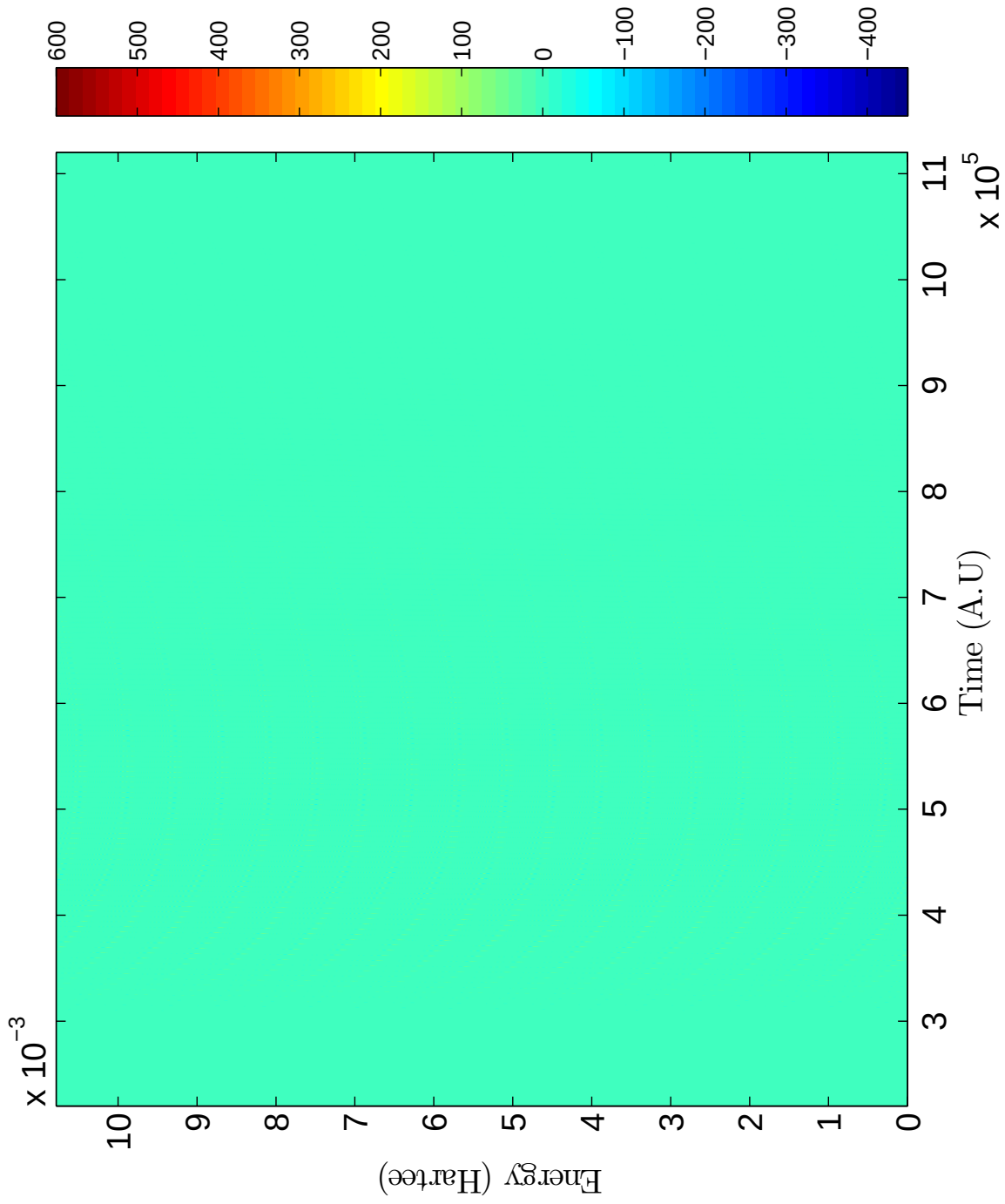


Figure 6.101: Scattering Wigner Distribution Function for Rb+Ne system with reactant Møller state in $|^{\frac{3}{2}}_{\frac{1}{2}}>$, product Møller state in $|^{\frac{3}{2}}_{\frac{3}{2}}>$, and $J = 50.5$

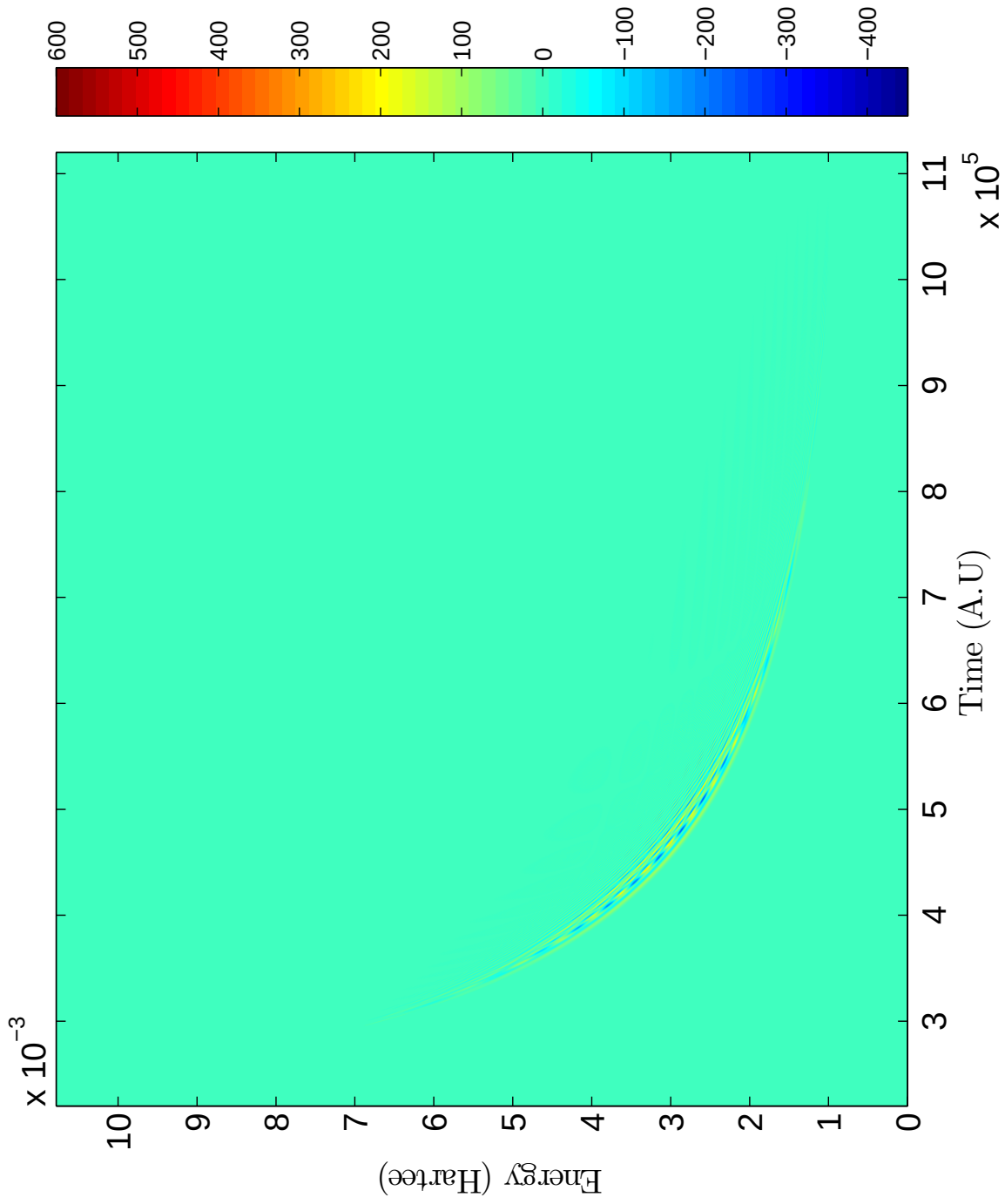


Figure 6.102: Scattering Wigner Distribution Function for Rb+Ne system with reactant Møller state in $|\frac{3}{2}\frac{1}{2}>$, product Møller state in $|\frac{3}{2}\frac{3}{2}>$, and $J = 100.5$

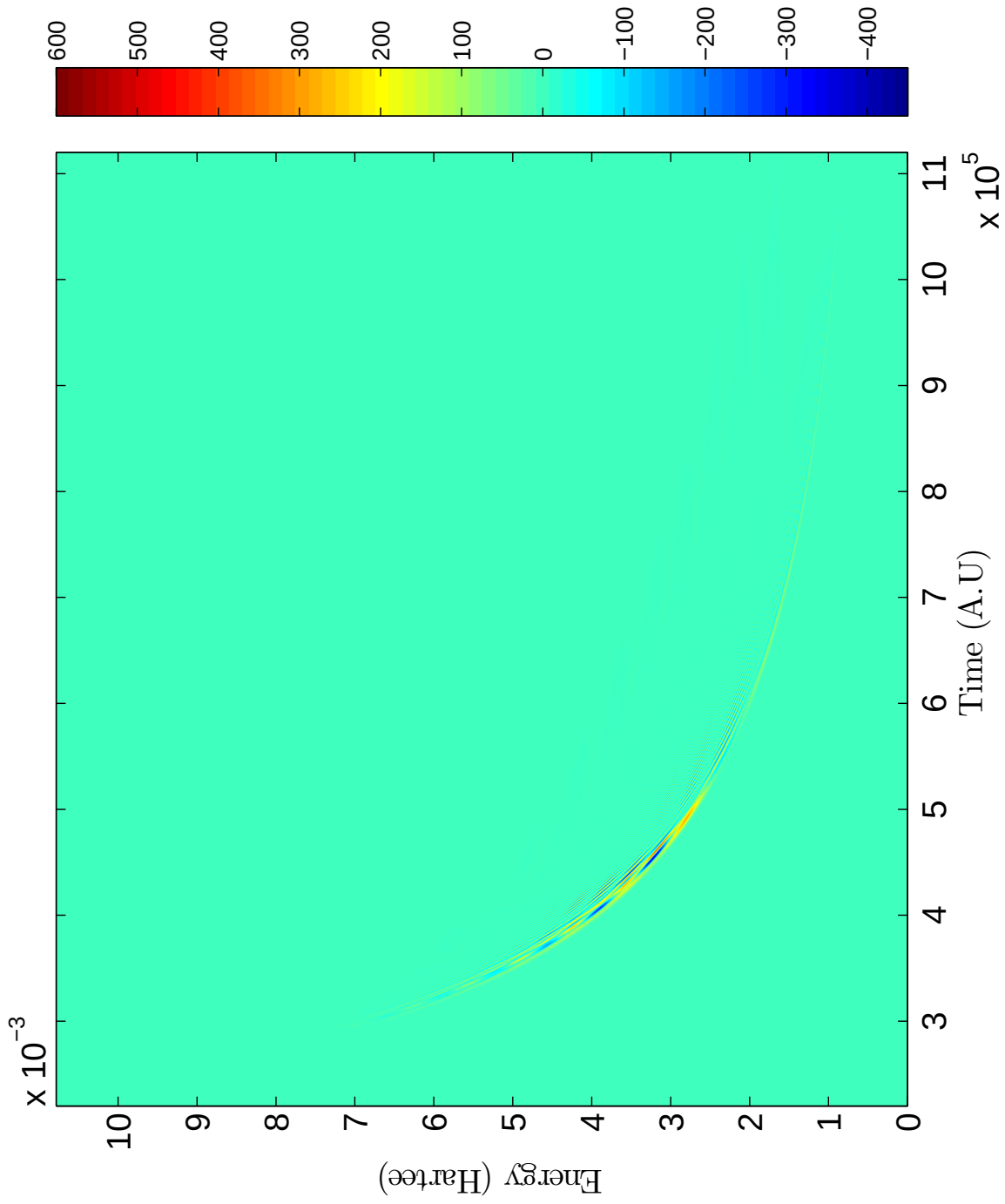


Figure 6.103: Scattering Wigner Distribution Function for Rb+Ne system with reactant Møller state in $|^{\frac{3}{2}}_{\frac{1}{2}}>$, product Møller state in $|^{\frac{3}{2}}_{\frac{3}{2}}>$, and $J = 150.5$

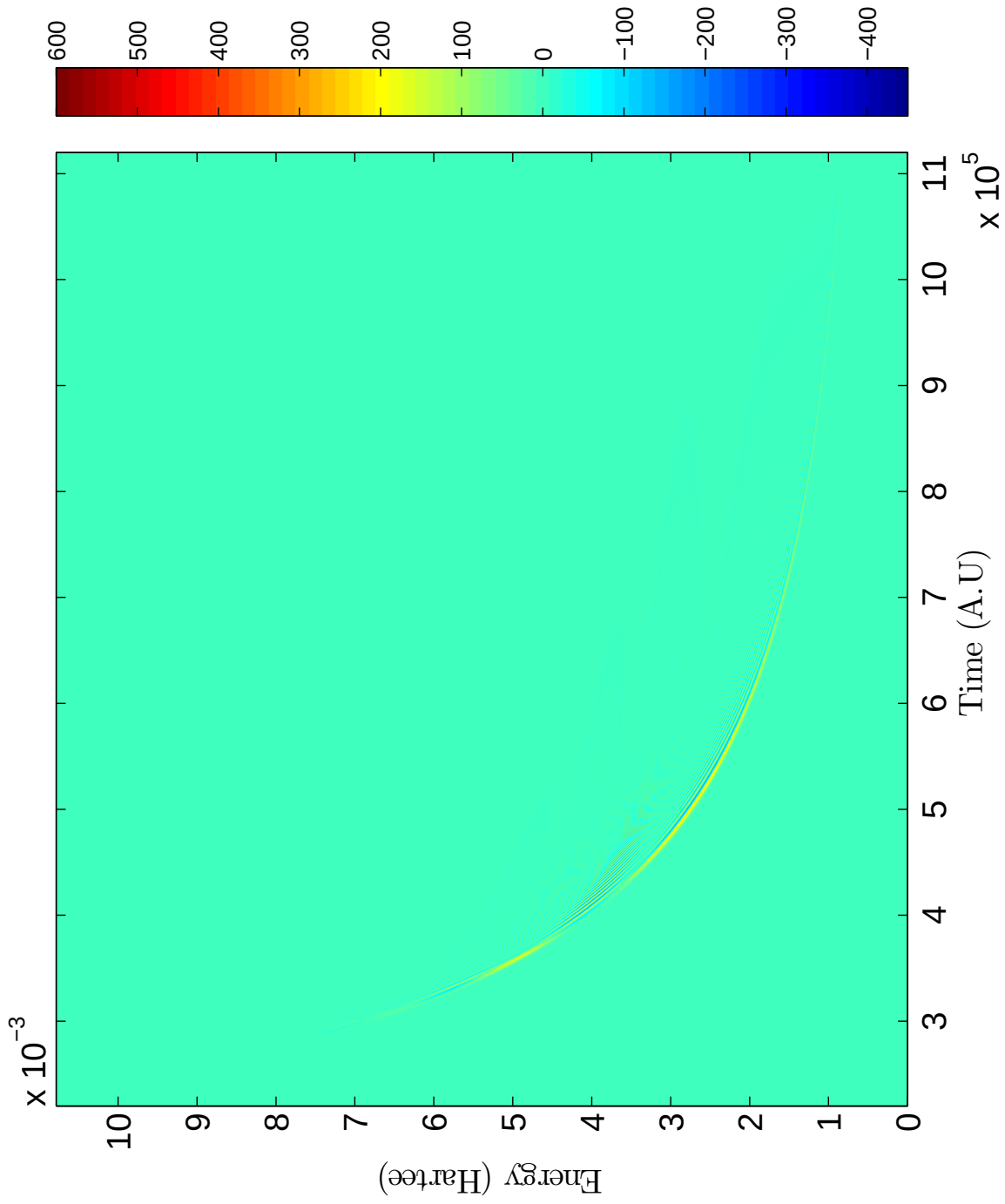


Figure 6.104: Scattering Wigner Distribution Function for Rb+Ne system with reactant Møller state in $|^{\frac{3}{2}}_{\frac{1}{2}}>$, product Møller state in $|^{\frac{3}{2}}_{\frac{3}{2}}>$, and $J = 200.5$

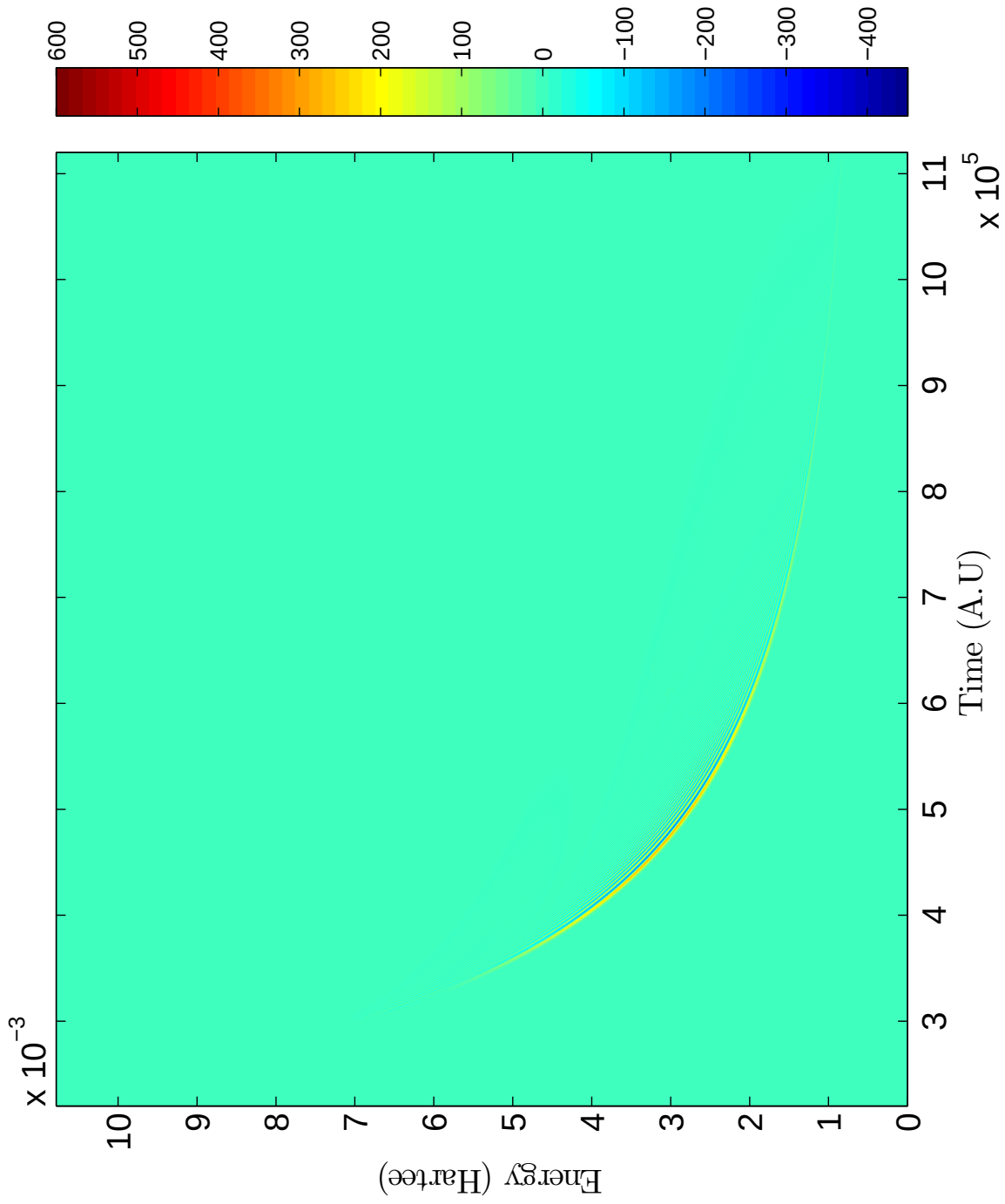


Figure 6.105: Scattering Wigner Distribution Function for Rb+Ne system with reactant Møller state in $|^{\frac{3}{2}}_{\frac{1}{2}}>$, product Møller state in $|^{\frac{3}{2}}_{\frac{3}{2}}>$, and $J = 250.5$

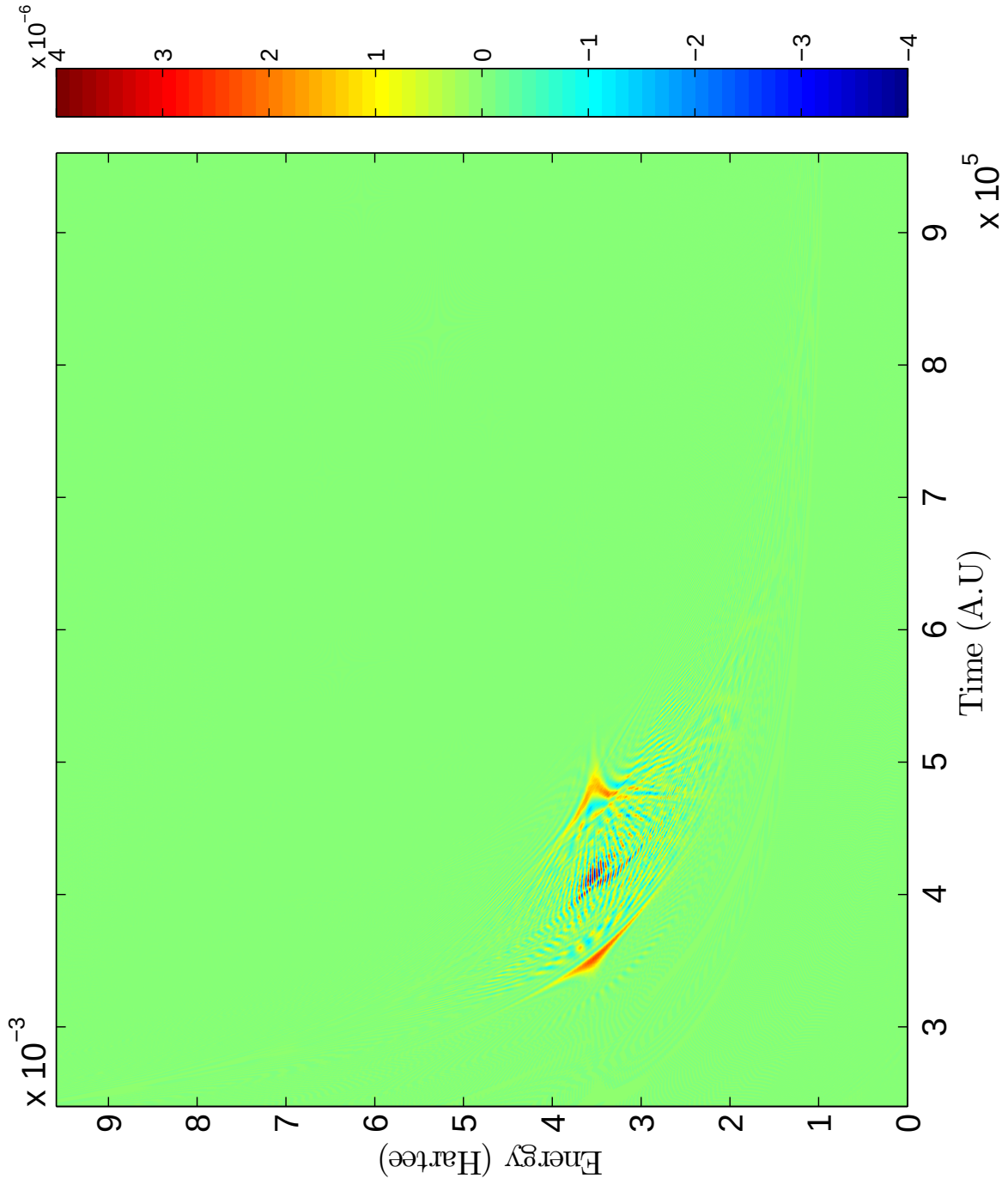


Figure 6.106: Scattering Wigner Distribution Function for Cs+Ne system with reactant Møller state in $|^{\frac{3}{2}}_{\frac{1}{2}}>$, product Møller state in $|^{\frac{1}{2}}_{\frac{1}{2}}>$, and $J = 1.5$. Note that most of the detail in this figure is numerical error associated with the Fourier transform. The error is visible because the scale is on the order of $10^{-6}$.

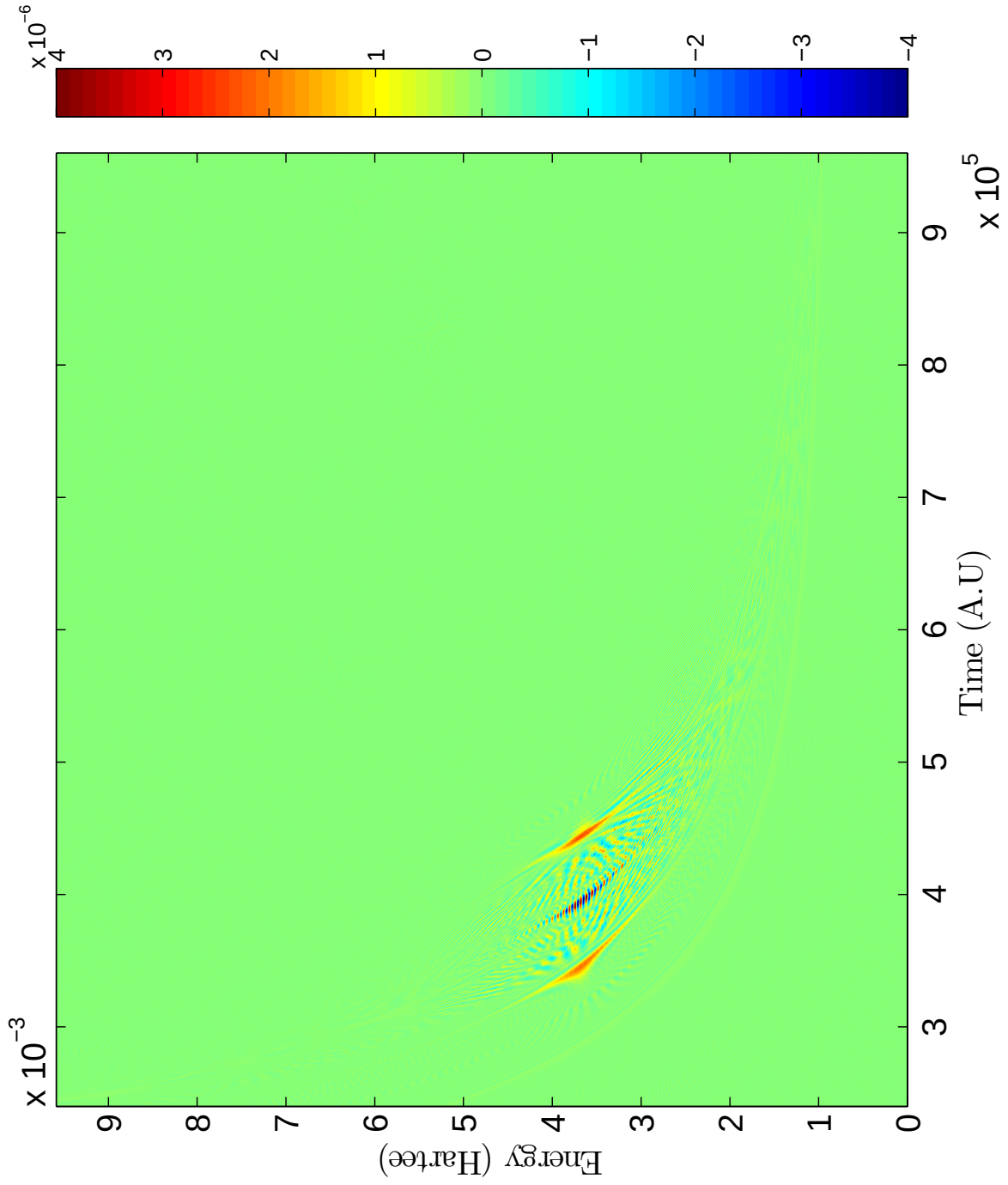


Figure 6.107: Scattering Wigner Distribution Function for Cs+Ne system with reactant Møller state in $|^{\frac{3}{2}}_{\frac{1}{2}}>$, product Møller state in $|^{\frac{1}{2}}_{\frac{1}{2}}>$, and $J = 50.5$. Note that most of the detail in this figure is numerical error associated with the Fourier transform. The error is visible because the scale is on the order of $10^{-6}$.

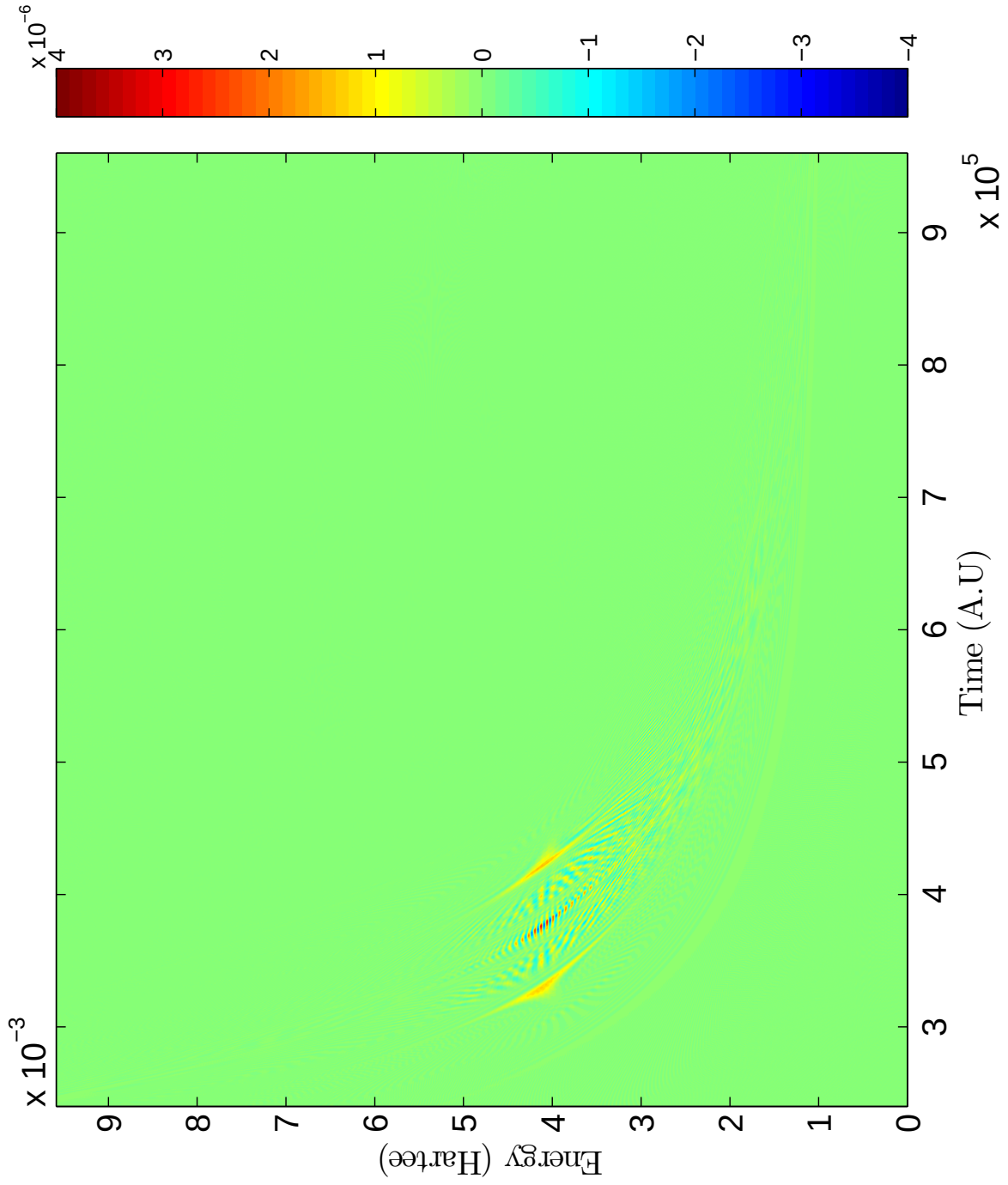


Figure 6.108: Scattering Wigner Distribution Function for Cs+Ne system with reactant Møller state in $|^{\frac{3}{2}}_{\frac{1}{2}}>$, product Møller state in $|^{\frac{1}{2}}_{\frac{1}{2}}>$, and $J = 100.5$. Note that most of the detail in this figure is numerical error associated with the Fourier transform. The error is visible because the scale is on the order of $10^{-6}$.

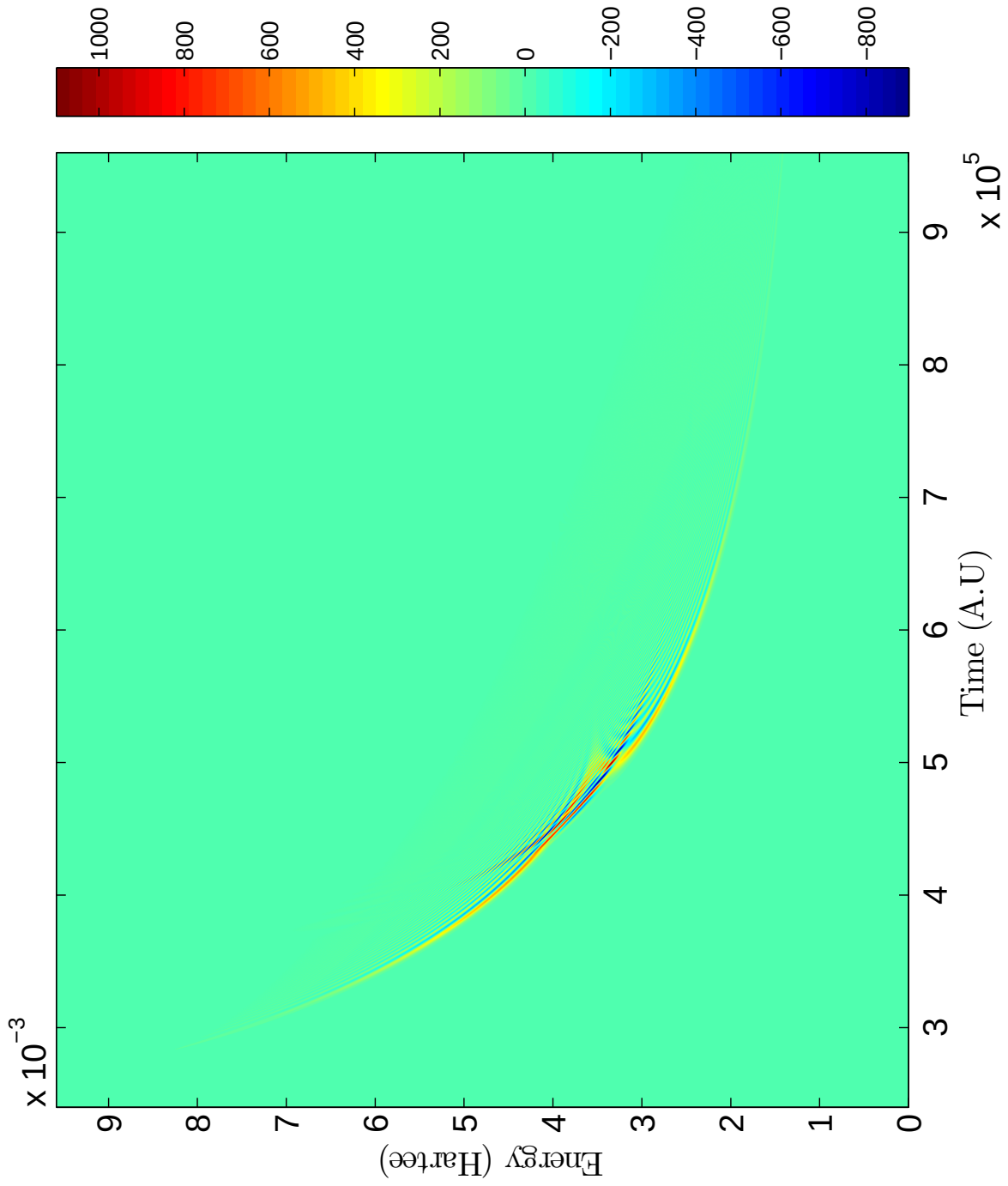


Figure 6.109: Scattering Wigner Distribution Function for Cs+Ne system with reactant Møller state in $|^{\frac{3}{2}}_{\frac{1}{2}}>$, product Møller state in $|^{\frac{3}{2}}_{\frac{1}{2}}>$, and $J = 1.5$

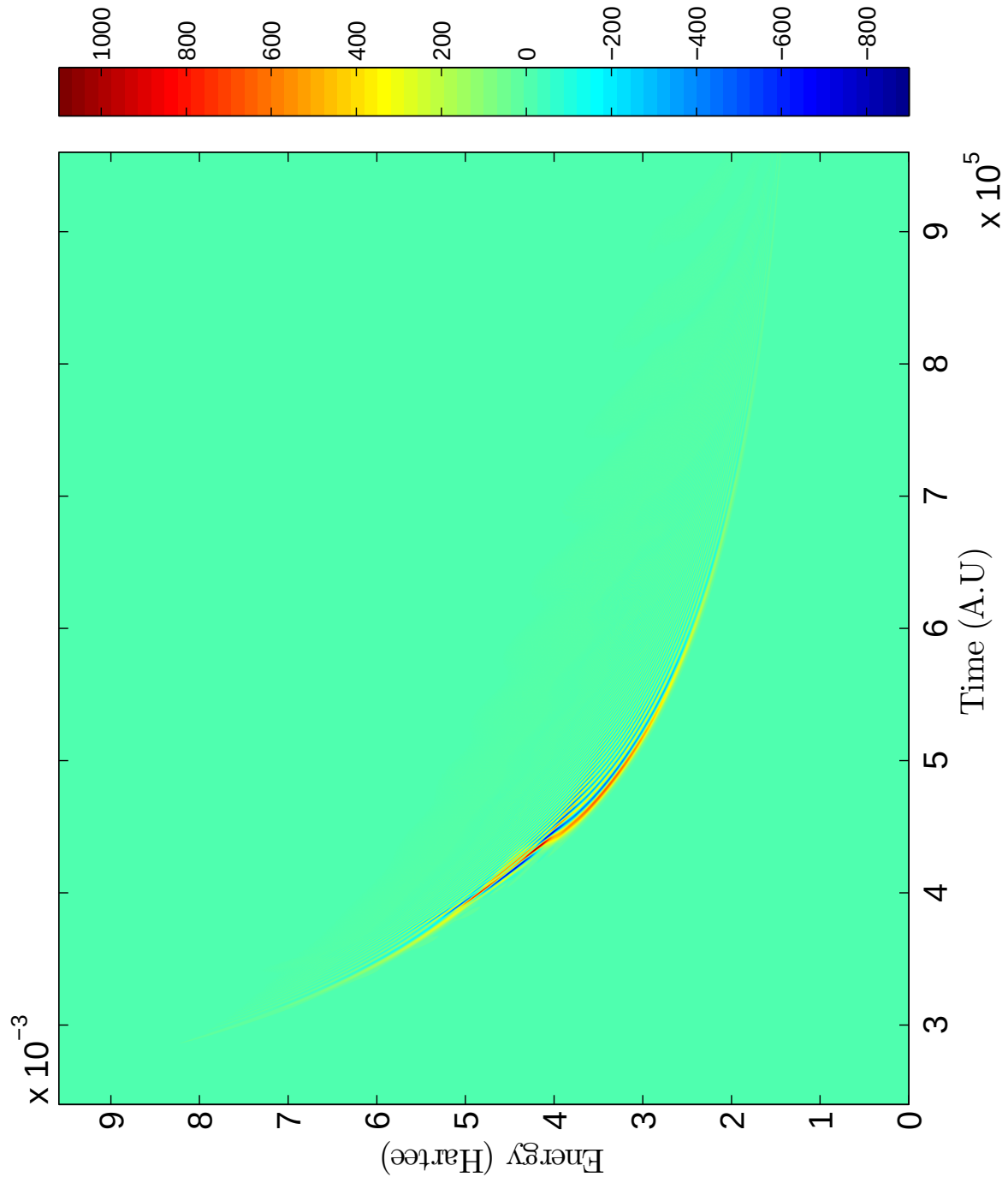


Figure 6.110: Scattering Wigner Distribution Function for Cs+Ne system with reactant Møller state in $|^{\frac{3}{2}}_{\frac{1}{2}}>$, product Møller state in $|^{\frac{3}{2}}_{\frac{1}{2}}>$, and $J = 50.5$

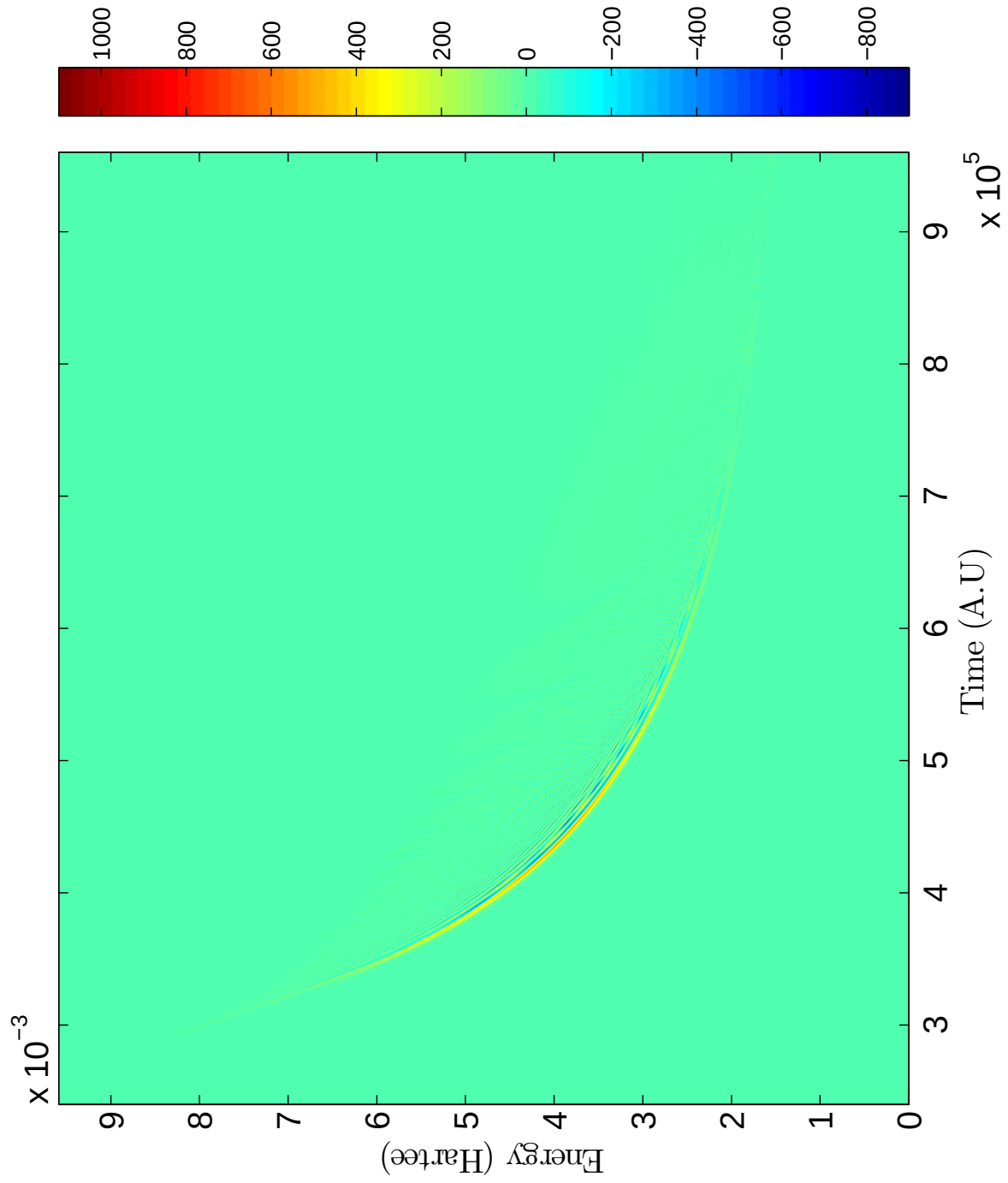


Figure 6.111: Scattering Wigner Distribution Function for Cs+Ne system with reactant Møller state in $|^{\frac{3}{2}}_{\frac{1}{2}}>$, product Møller state in $|^{\frac{3}{2}}_{\frac{1}{2}}>$, and $J = 100.5$

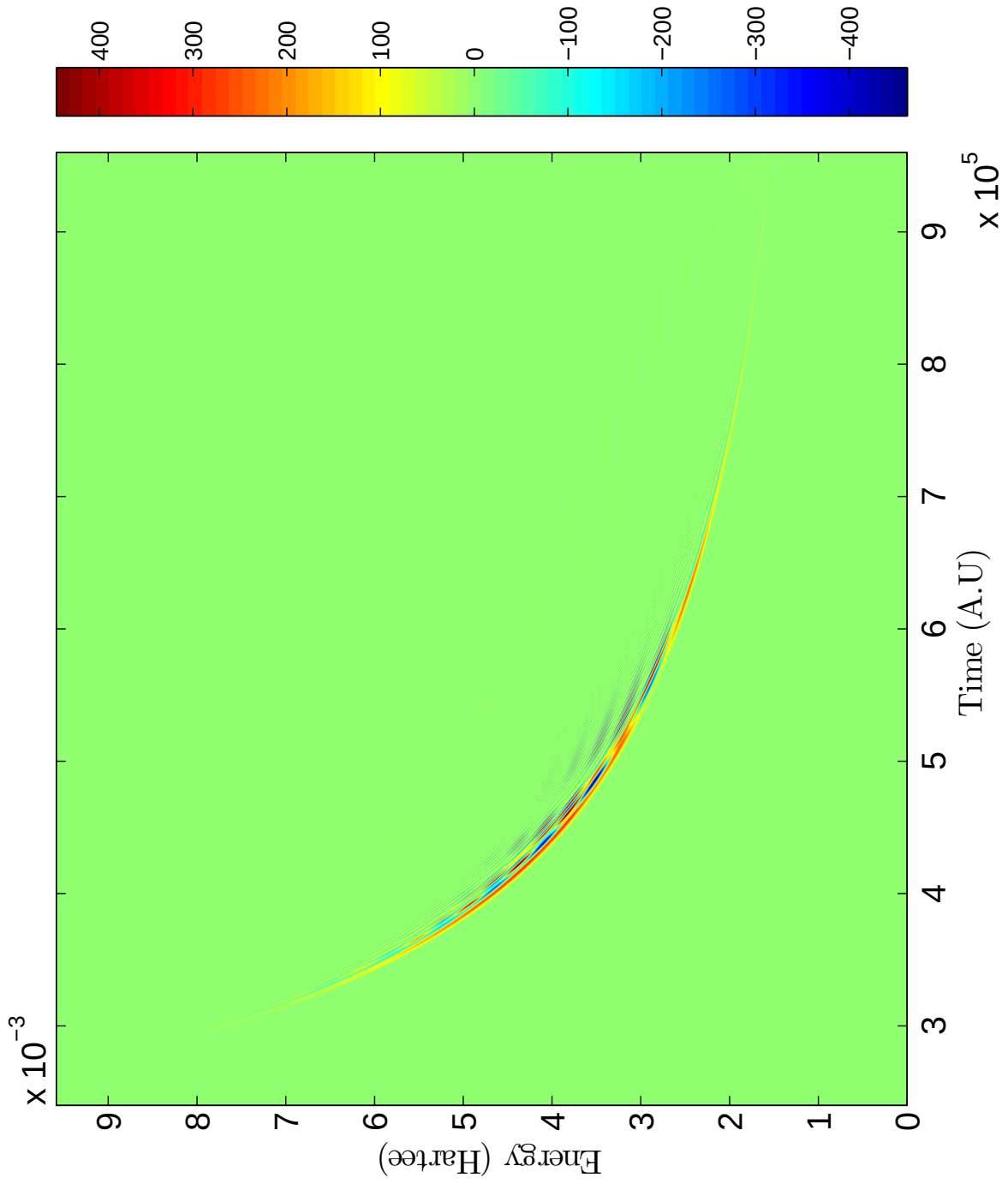


Figure 6.112: Scattering Wigner Distribution Function for Cs+Ne system with reactant Møller state in $|^{\frac{3}{2}}_{\frac{1}{2}}>$, product Møller state in $|^{\frac{3}{2}}_{\frac{1}{2}}>$, and $J = 150.5$

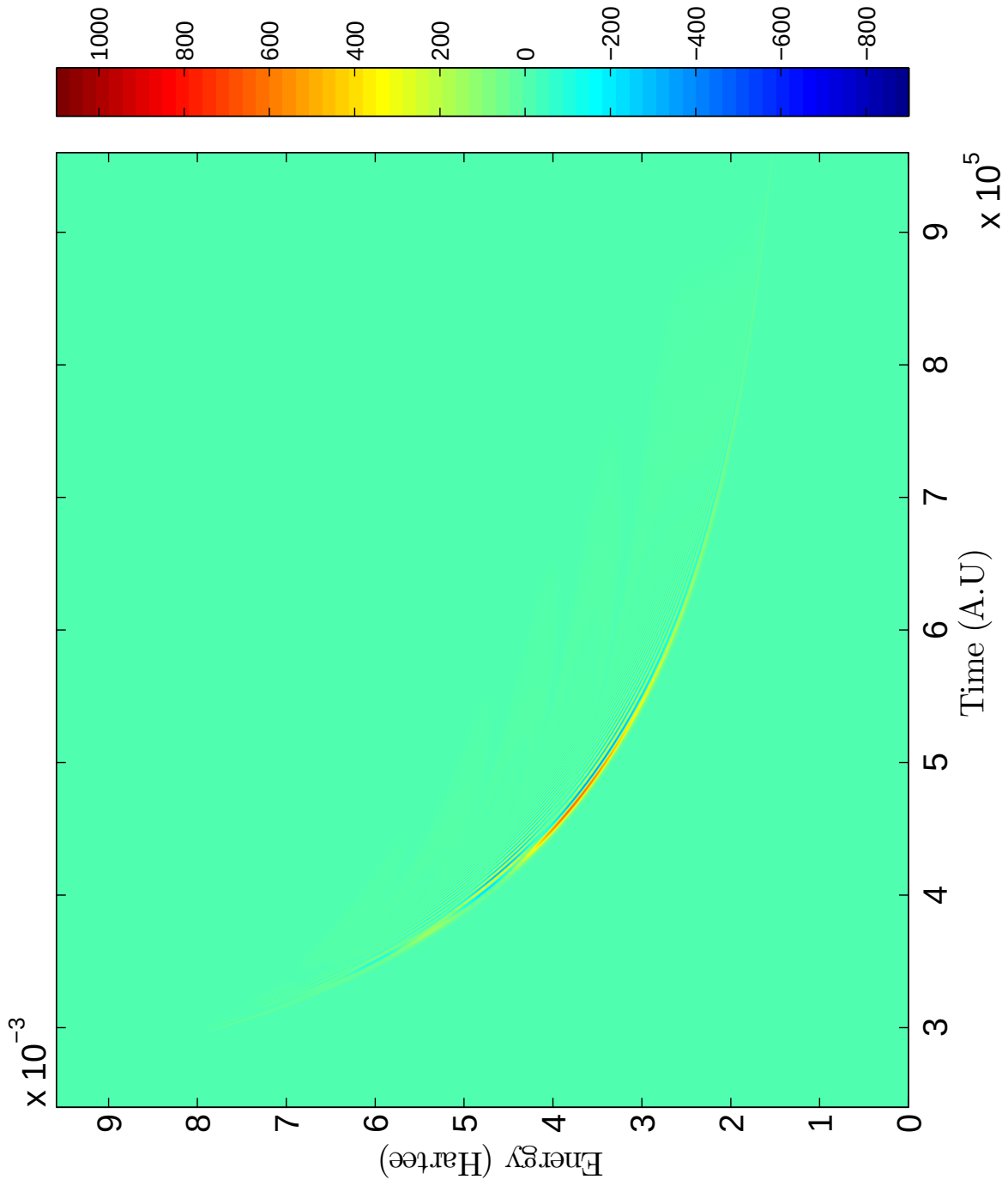


Figure 6.113: Scattering Wigner Distribution Function for Cs+Ne system with reactant Møller state in $|^{\frac{3}{2}}_{\frac{1}{2}}>$, product Møller state in $|^{\frac{3}{2}}_{\frac{1}{2}}>$, and $J = 200.5$

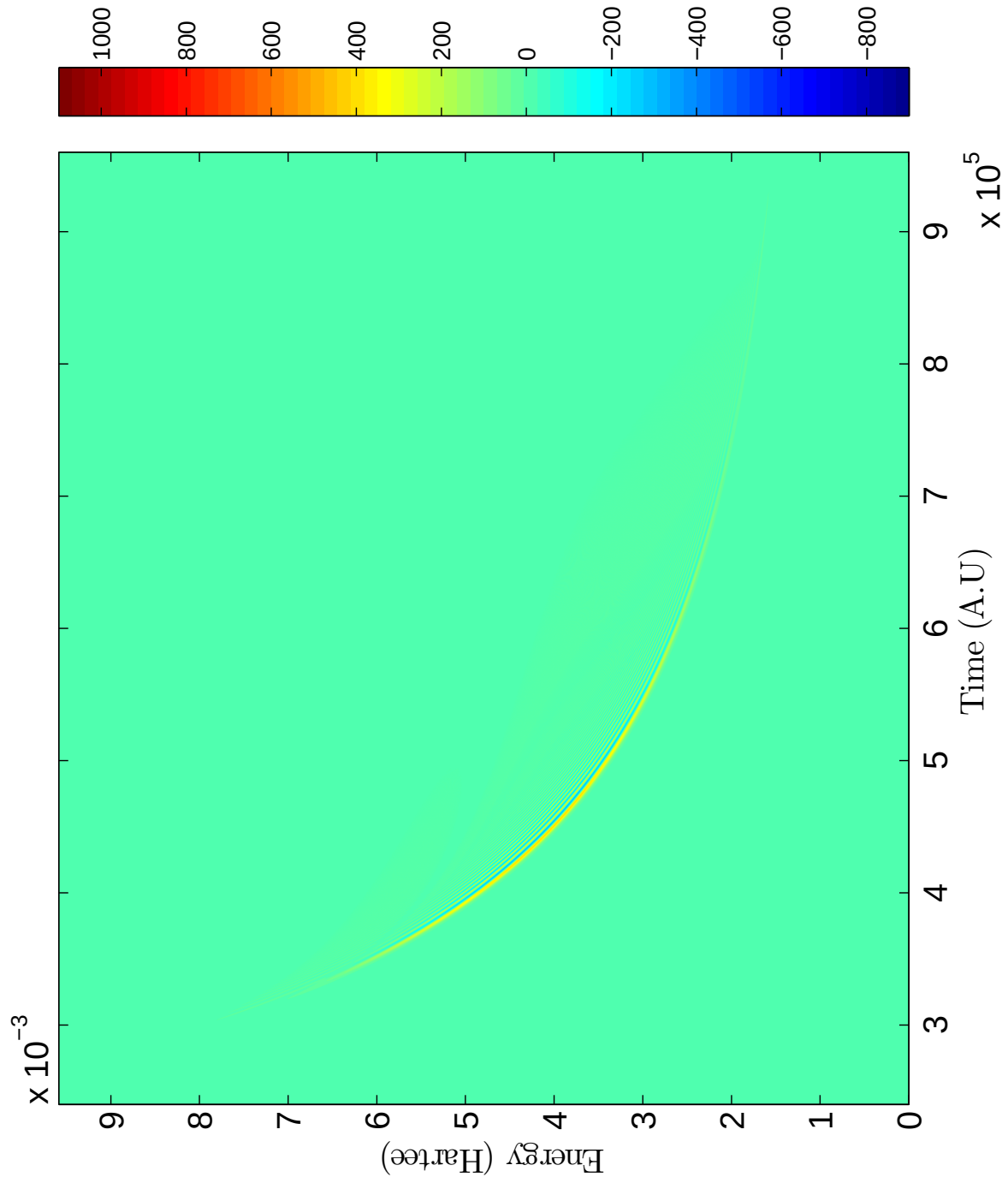


Figure 6.114: Scattering Wigner Distribution Function for Cs+Ne system with reactant Møller state in $|^{\frac{3}{2}}_{\frac{1}{2}}>$, product Møller state in $|^{\frac{3}{2}}_{\frac{1}{2}}>$, and $J = 250.5$

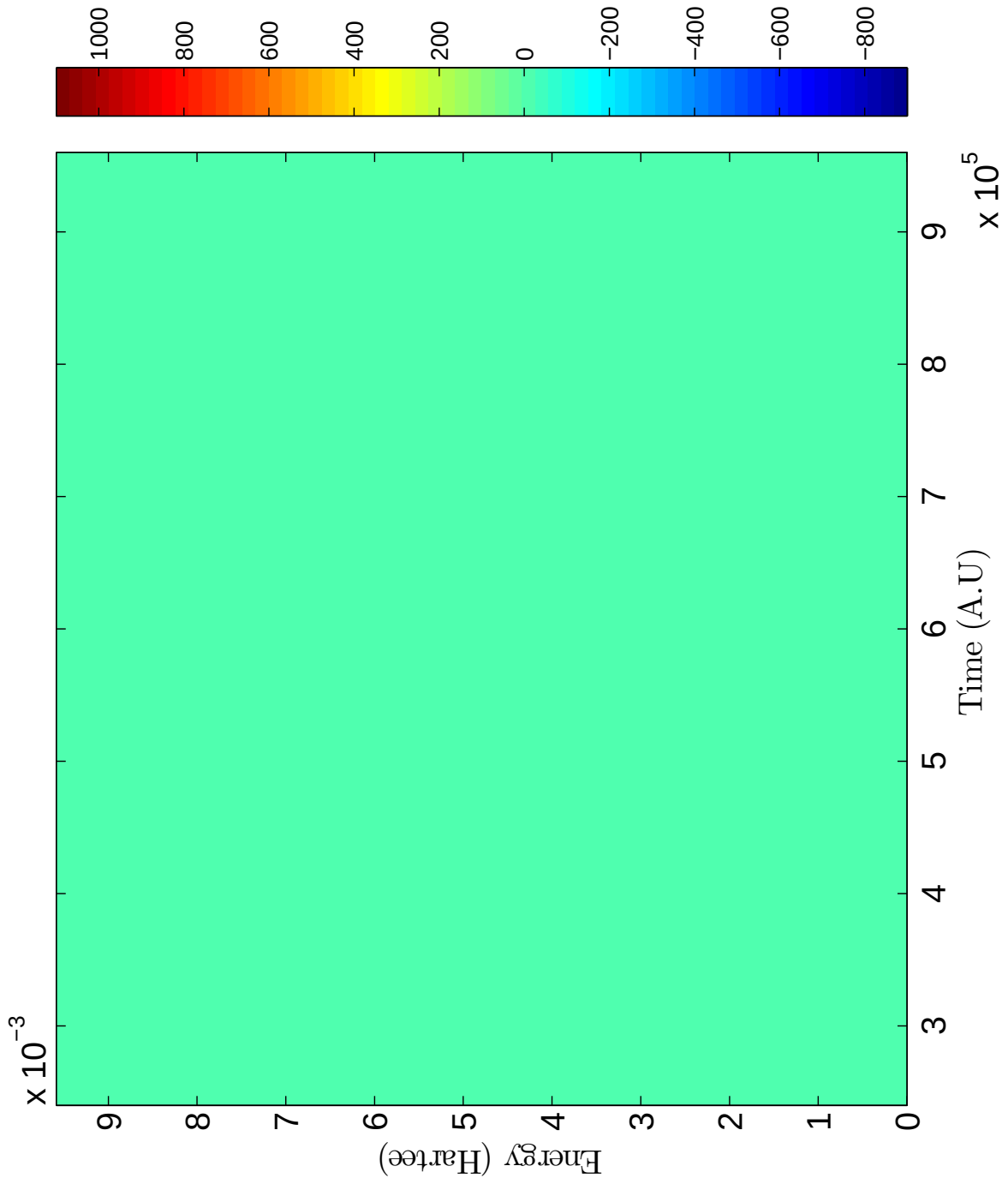


Figure 6.115: Scattering Wigner Distribution Function for Cs+Ne system with reactant Møller state in $|^{\frac{3}{2}}_{\frac{1}{2}}>$, product Møller state in $|^{\frac{3}{2}}_{\frac{3}{2}}>$, and $J = 1.5$

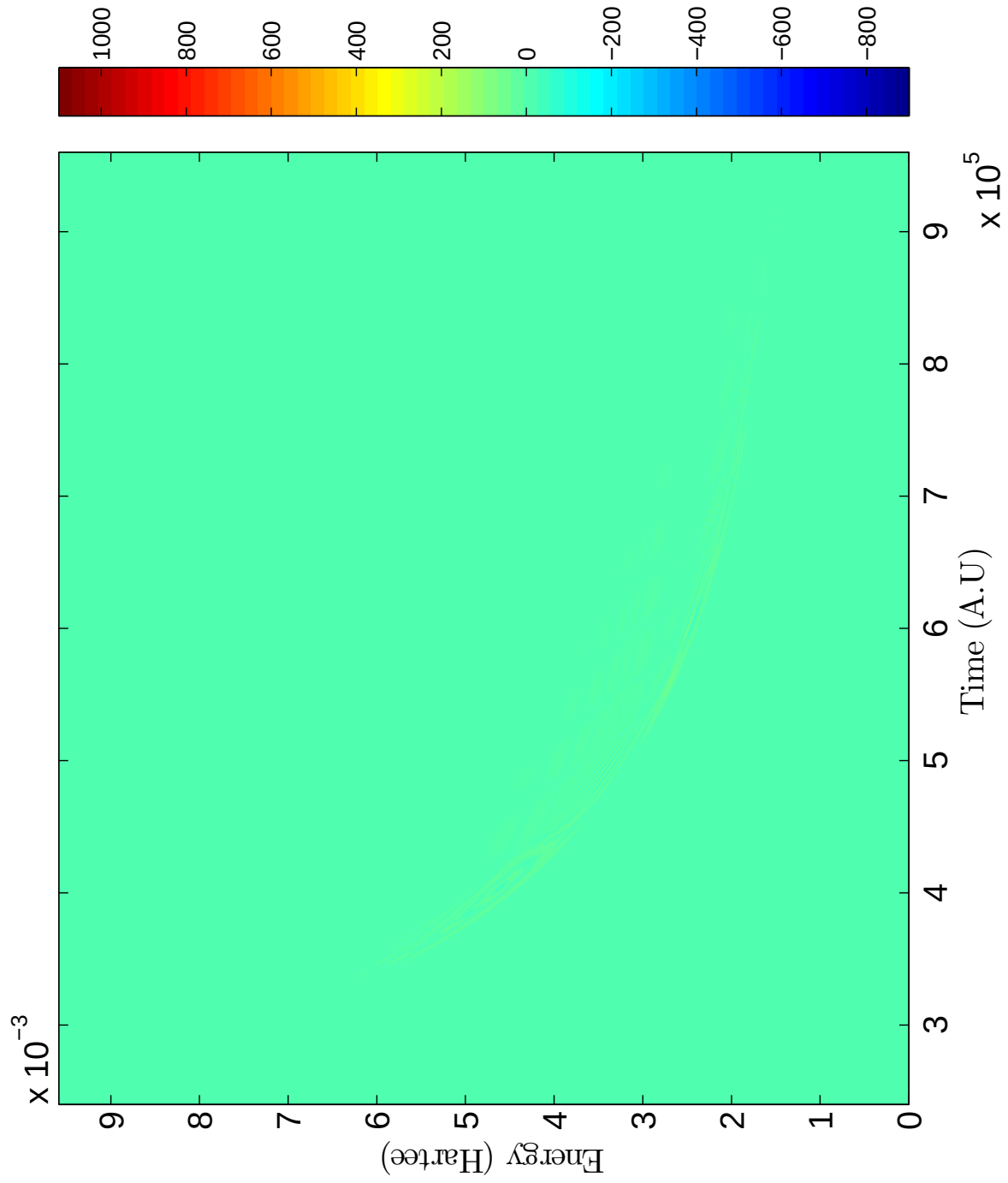


Figure 6.116: Scattering Wigner Distribution Function for Cs+Ne system with reactant Møller state in $|^{\frac{3}{2}}_{\frac{1}{2}}>$, product Møller state in $|^{\frac{3}{2}}_{\frac{3}{2}}>$, and $J = 50.5$

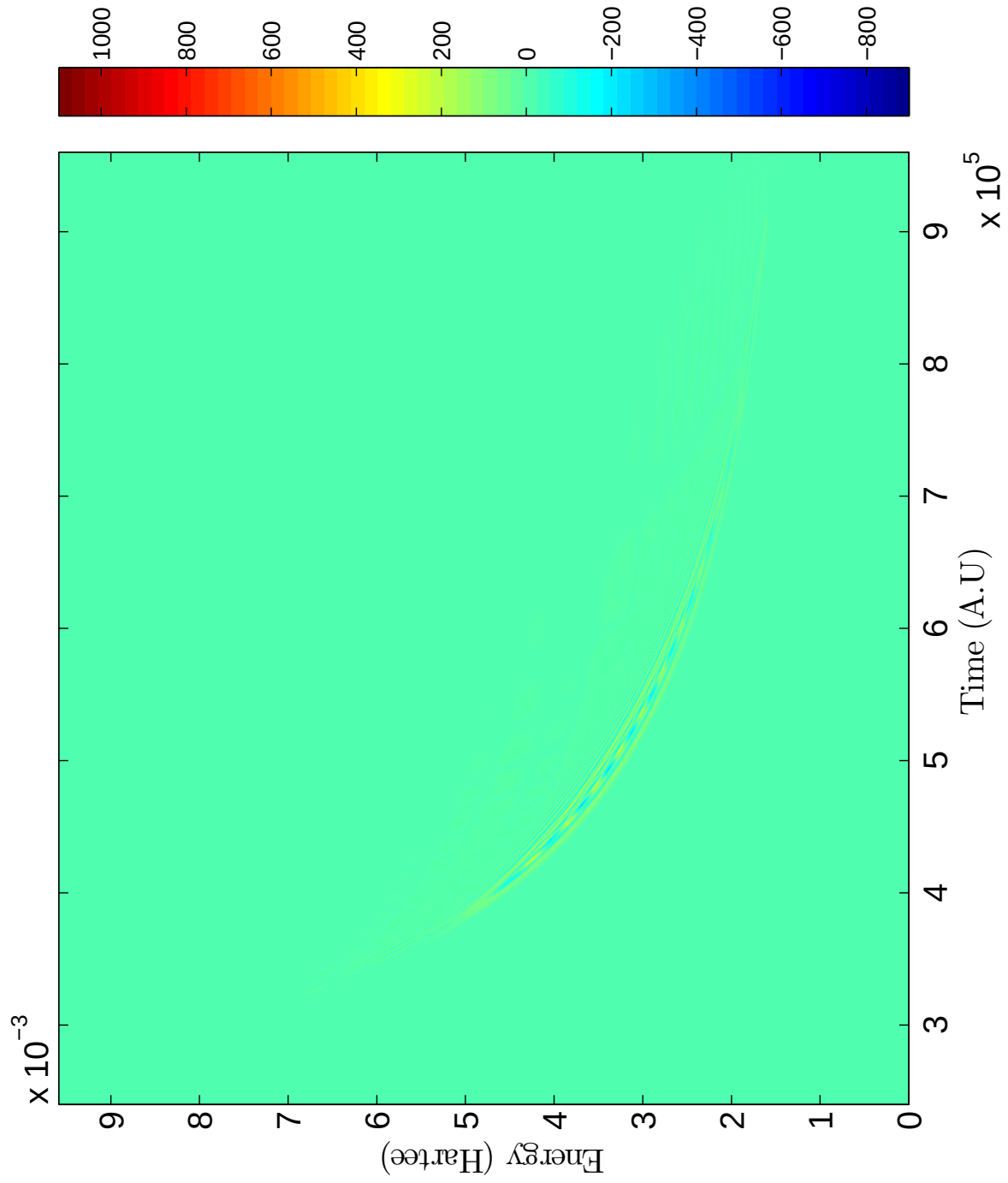


Figure 6.117: Scattering Wigner Distribution Function for Cs+Ne system with reactant Møller state in $|^{\frac{3}{2}}_{\frac{1}{2}}>$, product Møller state in $|^{\frac{3}{2}}_{\frac{3}{2}}>$, and $J = 100.5$

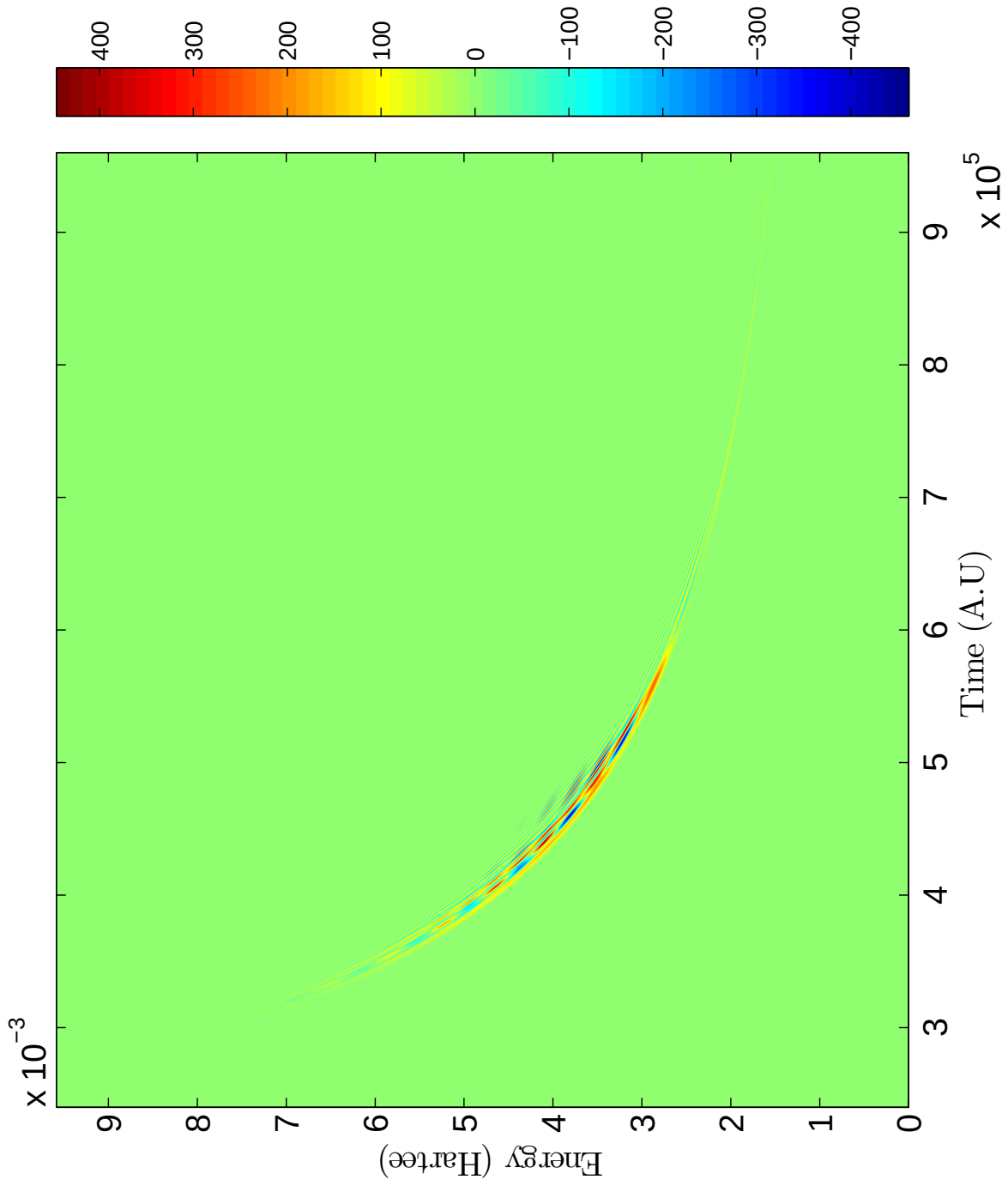


Figure 6.118: Scattering Wigner Distribution Function for Cs+Ne system with reactant Møller state in $|^{\frac{3}{2}}_{\frac{1}{2}}>$, product Møller state in $|^{\frac{3}{2}}_{\frac{3}{2}}>$, and $J = 150.5$

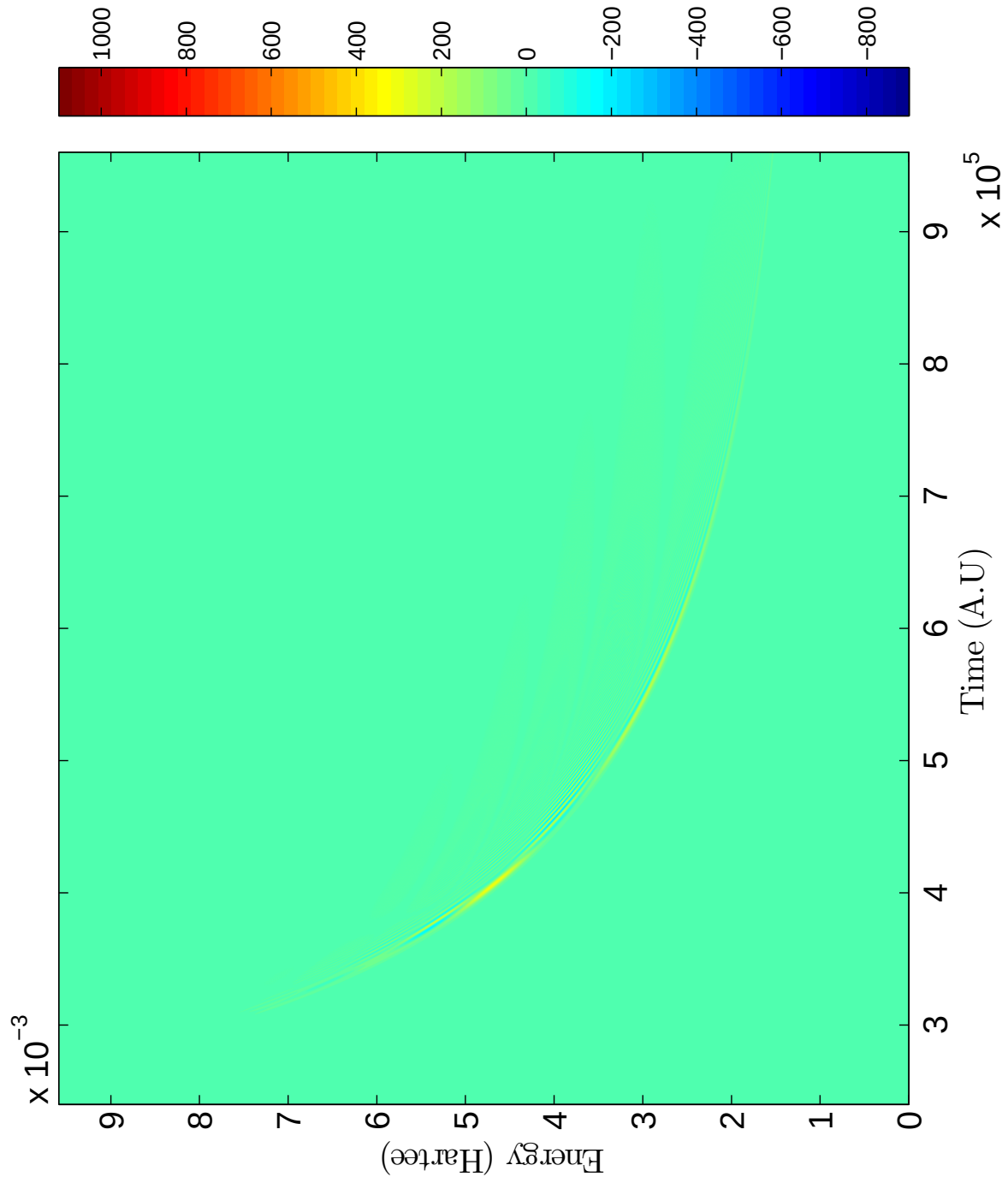


Figure 6.119: Scattering Wigner Distribution Function for Cs+Ne system with reactant Møller state in $|^{\frac{3}{2}}_{\frac{1}{2}}>$, product Møller state in $|^{\frac{3}{2}}_{\frac{3}{2}}>$, and $J = 200.5$

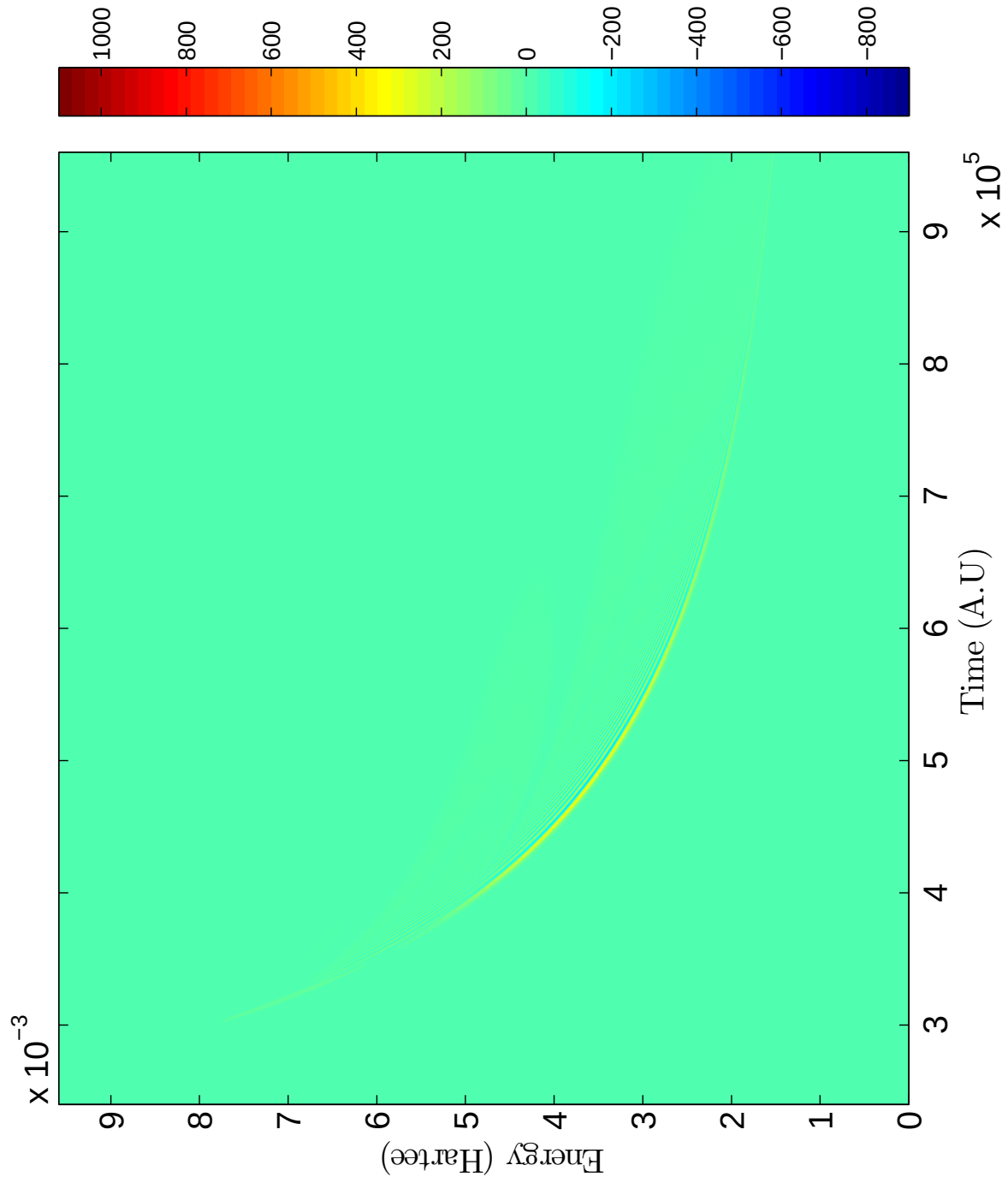


Figure 6.120: Scattering Wigner Distribution Function for Cs+Ne system with reactant Møller state in $|^{\frac{3}{2}}_{\frac{1}{2}}>$, product Møller state in $|^{\frac{3}{2}}_{\frac{3}{2}}>$, and $J = 250.5$

### *6.2.6 Negative Chirp.*

Like the square well problem, we are interested in the shape of the negative Chirp that the scattering WDF makes in the time-energy axis. We to get a rough idea of the classical trajectory that a particle with a certain energy makes while under the influence of the Hamiltonian defined in Eq. 6.2. From the adiabatic potential energy surfaces, we assume that we have a particle in a zero-potential field. This particle will collide elastically with an infinitely high wall. The location of the wall is determined by the intersection of the peak momentum of the reactant Møller state with the adiabatic potential energy surface. The potential energy surface used is the surface at which the reactant Møller state starts on. For this example, we will use the $|^{\frac{1}{2}}_{\frac{1}{2}}>$ adiabatic surface. Let $d$ be the distance between the location of the wall and the location of reactant Møller state. Because the classical particle experiences no potential, the total energy is the kinetic energy which is $E = \frac{1}{2}\mu v^2$. For a given velocity $v$, the time the particle takes to travel to the wall and back to the starting location (which is where the product Møller state is located) is given by $t = \frac{2d}{v}$. In this model, the energy time relation is given by

$$E = \frac{2d^2\mu}{t^2} \tag{6.4}$$

Although this model is simple, the square well and barrier like features on the adiabatic PES will have a perturbing effect on Eq. 6.4. Using the same Matlab imaging statistical analysis techniques that were used for the square well chirp, we can arrive at an energy-time relation. A power curve of the form $E = at^b$, where $a$, $b$, and $c$ are fit parameters, provided the best fit with $b = -2.119 \pm 0.001$ on a 99 % confidence interval. The same curve was also placed on top of the scattering WDF associated with $c^{\frac{1}{2},\frac{3}{2}}_{\frac{1}{2},\frac{3}{2}}(t)$ and $c^{\frac{3}{2},\frac{3}{2}}_{\frac{3}{2},\frac{3}{2}}(t)$ correlation functions. The values of the scattering WDF for each correlation function were plotted on the same scale in order to see the overlap of peaks within each band as shown in Fig. 6.121. This calculation was repeated for multiple bands. At high energies and short

times, the peaks are relatively out of phase at low energies and long times, the peaks are relatively in phase.

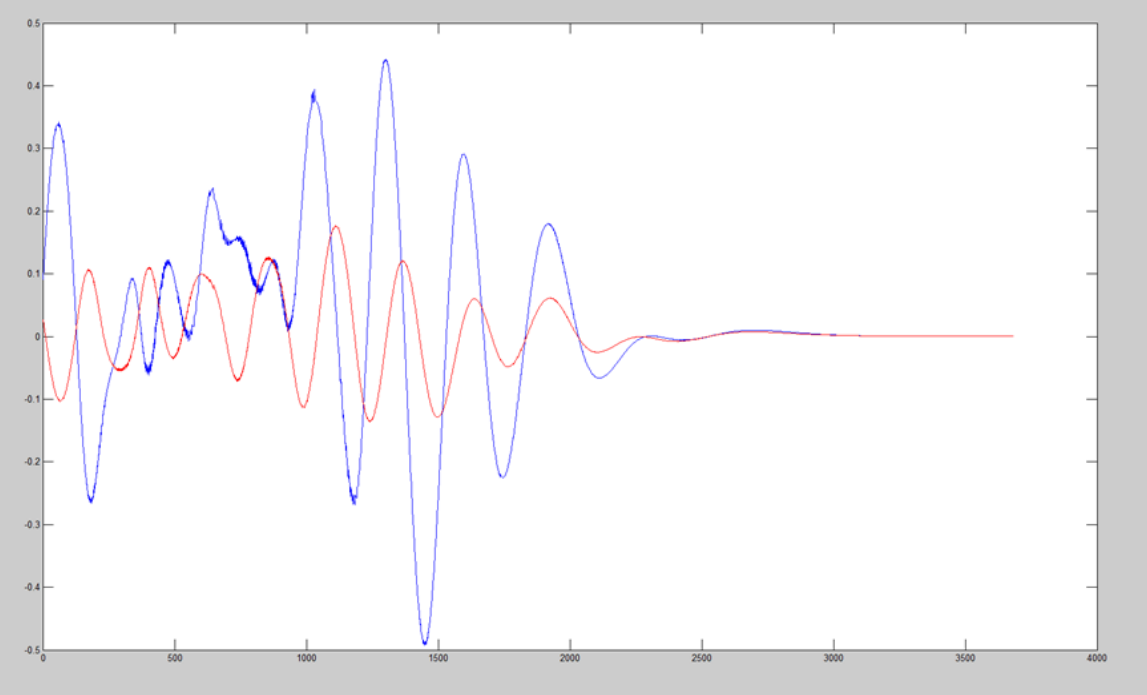


Figure 6.121: Amplitude of the Scattering WDF for the product Møller states on the $|^{\frac{3}{2}}_{\frac{1}{2}}>$ (blue line) and the $|^{\frac{3}{2}}_{\frac{3}{2}}>$ (red line) surfaces along the chirp at $J = 100.5$ for the $K + Ne$ system. The shape of the chirp was determined from the scattering WDF for the $|^{\frac{1}{2}}_{\frac{1}{2}}>$ surface. The x-axis corresponds to a point along the chirp while the y-axis is the amplitude of the scattering WDF.

# VII. Conclusion

The scattering Wigner Distribution Function was able to give us some insight into the alkali metal plus noble gas collision. The square well scattering WDF provided insight into interpreting the meaning behind the positive and negative values of the scattering WDF. Due to the property of the scattering WDF that the integrated projection must be the related to the s-matrix element up to a normalization factor, the positive values corresponds to the presence of probability at a particular energy in a moment in time. The negative values correspond to the loss of probability at that surface at a particular energy in a moment of time. The location of this "lost" probability most likely ended up in the reflection coefficient, but further analysis must be done before this can be confirmed. The zero value of the scattering WDF means that the probability was elsewhere in the system.

Using this interpretation for the meaning behind the values of the scattering WDF, we were able to comprehend the meaning behind the scattering WDF for the $M + Ng$ collision. As the total angular momentum $J$ increased, the Coriolis coupling and effective potential grew stronger while the strength of the radial coupling remained constant. If the reactant Møller state started on the $|^{\frac{3}{2}}_{\frac{1}{2}}>$ surface, there was a value of $J$ such that the transfer of probability to the $|^{\frac{3}{2}}_{\frac{1}{2}}>$ surface was cut drastically reduced compared to when $J = 1.5$. As the mass of the noble gas partner increased, the value of $J$ at which the probability on the $|^{\frac{1}{2}}_{\frac{1}{2}}>$ surface began to diminish increased. Although the peak amount of probability transferred to the $|^{\frac{1}{2}}_{\frac{1}{2}}>$ was diminished for heavier noble gas atoms than lighter atoms, the range of total angular momentum for which there were significant probability transfer was much greater for the heavier noble gas atoms.

Future work can focus on further investigating the correlation between the number of bands with oscillating peaks and valleys and the amplitude of the scattering WDF. From the square well, we see that the number of bands with oscillating peaks and valleys increased

as the well depth increased which corresponded to an increase in probability of being transmitted through the square well on the secondary transmissions. The appearance of these bands of oscillating peaks and valleys in the $M + Ng$ system correlated with the amplitude of the scattering WDF. The dip like structure that was found in the amplitude of the scattering WDF for the product Møller state on the $|^{\frac{3}{2}}_{\frac{1}{2}}>$ surface corresponded to the absence of these bands. The amplitude of the scattering WDF for the $|^{\frac{1}{2}}_{\frac{1}{2}}>$ surface should be plotted in order to see if there is a corresponding peak at this surface. Work was focused on the frequency at which the bands present in the scattering WDF for the $M + Ng$ arrived at the product Møller state; however, perhaps the frequency of bands with oscillating peaks and valleys or the number of oscillating peaks and valleys should be focused on instead. Future work could also focus on different phase space representations of the scattering event. The Wigner Distribution Function belongs to the Cohen class of distributions[2, 15]. One such function that can be studied is the ambiguity function. The ambiguity function is the double Fourier transform of the Wigner Distribution Function with respect to delay time and energy values, $\tau$ and $\xi$. Future work can involve applying the scattering WDF to various other collisional systems of interest or could involve more detailed studies of the current systems of interest. For example, the scattering WDF could be computed for the coupling between higher energy states in the $H + H_2$, $OH + CO$, and $M + Ng$ systems.

## Bibliography


[1] Verdeyen, J. *Laser Electronics*, Upper Saddle River, New Jersey: Prentice Hall, 1995

[2] Testorf, M., Hennelly, B., and Ojega-Castaneda, J. *Phase-Space Optics: Fundamentals and Applications*, The McGraw-Hill Companies, 2010

[3] Press W., Teukolsky, S., Vetterling, W., and Flannery B. *Numerical Recipes in Fortran 77*, Second Edition, Cambridge University Press, 1992

[4] Cohen-Tannoudji, C., Diu, B., and Laloe, F. *Quantum Mechanics* John Wiley and Sons, Inc., 2005

[5] Griffiths, D. *Introduction to Quantum Mechanics*, Second Edition, New Jersey: Prentice Hall, 2005

[6] Taylor, J. *Classical Mechanics*,University of Science, 2005

[7] Lacy, B. *A Wigner Distribution Analysis of One Dimensional Scattering*, Masters Thesis, Air Force Institute of Technology, 2009

[8] Lewis, C. *Non-Adiabatic Atomic Transitions: Computational Cross Section Calculations of Alkali Metal-Noble Gas Collions*, PhD Dissertation, Air Force Institute of Technology, 2011

[9] Loper, R. *Collisional Broadening and Shift of D1 and D2 Spectral Lines in Atomic Alkali Vapor-Noble Gas Systems*, PhD Dissertation, Air Force Institute of Technology, 2013

[10] Schatz, G. and Dyck, J. *Chem. Phys. Letters*, 188:11,1992

[11] Calfas, R. and Weeks, D. "A new application of absorbing boundary conditions for computing collinear quantum reactive scattering matrix elements". *Chem. Phys. Letters* 263:292-296,1996

[12] Siegbahn, P. and Liu, B. *Journal of Chem. Phys.*, 68:2457,1978

[13] Truhlar, D. and Horowitz, C. *Journal of Chem. Phys.* 68:2466,1978

[14] Case, W. "Wigner functions and Weryl transforms for pedestrians" *Am. Journal Phys.*, 76(10):937-946,2008

[15] Hillary, M., O'Connel, R., Scully, M, and Wigner, E. "Distribution Functions in Physics: Fundamentals" *Phys. Reports*, 106(3):121-167, 1984

[16] Tannor, D. and Weeks, D. "Wave packet correlation function formulation of scattering theory: The quantum analog of classical S-matrix theory" *Journal of Chem. Phys.*,98(5):3884-3893,1993

[17] Weeks, D. Niday, T., and Yang, S. "Inelastic scattering matrix elements for the nonadiabatic collision $B(^2P_{\frac{1}{2}}) + H_2(^1\Sigma_g^+, j) \leftrightarrow B(^2P_{\frac{3}{2}}) + H_2(^1\Sigma_g^+, j')$" *Journal of Chem Phys.*,125(164301):1-14,2006

[18] Blank, L., Weeks, D., and Kedziora, G. "M+Ng potential energy curves including spin-orbit coupling for M=K, Rb, Cs and Ng=He, Ne, Ar" *Journal of Chem. Phys.*,136(124315):1-8, 2012

[19] Stakgold, I. and Holst, M. *Green's Functions and Boundary Value Problems*, Third Edition, New Jersey: John Wiley and Sons Inc, 2011

[20] Combes, J. and Seiler, R. "Spectral Properties of Atomic and Molecular Systems". *Quantum Dynamics of Molecules*, Plentum Press,pg. 435-482, 1980

[21] Claasen, T. and Mecklenbrauker, W. "The Wigner Distribution-A Tool for Time-Frequency Signal Analysis part 1: Continuous-Time Signals". *Phillips Journal of Research*,35(3)1980

[22] Brenath, P. *Spectra of Atoms and Molecules*, Second Edition, Oxford University Press, 2005

[23] Taylor, J. *Scattering Theory: The Quatnum Theory of Nonrelativistic Collisions*, Florida: Krieger Publishing Company, 1972

[24] Merzbacher, E. *Quantum Mechanics* Second Edition, John Wiley and Sons Inc, 1970

[25] Zhang, J. *Theory and Application of Quantum Molecular Dynamics*, World Scientific Pub Co, 1999

# REPORT DOCUMENTATION PAGE

*Form Approved*
*OMB No. 0704–0188*



| 1. REPORT DATE *(DD–MM–YYYY)* | 2. REPORT TYPE | 3. DATES COVERED *(From — To)* |
|---|---|---|
| 27–03–2014 | Master's Thesis | Oct 2012–Mar 2014 |

**4. TITLE AND SUBTITLE**

Wigner Distribution Functions as a Tool for Studying Gas Phase Alkali Metal Plus Noble Gas Collisions

**5a. CONTRACT NUMBER**

**5b. GRANT NUMBER**

**5c. PROGRAM ELEMENT NUMBER**

**6. AUTHOR(S)**

Wyman, Keith A., Second Lieutenant, USAF

**5d. PROJECT NUMBER**

**5e. TASK NUMBER**

**5f. WORK UNIT NUMBER**

**7. PERFORMING ORGANIZATION NAME(S) AND ADDRESS(ES)**

Air Force Institute of Technology
Graduate School of Engineering and Management (AFIT/EN)
2950 Hobson Way
WPAFB, OH 45433-7765

**8. PERFORMING ORGANIZATION REPORT NUMBER**

AFIT-ENP-14-M-39

**9. SPONSORING / MONITORING AGENCY NAME(S) AND ADDRESS(ES)**

High-Energy Laser Joint Technology Office
801 University Blvd Se
Ste 209
Albuquerque, NM 87106
505-248-8208, Harro.Ackerman@jto.hpc.mil

**10. SPONSOR/MONITOR'S ACRONYM(S)**

HEL JTO

**11. SPONSOR/MONITOR'S REPORT NUMBER(S)**

**12. DISTRIBUTION / AVAILABILITY STATEMENT**

DISTRIBUTION STATEMENT A: APPROVED FOR PUBLIC RELEASE; DISTRIBUTION UNLIMITED

**13. SUPPLEMENTARY NOTES**



**14. ABSTRACT**

Wave packet propagation methods are used to compute scattering Wigner Distribution Functions (WDF) for the square well potential, square barrier potential, and the $H+H_2$ and $OH+CO$, and several $M+Ng$ collisions. The scattering WDF are used to interpret how probabilities flow among various potential energy surfaces as a function of time during a collision. Positive values of the scattering WDF correspond to the addition of probability to scatter into the state that corresponds to the asymptotic limit of the potential energy surface of interest. Negative values correspond to the loss of probability to scatter into the state that corresponds to the asymptotic limit of the surface of interest, and zero values correspond to probability associated with the wave packet that is still in the interaction region. The loss of probability on one surface corresponds to the addition of probability on another surface at different times. Bands of oscillating peaks and valleys that form in the structure of the scattering WDF correspond to presence of secondary transmission or reflection with significant probability. The square well frequencies at which probability arrive in a scattering channel corresponds to the depth and width of the well. Scattering WDF were computed for the following combinations: $K+He$, $K+Ne$, $K+Ar$, $Rb+He$, $Rb+Ne$, $Rb+Ar$, $Cs+Ne$, and $Cs+Ar$. The scattering WDF revealed that as the mass of the noble gas increased, a significant proportion of probability was transferred from the $^2P_{3/2}$ pump state to the $^2P_{1/2}$ lasing state for a larger number of total angular momentum values. Similarily, as the mass of the alkali metal decreased, there was a reduced transfer of probability to make a transition from the $^2P_{3/2}$ state to the $^2P_{1/2}$ state. The reduced probability to make a transition from the $^2P_{3/2}$ to the $^2P_{1/2}$ manifolds for the $M+He$ collisions is compensated by the large average velocity of $He$. As a result, the $K+He$ system exhibits a large collisional transition rate despite the kinetic bottleneck caused by the light mass of $He$.

**15. SUBJECT TERMS**

scattering Wigner Distribution Function, square well, Alkali Plus Noble gas collisions, HOCO,$H + H_2$

| 16. SECURITY CLASSIFICATION OF: | | | 17. LIMITATION OF ABSTRACT | 18. NUMBER OF PAGES | 19a. NAME OF RESPONSIBLE PERSON |
|---|---|---|---|---|---|
| a. REPORT | b. ABSTRACT | c. THIS PAGE | | | Dr. David E.Weeks, AFIT/ENP |
| U | U | U | UU | 243 | 19b. TELEPHONE NUMBER *(include area code)* (937) 255-3636 x4561 David.Weeks@afit.edu |